ASSESSMENT OF POROUS HYDROXYAPATITE FOR BONE REPLACEMENT

KARIN A. HING

THESIS SUBMITTED FOR THE DEGREE OF DOCTOR OF PHILOSOPHY.

FEBRUARY 1996

INTERDISCIPLINARY RESEARCH CENTRE IN BIOMEDICAL MATERIALS, QUEEN MARY AND WESTFIELD COLLEGE.

UNIVERSITY OF LONDON.

"THE HIGHEST REWARD FOR A PERSON'S TOIL
IS NOT WHAT THEY GET FOR IT
BUT WHAT THEY BECOME BY IT."

- JOHN RUSKIN

TO:

MUM, DAD, ZANNA, AND DONALD

"HUMAN BEINGS ARE THE ONLY CREATURES ON EARTH
THAT ALLOW THEIR CHILDREN TO COME BACK HOME."

- BILL COSBY

ABSTRACT

Hydroxyapatite (HA) is a highly biocompatible calcium phosphate which closely resembles the mineral component of bone. Porous structures composed of biocompatible materials are believed to enhance fixation (and integration) as they encourage the ingrowth of bone into the implant. Consequently there is great interest in the potential of porous HA as an alternative to bone homografts and autografts. However, despite the interest in the field, there has been no thorough investigation into the physical and structural properties of porous HA and their effects on bone ingrowth.

The material used in this study was a carbonated apatite (containing < 0.9 % levels of trace element impurities) with a trabecular macrostructure, that had been converted from bovine cancellous bone. The apparent density of the material ranged from 0.35 -1.45 $g.cm^{-3}$ and the macrostructural morphology varied from an open equiaxed foam to a columnar honeycomb-like structure. The ultimate compressive stress was strongly related ($r = 0.9$) to the square of the apparent density, while compressive modulus was influenced by both apparent density and macrostructural morphology. Transmission electron microscopy of human osteoblast-like cells cultured on the material demonstrated that cells were closely associated with the surface. Specimens with densities of 0.6, 0.9 and 1.2 $g.cm^{-3}$ were then implanted in a lapine cancellous site for periods of 10 days, 3, 5, 13 and 26 weeks. After implantation all specimens elicited a highly biocompatible response, with active areas of bone deposition, remodelling and revascularization and no fibrous encapsulation. The amount of bone ingrowth within the implant (25-10%) after 5 weeks was found to vary with apparent density (0.6-1.2 $g.cm^{-3}$) indicating that osseointegration was a function of macrostructural morphology. Pushout testing of retrieved specimens indicated that all implants were securely fixed by 5 weeks (2-3 MPa). Compression testing demonstrated that after 5 weeks low density implants were sufficiently reinforced by bone ingrowth to equal the compressive strength of the host tissue (6 MPa) which increased to approximately 20 MPa at 3 and 6 months.

ACKNOWLEDGEMENTS

I would like to thank Professor William Bonfield and Dr. Serena Best for their supervision and support throughout the length of my PhD, and I would like to acknowledge that the *in vivo* work would have been impossible without the expertise of Professor Peter Revell and Dr. Liz Tanner.

I am indebted to the members of The Orthopaedic Institute at The Royal National Orthopaedic Hospital, Stanmore, for my crash course in cell culture and EM preparation, particularly David Lee, Lucy Di-Silvio and Mike Kayser.

The skills of Danny Osei, Chris Pirie and Simon Smith (all previously of the Histopathology Department at the Royal Free Hospital, Hampstead, and now scattered to the four corners of the globe - was it something I said?) with the Exakt cutting and grinding system were highly appreciated.

Thanks go to Johnathan Knowles and Ihtesham Rehmen for providing the XRD and FT-IR analysis respectively.

I would also like to thank:

- Catherine Belsham and Julie Spanton for their assorted secretarial skills.
- Bob Whitenstall of the EM unit at QMW for his assistance at × 1000.
- The denizens of QMW Media Services (Dave Bacon, Ray Crunwell, Terry Storey and Carol King) for their artistic input.
- The QMW engineering workshop technicians and Nigel Heath, of Heath Engineering, Whitney, for help with the design, and manufacture of the mechanical testing jigs (and the cork screw).

Finally, thanks to Mum and Dad for putting up with key tapping at 2.00 am, Donald for translating portions of my "work" (eventually) and, to the inmates (past, present, and future) of Room 207, and other assorted PhD "students", thanks for all the moral support, floor space, beer, and fish.

TABLE OF CONTENTS

CHAPTER 2 SYNTHETIC HYDROXYAPATITE

CHAPTER 3 MECHANICAL PROPERTIES OF BONE AND HYDROXYAPATITE

CHAPTER 4 BONE REPLACEMENT

LIST OF TABLES

CHAPTER 2

CHAPTER 3

CHAPTER 4

CHAPTER 5

CHAPTER 6

CHAPTER 7

LIST OF FIGURES

CHAPTER 1

CHAPTER 2

CHAPTER 3

CHAPTER 4

CHAPTER 5

CHAPTER 6

CHAPTER 7

APPENDIX

INTRODUCTION

The biocompatibility of hydroxyapatite $\{Ca_{10}(PO_4)_6OH_2\}$ and the similarities between the crystal structure of hydroxyapatite (HA) and bone mineral have led to considerable interest in HA as a material for the augmentation of osseous defects. However, in bone, apatite crystals form in the presence of many complex and varied physiological fluids and as a result of this environment, the calcium ions undergo substitution by elements such as strontium and sodium, while the hydroxyl and phosphate groups are reported to be readily exchanged with carbonate groups. In contrast, synthetic hydroxyapatites are generally produced in as pure a form as possible. Bone is not only responsible for load bearing, but it also acts as a calcium and mineral reservoir, with impurities playing important roles in the mineral homeostasis and metabolic processes of the surrounding tissue. It therefore follows that the identification and introduction of controlled levels of impurities in any hydroxyapatite introduced *in vivo* could be advantageous, in order to encourage interaction between host tissue and implant. The use of low density HA, with highly interconnected porosity, has recently been advocated as a viable alternative to bone grafts without the sterilisation, infection, rejection and supply complications. The porous structure encourages the ingrowth of bone into the implant, presenting a more mechanically and biologically integrated repair. However, although the morphology of biomedical implants has been of interest since the use of a porous aluminate ceramic, impregnated with epoxy resin, was described by Smith (1963a), there has been no systematic study on the effects of varying pore morphology on bone ingrowth within HA implants. Similarily, the effect of morphology on the mechanical properties of implants must also be considered, since any substitute material for bone should ideally match the load-bearing capabilities of the host tissue in order to avoid stress shielding in the bone, or mechanical failure of the implant.

This thesis details a systematic study of a novel porous hydroxyapatite implant material, which is produced from bovine cancellous bone. The chemical composition, morphological characteristics and mechanical properties of the material were all thouroughly investigated, in conjunction with an assessment of biocompatibility, both *in vitro* and *in vivo*.

CHAPTER 1

BONE PHYSIOLOGY

1.1 Introduction

Bone is a living, highly vascular, dynamic, mineralised, connective tissue, which is characterised by its hardness, resilience, growth mechanisms, and ability to regenerate. Simply, bone is a dense multi-phase material or "composite" made up of cells embedded in a matrix composed of both organic (collagen fibres, lipids, proteins, polysaccharides) and inorganic (calcium-phosphates, carbonates, sodium, magnesium, fluoride salts) elements. However, its structure and proportion of its components differ widely with age, site, and history, resulting in many different classifications of bone which exhibit totally different mechanical and functional characteristics (Williams and Warwick, 1989).

Bone is not purely a structural tissue, but also acts as a mineral reservoir for the rest of the body; consequently, bone in its natural environment undergoes constant remodelling and chemical exchange with the rest of the body, and is subject to continual changes in its composition and structure, due to both sporadic cellular activity and external mechanical demands. Furthermore, when necessary, the mineral function supersedes the structural function, resulting in loss of integrity in the bone structure.

1.2 Constituents of Bone

On an elementary level bone may be split into three main components: bone matrix, bone cells, and bone marrow. The bone matrix provides mechanical strength and stores the minerals required by the body, the various bone cells are responsible for maintaining the structure of the matrix, regulating its oxygen and nutrient supply, and storing or releasing minerals as required, while the marrow provides the source of bone cells, oxygen and nutrients.

1.2.1 Bone Matrix

The bone matrix may be split into three main constituents: the collagen fibres, the bone mineral crystals, and the ground substance,which is composed of a number of organic and inorganic compounds. Together the inorganic crystals and collagen make up the bulk of bone matrix. In mature bone 10-20% of the matrix is water, and of its dry weight approximately 60-70% is made up of inorganic bone mineral and 30-40% is collagen, the remainder (2-5%) being composed of other organic molecules, proteins and inorganic salts.

1.2.1.1 Collagen

Collagen is the most abundant protein found in the body, and occurs in a number of different connective tissues both calcified and non-calcified. Collagen accounts for 70-90% of the non-mineralised component of the bone matrix and varies from an almost random network of coarse bundles to a highly organised system of parallel-fibred sheets or helical bundles. Collagen consists of carefully arranged arrays of tropocollagen molecules, which are long rigid molecules (300nm long, 1.5nm wide) composed of three left handed helices of peptides ("monomers" of proteins composed of amino acid sequences) known as α-chains that are bound together in a right handed triple helix. The triplet amino acid sequence, glycine-X-Y, repeats throughout each α-chain, where X is usually proline, and Y is often hydroxyproline or hydroxylysine. Although all α-chains contain the glycine-X-Y sequence, different types of collagen may be produced via the combination of different amounts and sequences of other amino acids within the tropocollogen molecule. To date 13 different types of collagen have been identified, although only the five principal types have been fully characterised. Bone contains mostly type I collagen with some type V collagen. Type I collagen is the most abundant form, accounting for 90% of the body's total collagen; it contains two

identical and one dissimilar α-chains ($\alpha1(I)_2\alpha2$) within its tropocollogen molecule. Molecules of both types I and V are organised into collagen fibrils, which are formed by the assembly of tropocollagen molecules in a $^3/_4$ stagger, parallel array (Figure 1.2.1).

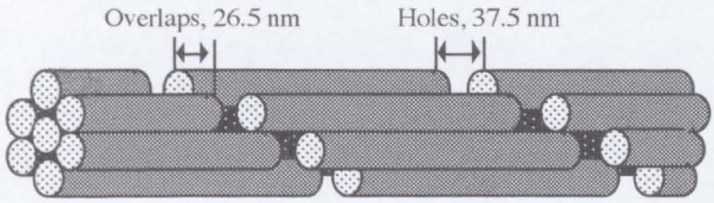

Figure 1.2.1 Model of the collagen fibril arrangement

As a result of this assembly the fibrils exhibit characteristic cross striations or banding which occurs in a repeating pattern every 55 - 75 nm, average 64 nm (Robinson & Watson, 1952). The fibrils are stabilised by inter and intra-molecular crosslinks (the number and distribution of which determine whether the tissue will mineralise), and have individual diameters of 40-120 nm, average 100 nm. In type I collagen the fibrils are wound into bundles to form collagen fibres which range in diameter from 0.2-12 μm (Figure 1.2.2) (Kielty *et al.*, 1993).

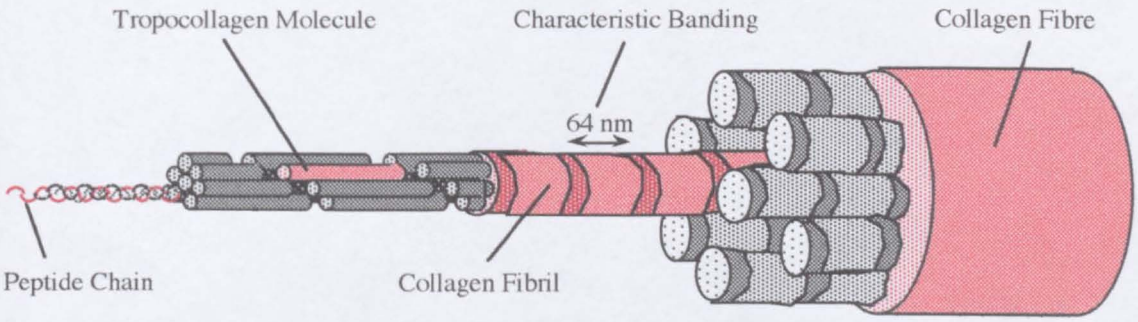

Figure 1.2.2 Hierarchical organisation of collagen fibres

Information on the mechanical properties of collagen is only available for cartilage, vertebrate tendon, and ligament (of which collagen makes up 70-80% of the dry weight). Tendon has a Young's modulus of 1.5 GPa and a tensile strength of 100 MPa (Bennett *et al.*, 1986). Collagen fibres *in vivo* are "crinkled", and under a tensile load these straighten out and become parallel before exhibiting elastic behaviour up to a strain of approximately 4%. They fracture at a strain of 8-10% due to the pulling apart of adjacent molecules.

1.2.1.2 Bone Mineral

The main inorganic phase within bone is usually referred to as hydroxyapatite (which has a chemical formula of $Ca_{10}(PO_4)_6(OH)_2$ and a Ca:P ratio of 5:3 {1.66}) as a result

10 : 6
5 : 3

of similarities between the X-ray diffraction patterns of synthetic hydroxyapatite and bone mineral crystals (de Jong, 1926). However, bone mineral is characterised by calcium and hydroxyl deficiency (reported Ca:P ratios of 1.37-1.87, Mc Connel,1973), ionic substitution within the apatite lattice, and internal crystal disorder - it is not a direct analogue of hydroxyapatite as is commonly believed. Precise information on the composition and chemistry is still unsure due to difficulties in applying standard analytical techniques to the small sized crystals and meagre quantities of material available. Work carried out by Posner (1969) indicated that bone mineral is about 10 % deficient in calcium, while more recently Driessens (1983) proposed that bone mineral consisted of 15 % magnesium Whitlockite $\{Ca_9Mg(HPO_4)(PO_4)_6\}$, 25 % sodium and carbonate substituted apatite $\{Ca_{8.5}Na_{1.5}[(PO_4)_{4.5}(CO_3)_{1.5}]CO_3\}$, and 60 % carbonated octacalcium phosphate $\{Ca_8(PO_4)_4(OH_2)_2CO_3\}$; a significant variation from pure hydroxyapatite. In addition to the confusion surrounding the exact content of the mineral, differing infra-red (IR) and X-ray diffraction (XRD) studies suggest alternatively that the planar CO_3^{2-} ions adsorb to the surface of bio-apatite or substitute for the tetrahedral PO_4^{3-} groups and the OH^- groups (Figure 2.2.2), inducing atomic misalignment in both poor and well crystallised bone mineral. IR studies also indicate much internal disorder in the crystal lattice (Montel, 1968; Boskey and Posner, 1984). These factors all contribute to an apatite which is insoluble enough for stability, yet sufficiently reactive to allow the *in vivo* sub-microscopic crystallites to be constantly resorbed and reformed as required by the body.

Another factor affecting the high solubility of the individual crystals is the sub-microscopic crystal size - the Gibbs-Kelvin equation states that beyond a certain cut off point, small crystals are more soluble due to their larger specific surface at which ionic bonding is weaker. However, there is much confusion in the literature regarding the size and shape of apatite crystals. Measurements of the size of bio-apatite crystals via direct observation using electron microscopy differ from calculated findings using X-ray diffraction techniques, and different researchers using electron microscopy disagree as to whether the crystals are plate-like or rod-like in shape. A typical study of bone from human, ox, and rabbit femora using both X-ray and electron microscope techniques reported that bio-apatite crystallites were plate shaped, 5-6 nm in their shortest dimension, and an average 32-36 nm in their longest dimension, with a maximum length of 100 nm (Francis *et al.*, 1973). Whereas, Posner (1978a) stated that theoretically, the average largest dimension of bone crystals should be 40-50 nm, with the other two dimensions being in the range 20-35 and 2.5-5 nm. There are also additional complications regarding species, age and health.

While many investigators of calcification agree that mineralisation originates within matrix vesicles (Anderson *et al.*, 1980), there is some disagreement about the exact mechanisms of the process (Landis, 1981). It seems likely that both cellular and physiochemical factors are involved. Generally amorphous calcium phosphates with a Ca:P ratio varying between 1.44-1.55 (Vaughan, 1975) are believed to be deposited under the control of osteoblasts; the mineral then slowly transforms into apatite independently of the cells. *In vitro* studies have been used to try to provide an insight into the formation of bio-apatite *in vivo*. Hydroxyapatites precipitated directly from solutions with low supersaturation are reported to form very fine dot-like crystals (Boskey and Posner, 1976), while hydroxyapatites prepared from solutions under physiological conditions with physiological calcium and phosphate contents form submicroscopic needle shaped crystals. Furthermore, hydroxyapatite precipitated from highly supersaturated calcium phosphate at a pH of 7 or more was preceded by an amorphous phase with a Ca:P ratio of 3:2 (1.5), which converted autocatalytically into finely divided non-stoichiometric hydroxyapatite. This non-stoichiometric compound then ripened slowly, approaching stoichiometry and growing in crystal size with time (Blumenthal and Posner, 1973).

Dense (i.e. >97% dense) synthetic hydroxyapatite has a Young's modulus of 80-117 GPa (Akao *et al.*, 1981; de With *et al.*, 1981b), and a tensile strength of 90-120 MPa (de With *et al.*, 1981b; Best, 1990); however, it has a low fracture toughness of 0.9-1.3 $MPa.m^{1/2}$ (Best, 1990). It has also been reported that both the tensile and fracture strength decrease by up to 25% in the presence of water (de With *et al.*, 1981a and b).

1.2.1.3 Ground Substance

In most regions of bone the collagen fibrils are so densely packed into fibres, and the fibres into bundles, that it is difficult to observe the ground substance; however there are certain areas where fibre free bands 1-2μm wide may be viewed with an optical microscope. From chemical analysis of bone it may be concluded that these bands contain primarily a number of sulphated and acid mucopolysaccharides, the latter being mainly hyaluronic acid, which forms a hydrated gel that is hydrophilic and therefore traps tissue fluid. The sulphated mucopolysaccharides stiffen the matrix. Glycoproteins, lipids, peptides, carbonates and citrates, as well as sodium, magnesium and fluoride salts are also present (Cameron, 1972). It has also been postulated that amorphous tricalcium phosphate is present as a reservoir for hydroxyapatite crystallite nucleation and growth (Bienenstock and Posner, 1968; Posner, 1969). Osteonectin binds the hydroxyapatite crystallites surrounding the collagen fibrils in a highly organised geometrical arrangement. Osteocalcin is thought to play a role in calcium

deposition, while other organic substances present in small amounts in the matrix are thought to be responsible for promoting the initial nucleation and deposition of bio-apatite, and regulating the orientation, size and rate of growth of the crystals (Williams and Warwick, 1989).

1.2.2 Bone Cells

Of the many cells associated with bone, three are of special interest: the osteoblast, osteocyte, and osteoclast, which are responsible for the production, maintenance, and resorption of bone, respectively. However, they are highly specialised differentiated cells and do not generally proliferate. Less differentiated cells of the same lineage are required for the control of the cell population, and, as demands are made on or by the bone, these cells proliferate and differentiate as required. Such cells are generally known as stem cells, and in the case of bone deposition are often referred to as osteogenic cells. The osteogenic cells originate from the bone marrow stromal cell line and exist in the endosteum and periosteum (Owen, 1978). Biochemical and mechanical triggers such as remodelling and fracture healing result in the requirement for local population increases in bone producing cells. The route of differentiation undertaken by an osteogenic cell is determined by the local environment, resulting in the evolution of either osteoblasts or chondroblasts (Bourne, 1972; Vaughan, 1975). High vascularity, i.e. the availability of nutrients and oxygen in the surrounding environment, is necessary for the growth and nourishment of healthy bone. Bone metabolises significant amounts of oxygen, but, being densely mineralised, is unable to sustain itself via osmosis or similar methods of diffusion over long distances. It therefore relies on Haversian canals, interconnected by Volkmann's canals and canaliculae, to circulate oxygen and essential nutrients, which then diffuse over shorter distances. Conversely, cartilage requires little or no oxygen for metabolism, and being composed mainly of unmineralised, although densely packed, collagen fibres is able to sustain itself via the diffusion of nutrients through the cartilaginous matrix. Thus if the environment surrounding a differentiating osteogenic cell has a high vascular content, as in healthy bone, the cell will differentiate into an osteoblast which will produce bone, then when the osteoblast has surrounded itself by bone it differentiates into an osteocyte and becomes involved in the nutrition and maintenance of the local bone (Figure 1.2.3). However, if the environment surrounding a differentiating osteogenic cell has little or no vascular content, as in a recent fracture site, the cell will differentiate into a chondroblast and cartilage will be produced. Once the chondroblast is surrounded by cartilage it then differentiates into a chondrocyte (Figure 1.2.3), which maintains the

surrounding collagenous matrix until it is replaced by bone during endochondral ossification (Jee and Kimmel, 1976; Owen, 1978). There is some evidence that chondrocytes may in some instances differentiate into osteoblasts during subsequent endochondral ossification, but in most cases they die and are replaced by new osteoblasts (Roach, 1995).

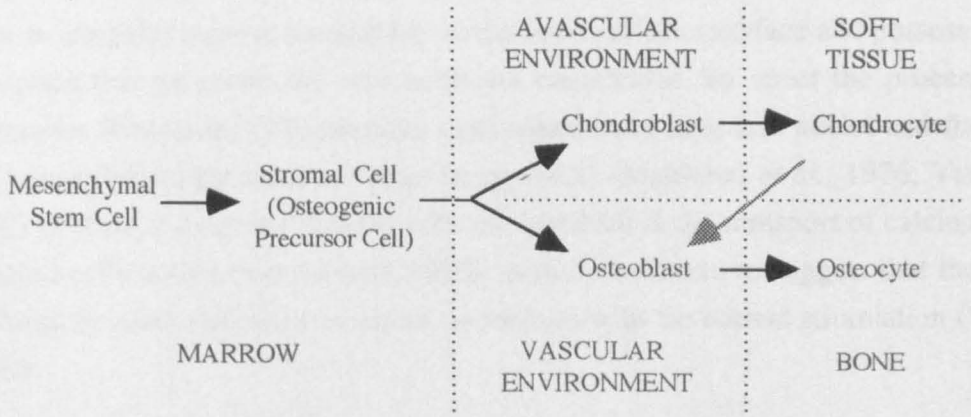

Figure 1.2.3 Differentiation of osteogenic cells

1.2.2.1 Osteoblast

Osteoblasts are found wherever new bone is being formed, in a layer covering the new unmineralised bone or osteoid. Osteoblasts possess three main cellular features: a large nucleus, usually at the pole furthest from osteoid deposition; a well developed Golgi apparatus, found in the juxtanuclear area; and a high concentration of granular endoplasmic reticulum and some free ribosomes, the bulk of which usually lie at the opposite end of the cell to the nucleus, with some spreading around both the nucleus and the Golgi apparatus. Throughout the cytoplasm there are scattered mitochondria and lysosomes (Figure 1.2.4) (Cameron, 1972; Vaughan, 1975; Revell, 1986; Williams and Warwick, 1989).

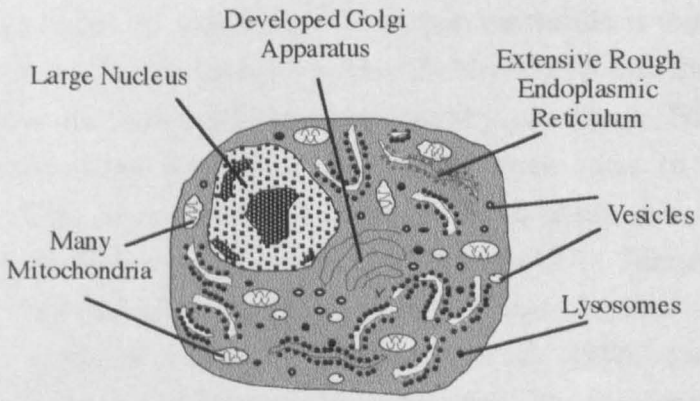

Figure 1.2.4 A sketch of an osteoblast showing cellular features.
Adapted from Revell, 1986.

The cells tend to be plump and elongated in one axis, although the shape of individual cells varies considerably and is dependent on the proximity of neighbouring cells and bone surface. There are also differences in appearance between "active" and "resting" osteoblasts. Active osteoblasts are found on bone surfaces where bone is being laid down, tend to be plumper with the nucleus at the end furthest from the bone surface, have an irregular contour particularly at the bone surface interface and possess fine processes that penetrate the new bone via canaliculae to meet the processes from osteocytes (Cameron, 1972). Resting osteoblasts have long thin nuclei and flat bodies, and are described by some as "bone lining cells" (Matthews *et al.*, 1976; Vanderweil, 1980) as there is evidence that the cells are involved in the transport of calcium and are metabolically active (Vanderweil, 1980), with no evidence to suggest that they cannot perform the same functions as active osteoblasts with the correct stimulation (Vaughan, 1975).

Osteoblast Function

The main function of osteoblasts is the laying down of bone and their activity in this respect may be divided into four main areas: the synthesis of collagen, the synthesis of some of the carbohydrate protein complexes present in the ground substance, the deposition of calcium (calcification), and the maintenance of the local concentration and exchange of calcium (mineral homeostasis). They may also be responsible for the concentration of proteins found in the bone matrix. Collagen is synthesised within the cell in the form of procollagen, which is a longer molecule than type I tropocollagen and contains a significant proportion (about one third of the molecule) of additional pro-peptides. This procollagen is then secreted into the matrix where cleavage to tropocollagen and assembly into the collagen fibril takes place. There are a variety of carbohydrate proteins present in bone matrix; some originate from the plasma, while others are synthesised by osteoblasts. Mucopolysaccharide is thought to be extruded from these cells via Golgi derived vesicles (Leblond & Weinstoccl, 1971), and some glycoproteins are also believed to be synthesised by osteoblasts (Triffit & Owen, 1973). Osteoblasts have been implicated in at least three roles in the mechanism of calcification. First as the origin of matrix vesicles (Anderson, 1978), secondly by controlling the movement of calcium ions (Talmage 1970; Talmage & Grubb, 1977), and lastly by their ability to store calcium in their mitochondria and pass it on to the matrix. As mentioned previously (Matthews *et al.*, 1976), there is evidence that osteoblasts are involved in the transport of calcium. The movement of ions is thought to be controlled by PTH (parathyroid hormone) which is known to stimulate both calcium uptake and loss (Cameron, 1972).

1.2.2.2 Osteocyte

During growth or remodelling, osteoblasts become "buried" in calcified tissue as they are walled in by overlying cells and subsequently differentiate into osteocytes. Osteocytes are spidery in shape with plump bodies and up to fifty long fine branching cytoplasmic processes (Figure 1.2.5). There is much variety in their size, shape and cytoplasmic detail as well as in their density and orientation in the matrix. When newly formed, they almost fill their lacunae and resemble the osteoblasts from which they originated, but as they mature, they lose some of their cytoplasm and become surrounded by amorphous material and loose collagen fibres within their lacunae. They also become flatter (that is more oval) and have less organelles. The Golgi apparatus, found in the juxtanuclear area, is no longer well developed and there is a reduced concentration of granular endoplasmic reticulum. Old osteocytes also contain some free ribosomes, centrioles and many small vesicles, some of which are coated. Young osteocytes have a more basophilic cytoplasm, a greater concentration of endoplasmic reticulum and a more prominent Golgi apparatus. (Cameron, 1972; Vaughan, 1975; Williams and Warwick 1989).

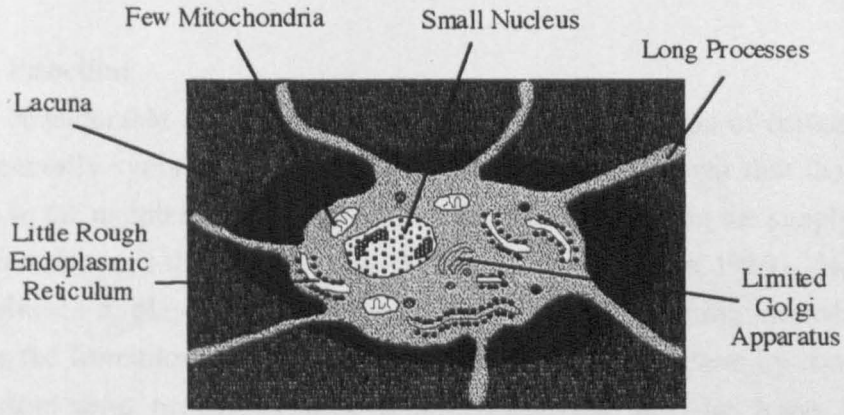

Figure 1.2.5 Some features of an osteocyte

Adapted from Revell, 1986.

Osteocytes occur in small holes called lacunae that are connected together via a network of interconnecting canaliculi containing anastomosing cell processes. In young woven-bone they are closely but irregularly packed and almost indistinguishable from the osteoblasts, and their processes are relatively few and short. In mature lamellar bone the osteocytes are evenly spaced, flattened, ovoid, and possess numerous fine branching processes. In cortical bone they tend to be oriented with their longest axis circumferential and the shortest axis radial to a vascular canal with a slight tendency to be more numerous at the periphery of an osteon (Pritchard, 1972). In cancellous bone (Figure 1.2.6) the long axis tends to be perpendicular to the direction of bone apposition of the lamellar system it occupies.

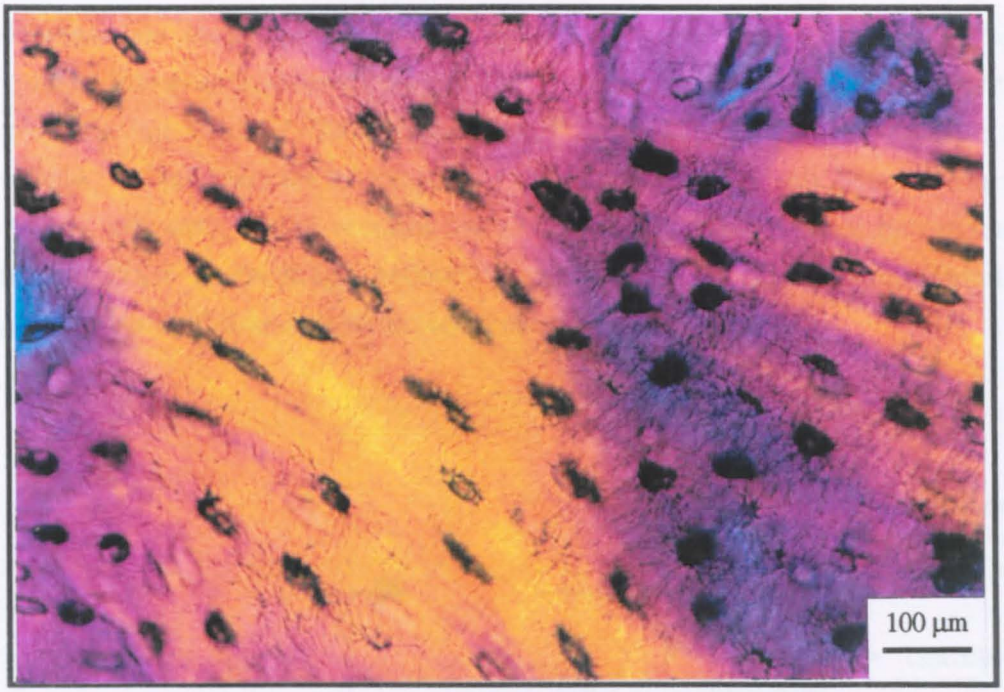

Figure 1.2.6 Photomicrograph of osteocytes in mature lamellar bone

Osteocyte Function

There is a considerable amount of dispute regarding the function of osteocytes. Their death is generally synonymous with bone death and it is thought that their processes play a role in the maintenance of canaliculi and thus in sustaining the supply of oxygen, nutrients and minerals throughout bone (Williams and Warwick 1989). However they are also believed to play a mechanosensory role in bone, detecting microfractures and modulating the formation and activity of osteoblasts and osteoclasts by contact through their anastomosing processes with other osteocytes and the bone lining cells (Bevelander and Ramaley, 1979; Lanyon, 1987). In conjunction with osteoblastic activity, osteoclasts may also be involved in the maintenance of constant levels of plasma calcium and inorganic phosphate (Cameron, 1972), and are capable of resorbing and depositing bone on their lacunae surfaces, phenomena known as osteolysis and osteoplasis, respectively. No osteocyte is further than 0.2 mm from a capillary that could act as a source of nutrients, and the network of osteocyte processes running through canaliculi form, according to Baud (1968), an exchange area of 250 mm^2 per mm^3. It has been shown that albumin is removed from blood plasma and concentrated in bone matrix as blood passes through the bone from the endosteal to the periosteal surface (Owen *et al.*, 1977).

1.2.2.3 Osteoclast

The osteoclast had long been thought to share a common stem cell with the bone forming cells, however it is now believed that a mononuclear blood cell is origin of osteoclast (Jee and Kimmel, 1976; Owen, 1978; Vaughan, 1975). Osteoclasts are believed to be derived from the hematopoietic cell (a mononuclear cell derived from the haemopoietic marrow), which reaches the tissue via the blood stream to become a mononuclear bone macrophage before fusing with either another mononuclear macrophage or an established multinucleated osteoclast (Figure 1.2.7).

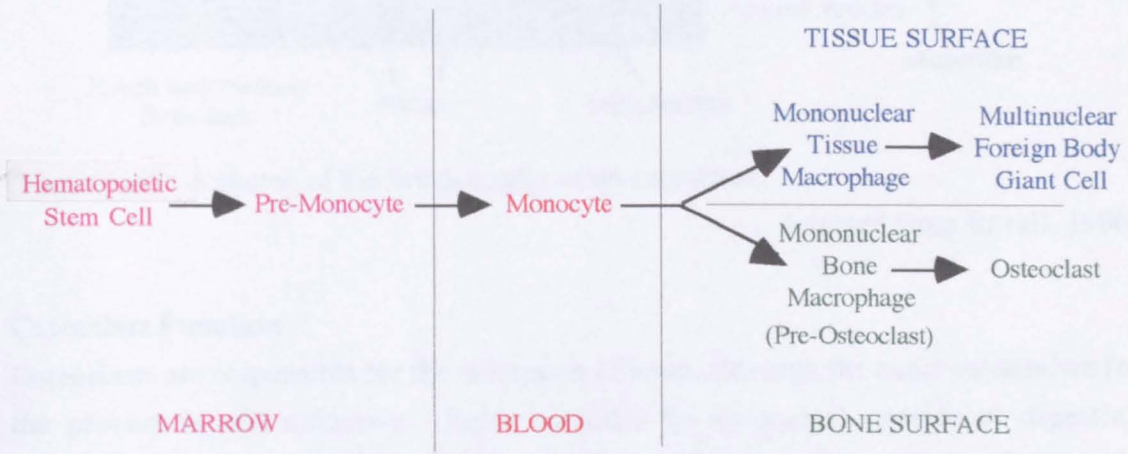

Figure 1.2.7 Differentiation of osteoclasts

Osteoclasts are aggressive cells that are responsible for the majority of bone resorption, although the mononuclear bone macrophages, are also involved in bone resorption during remodelling and fracture repair (Evans *et al.*, 1980; Baron *et al.*, 1980; Parfitt, 1993). They are easy to distinguish, being the multinucleated cells (the largest having 100 nuclei, the smallest two, with an average of 10-20) lying in Howship's lacunae on the bone surface undergoing resorption. Their cytoplasm contains many mitochondria, a low concentration of granular endoplasmic reticulum, a small Golgi apparatus and many smooth and coated vesicles (some of which contain fragments of dense materials). They also have characteristic brush borders, these have a ruffled appearance and are found at the active resorbing bone/cell interface, they are specialised areas of the plasma membrane composed of a collection of folds and finger like projections and there may be more than one such region per cell. The folding is not ordered but similar to that on the surface of macrophages and both apatite crystals and collagen fibrils can be found in between the folds.

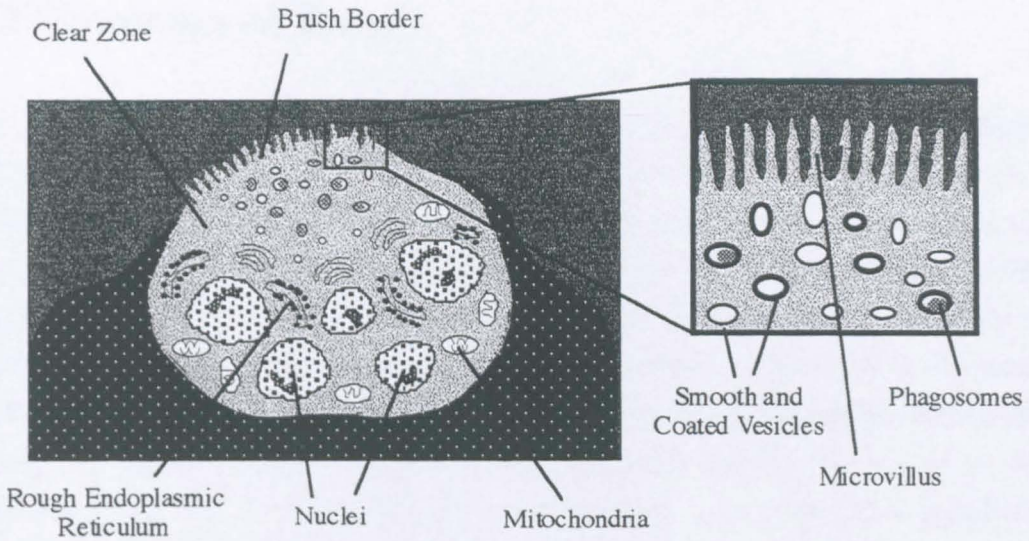

Figure 1.2.8 A sketch of the brush border of an osteoclast.

Adapted from Revell, 1986.

Osteoclast Function

Osteoclasts are responsible for the resorption of bone, although the exact mechanism for the process is still unknown. Some consider the osteoclast capable of digesting collagen fibres within their lysosomes or vesicles, as well as the secretion of citric and lactic acids which dissolve the mineral component of the bone matrix, thus releasing the fibres for digestion (Reynolds, 1968; Hancox, 1972), while others believe that mononuclear cells are solely responsible for the resorption of the fibres (Heersche, 1978).

1.2.3 Bone Marrow

Marrow takes no part in the supportive function of bone. In early life it consists of a frame work of reticular tissue, adipose (fat) tissue, stroma and hematopoietic cells and is known as red marrow. In some regions the hematopoietic cells disappear with age and is then termed yellow marrow (Williams and Warwick, 1989). The stroma cells of marrow have the potential for cartilage and bone formation whereas the hematopoietic cells differentiate into white and red blood cells.

1.3 Structure of Bone

The structure of bone has been classified (seemingly by default) into a number of different categories over a series of arbitrary levels of magnification. These levels are:- (a) macro-structure, (b) micro-structure, (c) ultra-structure and (d) molecular-structure. Architectural differences that can be distinguished by the eye are considered different categories of macrostructure examples of which include cortical and cancellous bone, however cancellous bone (especially that in long bones) may also be divided into regional classes with differing structural fabric, these being diaphysial, metaphysial or epiphysial. Distinguishing microstructural variations requires the aid of an optical microscope and typical categories at this level include woven, bundle or lamellar bone and distinctions between primary and secondary osteons. At the ultrastructural level the relative positions and degree of orientation between the collagen fibrils and inorganic crystals may be studied with the aid of scanning and transmission electron microscopy. Transmission electron microscopy is used along with chemical analysis techniques to discern the crystal structure and chemical content of the inorganic phase at the molecular level. As some aspects of the ultrastructure and microstructure of bone have been discussed with-in section 1.2 these topics will dealt with first.

1.3.1 Ultrastructure of Bone

There is much disagreement in the literature regarding almost all aspects of ultrastructure. This may be partly due to the complex techniques necessary for different methods of specimen preparation and the difficulty in avoiding artefacts from these methods. There are also different views held on apatite nucleation routes, sites and the relationship between the collagen and the apatite crystals.

Robinson (1952) was the first to demonstrate that the apatite crystals had their long axes parallel to that of the collagen fibrils and proposed that they were arranged at 64 nm intervals in rings around the fibrils. However the precise nature of the relationship between the two is still unsure. A number of authors (Cameron, 1972; Glimcher, 1976; Landis, 1981) have shown that the relationship between the collagen fibrils and the apatite crystals is characterised by highly ordered deposition of individual solid phase mineral particles within the collagen fibrils, where the particles are oriented with their long axes (c-axis) parallel to the long axis of the fibrils with regular periodic distributions (70 nm) of the mineral mass corresponding to the axial

periodicity of the collagen fibrils. Some also report preferential location of the mineral phase in discrete regions of the fibril during early mineralisation (in the holes found between the tropocollagen molecules) with larger proportions of mineral occurring between fibrils and in fibril overlap zones (Glimcher, 1976; Landis, 1981) and suggest that collagen acts as a nucleating agent. This view has been disputed by a number of authors (eg. Vaughan, 1975; Cameron, 1972; Boskey and Posner, 1984) who agree that there is an alignment between the crystals and fibrils, but believe that nucleation occurs as a result of biochemical and cellular activity and that ground substances such as osteonectin bind the bone mineral crystallites surrounding the collagen fibrils in a highly organised geometrical arrangement.

By looking at the variations in the thickness and arrangements of the collagen fibre bundles Wiedenreich (1930) distinguished five fundamental types of bone, these were:

(1) Bone with coarse parallel fibre bundles.
(2) Bone with coarse woven fibre bundles.
(3) Bone with fine parallel fibre bundles.
(4) Bone with fine lamellated fibre bundles.
(5) Bone with mixed coarse and fine fibre bundles.

For most purposes, although accurate this classification is reduced to three groups which are known as bundle bone, woven bone and fine fibred or lamellar bone.

1.3.1.1 Bundle Bone

This is made up from coarse parallel (1) and some of the coarse woven (2) bone described above, it is characterised by regularly arranged coarse fibre bundles which dominate the matrix and can be seen when stained with hematoxylin and eosin. The osteocytes follow the pattern of the fibre bundles and lie in columns between the bundles where the bundles run parallel. It is found at the interfaces between bone and tendon or ligaments and in foetal bone and early fracture callus. It develops in a very orderly manner by the osteoidisation and calcification of tendon or ligament whose cells are replaced by osteoblasts and osteocytes.

1.3.1.2 Woven Bone

This is a special type of the coarse woven bone (2), it forms very rapidly and rather erratically and contains a small number of stout, irregularly arranged fibre bundles of varying size (up to 30 μm in diameter). It is easily recognised when stained with hematoxylin and eosin due to the number of randomly packed osteocytes and the bluish-purplish staining of the matrix (high content of basophil cement). In micro-radiographs it stands out,as woven bone is more highly calcified that the other types.

Perhaps due to its capability for rapid formation, it is found only in early fracture callus, and is soon replaced by the more ordered lamellar bone.

1.3.1.3 Lamellar Bone

Fine fibred or lamellar bone is believed to be composed of fine parallel fibre bundles (3) and fine lamellated fibre bundles (4), the latter of which occurs in normal mammalian adult bone, while parallel fibre bundles are present in young endochondral bone and in simple primary osteons of mammalian foetal skeletons. In ordinary histological preparations fine fibred bone has a clear eosinophil matrix and the osteocytes are relatively small, uniformly ovoid and spaced at regular rather wide intervals. It develops slowly and deliberately as a thickening lining to vascular canals in existing bone or calcified cartilage or as a compact surface layer on an existing bone. Its formation is associated with the appearance of a single layer of osteoblasts on surfaces where bone is being laid down.

The characteristic lamellar appearance has been thought to be due to variations in the orientation (0-90°) of fibre bundles between successive layers (Gebhardt, 1906), where the parallel fibre bundles of each layer are all oriented in the same direction. Individual lamellae were then characterised by the alleged orientation of the fibres with respect to the axis of secondary osteons giving transverse or longitudinal lamellae. However, this widely excepted view has been disputed by Marotti (1993), who believes that the lamellar appearance is due to the alternating dense and loose packing of woven fibre bundles, and that the collagen forms a continuum throughout individual osteons.

1.3.2 Microstructure of Bone

Mature bone is composed of two types of tissue, one of which is dense, known as cortical or compact bone, the other consists of a network of struts or trabeculae surrounding interconnected spaces or cancelli, called trabecular, cancellous or spongy bone. Cortical bone is always found on the exterior of a bone and acts as a skin around the delicate trabeculae, while cancellous bone is found in the interior of bones, such as within the femoral head, and vertebra.

There are two kinds of cancellous bone, coarse and fine. Coarse cancellous is characteristic of healthy adult mammalian skeleton while fine cancellous bone is characteristic of the foetal skeleton, secondary centres of ossification or early fracture callus and comes in two forms, fine cancellous membranous bone and fine cancellous

cartilaginous bone. There are also several types of cortical bone; surface, primary and secondary osteonal cortical bone and as with the cancellous bone the distinctions are dependent on the age and origins of the bone.

1.3.2.1 Cortical Bone

Mammalian cortical bone is almost entirely comprised of lamellar bone. It is built up via either the consolidation of fine cancellous membrane and cartilage bone, in which cylinders of new bone called primary osteons are formed, or as a direct deposit of solid bone on the periosteal and medullary surfaces of existing bone shaft forming circumferential lamellae of bone, or finally, during remodelling of existing compact bone, in which existing cylinders of bone are eroded and then refilled with new bone to become secondary osteons. The relative amounts of primary and secondary osteons within osteonic bone varies considerably from bone to bone even within an individual, while some mammals (e.g. mice and rats) only develop secondary osteons as a result of skeletal injury. Very approximately however, primary osteon bone can be considered as characteristic of the cortex of long bones in young mammals, surface bone is added as the animal continues to grow, while the proportion of secondary osteons gradually increases with time as a result of remodelling. As put forward by Cohen and Harris (1958) osteons have no definite end when traced longitudinally, they are part of a dense three dimensional network of branching and converging tubular or cylindrical elements (Figure 1.3.1).

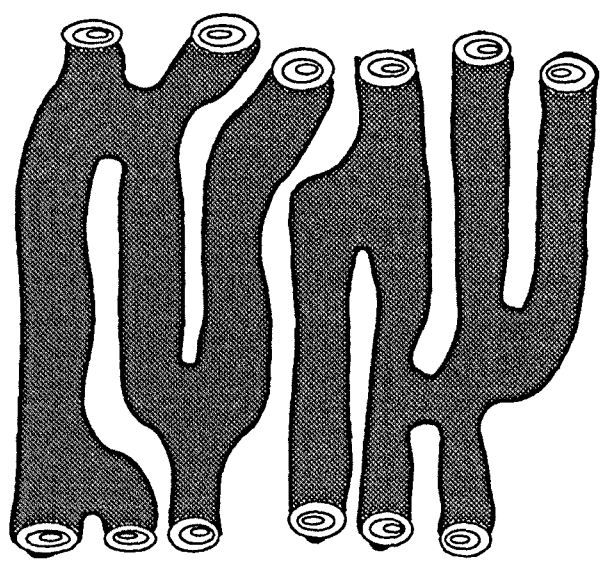

Figure 1.3.1 A schematic diagram of an osteonic network

Adapted from Martin and Burr, 1989.

Generally all osteons or Haversian systems consist of a small central or Haversian canal which is surrounded by concentric lamellae of bony tissue. Between these lamellae are

a number of small regularly arranged osteocyte lacunae which are connected with each other and the central Haversian canal by many fine interconnecting canaliculi. These contain the osteocyte processes which radiate out from the cells in all directions but soon turn to run in a radial direction, around the central canal. Osteocytes have a slight tendency to be more numerous at the periphery of an osteon than at the centre. With close examination it is possible to distinguish one type of osteon from the other. Fortunately most osteons have their long axis approximately parallel to the shaft of the bone so when sectioned in a transverse direction they appear with an essentially circular (as opposed to elliptical or parallel sided) profile. Secondary Haversian systems are easier to discern as they as larger (≈ 100 μm in diameter, Epker *et al.*, 1964), bounded by a clear "cement" line and their organisation stops abruptly at the cement line and does not conform with the organisation of adjacent osteons. The Haversian canal in a secondary Haversian system will usually contain only a single capillary or blood vessel. Haversian systems are separated by irregular angular wedges of "interstitial bone" which are the remains of older osteons partly resorbed during remodelling. Primary Haversian systems are smaller but may contain two or more vessels. They have no cement lines, their organisation fits in better with their neighbours and there is no interstitial bone between them.

Due to constant remodelling, the average life of an osteon has been reported at 15 years in adult humans (Lee, 1964) and will be much shorter in children, the bones of large mammals often contain developing and disappearing osteons. The former are much more numerous, as it seems osteons can be resorbed faster than they can be built, and are easy to recognise as the vascular canal possesses a large diameter and has a layer of plump osteoblasts on its wall. Osteons undergoing resorption also possess large central canals but their outlines are irregular and the cells present are osteocytes. It has been reported (Epker *et al.*, 1964) that osteons in mature mammals can be manufactured in 50-100 days depending on species. However, although the first 70% of the mineral may be laid down within a day or two of the formation of the osteoid matrix, the remaining 30% may take several months to complete. Thus in any piece of bone there will be osteons present with varying degrees of mineralisation.

Bone found encircling the inner and outer surfaces of whole bones consists of circumferential lamellae and Volkmann's canals. These canals contain blood vessels that connect the marrow cavity and the periosteum to the Haversian canals. The matrix and the osteocytes of surface bone are not organised with respect to the Volkmann's canals as they are to Haversian canals in osteonic bone, but conform with the surface

contours of the shaft. Surface bone is not deposited at a steady rate during growth resulting in cement lines termed accretion lines which mark the sites where growth was temporarily arrested. Similarly reversal lines, which are irregularly scalloped, mark where growth was resumed after a phase of bone resorption.

1.3.2.2 Cancellous Bone

Mature, or coarse cancellous bone is characteristic of the internal structure of healthy adult mammalian skeleton and within its macrostructure it is similar to cortical bone except that complete osteons are rarely present. The trabeculae tend to be made up from an irregular "brecchia" of osteon fragments (similar to the interstitial bone between secondary osteons), in which there are abundant cement lines indicating a complicated history of resorption and deposition. In places the trabeculae will be covered in osteoblasts or osteoclasts where bone is being either added or removed, respectively during remodelling. Haversian canals being few, the osteocytes are nourished from the vessels in the inter-trabecular spaces. The endosteum, a highly vascular membrane composed of osteogenic cells and collagenous fibres that also lines Haversian canals, covers any bony trabeculae that exist in the marrow cavity. The architecture is generally anisotropic in response to the applied loads, with the trabeculae orienting themselves in the direction of greatest loading (Wolff, 1870; 1892).

Immature, or fine cancellous bone occurs in the foetal skeleton, at secondary centres of ossification, and early fracture callus in mature bones. There are two forms; fine cancellous membrane-bone and fine cancellous cartilage-bone. Fine cancellous membrane-bone develops directly from mesenchyme (Section 1.4.1.1), and consists of interconnecting trabeculae of woven or bundle bone with inter-trabecular spaces containing blood vessels, osteogenic cells and an osteoblast layer one cell thick on the trabeculae surfaces. The architecture is anisotropic, when the bone is sectioned in a direction parallel to the blood vessels, the trabeculae appear to be arranged as a collection of parallel rods with few interconnections, however, when sectioned perpendicular to the vascular network the bone displays a more isotropic, honeycomb-like structure. Fine cancellous cartilage-bone is similar in structure, except that the trabeculae have a core of calcified cartilage matrix (as a result of the origin of the bone, Section 1.4.1.2) and the bone around this core is fine fibred not coarse fibred.

Almost as soon as fine cancellous bone is formed (be it of the membrane- or cartilage-type), it is remodelled into mature cortical or cancellous bone, and little of the original bone is left. However, it is still possible to distinguish between bone which has

developed from either fine cancellous membrane- or cartilage-bone by the presence (or lack) of calcified cartilage cores which are present within bone derived from fine cancellous cartilage-bone, as some of the calcified cartilage always escapes remodelling.

1.3.2.3 Periosteum

The periosteum is a layer of connective tissue similar to the endosteum which covers all external bone surfaces excepting those that articulate, which are covered by hyaline cartilage. The periosteum consists of an outer layer of densely packed collagenous fibrous tissue, containing blood vessels a few flat osteogenic cells and an inner layer of fine elastic fibres forming dense membranous networks which connects to strong ligaments or tendons thus attaching them to the bone. In young bones the periosteum is thick, very vascular and separated from the bone by a layer of soft cellular osteogenic tissue containing a number of granular cells or osteoblasts which are involved in surface ossification procedures. As the bone grows older the periosteum becomes thinner and less vascular, the inner layer containing flattened quiescent, although still potentially osteogenic, cells. As well as acting as an anchorage site for tendons the periosteum is also involved in the repair and regeneration of bone. A bone surface denuded of periosteum has an increased susceptibility to exfoliation and necrosis.

1.3.3 Macrostructure of Bone

The relative quantities of the two types of macrostructurally distinct bone - cortical and cancellous vary characteristically from bone to bone, depending on the bone shape, position and function. For example, in long bones (such as the femur and humerus) the load bearing bone ends are composed primarily of cancellous bone with a thin skin of cortical bone covering the surface, while the shaft is composed of a thick cylinder of cortical bone with a few trabeculae and spicules of bone on its inner surface (Figure 1.3.2). Furthermore, besides the macrostructural variation from cortical to cancellous bone there is a marked variation in the regional architecture or fabric of the cancellous bone as a result of the different loading conditions (uniaxial, biaxial, isostatic). This results from the ability of bone to remodel itself to best adapt to the mechanical requirements imposed upon it (Wolff, 1870; 1892) and is illustrated by the variation in structure through-out the proximal end of the human femur (Figure 1.3.2). Whitehouse and co-workers (1971, 1974, 1974a and b) demonstrated that the volume of bone, the degree of anisotropy and the thickness of the struts varied throughout the structure to

form coherent patterns. For instance, they reported that the medial trabeculae of the femoral head were composed of a thick trabeculae with relatively high volume of bone and that the metaphyseal part of the medial trabeculae were highly anisotropic, while isotropic structures with average bone volumes were concentrated in the interior of the bone.

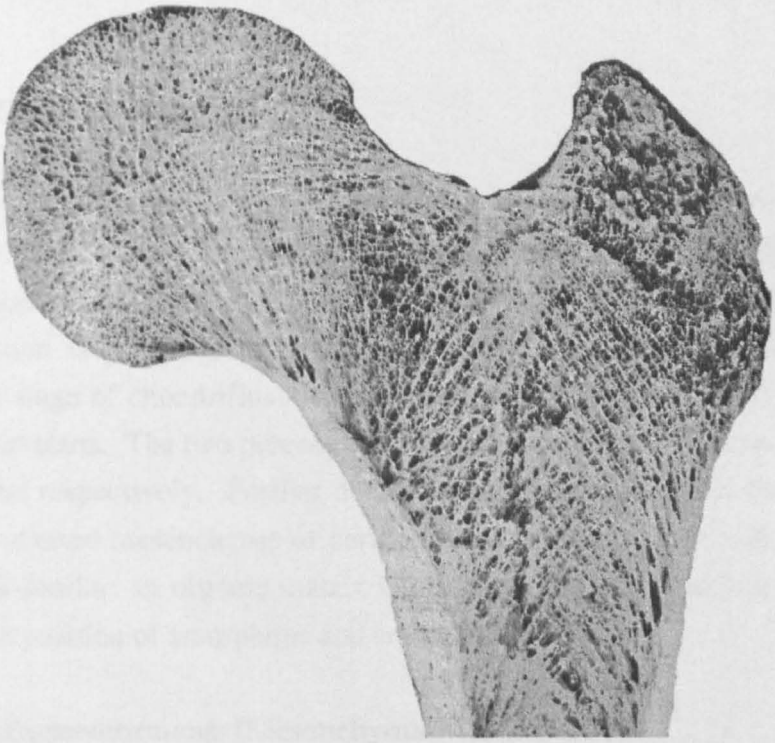

Figure 1.3.2 Detail of the human femoral head demonstrating the macrostructural variation in this region. Adapted from Blatcher, 1995.

In contrast to this, the architecture (bone volume) of the cancellous bone within human lumbar vertebra have been shown to be relatively constant (Whitehouse *et al.*, 1971).

1.4 Development, Growth and Repair of Bone

There are many different internal and external chemical and mechanical influences on the processes that determine, organise and maintain the external form and internal structure of bone. Many of which are still not fully understood.

1.4.1 Bone Development

All bones start as mesenchyme (primitive "fibrocellular" connective tissue containing undifferentiated cells) which undergoes condensation (cells proliferate and number of intercellular fibres increase). In some cases (e.g. bones of calvarium and skull) the condensation is predominately fibrous or membranous, most bones, however, go through a stage of chondrification (in which a cartilaginous model is formed) before ossification starts. The two processes are known as intramembranous and endochondral ossification respectively. Further development occurs via direct transformation from either condensed mesenchyme or cartilaginous model, in either case the fundamental process is similar; an organic matrix is laid down by osteoblasts and this is calcified with the deposition of amorphous and crystalline apatite.

1.4.1.1 Intramembranous (Mesenchymal) Ossification

As discussed, this is essentially the direct mineralisation of a highly vascular connective tissue. The early mesenchyme undergoes condensation during which a primary centre (or centres) of ossification is indicated by a localised increase in cells and fibres around a profuse capillary network. The osteogenic cells differentiate into osteoblasts (producing apatite as a differentiation product) and secrete the carbohydrates, protein complexes and collagen fibres that go to make up the organic matrix or osteoid of bone. The first trabeculae of bone are then calcified and built upon by further generations of osteoblasts differentiated from the surrounding vascular mesenchyme, trapping some of the original ones which then become osteocytes while others continue to add to the trabeculae. As the sequence of differentiation, matrix secretion, calcification and osteoblast entrapment proceeds old trabeculae thicken and new trabeculae are formed so the centre of ossification expands until the region to be transformed has been filled with fine cancellous bone. Where the bone is to persist as cancellous bone the trabeculae thicken, spaces become occupied by haemopoietic tissue and the process slows. In regions where compact bone is formed the process of trabecular thickening

continues, as this occurs the collagen fibres become more organised and the entrapped cells occupy concentric sequential rows centred around a central vascular canal, so forming primary osteons.

1.4.1.2 Intracartilaginous (Endochondral) Ossification

In this case mineralisation is preceded by chondrification of mesenchymal connective tissue. The early mesenchyme undergoes condensation during which cells with oval or round nuclei (chondroblasts) are packed together forming a model of the developing bone. These cells then surround themselves with a collagenous intracellular matrix while the mesenchymal cells at the periphery become oriented to form a perichondrium. The cells of the inner layer of the perichondrium then differentiate into osteoblasts and lay down a layer of osteoid, i.e., the organic matrix of bone. This then calcifies to become a collar of periosteal bone directly in contact with the cartilaginous model, during this process the mature chondroblasts at the centre of the model secrete phosphatase. The surrounding matrix calcifies slightly and the chondrocytes gradually die from lack of nutrition resulting in disintegration of the collagen matrix. Next capillaries from outside the model push through what is now the periosteum and invade the degenerating cartilage bringing in stromal cells. The cartilage is quickly destroyed by the new proliferating and differentiating cells, blood vessels and a circulation are rapidly established. Some cells then differentiate into osteoblasts and start to form bone around the remains of the calcified cartilage matrix, both in the region of original entry and at the advancing zone of cartilage removal. This results in a loose network of trabeculae which grow and fuse with each other and the periosteal shell as more bone is laid down around them. In long bones most of these trabeculae are removed almost as soon as they are formed to make way for a short marrow cavity, this slowly extends in both directions until it almost reaches the epiphysial lines which mark the zone of fusion between epiphysis and diaphysis occurring when growth in length has ceased.

1.4.2 Remodelling - Internal and External

During life bony tissue is continuously undergoing an almost continuous process of structural modification, known loosely as remodelling, which involves successive cycles of bone resorption and deposition. Bone remodelling can be split into two groups; internal and external remodelling. External remodelling is more often termed growth as, for a bone to increase in size yet keep its relative geometry constant, new tissue must be added in one location as old tissue is being removed from another.

Internal remodelling is more subtle, and occurs in both young "growing" bones and old "mature" bones, there is normally no net change in size or shape but a "renewal" of bone *in situ*. This is a perpetual process and may be triggered locally by the need for realignment or thickening of internal trabeculae and/or the external cortex as mechanical demands change, or the replacement of ageing bone with fresh bone.

14.2.1 External Remodelling - Bone Growth

Growth in the length of long bones is achieved by endochondral ossification (see part 1.4.1.2). Cartilage is produced at the epiphysial growth plates by chondroblasts in longitudinally aligned columns (Figure 1.4.1), so increasing the length of the shaft. The cartilage then calcifies as it is pushed further from the growth plate (by the proliferation of new cartilage tissue) and invaded by bone cells. As osteoclasts erode the degenerating cartilage osteoblasts replace the calcified spinicules of cartilage with new bone. This process continues until growth in the length of the bone is complete.

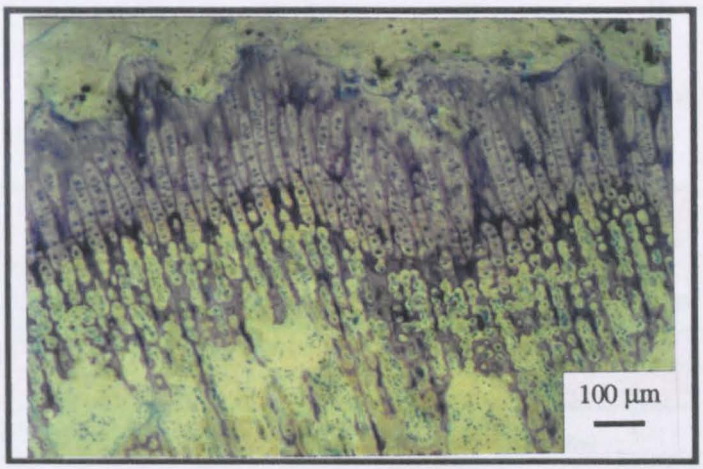

Figure 1.4.1 Detail of the epiphyseal growth plate at the distal end of the femur.

Bone grows in diameter by apposition or membranous ossification. Bone matrix is laid down by osteoblasts directly on existing bone surfaces. However, the mineralisation of this osteoid on the periosteal surface is extremely fast making it difficult to detect.

1.4.2.2 Internal Remodelling - Bone Renewal

Internal remodelling is cell mediated and occurs once bones have reached a certain age or size. The amount of bone renewed within a portion of a given part of the skeleton within a given time is dependant on many different variables. At one extreme, the rates of remodelling between left and right or symmetrical bones are so similar it is possible to use opposite bones as control comparisons in experiments. At the other extreme,

remodelling rates in the same types of bones from animals of different ages can be different by as much as an order of magnitude, as can the rates of remodelling in different types of bones from the same animal. There are also different remodelling routes for different types of bone. In compact bone,remodelling occurs via a process of excavating and refilling Haversian canals or osteons. Before a Haversian canal is ever remodelled it is known as a primary osteon or Haversian canal, once it is remodelled it is subsequently called a secondary osteon or Haversian canal.

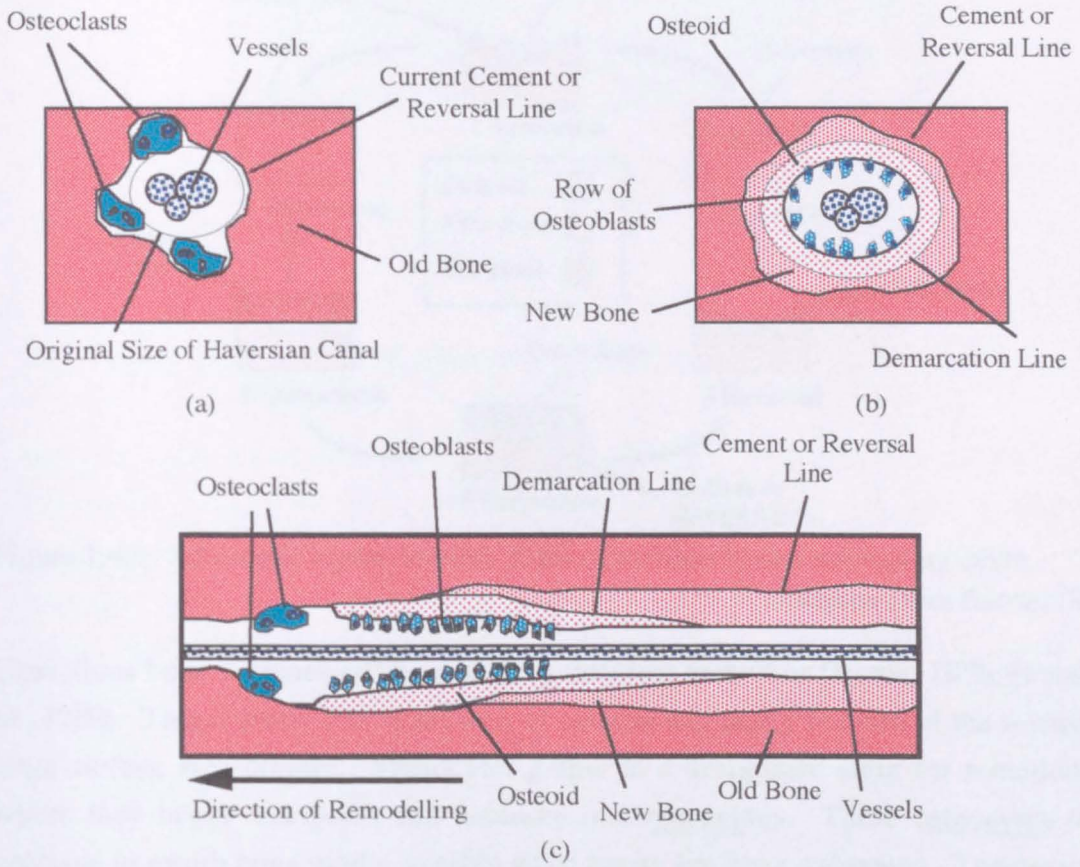

Figure 1.4.2 Schematic representation of a transverse section through a Haversian canal undergoing (a) resorption and (b) deposition, and (c) a longitudinal section through a Haversian canal undergoing remodelling.

Adapted from Martin and Burr, 1989.

The process of the remodelling of an osteon or Haversian canal is represented schematically in Figure 1.4.2. First, chemical or physical triggers activate the differentiation of monocytes and osteoclasts, these then resorb away the old bone from the vascular surface, Figure 1.4.2a, this is characterised by a scalloped appearance to the canal wall, with osteoclasts lying in Howship's lacunae. Once a certain "transverse depth" of erosion is reached reversal occurs and the osteoclasts move on along the length of the canal, progressively eroding away the whole osteon, Figure 1.4.2c. The

point at which reversal occurs is marked by a cement or reversal line. Osteoblasts then colonise the vacant surface and begin to lay down osteoid which then calcifies, so relining the canal walls with successive layers of new bone (Figure 1.4.2b). As the osteoid is laid down osteoblasts are entrapped and become osteocytes. In this manner old "stale" bone and cells may be replaced with fresh young "active" tissue, so maintaining the bone nourishing network of capillaries, canaliculi and canals.

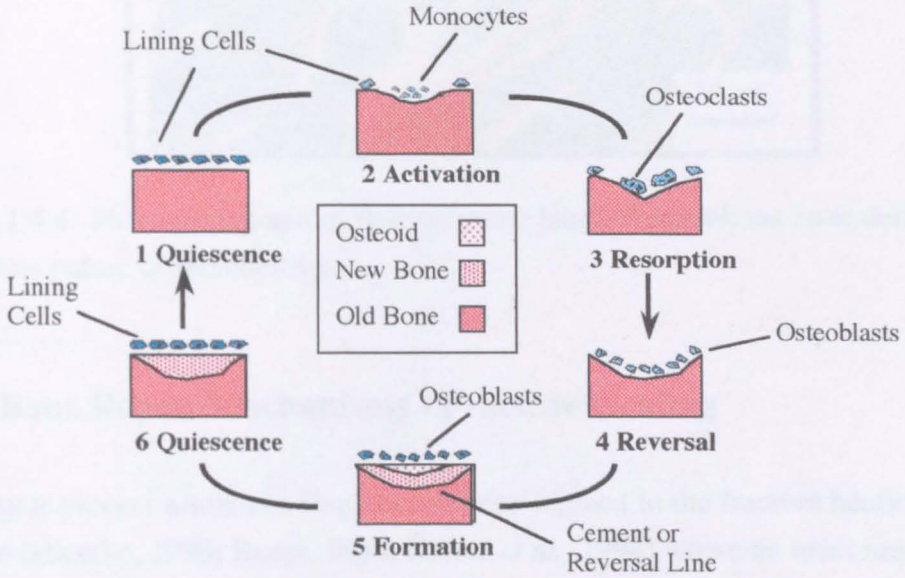

Figure 1.4.3 Schematic representation of the cancellous bone remodelling cycle.
Adapted from Baron, 1976.

Cancellous bone is "renewed" by a slightly different technique (Baron, 1976; Baron *et al.*, 1980). This is partly due to the lack of osteons and partly because of the relatively large surface area present. Monocytes gather at a designated sight for remodelling where they begin resorption and coalesce into osteocytes. These osteocytes then continue to resorb bone until a suitably sized cavity has been excavated. The cavity is then filled in with osteoid by osteoblasts which calcifies to become new bone (Figure 1.4.3). However, complications arise when some of the resorbing osteoclasts remain at the sight of excavation when the osteoblasts arrive, (Parfitt, 1993). This results in areas where resorption has been either aborted or interrupted leaving cavities waiting to be extended or filled, which may not occur until the next wave of remodelling. Furthermore, where excavation is completed there is a variation in the period of time of osteoblast arrival and bone deposition (Tam *et al.*, 1980). This results in a very complicated pattern of cavities and new, old and calcifying bone (Figure 1.4.4) and wide variations are observed in the linear rate of bone deposition from one part of a trabeculae to an other (Tam *et al.*, 1980).

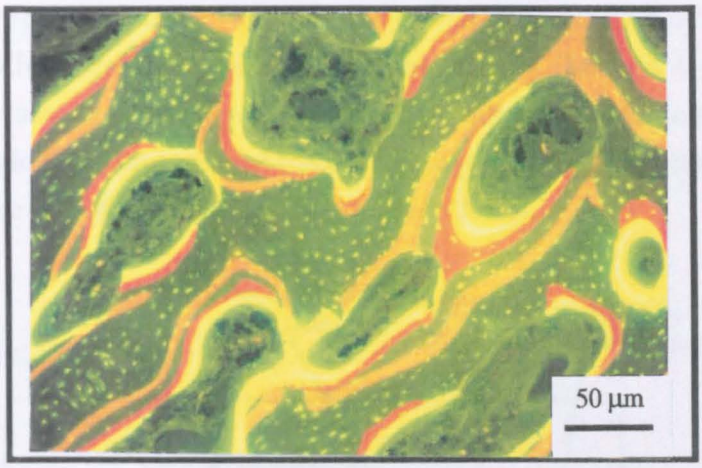

Figure 1.4.4 Photomicrograph of fluorochrome labelled cancellous bone demonstrating the erratic nature of remodelling.

1.4.3 Bone Repair Mechanisms - Fracture Healing

The repair process around an implant has been likened to the fracture healing response in bone (Hiemke, 1990; Bauer, 1990; Kühne *et al.*, 1994) where an ideal implant would induce an identical response resulting in complete fixation of the implant. Fracture invariably results in both the loss of load bearing capabilities and a disturbance to the blood supply of the damaged bone. Firstly, as a consequence of this disruption in the blood supply osteocytes nearest to the fracture die, resulting in local necrosis of the bone around the fracture, (under normal conditions these osteocytes are dependent on nourishment derived from the fluids circulating within the canaliculi, which in turn extend to the surface and make contact with the blood supply), this dead tissue must therefore be removed and replaced with healthy bone. Simultaneously there is a demand for the rapid growth of load bearing connective tissue to bridge the gap and stabilise the damaged area. This second demand is met by the normally quiescent cells that reside in the inner layer of the periosteum and the endosteum. The osteogenic cells of the periosteum proliferate resulting in an apparent thickening of the periosteum and start to produce collars of external fracture callus around the fracture site (Figure 1.4.5). Those osteogenic cells that lie close to undamaged bone (and are thus within reach of a ready supply of oxygen) differentiate into osteoblasts and form osteoid which is rapidly calcified into bone, while those farther away become chondroblasts and form cartilage, which requires little or no oxygen for metabolism and possesses an organic matrix which is an excellent medium for the diffusion of nutrients, in contrast to the highly mineralised and dense matrix of bone. Almost as soon as the cartilage has been formed,

so stabilising the fractured bone (with some load bearing properties restored), it is replaced by cancellous bone via endochondral ossification (Section 1.4.1.2) in which capillaries, osteoclasts and osteogenic cells invade slightly calcified, degenerating cartilage, the uncalcified cartilaginous material is resorbed and new bone is deposited on remaining spinicules of calcified cartilage (Figure 1.4.5).

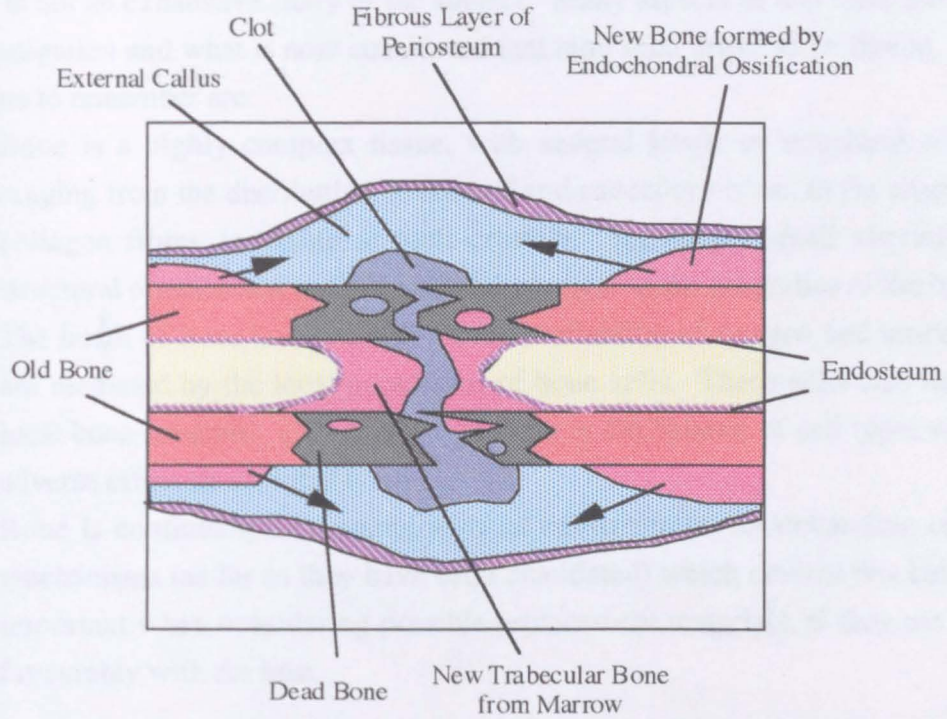

Figure 1.4.5 The Fracture Healing of Bone Adapted from Bourne, 1972.

In this manner all cartilage callus is replaced by cancellous bone, in direct line with the shaft the spaces between trabeculae are gradually filled in with successive layers of bone so forming new Haversian canals and compact bone. Thus load bearing capabilities are restored and a new system of capillaries are set up.

A similar sequence of events occurs within the bone shaft, in this case dead bone material must first be resorbed by monocytes, osteoclasts and other invasive cells before cancellous bone can begin to grow from the surfaces of the fracture and fill the gap. This takes time and under natural conditions the fragments are initially only held in place by the tension of surrounding muscles, hence the requirement for rapid production of fracture callus. The details of internal callus formation depend on the size of the resulting gap between the fracture surfaces, where a smaller gap results in a greater contribution of osteogenic cells from the endosteum and Haversian canals.

1.5 Summary

This chapter gives a general introduction to bone, regarding the subjects of bone physiology and structure, it is designed to convey the current status of understanding, and is not an exhaustive study of the subject. Many aspects of this topic are still under investigation and what is now considered fact may soon prove to be fiction. The main points to remember are:

- Bone is a highly complex tissue, with several levels of structural organisation ranging from the distribution of cortical and cancellous bone, to the arrangement of collagen fibres and bone mineral crystals. Seemingly small alterations in the structural organisation make significant changes in the properties of the bulk tissue.
- The health of bone is dependent on the availability of oxygen and nutrients which are mediated by the local population of bone cells. These cells also maintain the local bone structure. Cell death or changes in the balance of cell types will have an adverse effect on the local bone.
- Bone is continually interacting with its environment, understanding of the basic mechanisms (as far as they have been elucidated) which control this behaviour are important when considering possible replacement materials, if they are to interact favourably with the host.

CHAPTER 2

SYNTHETIC HYDROXYAPATITE

2.1 Introduction

Apatites, a broad group of calcium containing minerals based around the PO_4^{3-} group, (Table 2.1.1) have been of interest to geologists and mineralogists for many years as they represent a significant proportion of calcium and phosphorus in the earth's crust. Consequently, most of them possess, and are still referred to by mineral names. De Jong (1926) was the first to observe the similarities between the X-ray diffraction patterns of bone mineral and hydroxyapatite. Bone mineral is now widely (but incorrectly) regarded as being analogous to hydroxyapatite.

Table 2.1.1 Comparison of the various naturally occurring calcium phosphates

Name (Mineral Name)	Empirical Formula	Molar Ca:P Ratio
Tetracalcium Phosphate	$Ca_4(PO_4)_2O$	2.00
Hydroxyapatite	$Ca_{10}(PO_4)_6(OH)_2$	1.67
Fluorapatite	$Ca_{10}(PO_4)_6F_2$	1.67
Chlorapatite	$Ca_5(PO_4)_6Cl$	1.67
Carbonate Hydroxyapatite (Dahllite)	CO_3^{2-} substituted for OH^-	1.67
Carbonate Fluroapatite (Francolite)	CO_3^{2-} substituted for PO_4^{3-}	>1.67
Tricalcium Phosphate (Whitlockite)	$Ca_3(PO_4)_2$	1.50
Hydrated Calcium Phosphate (Brushite)	$CaHPO_4.2H_2O$	1.00
Anhydrous Calcium Phosphate (Monetite)	$CaHPO_4$	1.00

2.2 Crystallography

2.2.1 Crystal Structure of Hydroxyapatite

The space-group symmetry of apatite was postulated to be $P6_3/m$ or $C_6{}^2h$ by Hentschel (1923), the structure of fluorapatite being first resolved independently in 1930 by both Náray-Szabó and Mehmel as $P6_3/m$.

Posner *et al.*, (1958) demonstrated that the structure of hydroxyapatite was essentially the same as fluorapatite, with the fluorine ions being replaced by hydroxyl groups. Thus the unit cell of hydroxyapatite is characteristic of the hexagonal system where $a = b \neq c$, $\alpha=\beta=90^\circ$ and $\gamma=60^\circ$, as denoted by the letter P. The 6_3 symbol indicates that there is a screw axis (parallel to the c axis) and the /m symbol denotes the presence of a mirror plane, (perpendicular to the screw and c axes) about which the lattice points are symmetrically distributed. Thus, equivalent points will be brought into coincidence when the whole structure is:

a) Rotated around the c axis in 60° steps (1/**6** of 360°), i.e. there is a six fold, or hexad, axis parallel to the c axis.

b) Translated along the c axis a distance of one half (**3/6**) the length of the c axis.

The structure of hydroxyapatite is sketched in Figure 2.2.1.

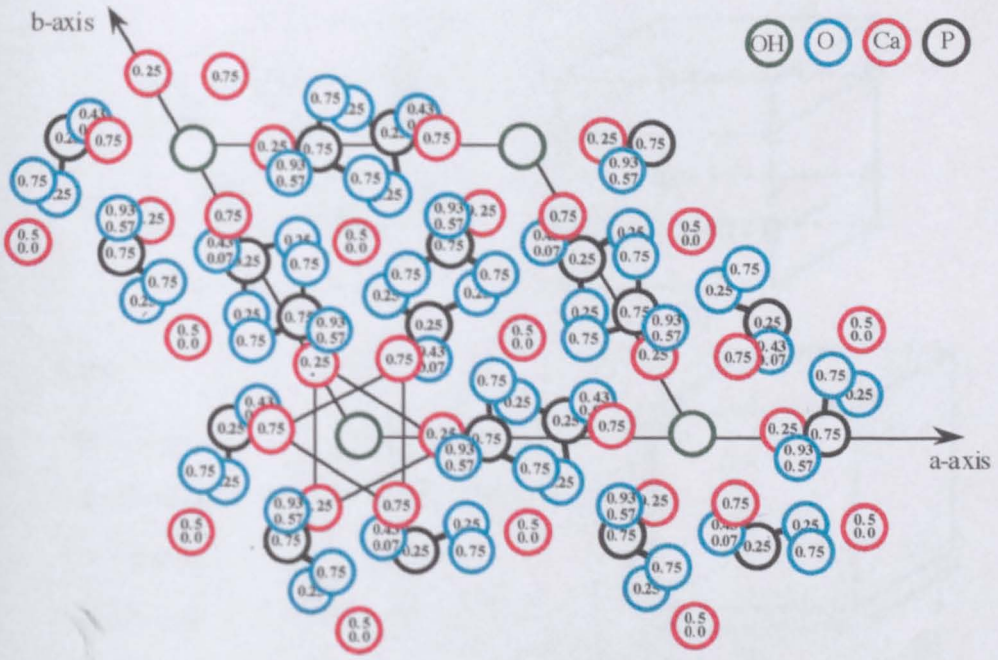

Figure 2.2.1 Structure of hydroxyapatite projected on the x,y plane, adapted from Kay *et al.*, 1964.

As can be seen from Figure 2.2.1 there are two distinct types of calcium position, these are illustrated in Figure 2.2.2 (a) and (b). In the first type, Ca(1), the calcium ions are located at c = 0 (or c =1) and c = $^1/_2$ with the co-ordinates a = b = $^1/_3$ and $^2/_3$. They are termed the columnar calciums and there are a net number of four per unit cell (Figure 2.2.2a). The second type of calcium, Ca(2), are found on planes parallel to the basal plane at c = $^1/_4$ and c = $^3/_4$ (Figure 2.2.2b), and the phosphate tetrahedral group can be regarded as similarly located (Figure 2.2.2c). Both the phosphate tetrahedral group and the Ca(2) calcium ions can be considered as arranged in equilateral triangles around the hydroxyl ions (Figure 2.2.2b). Thus if viewed down the c axis the arrangement can be considered to be made up of a stack of alternating calcium and phosphate triangles making up a hexagonal channel around the hydroxyl groups (Figure 2.2.3). These calcium ions are known as the hexagonal calciums and as with the phosphate tetrahedra there is a net number of six per unit cell.

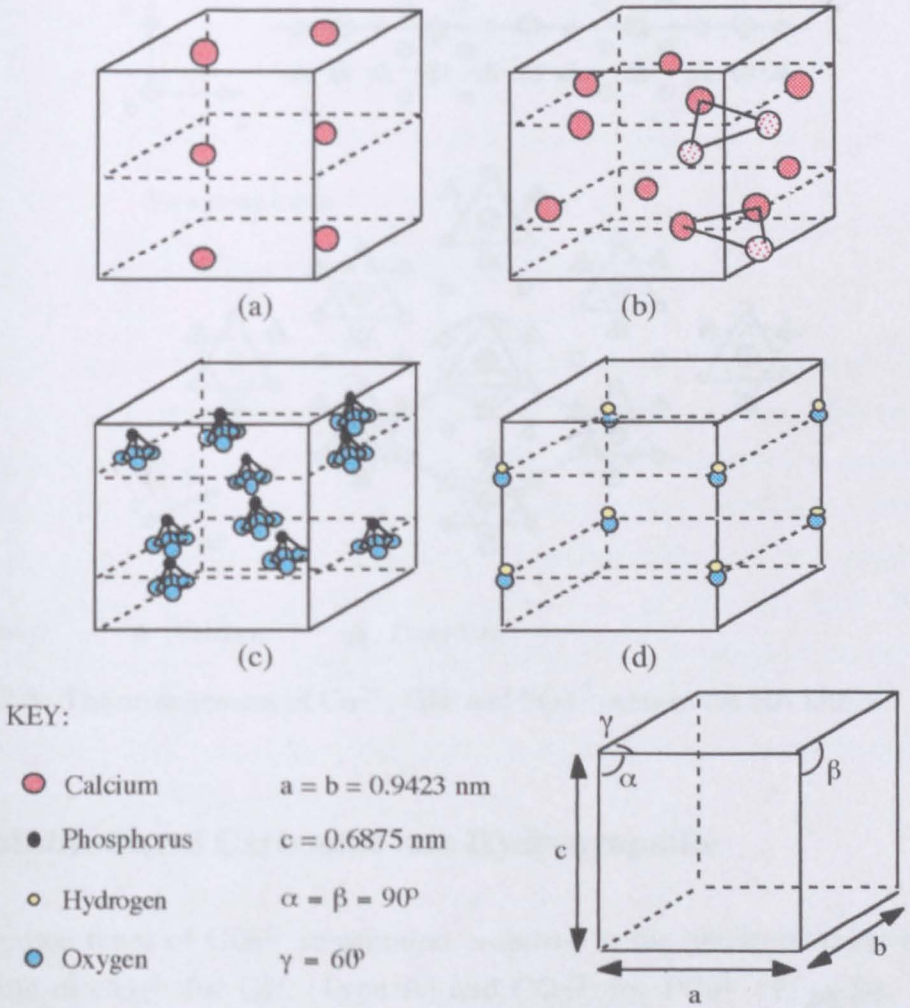

Figure 2.2.2 Theoretical positions of the ionic species within the unit cell of hydroxyapatite (Unit cell data from JCPDS, 1980)

The hydroxyl groups are located on the c axes at the corners of the unit cell (Figure 2.2.2 (d)) with a net number of 2 ions per unit cell. In fluorapatite the fluorine ions are placed at c = $^1/_4$ and c = $^3/_4$, exactly at the centre of the calcium triangles. However, due to the asymmetry of the hydroxyl ion, produced by the proton attached to the oxygen, it is geometrically impossible to place it at the intersection of a triad axis and a symmetry plane. This was demonstrated by Kay *et al.*, (1964) who showed the OH^- group to be displaced by up to 0.030 nm (0.3Å) above or below c = $^1/_4$ and c = $^3/_4$. In order to preserve the characteristics of a $P6_3/m$ structure and avoid too close a contact between ionic groups, the OH^- groups must be arranged in either ordered columns with all the OH^- groups oriented in the same direction, or in disordered columns with the polarity reversed at certain intervals along the c axis. The latter option being preferred by Kay *et al.*, (1964) as it facilitates the addition of fluoride impurities and OH^- vacancies.

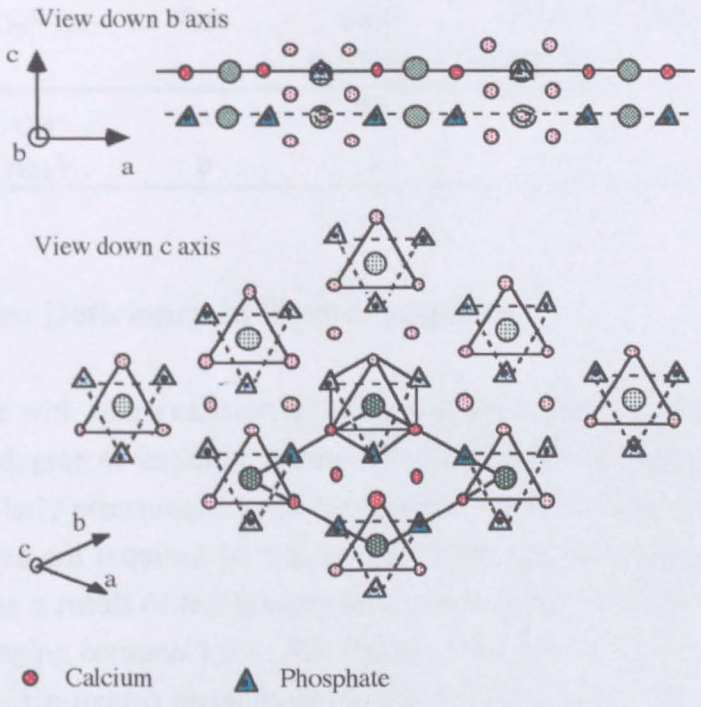

Figure 2.2.3 The arrangement of Ca^{2+}, OH^- and $PO4^{3-}$ ions in the HA lattice.

2.2.2 Substitution of Carbonate into Hydroxyapatite

There are two types of CO_3^{2-} substitution proposed in the literature, these being the substitution of CO_3^{2-} for OH^- (Type A) and CO_3^{2-} for PO_4^{3-} (Type B). Type A substitution was suggested by Eitel (1924) while Type B substitution was proposed by Borneman-Starinkevitch (1939). In Type A substitution the exchange of the larger

planar CO_3^{2-} group for the smaller linear OH^- group results in an expansion in the a-axis and a contraction in the c-axis and occurs when hydroxyapatite is treated with dry CO_2 at 1000°C (Elliot, 1964). However, Trombe *et al.*, (1967) found that when fluorapatite is treated with dry CO_2 at 900°C Type B substitution occurs, indicating that stronger ionic bonds exist between F and Ca than between OH and Ca. Le Geros *et al.*, (1968) have demonstrated the substitution of CO_3^{2-} for PO_4^{3-} in hydroxyapatites precipitated in solution. They found that the a-axis decreased in the length while the c-axis increased as the carbonate content was raised due to the planar carbonate ion being smaller than the tetrahedral phosphate ion. Le Geros and Tung, (1983) reported increasing solubility with increasing carbonate content in the apatite.

Table 2.2.1 Summary of CO_3^{2-} substitutions and effects on HA lattice parameters and crystallinity. (↑ increase and ↓ decrease, Le Geros and Le Geros, 1993)

CO_3^{2-} Site	Type	a-axis (0.9423 nm)	c-axis (0.6875 nm)	Crystallinity
OH^-	A	↑↑	↓	↓
PO_4^{3-}	B	↓	↑	↓

2.2.3 Calcium Deficiency in Hydroxyapatite

Due to the ease with which calcium is readily substituted for a number of cations there is always some degree of impurity present (Posner, 1969) as illustrated in Table 2.2.2. This is particularly pronounced when the apatite is synthesised via a precipitation route where additives are required to maintain solution pH (especially in large industrial processes). As a result of the substitution, commercially available preparations have Ca:P ratios ranging between 1.65-1.72 (Jarcho *et al.*, 1976; Akao *et al.*, 1981; de With *et al.*, 1981b). Un-treated precipitated powders tend to have lower than stoichiometric Ca:P ratios (Monma *et al.*, 1981), while heat treated powders have higher than stoichiometric Ca:P ratios. A general formula has been suggested for non-stoichiometric calcium deficient hydroxyapatites:

$$Ca_{10-x}H_x(PO_4)_6(OH)_{2-x} \qquad (2.2.1)$$

Where x varies from 0-2 (Berry, 1967; Meyer, 1979)

Table 2.2.2 Comparison of the levels of impurity in commercially available apatites.

Powder Origin (wt%)	Mg	Na	Al	Si	Pb	Mn	Cu	Fe
Merck◊*	0.2	0.3	0.06	0.05	<0.01	0.03	<0.01	0.1
Mallinckrodt*	<0.01	0.1	-	<0.01	-	<0.01	<0.01	<0.01
Lab made*	<0.01	0.04	0.04	0.02	<0.01	<0.01	<0.01	<0.01
Tricalcium Phosphate BDH#	0.15	<0.05	0.03	0.15	<0.01	0.02	<0.01	0.02

(Data from ◊Peelen *et al.*, 1978; *Denissen *et al.*, 1980a; #Driessen *et al.*, 1982)

As with carbonate ion substitutions, these substitutions affect the lattice parameters. The degree to which the lattice parameters are altered generally reflects the size and amount of the substituting ions. The crystallinity and dissolution properties are also affected (Table 2.2.3).

Table 2.2.3 Ionic species reported to substitute for calcium and the consequent effects on the HA lattice parameters and crystallinity.

Substituent	Ionic Radius	a-axis (0.9423 nm)	c-axis (0.6875 nm)	Crystallinity
Ca^{2+}	0.99			
Mg^{2+}	0.66	↓	↓	↓
Na^{+}	0.97	≈	≈	≈
Al^{3+}	0.51	↑	↑	↓
Pb^{2+}	1.20	↑	↑	↓
Mn^{2+}	0.80	↓	↓	↓
Sr^{2+}	1.12	↑	↑	≈
K^{+}	1.33	≈	≈	≈
Zn^{2+}	0.74	↑	↑	≈

Where, ↑ increase, ↓ decrease and ≈ no change, Le Geros and Le Geros, 1993.

Substitution of Ca by Sr or Mg results in increased solubility (Le Geros, 1984; Le Geros *et al.*, 1989), while the presence of Mg^{2+}, Fe^{2+}, Mn^{2+} and Al^{3+} ions in solution impede the growth of hydroxyapatite and promote formation of ß-tricalcium phosphate. Magnesium in saliva is believed to result in the formation of tricalcium phosphate in dental callus (Schroeder, 1969) as tricalcium phosphate can have up to 10% of Ca ions substituted by Mg^{2+} which has the effect of decreasing the overall acid dissolution rate (Jenson and Rowles, 1957; Ando, 1958). The presence of Mg^{2+} has also been shown to stabilise amorphous calcium phosphates in solution, increasing the time taken to

transform to apatite (Blumenthal and Cosma, 1992). Moreover, Mg^{2+} works synergistically with other chemical species (eg. diphosphonates, adenosine triphosphate) known to stabilise amorphous calcium phosphates (Posner, 1978a) and the presence of both Mg^{2+} and CO_3^{2-} substituents will have a synergistic effect on the solubility (Le Geros 1984).

2.2.4 Substitution of Hydroxyl in Hydroxyapatite

In addition to the carbonate substitution, OH^- may also be substituted by F^- and Cl^- ions. However Cl^- substitution results in a loss of the hexagonal symmetry due to the alternating positions of the Cl^- ions leading to a doubling in length of the b-axis. While substitution by F^- results in a decrease in the a-axis as a result of denser packing between the F^- and Ca(2) ions which leads to an increase in crystallinity and decrease in solubility (Young and Elliot, 1966). When F^- and CO_3^{2-} or Mg^{2+} ions are present as substituents, the effect of F^- is dominant. (Le Geros, 1984; Le Geros and Tung, 1983)

Table 2.2.4 Summary of OH substitutions and effects on HA lattice parameters and crystallinity. (↑ increase, ↓ decrease and ≈ no change, Le Geros and Le Geros, 1993)

Substituent for OH-	Ionic Radius	a-axis (0.9423 nm)	c-axis (0.6875 nm)	Crystallinity
Cl^-	0.81	↑	↓	≈
F^-	0.36	↓	≈	↑

2.2.5 Synthetic Hydroxyapatite vs. Bone Mineral

In bone, bone mineral is produced in solution in the presence of many complex and varied physiological fluids. Not surprisingly its calcium ions undergo substitution for many elements such as barium, lead, strontium and sodium while others (iron, copper, manganese, tin, aluminium, are believed to be adsorbed on to the crystal surfaces (Posner, 1969; Vaughan, 1975). Furthermore hydroxyl groups are also reported to be readily exchanged with fluorine (Posner *et al.*, 1963), resulting in a highly complex chemistry (Table 2.2.5). Bone may be regarded as a calcium and mineral reservoir with these impurities playing important roles in the mineral homeostasis and metabolic processes of the surrounding tissue. It therefore follows that the presence of controlled levels of the appropriate impurities in any hydroxyapatite introduced *in vivo* could be

advantageous. Similarly, synthetic hydroxyapatite contains relatively little carbonate, which is present in bone mineral in quantities ranging from 1.5% to 4.5% by weight (Bocchi and Valdre, 1993). If the aim of a bioceramic is to interact in an appropriate manner with its bio-surroundings then closer mimicry of natural bio-materials would be preferable,with a requirement for a knowledge of the constituents and their likely effects on the apatite at the least.

Table 2.2.5 Comparison of bone and hydroxyapatite.

wt%	Ca	P	Mg	Na	K	CO_2	F	Cl	Sr, Pb, Ba, Fe, Zn, Cu.	Ca:P Ratio
Bone ◊	26.7	12.5	0.44	0.73	0.06	3.48	0.07	0.08	Sr = 0.04	1.66
Bone +	36.7	16.0	0.46	0.77	-	8.00	0.04	-	-	1.77
Bone #	34.0	15.0	0.50	0.80	0.20	1.60	0.08	0.2	-	1.75
Bone *	24.5	11.5	0.55	0.70	0.03	5.80	0.02	0.10	Traces	1.65
HA Δ	39.89	18.5	-	-	-	-	-	-	-	1.67

Data from: ◊ McConnel, 1973; + Driessens, 1980; # Aoki, 1991; * Le Geros, 1992; Δ Theoretical values, see Appendix.

2.3 Preparation of Synthetic Hydroxyapatite

Synthetic hydroxyapatite specimens are usually produced in a discontinuous manner. First a hydroxyapatite powder is prepared, the powder is formed into a green body by either compaction or slip casting and the green body is consolidated by sintering.

2.3.1 Powder Preparation

Synthetic hydroxyapatite powders can be prepared by a number of different routes. These can be generally split into three groups, aqueous reactions, solid state reactions and hydrothermal reactions. Hydroxyapatite powders produced by aqueous reactions tend to be calcium deficient as a result of cationic substitution, which results in the formation of ß-tricalcium phosphate upon sintering and, if conditions are highly basic carbonate substitution may occur. Pure powders may only be reliably produced by the other routes.

2.3.1.1 Aqueous Techniques

These may be split into two groups, precipitation and hydrolysis methods.

Precipitation

Commercial preparations are generally produced by the precipitation method, which involves mixing reactants together in the presence of water (usually at a controlled temperature, atmosphere and pH) and leaving the resulting precipitate to age under conditions of continuous stirring for periods of up to 12 hours. Once aged, the precipitate is thoroughly washed, filtered and dried. The two most common methods quoted in the literature are that of Rathje, (1939) equation 2.3.1, and Hayek and Newesely, (1963) equation 2.3.2.

$$10\,CaCO_3 + 6\,H_3PO_4 \rightarrow \quad Ca_{10}(PO_4)_6(OH)_2 + 10\,CO_2\uparrow + 8\,H_2O \qquad (2.3.1)$$

$$10\,Ca(NO_3)_2 + 6\,(NH_4)_2HPO_4 + 2\,H_2O \rightarrow \quad Ca_{10}(PO_4)_6(OH)_2 + 12\,NH_4NO_3 + 8\,HNO_3 \qquad (2.3.2)$$

In the first method (equation 2.3.1) phosphoric acid is added dropwise to a stirred suspension of calcium carbonate in water. The method may be modified by the addition of ammonium hydroxide to keep the pH of the reaction alkaline to ensure that

hydroxyapatite does not decompose after sintering (Akao, 1981). In the second method (equation 2.3.2) aqueous solutions of calcium nitrate and ammonium phosphate are prepared (again ammonium hydroxide may be added to control the solution pH, Jarcho *et al.*, 1976). The phosphate solution is then added dropwise to the stirred calcium solution. This method is highly sensitive to the concentrations of the reactants and the solution pH for formation of hydroxyapatite upon sintering.

Hydrolysis

Hydrolysis methods involve the hydrolysis of acid calcium phosphates (eg, dicalcium phosphate dihydrate) in carbonate, fluoride, chloride, ammonium, sodium or potassium hydroxide solutions depending on the desired composition of apatite. Calcium carbonate may also be hydrolysed to apatite in ammonium or sodium phosphate solutions (Le Geros *et al.*, 1980).

2.3.1.2 Solid State Reactions

In solid state reactions hydroxyapatite is produced via the stoichiometric mixing of reactants at specific temperatures. Examples of this method are given in equations 2.3.3 and 2.3.4. The calcium compounds are mixed, formed and then sintered above 950°C.

$$6\,CaHPO_4 + 4\,Ca(OH)_2 \rightarrow Ca_{10}(PO_4)_6(OH)_2 + 6\,H_2O\uparrow \qquad (2.3.3)$$

$$3\,Ca_3(PO_4)_2 + Ca(OH)_2 \rightarrow Ca_{10}(PO_4)_6(OH)_2 \qquad (2.3.4)$$

Le Geros and Le Geros, 1993.

2.3.1.3 Hydrothermal Transformations

The third method of synthesising hydroxyapatite is that of hydrothermal transformation. This process employs the use of elevated temperatures, pressures and controlled atmospheres to convert one substance into another via an exchange reaction. The reactions in equations 2.3.3 and 2.3.4 could be carried out hydrothermally by heating at 275°C under steam pressure of 84 MPa (12000psi). This route has the added benefit of the option to preserve the original architecture, as in the production of porous hydroxyapatite from calcium carbonate corals or denatured bovine cancellous bone. Typical exchange reactions include that of Roy and Linnehan, (1974) which is carried out at 180-360°C under 105 MPa for 12 - 48 hours equation 2.3.5, and Yamasaki *et al.*, (1990) which is carried out at 300°C under 30MPa for 2 hours equation 2.3.6.

$$4\,CaCO_3 + 6\,CaHPO_4 \rightarrow Ca_{10}(PO_4)_6(OH)_2 + 2\,H_2O + 4\,CO_2\uparrow \quad (2.3.5)$$

$$10\,Ca(OH)_2 + 6\,(NH_4)_2HPO_4 \rightarrow Ca_{10}(PO_4)_6(OH)_2 + 18\,H_2O + 12\,NH_3\uparrow \quad (2.3.6)$$

2.3.2 Production of Dense Hydroxyapatite

Following preparation of the hydroxyapatite powder, fabrication of a dense body (>95% of the theoretical density of 3.151 $g.cm^{-3}$, Barralet, 1995) from the material is usually achieved via the standard ceramics processing route of:

- Cold compaction of the power into a green body via uniaxial or isostatic pressing.
- Densification of the green body into a solid specimen by providing sufficient heat or microwave energy for the powder particles to coalesce or sinter.

Much work has been carried out on the preparation and characterisation of specimens processed in this way. With many studies into the effects processing parameters on density, pore morphology and grain size, which in turn effects the physical properties of the specimen. Other methods have been proposed,but they are generally variations on this theme. For instance, Denissen *et al.*, (1980a&b) have successfully produced 97% dense compacts with a grain size of 0.25 μm via the hot pressing of hydroxyapatite at 900°C.

2.3.2.1 Powder Compaction

A reduced compaction pressure leads to reduced particle contact and thus restricts the area available for sintering. However Rootare *et al.*, (1978b) studied the sintering process of hydroxyapatite and found that while plastic deformation introduced in compaction is responsible for bringing the particles into close enough contact for sintering to occur. If compacted above a threshold pressure of 35 MPa (5000psi) the reduction in open pore volume was compensated for by the formation of increasing amounts of closed pore volume which inhibits shrinkage and thus densification during subsequent sintering. Production of a fully dense compact via the cold compaction method is therefore unlikely.

The selection of appropriate particle size optimises the driving force for reducing the surface area:volume ratio of a ceramic body, and to a certain extent controls the grain size. De With *et al.*, (1981a) highlighted the importance of powder morphology by

compacting two powders with differing surface areas in a similar manner and comparing the results, unfortunately no particle sizes were given. However the powder with the higher surface area (smaller particles) was found to produce a more dense compact (with smaller sized pores) even though it was sintered at a lower temperature. It was also shown to have finer grains but this may be a result of the lower sintering temperature. In contrast Matsuno *et al.*, 1992 studied the effects of using very fine powder particles (0.32-1.03 μm) and found that the larger particles led to improved densification. This implies the existence of an optimum particle size for maximising densification. Shareef *et al.*, (1993) combined mixtures of fine (sub micron), medium (3μm) and coarse (50μm) particle powders as a method of producing machinable ceramics with a fine inter-connected porosity.

2.3.2.2 Sintering

Sintering is driven by energetic forces which compel a ceramic body to replace its high energy external (gas:solid) interfaces with lower energy internal (solid:solid) interfaces, so reducing its surface area:volume ratio. Sintering generally occurs by a mixture of liquid and solid state diffusion resulting in neck formation between particles, which then bond and become grains (Jarcho *et al.*, 1976). Once bonded, further diffusion of matter occurs across grain boundaries, resulting in the apparent movement of grains closer to their neighbours, so facilitating pore shrinkage and further reduction of external interfaces which produces the characteristic densification associated with sintering. Once pores have shrunk to a point where they are spherical and no longer interconnecting it becomes energetically favourable to reduce internal (solid:solid) interfaces as opposed to external (solid:gas) interfaces, which results in grain growth. Therefore, selection of optimum sintering times and temperatures are important, "under" sintering (reduced temperature or dwell time) results in insufficient energy to drive, or insufficient time to complete the sintering process, while "over" sintering (excess temperature or dwell time) may result in decomposition of the ceramic, or dense compacts with large grains which are detrimental to mechanical properties.

Rootare *et al.*, (1978a) demonstrated that a maximum density of 97-98% is obtained after 3 hours sintering at 1200°C. In contrast, Jarcho *et al.*, (1976) reported that HA powder cold pressed and sintered at 1000 or 1200°C for 1 hour produced compacts with grain sizes of 0.15-0.71μm and 99.6% theoretical density while Rao and Boehm (1974) found no increase in density with sintering beyond 2 hours at 900°C and 1 hour at 950, 1000, 1100 and 1200°C. Akao *et al.*, (1981) varied sinter temperature from 1150 to 1300°C and noted that density increases of 80.6-97.2% were accompanied by grain size increases from 1.32 to 3.04 μm when specimens were held for 3 hours at peak

temperature, similarly, De With *et al.*, (1981b) found that density increased from approximately 72%-97% with sinter temperatures from 1100-1250°C while grain size increased from 1.5 to over 5.0 μm when specimens were sintered at peak temperature for 6 hours. These differences in behaviour are a result of differences in the morphologies (i.e., particle size and surface area) of the starting powders used in the various studies. Powders with smaller particle sizes (larger surface areas) require lower sinter temperatures and soak times to produce high density compacts (de With *et al.*, 1981a), however, powders with too fine a particle size are difficult to process (Matsuno and Koishi, 1992).

Fang *et al.*, (1992) produced hydroxyapatite compacts of up to 91.2% dense using a microwave oven. Samples were first compacted in a cold press at pressures ranging between 35-140 MPa. Sintering was then carried out in air at temperatures of 1150-1200°C for lengths of 1-5 minutes at peak temperature. Not only were they able to produce a wide range of densities (27-91% dense) but as sintering was completed within a few minutes there were large savings (over 90%) in both time and energy.

2.3.2.3 Decomposition of Hydroxyapatite at Elevated Temperatures

In addition to the limitations on sintering regime imposed by grain growth "hydroxyapatite" powders can decompose at high temperatures (i.e., during sintering). De With *et al.*, (1981b) noted the presence of ß-tricalcium phosphate in specimens sintered above 1150°C, while Wang and Chaki (1993) varied both the sintering atmospheres and temperatures and found that in air, loss of OH^- (dehydroxylation) occurred between 900-1000°C, with the appearance of ß-tricalcium phosphate impurities at 1100°C as a result of decomposition of the hydroxyapatite. This dehydroxylation progressed with the appearance of tetracalcium phosphate at 1300°C and transition of ß-tricalcium phosphate to α-tricalcium phosphate at 1350°C and was enhanced when the material was sintered under vacuum. However, in a moist atmosphere there was no evidence of dehydroxylation at any temperature. Conversely, XRD studies carried out by Knowles *et al.*, (1994) and Abrahams and Knowles (1994) found that hydroxyapatite sintered in air did not decompose until sintered at 1450 °C, although significant changes were seen in the lattice parameters above 1000 °C, these were ascribed to loss of carbonate from hydroxyl sites. As with the sintering parameters for optimum densification, the disparity between different investigations regarding chemical stability and changes in the sintering temperature and soak time, were related to the characteristics of starting powders, namely, the precise chemical composition and history of the powder. The calcium to phosphorous ratio for the various powders are given in Table 2.3.1.

Table 2.3.1 Differences in Ca:P ratios of laboratory made and commercial powders.

Powder	Ca:P Ratio
Merck (De With *et al.*, 1981 a and b)	1.62
Laboratory made (De With *et al.*, 1981a)	1.64
Laboratory made (Wang and Chaki, 1993)	1.69
Plasma Biotal - P120 (Knowles *et al.*, 1994)	1.70*
Plasma Biotal - P81 (Abrahams and Knowles, 1994)	1.69*

*Data from Best, 1996.

2.3.3 Production of Porous Hydroxyapatite

Until recently relatively little work had been carried out on the preparation of intentionally porous materials (excluding the hydrothermal conversion of coralline material). Most work seems to have been directed at producing 100% dense bodies or applying a porous coating to metallic implants (eg. Bobyn *et al.*, 1980). Many of the porous materials that have been produced are as a result of studies into compaction pressure of green bodies (Rootare *et al.*, 1978a; Matsuno and Koishi, 1992) and varying sintering temperature or time, (Akao *et al.*, 1981; Rao and Boehm, 1974; Matsuno and Koishi, 1992). The degree of porosity produced via such methods ranges from 50-20% however materials properties may be unsatisfactory as under-pressing and under-sintering can lead to inhomogeneities in the dispersion of the powder as a result of uneven pressing and loss of strength as a result of incomplete consolidation of powder particles. Moreover, the pore size of materials produced via these methods, (0.1-20 μm depending on processing conditions and starting powders), is usually too small for successful osseointegration and the porosity is usually unconnected. As established in 1970 by Klawitter a minimum pore size of 100-150 μm is required for healthy bone ingrowth. Furthermore Holmes (1979) found that interconnecting porosity is required of an osteonic diameter to allow paths for nutrients to reach the ingrown bone else it will die.

2.3.3.1 Foaming Methods

A more successful approach is that of Peelen *et al.*, (1978) who introduced macro-porosity into hydroxyapatite green bodies via the use of hydrogen peroxide. H_2O_2 was mixed with an aqueous slurry of the hydroxyapatite precursor, this was then cast, allowed to "rise", carefully dried and then sintered at a range of temperatures (1100-1350°C). Sintered bodies were produced with porosities of up to 70% and pore sizes of 150-250 μm (macro pores formed as a result of the additions) and 0.5-1.5 μm (micro

pores formed as a result of densification during sintering). This technique was also used by Driessen *et al.*, (1982) to produce porous compacts of ß-tricalcium phosphate and hydroxyapatite, a porosity of 35-40% being achieved.

2.3.3.2 Burn-Out Methods

Lin *et al.*, (1994b) produced porous compacts of hydroxyapatite and Bioglass by combining either the ceramic or glass powders with 5 and 500 μm diameter polyethylene glycol particles before pressing the material under a hydrostatic pressure of 270 MPa. During sintering the polymer was burnt out leaving behind a structure with interconnected porosity and pore sizes of approximately 120-240μm.

Fang *et al.*, (1992) produced hydroxyapatite compacts ranging in density from 91-27% with the use of a microwave oven. The variations in porosity were achieved by altering the pressures of cold compaction from 35-140 MPa or with the use of differing quantities of ammonium carbonate additions (which was found to be successful whether it was burnt off in or out of the microwave) and compacting at 140 MPa. However, pore sizes were found to be too small to encourage osseointegration although pore were inter-connecting in specimens with over 50% porosity.

2.3.3.3 Hydrothermal Conversion

Yamasaki *et al.*, (1990) reported the preparation of porous ceramics via the hydrothermal hot pressing of $Ca(OH)_2$ and $(NH_4)_2HPO_4$. "Semi-green" specimens were prepared by hot pressing at 300°C under 30MPa for 2 hours with porosity being introduced by the evolution of ammonium gas during the hydrothermal conversion. These specimens had a 51% density and 40% of the total porosity was interconnected with pore sizes of 100 - 400μm. The semi green specimens were then sintered at 1050°C for 3 hours in air resulting in a density increase to 58% due to micro-pore shrinkage, so maintaining the macro-pore structure.

Another reported hydrothermal technique for the production of porous hydroxyapatite is the hydrothermal exchange of calcium carbonate coral into hydroxyapatite (Roy and Linnehan, 1974). This method preserves the architecture of the coral resulting in highly inter-connected pores with porosity of 66% (Holmes *et al.*, 1984). This is achieved by holding specimens under pressure 105 MPa (15 000psi) in the presence of $(NH_4)_2HPO_4$ at temperatures of 180-360°C for 12 - 48 hours.

2.4 Characterisation of Synthetic Hydroxyapatite

2.4.1 Chemical Analysis

Knowledge of the chemical content of any implant is important from a perspective of possible toxin contamination. However interest has recently developed in "impurity" levels as a result of the promotion of controlled levels of different elements to enhance biocompatibility (Andersson, 1995; Lau *et al.*, 1991; Li *et al.*, 1994). Posner (1969) determined the levels of calcium deficiency in bio-apatite by comparing specimens before and after heating them above 800°C. Calcium deficient hydroxyapatites, when heated above 800°C dehydrate to form $Ca_3(PO_4)_2$ plus some residual apatite. If the Ca:P ratio is less than or equal to 1.5 then there is no residual apatite seen after pyrolysis. However, in order to determine the presence of any substituents in the material, assess its purity, crystallinity and determine the lattice parameters it is necessary to perform a combination of X-ray fluorescence, inductively coupled plasma spectroscopy, X-ray diffraction, and infrared spectroscopy.

2.4.1.1 Detection and Quantification of Ionic Impurities

Inductively coupled plasma spectroscopy (ICP) and X-ray fluorescence (XRF) are commonly used to determine the levels of rare earth and metallic impurities that may be present as substituents such as magnesium, sodium, aluminium, silicon, manganese copper and iron (Le Geros and Le Geros, 1993). However, only ICP is suitable for determining the presence of "light" elements such as fluorine and chlorine. XRF is also unsuitable for determining the levels of elements that have oxides with low vapour pressures such as carbon or mercury.

Table 2.4.1 Results of ICP for some commercially available porous apatites.

	Ca	P	Mg	Sr	Na	K	Al
Alveograf	43	19	-	0.096	0.0081	-	-
Algipore	38	17	2.5	0.18	0.67	0.048	0.018
Calcitite	41	19	0.0011	0.009	0.0084	-	-
Interpore 2000	43	18	0.1	0.75	0.27	0.071	-
	Si	Zn	Fe	Mn	S	F	
Alveograf	0.017	-	-	-	0.078	-	
Algipore	0.056	0.0037	0.011	0.013	0.25	3.52	
Calcitite	0.036	-	-	-	0.073	-	
Interpore 2000	0.069	-	-	-	0.2	-	

Data from Pinholt *et al.*, (1992).

2.4.1.2 X-Ray Diffraction

This technique may be used to identify the presence of any solid crystalline compound provided its characteristic X-ray diffraction (XRD) pattern is known (Table 2.4.2). It provides information about the phases present rather than the combination of elements and can be used to assess the phase purity (single or multiphase) of a material, but is not generally used as a quantitative technique.

Table 2.4.2 Relative intensities of some XRD reflections for hydroxyapatite.

Relative Intensity (%)	100	50-70	20-50	20-10
Reflection	211	112	002	200
		300	202	102
			310	210

Data from McConnel, (1973).

XRD is also used to assess the degree of crystallinity which is generally indicated by the sharpness of the peaks in a XRD pattern, however when applied to small crystallites broad patterns may be obtained which do not reflect the crystallinity of the material (Posner, 1978a). Similarly, stresses within the crystal lattice may be evaluated by peak broadening and peak shifting for example dehydroxylation (loss of OH^-) is said to result in a 1-2° peak shift (Wang, 1993). However, refinement of the structure using techniques such as the Rietveld method (Knowles *et al.*, 1994) are more accurate and may be used to obtain precise information concerning parameters such as the unit cell dimensions or the position and size of an ionic group present in the lattice. When assessing hydroxyapatites, specific attention is usually paid to the a- and c-axis lengths, the unit cell volume, the occupancy of the hydroxyl oxygen site [O(H)] (theoretical value = 0.5), the [O-P-O] angles and the [Ca(2)-O(H)] and [Ca(2)-Ca(2)] bond lengths (d), the latter of which can be used to calculate the hydroxyl channel radius, r_c, using equation 2.4.1.

$$r_c = \frac{d_{[Ca(2)-Ca(2)]}}{2} \tan\frac{\pi}{6} \qquad (2.4.1)$$

These values are of particular interest as an increase in r_c and a higher O(H) site occupancy indicates the presence of carbonate when in conjunction with an increase in unit cell volume and a-axis length. While an increase in c-axis length tends to indicate the formation of oxide ions (reported at temperatures in excess of 1450°C as a result of H_2O loss). The values of the [O-P-O] angles (θ_i) can be used to calculate the tetrahedral distortion index ($^aD_{ind}$) as in equation 2.4.2.

$$^{a}D_{ind} = \frac{\sum_{i=1}^{i=6} (\theta_i - 109.17)^2}{6} \qquad (2.4.2)$$

This value is a measure of the PO_4 moiety, it may be used to assess the extent of relaxation in the crystal structure and indicates the likelihood of carbonate substitution at this site. Lower values denote a more regular tetrahedral environment (Abrahams and Knowles, 1994). One drawback is the fact that any amorphous material may not be characterised using this method (it appears as background scatter or raises the base line) as a result of not having a distinct, ordered structure.

2.4.1.3 Infra-Red Spectroscopy

This technique provides information about the ionic arrangements present and may be used to study amorphous material. It is the most suitable method for determining the presence of carbonate and distinguishing between the two types of substitution. There are two types of infra-red technique, Fourier transform infra-red spectroscopy (FTIR) and Raman spectroscopy. FTIR is concerned with the vibrations of polar bonds were a change in dipole moment occurs as a result in vibration. Raman spectroscopy is associated with vibrations of non-polar covalent bonds where polarisation can be induced. The characteristic absorption bands of FTIR apatite spectra are summarised in Table 2.4.3. In addition to possessing different band locations within their spectra, the two carbonate types also affect the bands of the other ionic groups in the spectra. In A Type substitutions the stretch and libration (different modes of ionic vibration) hydroxyl bands decrease in intensity with increasing carbonate content and the phosphate bands in the 1200-1100 cm^{-1} region lose their definition (Doi *et al.*, 1982). While in B Type substitutions the phosphate band at 1088 cm^{-1} decreases in intensity with increasing carbonate content. In spectra produced at high temperatures (600°C) the hydroxyl stretch band drops to 3565 cm^{-1} and an extra peak appears at 3537 cm^{-1}. This is believed to be due to the rearrangement of hydroxyl ions in the columns along the c-axis (Cant *et al.*, 1971).

Table 2.4.3 Wavenumbers of IR peaks observed in apatite related specimens (cm^{-1}).

Phosphate+	ν_1	ν_2	ν_3	ν_4
	962	473	1088	601
			1057	580
			1042	570

Table 2.4.3 continued over page.

Table 2.4.3 continued.

Hydroxyl◊	Libration	Stretch		
	633	3660 3573		
Carbonate#	ν_2	ν_3		
A Type	878	1450 1550		
B Type	875	1410 1460		
Surface absorbed ionic groups	Water◊	Carbonate#	Ammonium◊	Hydrocarbons◊
	1640 2500-3600	2200, 2330	3420 3385 3280	2900
Substituants for Hydroxyl	Chloride$^{\Delta}$	Fluoride◊		
	3500	3546		
Ionic groups associated with Hydroxyl	Phosphate◊	Silicate*		
	880	3645 3698		
Oxygenated Hydroxyapatite*	436 473	peak at 633 decreases		

(Data from +Klee and Engle 1970; ◊Cant *et al.*, 1971; $^{\Delta}$Blumenthal and Posner, 1973; #Dowker and Elliot 1983; *Pinholt *et al.*, 1992)

2.4.1.4 Quantitative Determination of Carbonate Content

Infrared techniques for the determination of carbonate have been developed, but tend to be limited to the machine upon which they were developed. Most other techniques involve measuring the amount of carbon dioxide produced by reacting specimens with acid or heating them in oxygen. The most common technique cited in the literature is that developed by Conway (1962). This involves reacting the carbonate containing specimen with hydrochloric acid in one compartment of a partitioned and sealed container. While an other compartment contains a quantity of barium hydroxide which reacts with the carbon dioxide to form insoluble barium carbonate. After all the carbon dioxide evolved is assumed to have reacted with the barium hydroxide the remaining barium hydroxide is titrated with hydrochloric acid using a microburette and indicator. Thermal gravimetric analysis (TGA) may also be used to determine carbonate content as it measures the weight loss during heating of specimens over the temperature range at which carbonate is transformed to carbon dioxide (400°C to 1000°C).

2.4.2 Assessment of Microstructure

The roughness of a surface has recently been demonstrated to have an effect on cell response *in vitro* (Best *et al.*, 1994). Gomi *et al.*, (1993) have demonstrated that *in vitro* rougher surfaces induced a more aggressive response from osteoclasts resulting in greater degrees of resorption. While Eggli *et al.*, (1988) found the presence of interconnecting pores with a mean diameter of 20μm, when compared to material with little or no interconnecting porosity, improved the tissue response to macroporous ceramics. Therefore a thorough knowledge of the microstructural characteristics is important in order to fully assess implant behaviour. The microstructure (in particular the grain size and degree of microporosity) may also effect the mechanical characteristics of the material (Section 3.3.1).

2.4.2.1 Grain Size Measurement

There are many different procedures for the estimation of grain size. These may be classified into three basic groups and in order of increasing accuracy these are the comparative, planimetric and intercept methods. Guidelines for the use of these methods and the accuracy with which they can be used are set down in ASTM E 112 - 91. Briefly, comparative methods are carried out via the visual estimation of grain size with the use of comparison charts of grains of known dimensions. This method is accurate to a whole grain size. Planimetric methods are carried out on micrographs. For instance in the Jeffries planimetric method a test circle of known diameter (78.8mm) and area (5000mm^2) is placed over a micrograph (the magnification of which is usually manipulated so that around 50 grains fall with in the test circle) and both the number of grains that fall completely within the circle and the number of grains that are intersected by the circle are counted. The average grain size (in millimetres) is then obtained from:

$$\bar{d} = \sqrt[2]{\left\{\frac{5000}{M^2}\left(\frac{1}{n_1 + \frac{n_2}{2}}\right)\right\}} \qquad (2.4.3)$$

Where, $\bar{d}$ = Average diameter; M = Magnification; n_1 = Number of grains intersecting circle; n_2 = Number of grains within circle

This is accurate to within half a grain size (or one quarter if sufficient measurements have been made to comply with Section 13 of ASTM E 112 - 91). Intercept methods employ the use of a test line of known length (usually 500mm), and either the number of

grains intercepted by the line (N), or the number of grain boundary intersections are counted (P). A magnification is usually selected so that 70-150 grain or grain boundary interceptions are obtained. The average grain size (in millimetres) is given by:

$$\bar{d} = \left\{ \frac{1.125}{M} \left(\frac{L_T}{X} \right) \right\} \qquad (2.4.4)$$

Where, X = Either N or P; L_T = Length of test line.

This method is accurate to half a grain size (or one tenth if sufficient measurements have been made to comply with Section 13 of ASTM E 112 - 91). An estimate of the grain size uniformity can be obtained by dividing the diameter of the largest observed grain by the mean lineal intercept, $\bar{L}_3$ where:

$$\bar{L}_3 = \left\{ \frac{d}{1.125} \right\} \qquad (2.4.5)$$

The theoretical ratio of $L_{max} / \bar{L}_3$ is 1.872 for a uniform grain distribution if the grains are tetrakaidecahedric in shape, where a tetrakaidecahedron is a regular octahedron that has been truncated to form a 14 sided polyhedron (Figure 2.4.1a). The greater this ratio the greater the degree of non uniformity in the grain size. Also, by rotating the test line through 90° anisotropy in the grain structure can be detected.

These methods are devised for use with equiaxed, single phase microstructures and modifications are available to allow more flexibility in the type of material that may be studied, e.g., the use of "wavy" test lines in intercept methods to compensate for deviations from equiaxed grain shapes.

The parameters measured (e.g., average grain diameter) are generally planar and do not provide a measure of the true grain size or the nature of the true grain size distribution, as a result of stereological effects. Only spatial parameters (such as average grain volume), calculated by serial sectioning or complicated calculations based on grain shape models provide a measure of the true grain size. However, stereological investigations have developed simple relationships between the mean lineal intercept and the mean true volumetric grain diameter, $\bar{D}$, for instance, Fullman (1953) showed that $\bar{D} = 1.5\,\bar{L}_3$ if grains are considered to be spherical. Other studies in which the grains were assumed to be tetrakaidecahedral (Figure 2.4.1a) have produced similar equations e.g., $\bar{D} = 1.68\,\bar{L}_3$ (Smith, 1987; Miller *et al.*, 1966) and $\bar{D} = 1.776\,\bar{L}_3$ (Pereira de Silva,

1966) and if grains are assumed to be pentagondodechahedral $\overline{D}=1.62\overline{L}_3$ (Bodyako *et al.*, 1980; Smith, 1987), where a pentagondodecahedron is a 12 sided polyhedron each side being a regular pentagon (Figure 2.4.1b). Nevertheless development of three dimensional spatial grain size distributions from these methods is a very complex procedure and image analysis is generally employed for these evaluations.

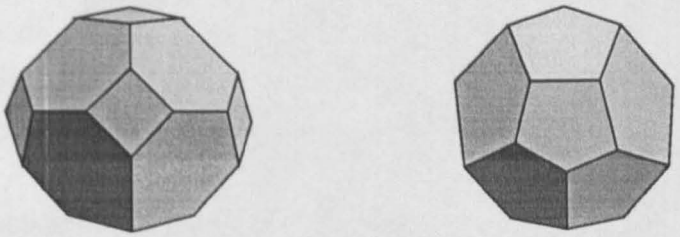

(a) (b)

Figure 2.4.1 Theoretical grain shapes, (a) tetrakaidecahedron and (b) pentagondodecahedron.

The use of image analysis in the determination of grain size requires that greater attention is given to specimen preparation, as grain boundary delineation must be very high and the extent of etching must be repeatable. It is usually necessary to edit the image in order to enhance grain boundary delineation and to remove preparation artefacts which may affect the results. When measuring grain area, grains intersecting the live frame border can influence measurement accuracy and should be deleted from the image so that only whole grains are counted. The lowest magnification at which the grain boundaries can be clearly seen should be used to ensure the best statistical data (van der Voort, 1984). Alternatively, for single-phase structures the length of the grain boundaries per unit area can be measured and divided by $\pi/2$ to obtain $1/\overline{L}_3$, or the grain interiors may be detected and chord lengths measured. The average chord length will be equal to $\overline{L}_3$. In the latter case rotation of the image and re-detection may be necessary to eliminate anisotropy effects along with the deletion of grains intersecting the frame border to prevent under sizing.

Further guidelines for the use of image analysis in the assessment of grain size are set out in ATSM E 1382 - 91.

2.4.2.2 Micro-Porosity Measurement

Modifications to the techniques described above for the calculation of grain size and distribution can be applied to micro-porosity, where the porosity can be considered as a second phase. For instance image analysis of unetched specimens could be used to

detect only the pores and subsequent measurement of chord length could then be carried out. Hamman (1987) compared measurements on cross (longitudinal) sections with those on planar (transverse) sections using image analysis and found, on the particular specimens under examination that measurements on cross sections gave 5% higher porosity values. He also found that linear intercept methods when compared with direct measurement from images tended to give a smaller pore size. This work highlights the influence choice of method and section plane can have on the results. However, conversion of the information to volumetric data is simplified by the fact that micropores can generally be considered as spherical (Smith, 1987).

In addition, gas and mercury porosimetry can be performed on pores in the size range 3 nm to 100 μm, although a minimum specimen size of 1 cm^3 is usually required (Rootare and Craig, 1974). Mercury porosimetry assesses pore size by measuring the pressure (P_r) required to force mercury into the pore. The pore size (μP_s) is calculated as in equation 2.4.6, and by measuring the amount of mercury that was forced into the body at that particular pressure the pore size distribution can be assessed.

$$P_r = \frac{-2\gamma \cos\theta}{\mu P_s} \qquad (2.4.6)$$

Where, γ is the surface tension of mercury (≈0.48 $N.m^{-1}$) and θ is the contact angle (134-140°). However there are several disadvantages associated with this technique, the main ones being the assumption of the surface tension and contact angle, sample compression at high pressures (up to 422 MPa) leading to false results in compliant materials and most significantly, network effects (i.e., a large pore with a small opening will be "measured" as a small pore) (Smith *et al.*, 1994).

2.4.3 Assessment of Macrostructure

Matching macrostructure to suit the host tissue has been established since 1970 when Klawitter determined that a minimum pore size of 100-150 μm is required for healthy bone ingrowth. Furthermore, Holmes (1979) found that interconnecting porosity is required to be of an osteonic diameter to allow paths for nutrients to reach the ingrown bone. The effect of morphology on the mechanical properties must also be considered since modification of the internal macrostructure, in order to distribute loads, so as to stimulate or match the intended host tissue, will improve the biocompatibility.

2.4.3.1 Density Measurements

Various techniques for the measurement of cancellous bone density, which may be applied to synthetic hydroxyapatite, were reviewed by Sharp *et al.*, (1990). These authors suggested a method for standardisation of density measurements and outlined the three different types of density applicable to cancellous bone, where apparent and actual density differ when there is a second non-air phase (such as marrow in cancellous bone).

$$\text{Apparent Density} = \frac{\text{Mineralised Mass}}{\text{Total Volume}} \tag{2.4.7}$$

$$\text{Real Density} = \frac{\text{Mineralised Mass}}{\text{Volume of Bony Matrix}} \tag{2.4.8}$$

$$\text{Actual Density} = \frac{\text{Total Mass}}{\text{Total Volume}} \tag{2.4.9}$$

Generally authors do not specify exactly which density they are quoting, although most authors measure the density of porous implants by weighing the specimens with a balance, measuring the dimensions with a micrometer and performing the appropriate calculation, giving apparent density. Some work has been carried out where Archimedes' principle of volume displacement has been used to calculate density. Specimens are weighed dry, submerged and saturated with water, the density being given by either equation 2.4.10 or 2.4.11, where ρ_{H_2O} = the density of water

$$\text{Apparent Density} = \frac{\text{Dry weight}}{(\text{Saturated weight} - \text{Submerged weight})} \times \rho_{H_2O} \tag{2.4.10}$$

$$\text{Real Density} = \frac{\text{Dry weight}}{(\text{Dry weight} - \text{Submerged weight})} \times \rho_{H_2O} \tag{2.4.11}$$

Real density may also be calculated using gas or mercury porosimetry (Rootare and Craig, 1974).

2.4.3.2 Macro-Porosity Characterisation

Shors *et al.*, (1987) reported that the use of mercury porosimetry was unsuitable for cancellous bone due to the large pore sizes and high degree of porosity. In addition to this the manual methods previously described in section 2.4.22 are unsuitable for very large pores (over 100 μm) as a result of the magnification and sample/view size constraints imposed by a typical optical microscope. As an example, statistical

constraints require that 70-150 "grains" are intersected by a test line when performing an intercept estimation method, if the "grains" are 100 μm in diameter the test line would need to be about 7-15 cm long at a magnification of × 10 (a minimum magnification for most optical microscopes). Similarly scanning electron microscopes cannot achieve magnifications below × 15-20.

Hamman (1987) compared two methods of image analysis by applying them to a number of different porous coatings (pore sizes of 50 - 550 μm). One of the methods employed a version of the linear intercept estimation, with serial measurements made in plane with the section (to reduce anisotropy effects), while the other is described as an "interactive user defined region measurement". Average values for percentage porosity and pore size were calculated from both methods in both longitudinal and transverse directions. Minor discrepancies were found between the two methods when calculating porosity, with a systematic increase in porosity of 5% in the longitudinal direction. However there were significant differences between pore size measurements, with the line intercept method consistently undersizing the average pore size. This was believed to be as a result of the inclusion of minimum values in the linear intercept calculations, whereas the other method required an operator to select "representative" pores (with the use of a light pen) from each measurement field. Although the levels of subjectivity as a result of operator discrimination were not investigated and stereological influences were not considered it was concluded that choice of method and selection plane had a significant influence on the results obtained.

Smith *et al.*, (1987) studied the use of stereology to correct for truncation effects encountered in the two dimensional measurement of three dimensional properties such as the pore size and pore size distribution of 0.1 - 0.5 mm diameter pores using $\overline{D}=1.50\,\overline{L}_3$ (i.e., pores are assumed to be spherical). They found uncorrected data to be biased towards larger average pore sizes and that pore size ranges were upgraded by a factor of 1.27 or 1.50 depending on the estimation method employed (intercept chord or pore diameter). They concluded that with the application of stereology image analysis can be used to provide accurate determination of true spatial characteristics from planar micrographs.

Shors *et al.*, (1987) who studied various corals and sea urchin structures, pointed out that it was generally difficult to obtain sufficient numbers of pores in a single frame for statistical significance in macroporous materials and therefore found that multiple measurements were necessary over different portions of the specimen. Once sufficient

measurements had been made they found that area fraction and internal perimeter were the two most useful and least ambiguous parameters.

Rice (1993a) discussed the characterisation of porous materials with respect to mechanical relationships. He proposed that information about the percentage or volume fraction of porosity alone was insufficient to fully characterise a porous structure and that parameters such as minimum solid area (which reflects pore shape) and co-ordination number (which reflects the openness of the porosity) should also be assessed.

Klein *et al.*, (1983b) pointed out that section thickness will affect porosity measurements as a result of pore orientation within the plane of section. This has recently (Johansson and Morberg, 1995a) been studied in specimens prepared for transmitted light microscopy, where sections thicker than 30μm were found to significantly overestimate the volume fraction of solid material.

2.4.3.3 Structural Architecture (or Fabric)

Image analysis has also been used to quantify structural/anisotropic parameters such as fabric and connectivity.

Garrahan *et al.*, (1986) assessed the use of measurements of various structural features seen in sections of cancellous bone. The features considered were the ratio of nodes to free ends and the total lengths of different "types" of strut (Table 2.4.4) expressed as a percentage of the total length of all struts. They carried out intra-observer, inter-observer and inter-section studies (i.e., tested the reproducibility of the method by measurement of a group of bone sections by the same and different operators) and found inter-section variation (measurements on different sections from the same sample) to be "considerable", intra-observer variation to be "low" and inter-observer to be "significant" for some of the measurements as a result of operators being required to define the borders of the measurement field. Significantly higher N:F ratio, N-L and N-N lengths and significantly lower C-F and F-F lengths were observed in healthy compared to osteoporotic patients, whereas there were no significant differences in N-F, C-C, C-N lengths. Correlation between the nodes and struts per mm^2 and actual trabecular bone area indicate that they may be an indicator of connectivity. It is also proposed that connectivity could be related to lengths between free ends and that anisotropy could be related to the lengths between nodes (Compston *et al.*, 1993).

Table 2.4.4 Features assessed by Garahan *et al.*, 1986, and Compston *et al.*, 1993.

Feature	Feature
Free ends (F)	% C-N Length
Nodes (N)	% N-N Length
F:N Ratio	% N-F Length
% Cortex(C) to F length	% N-Loop (L) Length
% C-C length	% F-F length

Shors *et al.*, (1987) used a series of pre-defined measurement parameters common to most image analyses (and thus operator independent) and related them to the structural properties of a number of different porous materials (e.g., various corals, sea urchin spine, sea star etc.). They concluded that the use of image analysis was appropriate for the structural characterisation of biomaterials. Reproducibility studies were carried out on inter-operator setting of grey levels and found to vary by less than 0.5%.

Table 2.4.5 Parameters measured and related properties (Shors *et al.*, 1987).

Parameter Measured	Related Property
Area fraction	Porosity
Internal perimeter	Internal surface area
Minimum crossing distance*	Pore size$^{\Delta}$
Number of feature per area (nA)	Connectivity #
Equivalent circular diameter (d)	Pore size$^{\Delta}$, Connectivity #

* Four test lines are radiated from a point at 45° increments until the adjacent phase was encountered. The minimum distance through the point across the feature is the minimum crossing distance.

$^{\Delta}$ The accuracy of these pore size measurement was highly dependant on the morphology of the voids.

\# A ratio between nA of the solid and nA of the voids in a sectioned specimen was representative of connectivity. In highly interconnected specimens nA is higher for the solid. In contrast the diameter of voids is greater for these materials.

Whitehouse and co-workers (Whitehouse *et al*, 1971; Whitehouse, 1974a and b; Whitehouse and Dyson, 1974) developed a method for the assessment of trabecular volume, trabecular widths and structural anisotropy using low magnification scanning electron micrographs of sections of polished, defatted but un-mounted cancellous bone. Images of the plane polished surface were traced and "Mean intercept lengths" were

calculated by dividing the length of a line that traverses an image of sectioned bone, by the number of times the line intersects a bone/void interface. This was done automatically and with the use of various graphical point counting methods (Whitehouse, 1974b) and found to be consistent. A polar plot of mean intercept length vs. angle of line (from an arbitrary reference point) was then produced. Generally the points fell on the circumference of an ellipse and the ratio of major to minor axis was used as a measure of anisotropy in the plane of measurement.

Hodgskinson and Currey (1990 a and b) used image analysis to evaluate connectivity and anisotropy in order to explain the variation of Young's Modulus in cancellous bone. Connectivity was assessed by counting the number of separate pieces of bone in an image, the reciprocal of which was termed "bone connectivity". "Marrow connectivity" being calculated in a similar way with the number of voids being counted. Anisotropy was evaluated using the technique described by Whitehouse (1974). Forty traverses were used in each direction with a 5° change of orientation between sets of traverses. (1400 scans over 180°) Hodgskinson and Currey then related anisotropy (or fabric) to Young's Modulus using equation 2.4.12.

$$\text{Fabric} = X(R - 1)\text{Cos}^{Y}\theta + \frac{1}{R^{Z}} \qquad (2.4.12)$$

Where, θ is the deviation of the major axis of the ellipse from the direction of loading, R is the ratio of the major axis to the minor one and X, Y, and Z were constants. The process was fully automated with no operator dependence.

Oxnard (1993) employed a non destructive method in which optical Fourier transformations of X-rays of cancellous bone were used to assess the anisotropy of bone specimens. However this technique appears to be limited to relatively large specimens (area of a vertebra) for statistical reasons associated with the variability of bone structure.

It is also possible that ultrasound could be applied to measure the anisotropy as it has been applied in the measurement of the Young's modulus of cancellous bone - a highly structure related property (Bonfield and Tully, 1982; Rho *et al.*, 1993).

2.5 Summary

This review of some of the literature regarding hydroxyapatite highlights the importance of adequate chemical characterisation. As a result of the complicated chemistry, the ease with which hydroxyapatite can decompose under certain conditions and the range of ionic substitutions which may take place, reproducible production of "pure" hydroxyapatite is inherently difficult (Tables 2.4.1 and 2.4.2). This, combined with a lack of standardisation in characterisation methods and insufficient information on the experimental techniques employed, makes comparison of results difficult. It therefore seems that one technique is inadequate for the full characterisation of the material and that a combination of techniques which assess both phase purity and elemental contamination is required.

Similarly, both micro and macro structure should be adequately assessed. Techniques for assessment of microstructure are fairly well developed, however assessment of macrostructural architecture, particularly anisotropy, appears to be more subjective. The methods adopted by Whitehouse and co-workers (Whitehouse *et al,* 1971; Whitehouse, 1974a and b; Whitehouse and Dyson, 1974) and Hodgkinson and Currey (1990 a and b) appear to be the most appropriate.

CHAPTER 3

MECHANICAL PROPERTIES OF BONE AND HYDROXYAPATITE

3.1 Introduction

A knowledge of the behaviour of bone under mechanical stress is vital when considering replacement materials. If not to enable prediction of the stresses and strains bones are expected to withstand in normal life, then to understand why bones behave (mechanically) as they do from a materials standpoint so that the effects of any changes in their environment or structure can be fully predicted. However as a result of the hierarchical structure possessed by bone, the properties tend to be characterised on several distinct levels, for instance; the properties of collagen (tendon) and bone mineral (hydroxyapatite) in comparison with the properties of individual trabeculae or bulk specimens of cancellous bone.

Moreover comparisons between studies on the mechanical properties of bone carried out by different workers in different laboratories are hampered by the fact that tests tend to be carried out on the bones of a large number of different species. Kuhn *et al.*, (1989) have shown that while human and canine trabecular bone from the distal femur possessed similar values of ash weight and apparent density, the variation of modulus and compressive stress with apparent density differed for the two groups. Similarly, Rice *et al.*, (1988) found data for human and bovine cancellous and cortical bone to be statistically distinct. This indicates that bone mechanical property relationships are species specific.

The mechanical properties of polycrystalline dense hydroxyapatite are fairy well documented, however the properties of porous material and the dependence on the volume fraction of porosity still requires some clarification.

3.2 Mechanical Properties of Bone

Bone can be considered as a highly complex composite consisting of 65-75 wt % mineral, 15-20 wt % collagen and 1-4 wt % assorted lipids and organic molecules. Furthermore, bone is a living tissue and constant remodelling must be accounted for when considering fatigue properties, mineral content or density dependence. Some of the main mechanical characteristics of bone are listed below:

- Bone is viscoelastic - all its mechanical properties are strain rate sensitive
- Bone is anisotropic - mechanical properties are sensitive to the direction of loading
- Bone is viscoplastic - with time it will deform until fracture under any constant load

Bone exhibits considerable variation in its structure as a result of species, age, environment and function which lead to significant differences in modulus, strength and toughness in both cortical and cancellous bone. The osteonal microstructure of cortical bone makes it highly anisotropic, although its density is relatively consistent (1.85-2.05 $g.cm^{-3}$ in human bone). While the mechanical properties of cancellous bone (which can be considered to be a foam) are highly dependent upon porosity and architecture, both of which vary widely, making it difficult to characterise. Indeed, quoting a single figure for the bulk mechanical properties of a piece of cancellous bone without discussing its anatomic site (Goldstein, 1987) and age (Burstein *et al.*, 1976; Wong *et al.*, 1985) is meaningless. In addition, the anisotropy due to the orientation of major trabeculae along lines of principle stress makes the mechanical characterisation of cancellous bone highly complex. Table 3.2.1 summarises some of the data available from the literature.

Table 3.2.1 Data for the mechanical properties of bone

	Compressive Strength (MPa)		Tensile Strength (MPa)	Young's Modulus (GPa)	
	Cortical	Cancellous	Cortical	Cortical	Cancellous
Longitudinal Direction	237‡ 193†	9.3 [4.5], 6.6 [6.3], 3.6 [2.3]#	150¥ 156‡ 133†	25¥ 18-22‡ 17-20†	0.90 [0.71], 0.62 [0.71], 0.26 [0.17]# 0.26 [0.13]§ 0.42 [0.21]$
Transverse Direction	178‡ 133†	4.9 [1.3], 1.0 [0.3], 0.6 [0.2]#	50¥ 50‡ 51†	12¥ 10-15‡ 11.5†	0.40 [0.07], 0.06 [0.01], 0.01 [0.01]# 0.16 [0.11]§ 0.20 [0.20]$
Unspecified Direction		2.4 - 6.2* 1 - 20§ 1 - 13+			0.10 - 0.64*

Data from: *Linde *et al.*, (1992) high and low values from human proximal tibia; ¥Bonfield (1989) human cortical bone; Kuhn *et al.*, (1989) §canine and $human distal femur; Cowin *et al.*, (1986) ‡bovine and †human cortical bone; +Goldstein *et al.*, (1983) human proximal tibia; #Martens *et al.*, (1983) human distal femur (bone from: head, neck, intertrochanter). Numbers in square parentheses are standard deviations.

In a study of the effects of apparent density on mechanical properties of both cortical and cancellous bone Rice *et al.*, (1988) determined that the mechanical properties of cortical bone could not be extrapolated from the properties of cancellous bone. Similarly, in a more recent study using conventional testing methods and ultrasound, Rho *et al.*, (1993) concluded that the mechanical properties determined for the individual trabeculae were not consistent with the properties of dense cortical bone, while agreement was found between interpolated results from bulk cancellous bone measurements and individual trabeculae.

3.2.1 Cortical Bone

3.2.1.1 Elastic Properties, Strength and Toughness

The elastic and strength properties of cortical bone have been found to be dependent on the direction of the load applied by a number of authors (Reilly and Burstein, 1975; Yoon and Katz, 1976b; Behiri and Bonfield, 1984). However, as a result of the osteonal microstructure, it displays a certain degree of symmetry and is considered to be transversely isotropic (Reilly and Burstein, 1975; Yoon and Katz, 1976b) as its elastic properties transverse to the longitudinal axis are approximately isotropic and substantially different from those in the longitudinal direction (Figure 3.2.1). In the longitudinal direction cortical bone is relatively tough and ductile, while in the transverse direction it is relatively brittle (de Groot, 1983). The strength of cortical bone is also dependant on the polarity of the load (tensile or compressive) as it is asymmetrical (Gibson and Ashby, 1988) - bone is stronger in compression than in tension (Figure 3.2.1).

The complexity of loading conditions *in vivo*, due to muscle actions as well as weight bearing, often results in multiaxial loading. Keaveny and Hayes (1993) demonstrated that by considering the forces applied to the femoral diaphysis through the abductor and the head, if bone were an isotropic material with equal strengths in tension and compression then it would be weaker along the medial aspect than along

the lateral one. This suggests that cortical bone has adapted this combination of asymmetry and anisotropy as a response to the multiaxial loading experienced *in vivo*.

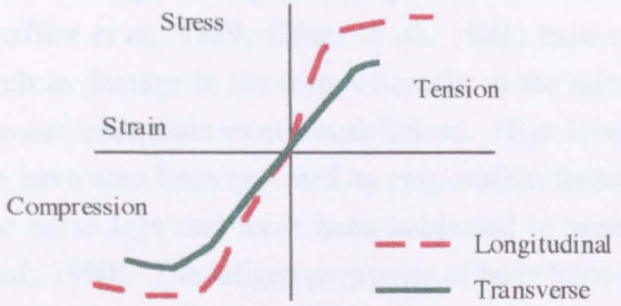

Figure 3.2.1 Compressive and tensile behaviour of cortical bone

3.2.1.2 Viscoelastic Properties

Cortical bone is both strain rate sensitive and viscoplastic. All its mechanical properties are time dependent (Behiri and Bonfield, 1984; Dabestani, 1989). Figure 3.2.2 demonstrates the type of stress-strain behaviour that occurs at different strain rates, from which it can be seen that:

- Cortical bone has a higher modulus at higher strain rates
- The yield and ultimate strengths of cortical bone increase as the strain rate increases over the complete range
- At very high (greater than 0.1 s^{-1}) strain rates cortical bone becomes more brittle
- At stain ratestypical of more normal activity (less than 0.1 s^{-1}) ductility increases as strain rate increases
- There is an optimum range of strain rates (in red) for maximum energy absorption.

On consideration of some typical physiological strain rates, slow walking = 0.001 sec^{-1}, brisk walking = 0.01 sec^{-1}, slow running = 0.03 sec^{-1} (Currey 1975; Lanyon *et al.*, 1982, O'Conner *et al.*, 1982) it becomes clear that bone has adapted to absorb energy arising from relatively high impact activities.

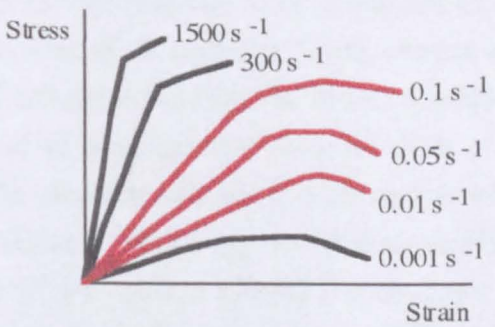

Figure 3.2.2 Schematic diagram illustrating the strain rate dependence of the mechanical properties of cortical bone.

3.2.1.3 Fatigue

In vivo, bone is continually undergoing repetitive low intensity loading, such as that experienced by the rib cage during breathing, or the femur when walking. A number of authors (Schaffler *et al.*, 1989, Carter *et al.*, 1981) have reported that this cyclic loading can result in damage in the form of cracks at the microstructural level which may accumulate and contribute to eventual failure. High levels of stress over shorter periods of time have also been reported as responsible for fatigue damage, as in the fracture of race horse legs that have been subjected to rigorous training programs (Nunamaker *et al.*, 1990). The fatigue properties of bone have usually been determined from non viable specimens, so the effects of remodelling are unknown. However, because physiological levels of loading have been reported to induce fatigue damage and failure *in vitro* (Schaffler *et al.*, 1989), a number of authors believe that bone remodelling occurs to repair micro-cracks (Burr, *et al.*, 1985, Lipson and Katz, 1984).

3.2.1.4 Apparent Density

The density dependence of cortical bone is some what overshadowed by its anisotropy and the fact that density is constantly changing as bone is being resorbed and remodelled. Mature cortical bone tends to be of a relatively uniform density throughout the volume of a specimen and provided comparisons are made between similar specimens, (specimens cut from comparable bones along the direction of osteons or transverse to them) the mechanical properties can be seen to increase with density in a linear fashion (Behiri *et al.*, 1985). However care must be taken to compare specimens at the same stage of skeletal maturity as density changes due to increased mineralisation during ageing, secondary ossification etc. will affect the results. A typical mean value of apparent density of hydrated human femoral cortical bone is 1.86 [0.06] $g.cm^{-3}$ (Snyder and Hayes, 1990).

3.2.1.5 Other Considerations

There are many other factors believed to be important to the mechanical properties of cortical bone, i.e., orientation of collagen fibres, content of the cement lines, bonding between mineral and collagen. Some of the more significant parameters being age, ash density (a measure of mineral content as a function of volume), osteon type, and collagen content. The modulus and strength properties of cortical bone progressively deteriorate with age (Currey 1969a) eg. the ultimate tensile strength of bone decreases from 140 MPa in the third decade to 120 MPa in the ninth decade. The most important change as far as fracture risk is concerned is the resulting reduction in energy absorption of 7% per decade (Burstein *et al.*, 1976). Thus bone is more brittle, less strong and more stiff with age. Currey (1969b) proposed that the variation in strength

with age may be related to changes in the average morphology of the apatite crystals with age. He also determined (1969a) that the median value of mineral within bone (66-67 wt %) is the optimum value for energy absorption and demonstrated (1988a) that up to 88% of the variance in modulus and strength can be explained using a power law model with volume fraction (proportional to apparent density) and mineral content as independent variables. Primary bone has been shown to be stronger and have a higher Young's modulus than Haversian bone possibly as a result of reduced amounts of mineralisation in the relatively new Haversian systems (Currey, 1975). Lipson and Katz (1984) demonstrated that primary bovine bone is isotropic while secondary (Haversian) bovine bone is transversely anisotropic. In studies of long bones Evans and Vincentelli (1969) identified two forms of osteon within cortical bone, one with collagen fibres predominantly parallel and one with collagen fibres predominantly perpendicular to the long axis of the osteons. They reported that variations in the relative proportions of these osteons affected the modulus and tensile strength of the bone. Similarly, Ascenzi *et al.*, (1986) reported the existence of "transverse" and "longitudinal" lamellae within interstitial bone and osteons. Furthermore, they suggested that the oriented lamellae are distributed with respect to the bending forces in bone. However, Marotti (1993) has suggested that lamellar bone is composed of alternating densely and loosely packed layers of interconnected collagen bundles with no orientation, and suggests that the findings of other authors may be due to preparation or analysis method, artefacts.

3.2.2 Cancellous Bone

The cancellous bone structure is between 30 and 70 % porous (bone with less than 30% porosity is classified as cortical). A typical mean value of apparent density of hydrated human femoral cortical bone is 1.86 [0.057] $g.cm^{-3}$ (Snyder and Hayes, 1990). In contrast a typical mean value of apparent density of hydrated human proximal tibia trabecular bone is 0.30 [0.09] $g.cm^{-3}$ (Carter and Hayes, 1977). The magnitudes of their variations are similar but the percentage deviations are much larger for cancellous bone (30% compared to 3%). This is particularly significant as the mechanical properties of trabecular bone are very density sensitive, eg: the mechanical properties of trabecular bone within the proximal tibia can vary by up to two orders of magnitude as a result of density variations (Goldstein *et al.*, 1983). Care must also be taken to define exactly what type of density is being measured (see part 2.4.3.1). These wide density fluctuations can be explained by Wolff's Law (1870, 1892) which states that bone

senses its mechanical environment and can adapt to a new one by the control of its geometry, texture and density. Thus the trabecular regions of long bones, such as the cancellous bone located in the femoral head (i.e., a load bearing region), display a higher density compared with that towards the shaft.

3.2.2.1 Elastic Properties, Strength and Toughness

Cancellous bone is a natural foam but behaves in a similar manner to an engineering foam. A number of authors have demonstrated that the modulus of trabecular bone is related to apparent density by a power law relationship of the form:-

$$E = a + b\rho^{c} \qquad (3.2.1)$$

where a, b, and c are constants which depend on architecture (Gibson, 1985; Rice, *et al.*, 1988) with c having a value of approximately two. This has also been found to be true for the compressive strength, (Rice *et al.*, 1988). Consequently a 25% reduction in density will result in a 56% decrease in mechanical properties.

Most mechanical testing of trabecular bone has been in the form of compression testing, as it is believed that *in vivo* failure of trabecular bone occurs primarily under compression loads (as a result of loading in bones occurring predominantly in that mode). In compression, wet cancellous bone behaves as an elastic-plastic foam, Figure 3.2.3, exhibiting a linear region at low stresses (where individual trabeculae are deforming elastically by bending), followed by a region of plastic deformation (where individual trabeculae are deforming plastically by bending) and a collapse plateau (denoting plastic deformation due to plastic yielding and buckling of the trabeculae), truncated by a region of densification in which the stress rises steeply (where trabeculae are compacted together) (Gibson and Ashby, 1988). The ability to deform plastically by as much as 50% allows trabecular bone to absorb considerable energy while maintaining a minimum mass, furthermore lower density specimens, which have more pore space, exhibit a "longer" collapse plateau due to densification occurring at higher strains.

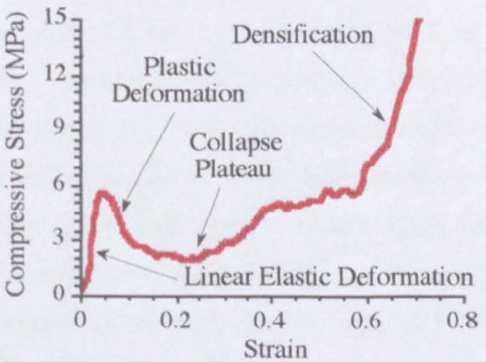

Figure 3.2.3 Stress strain behaviour of trabecular bone under compression

The behaviour of trabecular bone in tension, while being similar in the elastic region, is completely different post-yield (Figure 3.2.4). It exhibits elastic behaviour with sudden brittle failure at ultimate load,as yield occurs via the fracture of trabeculae,and as more trabeculae fracture the less load the specimen can take until complete fracture occurs. However, when the axis of load is skewed with respect to the main load bearing axis of the bone the stress stain curve is parabolic, with plastic deformation and greater energy absorption. This indicates that bone has adopted a structure which may absorb and distribute the stress concentrations in the vicinity of the articular surfaces of joints (Keaveny and Hayes, 1993).

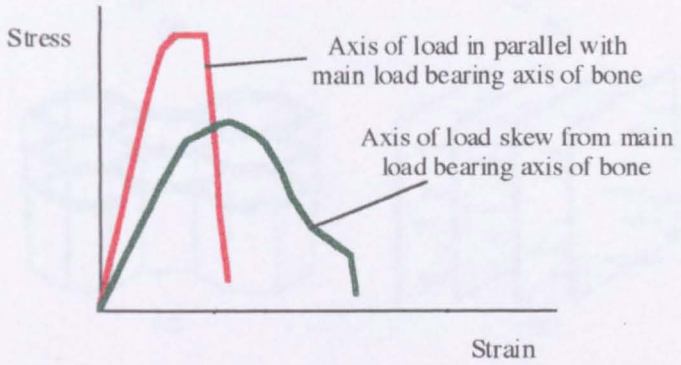

Figure 3.2.4 Stress strain behaviour of trabecular bone under tension

3.2.2.2 Effects of Anisotropy

Due to the aforementioned inherent texture in cancellous bone the mechanical properties are highly anisotropic, which has been demonstrated by a number of authors (Hodgkinson and Currey, 1990 a and b; Holmes *et al.*, 1984; Gibson, 1985; Harris, 1991; Hert, 1994). Anisotropy has been shown to be related to the location within the bone (Whitehouse and Dyson, 1974; Goldstein et al., 1983; Martens et al., 1983), and is believed to be a response to the physiological forces exerted on the bone (Wolff, 1870; 1892).

Gibson and Ashby (1988) described the special considerations required when studying the structure, properties and mechanical characteristics of highly porous materials. They propose that cellular materials can be divided into two groups *honeycombs* and *foams*. Honeycombs are made up from two dimensional cells and foams from three dimensional ones, where cell walls have random orientations in space. Foams may then be further subdivided into *open* and *closed*, where open foams have interconnecting cells and closed foams have cells which are sealed off from their neighbours. The cells of foams were found to have faces with an average of five edges irrespective of the number of faces per cell. Cancellous bone was classed as a mixed open and closed

foam with variable anisotropy, the extent of anisotropy and "openness" being dependent on its load bearing requirements (the principle requisite of bone being that as a frame it should carry sufficient load and have a reasonable stiffness, with minimum weight). These requirements were simplified into four cases and structures were modelled accordingly (Figure 3.2.5).

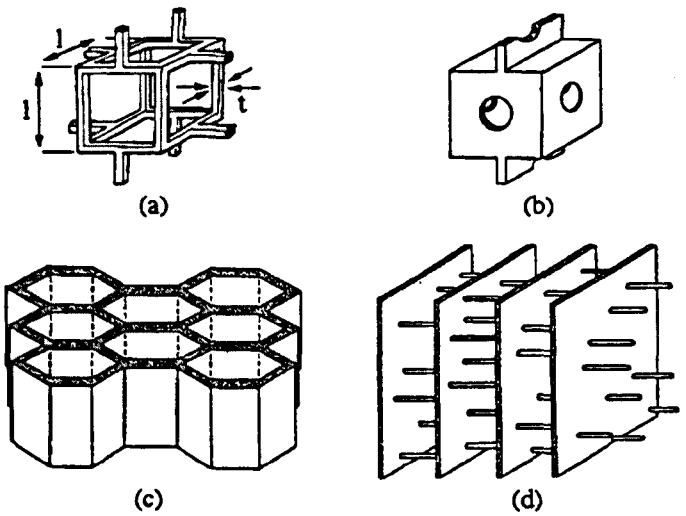

Figure 3.2.5 Models for the structure of cancellous bone.

From Gibson and Ashby, (1988).

Where bone is subject to low isotropic loads, it has a low density, open equiaxed structure (Figure 3.2.5a), while higher isotropic loads result in a higher density and therefore more closed structure (Figure 3.2.5b). Bones under relatively high uniaxial stress have a structure with thick cell walls and occasional cross members with the walls oriented in the direction of loading so as to contain the largest principle stress, resulting in an almost prismatic structure (Figure 3.2.5c). Biaxial loading, results in an array of parallel plates oriented to contain the directions of largest principle stresses separated by slender cross members which act as spacers (Figure 3.2.5d).

Thus bone with structures represented by Figure 3.2.5 a and b can be considered as a foam with open and closed equiaxed cells respectively, the behaviour of which was found to be dependent on density in the following manner:

$$\frac{E^*}{E_s} = C_1 \left(\frac{\rho^*}{\rho_s} \right)^2 \qquad \text{Open cells} \qquad (3.2.2)$$

$$\frac{E^*}{E_s} = C_2\left(\frac{\rho^*}{\rho_s}\right)^3 \qquad \text{Closed cells} \qquad (3.2.3)$$

$$\frac{\sigma^*}{E_s} = c_1\left(\frac{\rho^*}{\rho_s}\right)^2 \qquad \text{Open cells} \qquad (3.2.4)$$

$$\frac{\sigma^*}{\sigma_{ys}} = c_2\left(\frac{\rho^*}{\rho_s}\right)^{3/2} \qquad \text{Closed cells} \qquad (3.2.5)$$

Bone with a structure similar to Figure 3.2.6c (i.e., that of a foam with closed prismatic cells or a honey comb) or figure 3.2.6 d (plate like structure) can be considered as anisotropic and will vary with direction of loading where:

$$\frac{E_T^*}{E_s} = C_3\left(\frac{\rho^*}{\rho_s}\right)^3 \qquad \text{Transverse loading} \qquad (3.2.6)$$

$$\frac{E_L^*}{E_s} = C_4\left(\frac{\rho^*}{\rho_s}\right) \qquad \text{Longitudinal loading} \qquad (3.2.7)$$

Bone with an open prismatic structure will also be anisotropic, the behaviour of which will vary with direction of loading as follows:

$$\frac{E_T^*}{E_s} = C_5\left(\frac{\rho^*}{\rho_s}\right)^2 \qquad \text{Transverse loading} \qquad (3.2.8)$$

$$\frac{E_L^*}{E_s} = C_6\left(\frac{\rho^*}{\rho_s}\right) \qquad \text{Longitudinal loading} \qquad (3.2.9)$$

$$\frac{\sigma_T^*}{\sigma_{ys}} = c_5\left(\frac{\rho^*}{\rho_s}\right)^2 \qquad \text{Transverse loading} \qquad (3.2.10)$$

$$\frac{\sigma_L^*}{\sigma_{ys}} = c_6\left(\frac{\rho^*}{\rho_s}\right) \qquad \text{Longitudinal loading} \qquad (3.2.11)$$

Determination of whether a structure fell into the open or closed category was achieved by calculating the relative density. Generally specimens with a relative density below 0.2 (i.e., 80% porous) were considered as open foams, while those with relative densities above 0.2 were considered closed foams (Gibson, 1985; Gibson and Ashby, 1988).

Generally "real" bone structure combines two or more of these cases and is inherently more complicated as a result of influences due to the presence of "fluid" contained within the cells (i.e., bone marrow, lipids, etc.) and the fact that equations for both open and closed foams assume constant cell geometry, variations in which can lead to fluctuations in Poisson's ratio of 0.5 to -0.7 resulting in marked changes in mechanical behaviour. However, these relationships for the modulus and ultimate compressive stress of cancellous bone have been shown to be in agreement with experimental data (Gibson, 1985; Currey, 1988a; Linde *et al.*; 1991).

3.2.2.3 Viscoelastic Properties

Very few creep experiments have been performed on trabecular bone, therefore conclusions cannot be drawn regarding these characteristics. The effect of varying strain rate, however, is well documented, with both modulus and strength being weakly sensitive (Carter and Hayes 1976 and 1977; Linde *et al.*, 1991). Carter and Hayes, (1977) demonstrated that compressive strength and modulus are related to strain rate as follows:

$$\sigma_c \propto \varepsilon^{0.06} \rho^{2} \qquad (3.2.12)$$

$$E_c \propto \varepsilon^{0.06} \rho^{3} \qquad (3.2.13)$$

Thus an increase in strain rate from 0.001 sec^{-1} (slow walking) to 0.1 sec^{-1} (strenuous exercise) results in increases in strength and modulus of 30% (Keaveny and Hayes, 1993). The load bearing capacity of cancellous bone is also affected by the presence of bone marrow. At physiological loading rates the marrow plays no role in the behaviour of trabecular bone. However, at very high strain rates (indicative of severe traumatic compressive loading, such as being injured by gunfire) the flow of the marrow through the inter-trabecular spaces is restricted. This results in enhanced mechanical properties, i.e., significant increases in strength, modulus and energy absorption, when compared to physiological loading or similarly traumatic loading of bone with the marrow removed (Carter and Hayes, 1977).

3.2.2.4 Fatigue Properties

Fracture in individual trabeculae and tiny callus formations about these cracks have been observed by many authors (eg. Freeman *et al.*, 1974, Wong *et al.*, 1985). It has been suggested that these are fatigue cracks and that they are responsible for a number of bone disorders. However few controlled experiments have been performed and as a

result of the heterogeneity of bone, there is a large scatter in the available results. These results suggest that cancellous bone is more resistant to fatigue than cortical bone as a result of the differing mechanisms of failure (fracture and buckling of individual trabeculae vs. accumulation of micro-cracks which can propagate as cracks in cortical bone matrix).

3.2.2.5 Effects of Age and Ash Weight

Age has a significant effect on the mechanical properties of bone as a result of changes in density and architecture which may reduce the properties by as much as an order of magnitude. As bone ages its density is reduced as a result of a reduction in the thickness and number of the individual trabeculae resulting in an increase in size of inter-trabecular spaces (Mosekilde and Mosekilde, 1990; Snyder 1991). In the lumbar spine bone density has been shown to be reduced by as much 50% from the second to the eighth decade (Mosekilde *et al.*, 1987). Melsen *et al.*, (1976) found the ash weight (a measure of the total mineral content) of cylindrical cancellous bone specimens to be well correlated with the ultimate compressive strength of the cylinders.

3.3 Mechanical Properties of Hydroxyapatite

The mechanical properties of synthetic hydroxyapatite, as with all engineering ceramics, are highly dependent on processing route as a result of the effects of processing on the micro- and macrostructure of the final product. As discussed in Section 2.3 hydroxyapatite is generally produced by a cold pressing and sintering route. The microstructure of hydroxyapatite bodies produced via this method being a function of morphology of the starting powder, compaction pressure, sintering temperature and time. This leads to variations in grain size, micropore size and distribution. However, in porous hydroxyapatite (produced via either the addition of decomposing fillers to dry powders, or the addition of foaming additives (H_2O_2 or $(NH_4)_2CO_3$) to aqueous powder slurries, or the application of hydrothermal techniques to pre-formed materials such as coral) the porosity is the dominating factor in determining the mechanical properties. Some studies have also been conducted into the effects of phase purity on the properties of hydroxyapatites combined with other calcium phosphates.

3.3.1 Grain Size

Grain boundaries act as barriers to crack growth as a result of an increased energy requirement to propagate a crack across a grain boundary as opposed to through the grain (Orowan, 1933). Assuming that a crack initiates in a flaw within a grain due to a dislocation blockage (Petch, 1953), according to Griffith flaw theory (1920) the stress required to propagate a fracture across a grain boundary is inversely proportional to the square root of the length of fracture (3.3.1). Thus large grains will be detrimental to strength, as flaws in larger grains with lengths equal to the diameter of the grain will require less external energy to propagate across grain boundaries than similar flaws in smaller grains.

$$\sigma = \sigma_0 + Kd^{-1/2} \qquad (3.3.1)$$

Where σ = strength, σ_0 = applied stress required to move dislocations along a glide plane, K is an empirical constant and d = grain size.

Best (1990) found this relationship true for 90-98% dense hydroxyapatite specimens and de With *et al.*, (1981a) reported that 98% dense specimens with a fine grain size (1 μm) possessed a higher strength and fracture toughness (103 MPa, 1.33 MPa.$m^{1/2}$) than 94% dense specimens with a coarse grain size (2.9 μm) (94 MPa, 0.93 MPa.$m^{1/2}$). However, the effect of grain size may have been masked by the concurrent effect of

porosity. Knudsen (1959) combined relationships for grain size and porosity and tested his relationship (3.3.2) on thoria specimens with porosities of 6.7-31.1%, grain sizes of 6.1-42.9 and found it to hold in bending and compression.

$$S = kd^{-a} e^{-bP} \tag{3.3.2}$$

Where k and a are empirical constants, b is an empirical constant related to the porosity (assumed not to be affected by grain size) and P is the specimen porosity.

Similarly, Akao *et al.*, (1981) have demonstrated that an increase in density has a greater effect on compressive strength of hydroxyapatite than a coincidental increase in grain size and Matsuno *et al.*, (1992) studied the effects of porosity on fracture toughness and found it to increase linearly with density despite larger grain sizes.

3.3.2 Porosity

It seems there are several models regarding the contribution of porosity to the mechanical properties of porous materials. These may be classed into two broad groups; (a) models based on the effect of pores (spherical or shaped) as flaws or stress concentrators and (b) models based on the effects of pores as a second phase with no contribution to the mechanical properties i.e., load bearing is associated with average or minimum values of solid volume fraction.

By considering the pores as fissures and applying Griffiths (1920) flaw theory, Le Huec *et al.*, (1995) proposed that in ceramics of the same percentage porosity, variations in average pore size may affect mechanical properties. They produced a series of specimens with similar densities but varying proportions of macro (400 μm) and micro (100 μm) pores (although they ignored the presence of pores <5 μm in size). However, the data they presented appeared to indicate that specimens of similar densities containing a larger fraction of macropores possessed superior mechanical properties. In comparison Shareef *et al.*, (1993) found that by combining coarse (50 μm) and fine (3 μm) powders they were able to produce a machinable ceramic with a fracture toughness of 0.8 MPa.$m^{1/2}$ as a result of a fine interconnected pore structure.

Ryshkewitch (1953) demonstrated that the compressive strength (σ) of a ceramic varies with its average pore volume (V) in the following manner:

$$\sigma = \sigma_0 e^{-nV} \tag{3.3.3}$$

This relationship has been demonstrated for hydroxyapatite by a number of authors (Rao and Boehm, 1974; Peelen *et al.*, 1978; Akao *et al.*, 1981; Driessen *et al.*, 1982; Royer *et al.*, 1993). However, it does not appear to be suitable for ceramics with a porosity exceeding 50% (Duckworth, 1953). Similarly, Rice (1993b) has discussed the nature of the relationship between porosity and mechanical properties in denser specimens (pore volume fraction of 0.1-0.4) and concluded that stress concentration effects due to pore shape had little direct effect on the tensile or elastic properties but may affect mechanical behaviour in compression. He proposed that correlations between test results and predictions from previous models based on pore shape could be explained by considering pore shape as a function of minimum solid (or load bearing) area.

Gibson and Ashby (1988) demonstrated that the mechanical properties of highly porous ceramics (pore volume fraction 0.9-0.6) may be successfully predicted by modelling the structure as an open or closed isotropic elastic brittle foam, with behaviour as shown in Figure 3.3.1. This was achieved by considering the load bearing geometry and failure mechanisms of the individual struts. Furthermore, in work carried out by Hagiwara and Green (1987) on the elastic behaviour of alumina with porosities of 75-90 %, the modulus was found to comply with these predictions.

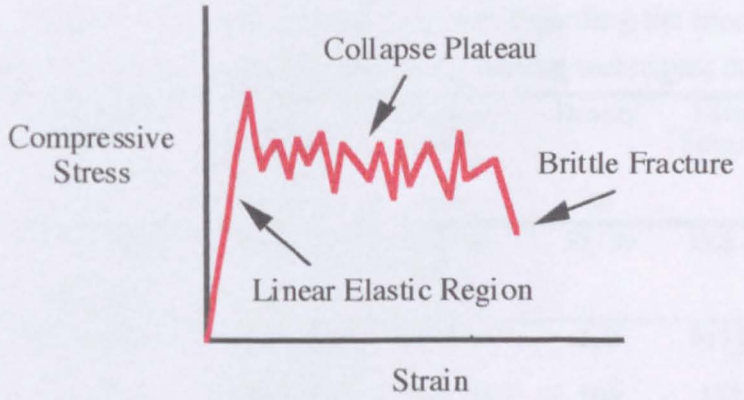

Figure 3.3.1 Behaviour of an elastic brittle foam in compression.
(Adapted from Gibson and Ashby, 1988)

The relationships derived by Gibson and Ashby (1988) for isotropic elastic brittle foams were similar to those derived for isotropic bone (section 3.2.2.2), where ultimate compressive stress was found to be related to the square of the density, and compressive modulus was dependent on the square or cube of the density, depending on whether the porous structure was open or closed respectively.

3.3.3 Phase Purity

Jarcho *et al.*, (1976) reported a reduction in fracture strength as a result of the presence of ß-tricalcium phosphate (196 MPa for 100%, 160 MPa for 87% dense hydroxyapatite). While Royer and Viguie, (1993) found that specimens containing small amounts of tricalcium phosphate which had transformed from the ß to the α type had enhanced mechanical properties (flexural strengths of up to 150 MPa, compared to 100 MPa for pure HA). This was attributed to the presence of a surface layer of tricalcium phosphate resulting in surface compaction and closing surface micro-cracks due to the volume increase that accompanies the transformation. They also found that the presence of CaO lowered the flexural strength to around 50 MPa. Wang and Chaki (1993) compared the mechanical properties of hydroxyapatite sintered in air moisture and vacuum. They found that as a result of dehydroxylation and subsequent decomposition of hydroxyapatite to tricalcium phosphate and tetracalcium phosphate, flexural strengths of specimen sintered in either air or vacuum atmospheres peaked at 14.7 MPa (78% dense, sintered in air at 1200°C) and 11.6 MPa (76% dense, sintered in vacuum at 1100°C). While material sintered in moisture was believed to have reduced sinterability but attained a flexural strength of 16.5 MPa (77% dense, sintered in moisture at 1300°C) with no signs of dehydroxylation up to 1350°C.

Table 3.2.1 Summary of some current literature regarding the mechanical properties of dense and porous hydroxyapatites and the processing techniques employed.

	Processing Route (Sinter Temp. in °C)	Test Conditions (CHV in mm min^{-1})	Specimen Details mm	Density %	Ultimate Stress MPa	Modulus GPa
Rao and Boehm 1974	Conventional (900 - 1300)	Compression (?)	6.35 Ø 12.7 l	50 - 99	13.8 - 138	-
Jarcho *et al.*, 1976	Conventional (1100)	Compression; 3 point bend (1.25)	4.6 Ø, 2 l 2x2x30 l	100 100 87	917 [138] 112 [11] 79 [19]	34.5
Peelen *et al.*, 1978	Slip cast with H_2O_2 (1100-1350)	Compression (2.5 - 5.0)	10 Ø 10-15 l	30 - 65	30 - 170	-
Rootare *et al.*, 1978a	Conventional (1200)	Compression (?)	7 Ø 14 l	98	376 [13]	121 [6]
Denissen *et al.*, 1980a	Conventional Differing start powders *Hot pressed (1200)	Compression (5)	4 Ø 6-7 l	92.5 97 97* 99.9	130 [30] 410 [75] 390 [40] 430 [95]	-

Table 2.3.1 Continued over page.

Table 3.2.1 Cont.

	Processing Route (Sinter Temp. in °C)	Test Conditions (CHV in mm min^{-1})	Specimen Details mm	Density %	Ultimate Stress MPa	Modulus GPa
De With *et al.*, 1981b	Conventional (1100-1250)	Compression (?) Ultrasound	5 Ø 12 l	90 - 95	798	105
Akao *et al.*, 1981	Conventional (1150-1300)	Compression (2)	5 Square 10 l.	80.6 90.9 96.1 97.2	308 [46] 415 [46] 465 [58] 509 [57]	42 [4] 75 [4] 79 [5] 81 [5]
		3 point bend (0.5)	2×4×15 l		61 [8] 104 [11] 106 [10] 113 [12]	44 [4] 80 [6] 85 [6] 88 [6]
Driessen *et al.*, 1982	Slip cast with H_2O_2 (1300)	Compression (5)	10 Square 30 l	60 - 65	50 [15]	-
Holmes *et al.*, 1984	Hydrothermal conversion of coral	Compression (?)	?	34	8.4 - 41.2	0.0128 - 1.48
Geesink *et al.*, 1988	Plasma sprayed	Compression Tension Shear (?)	Apatite coating on Ti substrate 4.5 Ø; 9 l	"dense"	650 85 74	
Yamasaki *et al.*, 1990	Hydrothermal hot pressing (1050)	Compression (?)	?	58	150 [20]	-
Fang *et al.*, 1992	Burn out of $(NH_4)_2CO_3$ in microwave (1150-1200)	Diametral (0.051)	12.7 Ø ? l	27 - 91	4.5 - 47 (tensile)	-
Royer and Viguie, 1993	Conventional Mixed TCP and HA (1250)	3 point biaxial flexure (0.1)	22 Ø 3.5 l Ca:P <1.6 1.6 - 1.66 > 1.66	 98 98 98	 30 150 30	-
Le Huec *et al.*, 1995		Compression (0.5)	15 [3] Ø 15 [3] l	22.5 ~30 ~36 ~44 ~51 ~58 65.0	348 141 [65] 117 77 [16] 32 [14] 23 [16] 13	
Poumarat and Squire, 1993	Retrieved from femur	Compression (0.025)	15×12.5×8 l Xenograft Bovine bone Human bone	 38 [7] 28 [7] - -	 9.6 [3.7] 5.9 [2.7] 8.5 [4.2] 8.9 [5.2]	 133 [52] 79 [37] 118 [62] 77 [55]

CHV = Cross head velocity; Ø = Diameter; l = Length, all ultimate stress and modulus values are compressive unless otherwise indicated and numbers in square parentheses are standard deviations.

3.4 Mechanical Testing of Cancellous Bone and Porous Hydroxyapatite

Conventional methods of mechanical characterisation such as tensile, diametral and impact testing are unsuitable when applied to cancellous bone or porous ceramics due to the difficulties encountered in machining and gripping test pieces securely without pre-damaging them (Currey, 1970).

The use of ultrasound to measure elastic properties has been reported for dense hydroxyapatite and cortical bone (Bonfield and Tully, 1982, de With *et al.*, 1981 a and b). For accurate measurements the diameter of the transducers must be smaller than that of the sample and the distance between the transducers (i.e., the length of the sample) should be as wide as possible so as to increase the length of the path of the sound wave through the sample and hence the difference in time interval to be detected (Krasil'nikov, 1963). Mechanical testing and ultrasound results were compared in a recent study by Rho *et al.*, (1993) on human cancellous bone. However, ultrasonic results for Young's modulus were found to be slightly higher than the values obtained via more conventional means.

Compression testing has been successfully used by a number of authors (Holmes *et al.*, 1984; Hodgskinson and Currey, 1990 a & b) in the characterisation of cancellous bone and has also been adopted in the testing of porous and dense hydroxyapatite, as discussed by Driessen *et al.*, (1982); Peelen *et al.*, (1978) and de Groot (1987). However, in addition to difficulties experienced in comparing tests in the same and different laboratories as a result of the inherent variation in bone samples, even from the same site and species, there seems to be little standardisation as regards testing parameters such as cross head velocity, specimen dimensions and testing conditions, which all have significant effects on the results.

3.4.1 Specimen Size

A study by Harrigan *et al.*, (1988), of the limitations of the continuum assumption in cancellous bone concluded that the accuracy of a measurement over a "small" (0.7 mean intercept lengths) samples of cancellous bone were unacceptable, and that accuracy increased as intercept length increased. This suggests that a specimen for mechanical testing should be of a certain minimum size if representative results are to be obtained and that any structural studies should sample as large an area as possible.

However, real bone varies from place to place and too large a specimens size may result in statistical uncertainty regarding the structural variation that may occur within the specimen. It has been shown by Kuhn *et al.*, (1988) that canine cancellous bone structure is only reliably consistent over distances of up to 8 mm. For human and bovine bone however, this value would be expected to rise as a result of the increased bone size.

3.4.2 Specimen Geometry

A further investigation into the effects of geometry (size, shape and aspect ratio) on the mechanical behaviour of trabecular bone was performed by Linde *et al.*, (1992), they found the most influential parameter to be the aspect ratio (length : diameter) which, on increasing, had the effect of decreasing values obtained for the loss tangent (damping) while increasing the Young's modulus, reproducibility and correlation between results. Other parameters under investigation were shape and size. Cylindrical and cubic shapes were compared and no significant differences were detected, while larger specimens had larger values of Young's modulus and failure energy. This was thought to be due to frictional effects arising from mismatch between the Poisson's ratios of the platens and the specimens, but was more likely to be as a result of movement between the essentially rigid platens and the free specimens. The authors concluded that in general, the Modulus results obtained during most tests are significantly underestimated. They proposed a standard specimen geometry of 6.5 mm side cube or 6.5×7.5 mm diameter cylinder which would have a modulus 20-40% too low. Following this Keaveny *et al.*, (1993b) decided to investigate the effects of geometry on ultimate compression strength (UCS) and concluded that UCS was also dependent on aspect ratio. They proposed that a cylinder with a large enough diameter to satisfy the continuum assumptions (Harrigan *et al.*, 1988) and an aspect ratio of 2:1 should be standardised. For human and bovine bone this works out at a diameter of 5 mm (minimum) and length of 10 mm. Cylinders were found to be better than cubes as they were easier to prepare with a greater degree of accuracy and surface area: volume ratio is reduced (density measurements more accurate).

3.4.3 Environment

Bone (especially cancellous) is highly sensitive to its environment during mechanical testing. *In vivo,* bone is kept at a relatively constant temperature of 37°C. However

much of the data available for the mechanical properties of bone has been obtained at room temperature. Smith and Walmaley (1959) observed a reduction in Young's modulus of 0.51% per °C increase in temperature and found these effects to be reversible over the range 9-43°C. Brear *et al.*, (1988) found that defatted specimens tested at 37°C had reduced mechanical properties when compared with results obtained from tests performed at room temperature (21-22°C). Modulus dropped by 7%, and strength by 13%. Sedlin and Hirsch (1966) found that the deflection to failure of wet cortical bone increased by 6% when temperature was raised from 21-37°C while Currey (1975) observed a similar 8% change in the immediate deflection following the application of a constant load over the range 17-37°C.

De With *et al.*, (1981b) demonstrated an average reduction in fracture strength of 24 MPa in porous hydroxyapatite specimens over a density range of 74-97% when tested wet, in comparison to similar specimens tested in the dry condition. A similar trend was noted with the fracture toughness which was reduced by an average of 0.25 $MPa.m^{1/2}$ over the same density range. In contrast Thomas *et al.*, (1980) carried out a similar study where hydroxyapatite specimens were stored in a number of physiological solutions at 37°C for 8 weeks and no significant changes in strength were noted. This may be due to the fact that these specimens were dried before testing. However, both sets of authors demonstrated that strength of dense hydroxyapatite is strain rate dependent. In contrast, wet cortical bone, as found in situ, is less brittle than fully dried cortical bone (Currey, 1988b; Evans, 1973), although rewetting after drying has been found to almost fully restore its original properties (Currey, 1988b).

3.4.4 Storage and Viability

Fixatives prevent degeneration of soft and hard tissue by the formation of crosslinks between tissue proteins (Robinson and Gray, 1990a). It is not surprising that this has a significant effect on the mechanical properties (Evans, 1973). Sedlin and Hirsch (1966) carried out a complicated series of experiments in which bone specimens were subjected to a range of different preservation techniques. They concluded that freezing bone at - 20° is a satisfactory method of tissue preservation, even though they found a 5 % increase in ultimate stress when comparing the properties of a group of fresh and frozen bones, as there was no significant change in Modulus or energy to failure. A number of authors (Lissner and Roberts, 1966; Greenberg *et al.*, 1968; Wall *et al.*, 1970; Evans, 1973; Black, 1984) have since questioned this conclusion and performed additional experiments to determine the effect of death on the mechanical properties of

bone. They found that the mechanical properties of dead and "live" bones were not significantly different if the dead bone was tested in the fresh or moist condition, however prolonged freezing was found to significantly alter the properties, probably as a result of freezing and defrosting cycles. This is not surprising when considering that trabecular bone may be over 50% soft tissue. Wall *et al.*, (1970) also proposed that freezing bone in saline could result in dehydration as a result of irregularly sized ice crystal formation.

3.4.5 Constrained Testing

Linde and Hvid (1989) tested cylinders of cancellous bone from the human proximal tibia under a series of different constraint conditions (i.e., specimens tested as normal, cemented to platens, on polished platens with oil lubrication, with external side constraints, *in situ* etc.) They found that fixing the specimen to the platens increased the modulus by 40% compared with specimens tested under normal conditions, while side constraint increased modulus by 22%, in situ testing increased modulus by 19% and coating polished platens with oil decreased the modulus by 6%.

3.4.6 Underestimation of Modulus

Odgaard and Linde (1991) studied the accuracy of determining Young's modulus by conventional compression testing of rectangular specimens from the human proximal tibia. Two independent strain measurements were made during each test, one was made by an extensometer attached to the platens and the other was made by an optical system. The mean modulus calculated from the results of the extensometer measurements was 689 MPa, compared with 871 MPa from the optical measurements. The authors proposed that this variation was due to uneven strain distribution at the platen specimen interface and that all conventional compression tests underestimate modulus by about 20%. They also proposed that the underestimation was independent of specimen density.

3.5 Summary

Bone mineral accounts for up to 70% of the weight of dry bone however both the mechanical behaviour and properties are completely different when compared to that of dense hydroxyapatite.

Both cortical and cancellous bone fail plastically as a result of the presence of collagen and exhibit anisotropic mechanical properties related to either the osteonal structure (in cortical bone) or the architecture of the trabeculae (in cancellous bone).

Dense hydroxyapatite fails by brittle fracture and its properties are isotropic. Porosity strongly influences the modulus and strength of hydroxyapatite, although it still fails by brittle fracture.

The differences in magnitude between the elastic modulus of dense HA and cortical bone is similar to that of titanium (Table 3.5.1). However, the tensile and compressive strengths are,in comparison to titanium similar to bone, although a lack of fracture toughness makes it unsuitable for use in critical load bearing applications such as in total hip replacements, other than as a bioactive coating.

Table 3.5.1 Comparison of mechanical properties for cortical bone, dense hydroxyapatite and titanium.

	Young's Modulus (GPa)	"Tensile" Strength (MPa)	Compressive Strength (MPa)	Fracture Toughness ($MPa.m^{1/2}$)
Cortical Bone	10 - 22[#]	50 - 156[#]	133 - 237[#]	2-12[*]
Dense HA	88[∞]- 121[◊]	90[Δ] - 124[+]	376[◊] - 509[∞]	0.9[Δ] - 1.3[+]
Titanium Alloy	106	900	-	≈ 80

Data from: [∞]Akao *et al.*, (1981); [Δ] Best (1990); [*] Bonfield, (1984); [#] Cowin *et al.*, (1986); [◊] Rootare *et al.*, (1978a); [+] de With *et al.*, (1991a and b).

The variation in the reported values of the mechanical properties of hydroxyapatite, indicated by the ranges in Table 3.5.1, is a result of the strong dependence of mechanical properties on specimen size and microstructure, a common trait in engineering ceramics. This variation in mechanical properties is in stark contrast to the behaviour of titanium alloys.

CHAPTER 4

BONE REPLACEMENT

4.1 Introduction

The replacement of old, damaged or diseased bone is now an established procedure, an estimated 40 000 hip replacements are performed annually within Britain alone, of which 18 % are revisions (1995). As surgical technique and medical knowledge continues to advance, there is a growth in the demand for synthetic bone replacement materials, especially with health concerns regarding homologous bone grafts, which are associated with the risks of viral infections such as Hepatitis B and Human Immune deficiency Virus. Consequently, there is increasing interest in the development of synthetic bone replacement materials for the filling of both load bearing and non load bearing osseous defects such as in joint and facial reconstruction, with a resulting expansion in this field of research. However, there are many variables to consider when assessing a candidate implant material. The decision must be based on consideration of not only the "pure" material but also the bulk end product (intrinsic and extrinsic materials properties), the intended end use (physiological environment and loading requirements) and the biological response (toxicology, immediate and long term tissue response). Many materials have been proposed for bone replacement, ranging from stainless steel to ceramic/polymer composites, the biological and mechanical diversity of which is matched only by the variety of the methods used to assess them. This lack of test standardisation makes comparison of results between different laboratories almost impossible.

As the subject of this thesis is the evaluation of a porous hydroxyapatite, this review will concentrate on bioceramic materials, although where necessary reference to ceramic coated metal implants and ceramic/polymer composites may be made.

4.2 Bioceramics

Records of attempts to repair the human body with implant materials have been found dating from the era of the Egyptian, Greek and Hindu civilisations. The first use of bioceramics was recorded by Dreesman (1894) who reported the use of plaster of Paris to fill defects in bone. However, while being resorbable and causing little or no adverse tissue response, plaster of Paris was deemed unsuitable as it is inherently weak and lost strength rapidly as a result of resorption, thus the race to find a perfect bone replacement material began. Since then, a number of different materials have been proposed, from metal oxides such as alumina and zirconia to various calcium - phosphate based ceramics, glasses and polymer composites.

4.2.1 Bioceramic Classifications

Bioceramics have been split into three broad classifications depending on the response they elicit from bone (Dobson *et al.*, 1978; Hulbert *et al.*, 1983; Hench and Wilson, 1993). These are summarised in Table 4.1.1:

Table 4.1.1 Bioceramic classifications proposed by Hench and Wilson (1993).

Classification	Tissue Response	Implant / Tissue Bond	Examples
Toxic	Tissue dies	None	Lead Oxide Arsenic Oxide
Near Inert	Formation of a non-adherent fibrous membrane around implant	None	Alumina Zirconia Carbon
Bioactive	Formation of an interfacial bond with the implant	Chemical	Hydroxyapatite Bioactive glasses & Glass-ceramics
Resorbable	Tissue replaces implant as it degrades	None	Tricalcium phosphate Bioactive glasses

These different tissue reactions to implant material can be partly explained by considering the surface reactions which may occur *in vivo*. Surgery always results in an initial inflammatory response with the arrival of phagocytes and other cells involved in the repair process. No material is ever totally inert when introduced to the body and at worst materials can be **toxic** causing the death of the surrounding cells and tissue, either directly, or by the release of by-products that may also migrate with tissue fluids causing systemic damage to the patient (Black, 1984).

At the other extreme, introduction of materials that are **near-inert** or **bioinert** triggers the formation of a thin 1-3 μm thick "protective" layer absorbed to the surface of the implant (Hench and Wilson, 1993). This results in the "camoflage" of the implant such that cell differentiation and proliferation are not effected and there is no aggressive foreign body response (Heimke, 1990). However, there is no bonding between implant and host-tissue, therefore if motion occurs between the two, as a result of normal physiological activity, a collagen rich inter-layer will be formed (fibrous encapsulation).

Fibrous encapsulation is the most common response to a foreign body, most metals and polymers demonstrate this type of reaction, which is termed **biotolerant** (Heimke, 1990). The fibrous layer effectively isolates the implant from the tissue and the thickness of the fibrous layer is dependent on a combination of the chemical reactivity of the material and the relative motion between tissue and implant. More reactive materials, such metals that release metal ions and polymers that leach out monomers induce a thicker layer as the body attempts to isolate the source of irritation. Similarly increased relative motion between an implant and the host tissue also induces a thicker fibrous inter-layer (Heimke, 1990).

Bioactive materials possess the ability to undergo continuing surface reactions with the host tissue, acting in a more "natural" manner. These materials are reported to rapidly form chemical bonds with the host tissue, therefore no fibrous layer is formed as there are no "hostile" chemical reactants or any subsequent motion. Examples of materials that exhibit this behaviour being certain bioglasses and calcium phosphate ceramics that bond to bone (Hench and Wilson, 1993; de Bruijn, 1993).

Resorbable materials are required to be of a composition that can be either degraded chemically by the body fluids or digested by macrophages,and in reality, biodegradation usually occurs via a combination of the two. It is important that the degradation products are not toxic and should be easily disposed of by the cells. The difficulty lies in controlling the rate of degradation, which is controlled by a combination of chemistry and physical morphology (where parameters such as the surface area and density may be manipulated to fine tune the rate of degradation of a series of chemically identical implants). An example of a material that exhibits this behaviour being tricalcium phosphate which is rapidly resorbed into the body when placed in bony defects (Klein *et al.*, 1983 a and b).

4.2.2 Bioceramic Morphology

The morphology of ceramic implants has been considered since the use of porous material was first described by Smith (1963). Hulbert *et al.*, (1972) showed that porous disks of a near inert ceramic exhibited thinner fibrous encapsulation with faster healing in surrounding muscle and connective tissue than dense disks, as a result of a mechanical interlock which reduced motion between host tissue and implant. However, there still seems to be some dispute regarding the optimum "type" of porosity (perhaps as a result of inadequate characterisation of morphology). Klawitter *et al.*, (1976) suggested that the optimum pore size for healthy ingrowth in polyethylene was 100-135 μm with ingrowth observed in pores as small as 40 μm, however no comment was made on the connectivity of the structure. A number of authors have suggested that the degree of interconnectivity is more critical than the pore size, Eggli *et al.*, (1988) demonstrated improved integration in interconnected 50-100 μm pores compared with less connected pores with a size of 200-400 μm. Similarly Kühne *et al.*, (1994) compared two grades of 25-35% porous coralline apatite with average pore sizes of 200 and 500 μm and reported bone ingrowth to be improved in the 500 μm pore sized ceramic as a result of numerous 260 μm interconnections which were not present in the ceramic with 200 μm pores. Holmes (1979) who also studied a porous coralline apatite suggested that when implanted in cortical bone interconnections of osteonic diameter were required for transport of nutrients to the bone ingrowth. A number of authors have demonstrated the effect of porosity on the rate of resorption in resorbable bioceramics. Klein *et al.*, (1983a and b) and de Groot (1983) studied the mechanism of ceramic degradation concluding that the solid body broke down by dissolution of necks between grains, the free particles then being phagocytosed. Eggli *et al.*, (1988) demonstrated that increased surface area led to faster resorption by comparing the *in vivo* behaviour of tricalcium phosphate cylinders with identical volume porosity but two different pore sizes.

The effect of morphology on mechanical properties must also be considered and any substitute material for bone must allow elastic deformation and load distribution so as not to produce load concentrations (Holmes, 1979) or stress shielding. Stress analysis investigations have demonstrated that anisotropic structures reduce stress concentrations in comparison with isotropic ones when placed in systems likely to be preferentially loaded in one direction (Oxnard, 1993). Thus appropriate modification of the internal macrostructure to distribute loads and match the intended host tissue will improve the biocompatibility, such as has been demonstrated in the use of

hydrothermally converted corals with structures similar to anisotropic cancellous bone in the filling of cancellous bone defects (Holmes *et al.*, 1984). The converted corals were reported to possess a similar stiffness to cancellous bone, but to have lower strengths and no plastic behaviour. However, after six months *in vivo* the resultant bone/ implant composite exhibited similar behaviour to the original bone.

4.2.3 Hydroxyapatite

The case for using hydroxyapatite in the filling of osseous defects is fairly obvious since it has a remarkably similar crystal structure to that of bone mineral (de Jong, 1926), which accounts for approximately 70% by weight (50% by volume) of natural bone. Much of the reported work in the field concentrates on the implantation of dense metallic or ceramic implants with porous hydroxyapatite coatings applied, while some work has studied the effects of implanting whole bodies of porous synthetic hydroxyapatite, tricalcium phosphate, an admixture of the two, or hydrothermally converted coral in small mammals. All authors agree that HA is bioactive, but there is considerable confusion regarding its osseoconductive or osseoinductive properties, where:

- Osseoconduction is the ability of a material to encourage bone growth along its surface when placed in the vicinity of viable bone or differentiated bone forming cells.
- Osseoinduction (osteogenesis) is the ability of a material to promote bone growth on its surface when placed in a non osseous site by inducing osteoblast-like cell differentiation (Pinholt *et al.*, 1992).

There is considerable evidence to suggest that hydroxyapatite is osseoconductive, the most convincing is that which compares the depth of bone ingrowth into cavities or porosity with and without the presence of hydroxyapatite (Stephenson *et al.*, 1991; Moroni *et al.*, 1994). Similarly, hydroxyapatite has been reported to encourage bone to bridge gaps (Maxian *et al.*, 1994; Rahn *et al.*, 1986). Although a gap 2 mm around an implant was reported to result in reduced bone apposition indicating that there is a finite maximum gap which can be bridged (Clemens *et al.*, 1995).

In contrast, the matter of osseoinduction is somewhat vague. Ohgushi *et al.*, (1992) reported that porous hydroxyapatite implants implanted subcutaneously in rats exhibited only fibrovascular ingrowth, whereas implants dosed with bone marrow displayed bone formation. They suggested that this indicated that marrow stromal cells

were differentiating in the presence of HA indicating HA was osteogenic. Similar work was carried out by Kurashina *et al.*, (1995) with identical results using porous rods of hydroxyapatite filled with autogenous periosteum in the muscle of rabbits. Unfortunately neither studies carried out any control experiments, where marrow cells placed either alone or in an inert capsule were introduced subcutaneously, to determine whether or not the presence of the hydroxyapatite induced cell differentiation or merely supported it. Conversely, Pinholt *et al.*, (1992) reported a lack of osseoconductive or osseoinductive activity for granules of four commercial "apatite" materials when implanted subperiosteally in rats, despite observing bony tissue "encasing" granules in one instance, which was interpreted as osseoconduction. These differences may be explained by the work of Ripamonti (1996) in which porous hydroxyapatite was implanted in the muscle of baboons, rabbits and dogs. Significant differences were detected in the amount of bone induction between the three species (11.3% in the baboon, 0.5 % in the rabbit and 0.75% in the dog).

Ideally one would wish for a replacement material to be slowly resorbed by the body once its task of acting as a scaffold for new bone has been completed. Degradation or resorption *in vivo* occurs via a combination of phagocytosis of particles and the production of acids which cause partial dissolution of hydroxyapatite. However, there seems to be some disagreement in the literature regarding the solubility of hydroxyapatite in a physiological environment. Gomi *et al.*, (1993) reported resorption of hydroxyapatite by osteoclasts *in vitro* and demonstrated that rougher surfaces induced a more aggressive response. Dhert *et al.*, (1991) and Kangasniemi *et al.*, (1994) reported the degradation of hydroxyapatite coatings with time *in vivo*. Martin *et al.*, (1993) found that porous hydroxyapatite in a cortical site was resorbed while a similar implant in a cancellous site remained intact after a year *in vivo*. Similarly, Holmes (1979) reported the resorption of a coralline hydroxyapatite implant after 12 months in canine mandibles, while in a later publication Holmes *et al.*, (1984) reported little or no resorption for an identical implant in a "less load bearing" cortical site (distal radial diaphysis). Eggli *et al.*, (1988) Renooij *et al.*, (1985) and Kühne *et al.*, (1994) all observed little or no resorption of porous hydroxyapatite in a cancellous site. The reason for much of the variation in reported behaviour could be due to variations in the porosity, Ca:P ratio and crystallinity of the different implants and coatings in different studies.

Klein *et al.*, (1983 a and b) proposed that the rate and extent of biodegradation of calcium phosphate ceramics is dependent on porosity, crystallinity (i.e., grain size and

crystal strains) and composition, reflecting the ease with which particles may be detached and resorbed by cells. Hench and Wilson (1993) proposed that the extent of biodegradation decreases as Ca:P ratio increases. Eggli *et al.*, (1988) found porosity to have a strong influence on the rate of resorption of tricalcium phosphates and Maxian *et al.*, (1993, 1994) demonstrated the improved resorption of amorphous coatings when compared to crystalline ones. However, Dhert *et al.*, (1994) reported that fluorapatite coatings on implants placed in the patella groove were partially resorbed on the upper (load bearing) surface whereas coatings on the sides of the implant and in previous studies Dhert *et al.*, (1991) had remained intact. This is particularly significant as fluorapatite is believed to be less soluble than hydroxyapatite. The authors suggested that the resorption could have been due to either exposure to synovial fluid, mechanical abrasion or the thickness of the coating (it was only 20 μm on top compared with 50 μm at the sides), before implants were encapsulated by overgrowth. However, the authors reported no difference in resorption between healthy and arthritic joints, the synovial fluid of which would have been expected to be more acidic. Unfortunately all implants were retrieved at the same time point so it was not possible to determine if mechanical abrasion was solely responsible. Recently Róudier *et al.*, (1995) reported that the resorption of coralline hydroxyapatite was dependent on porosity and host reaction with ingrowth and resorption occurring in the more porous (42.79 and 40.72 % open porosity) corals and fibrous encapsulation with little/no resorption occurring in the denser (17.48 % open porosity) coral. Unfortunately while total and open porosity was calculated for the three apatites pore sizes were not given.

Thus, it would seem that there are a number of parameters which can considerably alter the *in vivo* behaviour of "hydroxyapatite" implants, and that they may be classified into two groups, host parameters and implant parameters. Examples of host parameters would be the species, implantation site and surgical technique (open or tight fit). Typical implant parameters include chemical stoichiometry, crystallinity and morphology. Understanding, characterisation and control of these variables should be accomplished where possible.

4.3 Biological Assessment

Biological assessment can be considered as a two stage process, where candidate-materials are screened for local cellular response *in vitro*, and "bulk" tested *in vivo*. Knowledge of the behaviour of the material in both situations is vital for the tailoring of implant to host site. Cell culture allows the controlled study of cellular response at the candidate-material interface, for example, the degree of adhesion and proliferation of osteoblast-like cells on a candidate-material surface, and the rate and quality of extra-cellular matrix production will be of particular interest in the study of bone replacement materials. Similarly, knowledge of the influence of the presence of an implant in a surgical site on the local inflammatory and healing responses will be of importance. This is a highly complex interactive process (Kasemo and Lausmaa, 1991; Thomsen and Ericson, 1991; Glowacki and Spector, 1991), ranging from molecular reactions at the implant surface (Davies *et al.*, 1991a and b) to the effects of implant micro-motion (Bobyn *et al.*, 1987), although the complexity of *in vivo* responses can be broken down by the study of responses of isolated cell lines to specific conditions *in vitro*. However, the methods adopted for the *in vitro* and *in vivo* assessment of a material have become increasingly controversial. Many recent studies have focused on the advantages and disadvantages of different "test parameters" and the effects on the reliability or reproducibility of the "results" with varying "test methods". For instance, Hunter *et al.*, (1995) considered the significance of the type of cell line used *in vitro* as regards the applicability to the *in vivo* response. While the effects of implant site (Kangasniemi *et al.*, 1994) and host species (Ripamonti, 1996) on the tissue response, and section thickness or direction (Johansson and Morberg, 1995a and b) have demonstrated the scope for artefact induced variation *in vivo* . Furthermore, the many differing methods of assessment result in difficulties in comparing the results of separate investigations.

4.3.1 Biocompatibility

Biocompatibility does not solely imply a lack of toxicity or the ability to be chemically compatible with the host tissue. It has previously been described as the ability of a material to illicit no response from the host tissue, however the current accepted definition is that of Williams (1987; 1994), where a material should perform "appropriately and in concert with a certain host response in a specific application". Therefore, in the correct applications the near-inert, bioactive and resorbable groups of materials may all be regarded as biocompatible despite their different tissue responses

and chemical and mechanical properties. For instance, where fixation is required, such as in bone filling applications, a bioactive material seems the logical choice, while in applications where blood comes into direct contact with the biomaterial, a passive response may be preferred, thus an inert material may be more appropriate. Resorbable biomaterials are finding considerable use in slow drug release applications.

In the case of this study biocompatibility is considered as the ability of the material to support cellular colonisation and proliferation and promote the production of an extra-cellular matrix *in vitro*. An implant placed within a bony defect *in vivo* should enhance the strength of the defect during healing, bond with the host tissue (i.e., bone) invite and maintain the integration of bone.

4.3.2 *In Vitro* Assessment of Bone Analogues

4.3.2.1 Cell Lines and Culture Conditions

There are a wide range of cloned cell lines available for use in the *in vitro* modelling of osteoblastic behaviour, however they are derived from a number of species (typically mouse, rat and human) and are usually from either sarcoma tissue or artificially transformed in order to provide an immortalised cell line that will not de-differentiate or reduce activity with increasing passage number in culture (Serre *et al.*, 1993). Those studies that do use primary cultures tend to use cells extracted from foetal bone, which will exhibit different growth characteristics from adult bone (Courteney-Harris *et al.*, 1995). Akedo *et al.*, (1992) demonstrated species variations in the relative amount of cell proliferation between human osteosarcoma TE85 and mouse MC3T3-E1 cell lines in response to treatment with vitamin K_2, while Clover and Gowen (1994) reported that MG-63 and HOS TE85 cells proliferated more rapidly than un-transformed HOb cells, with HOS cells being the most proliferate. These authors also reported that unlike MG-63 and un-transformed HOb cells, the levels of alkaline phosphatase and osteocalcin secreted by HOS cells did not respond to treatment with $1,25(OH)_2D_3$. This is in contrast to Mulkins *et al.*, (1983) who found that although the relative alkaline phosphatase activity in two HOS cell lines, SAOS and TE85, were different, alkaline phosphatase activity was increased with $1,25(OH)_2D_3$, possibly as a result of different culture conditions (10% FCS and 5% FCS respectively). Tremollieres *et al.*, (1992) reported variations in the absolute levels of cell proliferation (but similar trends) between HOS TE85 and un-transformed HOb cells treated with progesterone and promegestone, while Hassager *et al.*, (1992) reported that HOS U-2, TE85 and MG-63

cell lines secreted different patterns of insulin-like growth factor binding proteins to untransformed human osteoblast-like cells. The reported disparity between the behaviour of cloned cell lines indicates that the use of these cell lines is compromised by the unpredictability of the relationship between these cells and un-transformed human osteoblast-like cells.

The use of bone marrow or organ culture where several cell lines are simultaneously incubated may be a more accurate model of *in vivo* behaviour (de Bruijn, 1993; Courteney-Harris *et al.*, 1995). However, fibroblastic overgrowth can be a problem with extended culture time (Robey and Termine, 1985).

High density cultures in which cells may form 3-D spatial networks have been advocated by a number of authors (Ahrens *et al.*, 1977; Casser-Bette *et al.*, 1990; Hunter *et al.*, 1995) and are proposed to emulate the *in vivo* environment, so promoting terminal osteoblastic differentiation and calcification of the extra-cellular matrix. However, in a comparison between monolayer and micromass cultures of HOS TE85 and un-transformed HOb cells Di-Silvio (1995) reported monolayer cultures to favour proliferation and differentiation of both HOS and HOb cells. Spontaneous calcification of extra-cellular matrix was also observed in HOb cultures at 21 days *in vitro*.

Similarly, the conditions for calcification also seem to vary from one investigation to another. Some authors maintain that the presence of ß-glycophosphate is necessary for matrix calcification (Tenenbaum and Heersche, 1982; Ecarot-Charrier *et al.*, 1983), while others have reported successful matrix production and calcification with out special supplements (Serre *et al.*, 1993; Di-Silvio, 1995).

4.3.2.2 Qualitative Assessment

The use of osteoblasts or osteoblast-like cells or precursors is most common in this line of investigation. Parameters that are most often assessed are the production and subsequent calcification of an extra-cellular matrix, and the morphology and attachment of cells at the material/cell interface.

Extra-Cellular Matrix Production and Calcification

In many studies biocompatibility is assessed by the successful production of a fibrous extra-cellular matrix by osteoblast-like cells, which is interpreted as expression of the osteoblastic phenotype (Robey and Termine, 1985; Faucheux *et al.*, 1994; Doherty *et al.*, 1994; Couteney-Harris *et al.*, 1995), however the instances when conclusive

evidence is reported for subsequent calcification of the matrix are few (de Bruijn, 1993; Serre *et al.*, 1993; Di-Silvio, 1995; Ozawa and Kasugai, 1996).

Cell Attachment and Morphology

The formation and deposition of bone directly on an implant is believed to be dependent on the ability of osteoblast-like cells to adhere and spread on the material surface (Bagambisa and Joos, 1990). Hunter *et al.*, (1995) studied the attachment of cells on the surfaces of various biomaterials and determined that well spread,flat cells possessed the greatest number of adhesion plaques per cell. Thus cell morphology may also be considered as an indicator of biocompatibility. Furthermore, cell shape has been shown to affect proliferation, Folkman and Moscona (1978) suggested that rounder cells proliferate at a lower rate than flatter cells, while gene expression may also be affected by cell shape as a function of intracellular remodelling of the nuclear matrix (Jones and Boyde, 1976; Ben-Ze'ev, 1991).

4.3.2.3 Quantitative Assessment

Besides the production and calcification of an extra-cellular fibrous matrix by osteoblast-like cells, authors concentrate on cell viability, proliferation and expressions of osteoblastic phenotype to determine the biocompatibility of materials for use in the skeleton (Serre *et al.*, 1993; Clover and Gowen, 1994; Courteney-Harris *et al.*, 1995; Di-Silvio, 1995). Bone specific proteins such as osteocalcin and osteonectin, alkaline phosphatase activity and nucleic acid turnover are assayed to provide a measure of the degree and rate of differentiation undergone by cells within the culture (Best *et al.*, 1995; Clifford and Downes, 1995; Faucheux *et al.*, 1994; Maxian *et al.*, 1995). Again, the use of osteoblasts or osteoblast-like cells or precursors is most common in this line of investigation (Bagambisa and Joos, 1990; Couteney-Harris *et al.*, 1995; Serre *et al.*, 1993), although some studies have been carried out using osteoclast-like cells (de Bruijn *et al.*, 1993f; Gomi *et al.*, 1993a, 1993b).

4.3.2.4 Porous Hydroxyapatite *In Vitro*

Hydroxyapatite surfaces appear to be able to support the proliferation of most cell types, with many monoclonal studies performed using macrophages, fibroblasts, osteoclasts and osteoblasts (de Bruijn, 1993; Gomi *et al.*, 1993; Hunter *et al.*, 1995).

Chemical Composition & Crystallographic Phase

Micro-molar concentrations of Al and Si have been reported to stimulate osteoblast proliferation and differentiation (Lau *et al.*, 1991), however, high concentrations of aluminium suppress bone mineral formation (Blumenthal and Posner, 1984). Magnesium ions have also been reported to inhibit hydroxyapatite formation (Blumenthal and Cosma, 1992).

De Bruijn, *et al.*, (1993c) assessed the osteoblastic cell response to plasma sprayed HA coatings with differing amounts of amorphous material and demonstrated that the more amorphous material invited a more intimate association between the extra-cellular matrix and the coating. In contrast, Best *et al.*, (1995) demonstrated that the presence of TCP in a HA substrate led to substrate/cell interface degeneration resulting in reduced viability in osteoblast cells on the surface and particle phagocytosis . Levels of alkaline phosphatase and DNA were reduced by 50% in comparison with cultures incubated on pure HA compacts. However, the TCP containing material also possessed a greater degree of surface porosity which may have contributed to the cellular behaviour. Maxian *et al.*, (1995) reported that chemical resorption occurring in low crystalline HA enhanced osteoblast cell proliferation, cell attachment and growth, but reduced alkaline phosphatase activity, which may be a result of local variations in solution pH. A component detected in Endobon® and described as "amorphous" by Saalfeld *et al.*, (1994) was reported to leach out in H_2O with time, altering the solution pH to 12.5 after a "few minutes" before dropping to a pH of 10.5 after 1 day and a pH of 8 after 3 days.

De Bruijn *et al.*, (1993) carried out two-stage cultures on TCP and well crystallised HA, in which a bone like matrix was deposited on the substrata by osteoblast-like cells in the first stage and then subsequently resorbed by osteoclast-like cells in the second stage. They found that matrix deposited on both the TCP and HA was resorbed by the osteoclast-like cells, but while some TCP was also removed the HA substrate remained intact. When single stage cultures were carried out in which osteoclast-like cells were introduced directly onto the substrates no resorption occurred on either material.

Surface morphology

Doherty *et al.*, (1994) reported that increased roughness in the surface of HA substrata resulted in reduced proliferation and attachment of osteoblast-like cells. Hunter *et al.*, (1995) found that where surfaces were rough, cells were less inclined to flatten out and spread which resulted in a reduced rate of proliferation as rounded cells divide at a lower rate than flattened cells. However, they suggested that flattening out on smooth surfaces may encourage osteoblastic cells to differentiate to fibroblastic cells.

In an investigation on the effects of surface roughness on the behaviour of osteoclast-like cells, rougher surfaces were reported to be more densely populated by osteoclasts, (Gomi *et al.*, 1993a and b). These authors also investigated the effects of processing (Gomi *et al.*, 1993b) and determined that the sintered (1250°C for 6 hours), well crystalline HA (with reduced microporosity) was not resorbed where as resorption pits were identified on the as-received and calcined (1130°C for 30mins) HA disks.

4.3.3 *In Vivo* Assessment of Bone Analogues

4.3.3.1 Implantation Site, Biological Controls and Choice of Host

Histological response may also be dependent on the site of implantation or seemingly small variations in the orientation of the implant. Uchida *et al.*, (1984) observed little or no bone ingrowth in the majority of porous ceramics (calcium aluminate, hydroxyapatite and tricalcium phosphate) embedded in the skulls of rabbits and rats. However, in one hydroxyapatite implant considerable bony ingrowth was noted as a result of the presence of bone marrow which is believed to facilitate new bone growth (Ohgushi *et al.*, 1992). Holmes *et al.*, (1984) observed osteonal bony ingrowth in cortical sites and trabecular bony ingrowth in cancellous sites, while Martin *et al.*, (1993) studied the ingrowth of bone into coralline hydroxyapatite in cortical and cancellous sites over a period of a year. They reported that in cortical bone, ingrowth occurred at an elevated rate in the first 3 months and continued throughout the rest of the year. However in cancellous bone they found that ingrowth was greatest at 4 weeks post implantation and decreased significantly throughout the rest of the year.

Many reports of hydroxyapatite integration lack biological controls (such as creating a defect and allowing it to heal with an implant present, or substituting bone graft for the implant). This is possibly as a result of the difficulty in selecting and justifying an appropriate control which will not generate its own response above the response of host tissue to space filler (i.e., fibrous encapsulation, macrophage activation), and difficulties in reproducing mechanical behaviour and structure in such a material. Kühne *et al.*, (1994) carried out two control studies as well as investigating the response of cancellous bone to porous hydroxyapatite with two pore sizes of 200 and 500 μm. The controls employed were a 6 mm diameter empty cavity and bone allografts. They reported different mechanisms for integration between the two controls with the cavity control exhibiting a mechanism similar to fracture healing. However, although no bone formation was observed in the 200 μm pore material, the 500 μm material appeared to

follow a broadly similar route of bone repair to the graft control, with stabilisation by woven bone, cellular invasion, bone formation and vascularisation.

The choice of host also has a significant affect on the observed response to the implant, for example, the mineral apposition rate in normal human bone has been reported as 0.8 $\pm$ 0.2 $\mu m\ day^{-1}$ (Bloebaum, 1994), while in rats Heershe *et al.*, (1981) found it to be 3.0 $\mu m\ day^{-1}$, while a similar rate has also been reported for rabbits (3.5 μm day - Revell, 1995). Furthermore in a recent study by Ripamont (1996) significant differences were detected in the amount of bone induction in porous hydroxyapatite implanted in the muscles of three species (baboon, rabbit and dog). Similarly, Rice *et al.*, (1988) and Kuhn *et al.*, (1989) have demonstrated that the mechanical properties of inter-species bones cannot be compared even when considering differences in apparent densities.

4.3.3.2 Qualitative Histology

There are several features that should be studied when making a qualitative assessment of tissue response, these are:

- Presence of inflammatory cells
- Presence of reparative cells
- Presence of fibrous tissue encapsulation
- Presence of normal (bone) tissue regeneration
- Direction of tissue regeneration
- Response of tissue surrounding the implant
- Response of the implant material

Generally, inflammatory cells such as multinuclear giant cells or phagocytes are rarely seen in the proximity of hydroxyapatite implants more than one week post-operatively, and the presence of fibrous tissue around hydroxyapatite is rare. However, the precise response from implant to implant may vary as a result of variations in defect size or surgical damage. Ogiso *et al.*, (1994) suggested that encapsulation of hydroxyapatite may be due to fibrous ingrowth before bone formation from distant trabeculae can take place. Pinholt *et al.*, (1992) observed fibrous encapsulation around a series of calcium phosphate materials placed subperiosteally except in instances where surgical insult had accidentally occurred to the neighbouring bone in which case some bone growth had occurred around the granules.

There is considerable variation in the reported histological response to porous hydroxyapatite. Holmes *et al.*, (1984) reported osteoclastic activity on hydroxyapatite implants up to 6 months post operatively with woven bone present until 2 months and complete integration of the implant with bone. Conversely, Lin *et al.*, (1994b) studied

the histological response of bone into porous hydroxyapatite at 2, 4, 8 and 32 weeks and did not observe any foreign body response with new bone formed on the surfaces at 2 weeks. However, they reported inhibited vascularisation, with the centres of the pores remaining empty. Renooji *et al.*, (1985) recorded lamella bone apposition directly on hydroxyapatite surfaces, extensive contact between bone and hydroxyapatite, pores partially filled with bone and no evidence of cell mediated resorption. However, this variation in results may reflect variations in implant morphology (pore size and connectivity) and chemistry. Bobyn *et al.*, found that pores in chemically identical metallic porous implants with pore size ranges of 400-800 μm contained fibrous tissue 12 weeks after implantation whereas smaller pores (50-400 μm) were fully integrated with bone. Similarly, Eggli *et al.*, (1988) reported reduced amounts of integration in the centre of porous hydroxyapatite implants with large pores (200-400 μm) but little connectivity, while the amount of integration in hydroxyapatite with smaller interconnected (50-100 μm) pores was significantly higher. They also reported the histological response of porous hydroxyapatite and tricalcium phosphate implants with identical porosity which demonstrated the significant difference in phagocytic reaction between the two compounds.

4.3.3.3 Histomorphometry

There are a number of standard methods currently practised in the examination of bone biopsies (Melsen *et al.*, 1978; Revell, 1986) and these techniques have been adapted for the quantitative assessment of implant integration. There are two main groups of techniques, point counting and linear intercept analysis and both types have been successfully used to assess a number of different parameters. Some of the more commonly cited ones include:

- Bone ingrowth in frame or defect area.
- Bone ingrowth in pore space.
- Implant surface covered by bone on-growth.
- Thickness or depth of bone on-growth or ingrowth.

Point counting methods are used to measure relative areas such as bone ingrowth within pore space or defect area. Lattices of points (that may be arranged in a network regularly or randomly) are laid over micrographs or placed in the eyepiece of an optical microscope, a typical example being the Weibel lattice (Weibel and Elias, 1967). The number of "hits" are counted, where a hit consists of a point occurring on the feature under investigation. The percentage of area occupied by the feature in the view frame is then calculated from:

$$\text{Area (\%)} = \frac{\sum_{x=1}^{x=n} H_x}{P_t} \times 100 \qquad (4.3.1)$$

Where H is a hit, n the number of hits and P_t is the total number of points on the grid. Repeated counting at different areas of the specimen is usually advised to improve the accuracy of the estimate. The optimal number of points to count in order to achieve a reproducible result may be calculated from the formula developed by Hally (1964) for the relative standard error, where:

$$\text{Relative Standard Error} = \frac{\sqrt{1 - \text{Estimated Area}}}{\sqrt{\text{Number of Points}}} \qquad (4.3.2)$$

Linear intercept methods are generally used to quantify surface features such as bone coverage. Lines are superimposed on the image and a hit is regarded as a place where a line intersects a feature. This method is used to estimate the coverage of a feature on a bone surfaces where

$$\text{Coverage (\%)} = \frac{\text{Number places where feature surface is intersected}}{\text{Number of places where bone surface is intersected}} \qquad (4.3.3)$$

As before, measurements are made on a number of fields until an accurate estimate is obtained. Different types of grid are available, they are typically composed of straight lines a notable exception being a Merz grid (1967; 1970). Merz grids are composed of alternating semicircles which build up a wave pattern This overcomes problems associated with anisotropy, and also incorporates an array of points for point counting methods (Revell, 1986; Moroni *et al.*, 1994).

As with the estimation of grain size and porosity these manual techniques may be adapted for use with image analysis. However, special staining (Revell, 1986) or processing techniques are usually required in order to obtain a suitably delineated image. One such technique being the preparation of thick (100-200 μm) sections for back scattered scanning electron microscopy, in which bone appears grey, ceramic implant white and soft tissue black (Holmes *et al.*, 1987)

A number of studies have been performed to assess the accuracy, reproducibility variability and degree of bias in Histomorphometry methods with regard to:

- Inter and intra observer variation (Dequeker, 1976; Birkenhäger-Frenkel *et al.*, 1976; Delling *et al.*, 1980)
- Magnification (Olah, 1976)

- Biological variation (Sectioning) (Visser *et al.*, 1976 and 1980; Johansson and Morberg, 1995b) Visser *et al.*, (1976) suggested that the trabecular volume of a second section should vary by >40% from the first to be significantly different.
- Measurement Methods (Kimmel and Jee, 1976; Parfitt, 1976; Kuntz *et al.*, 1980; Malluche *et al.*, 1980; Birkenhäger-Frenkel *et al.*, 1980; Morey and Wronski, 1980)
- Section thickness (Johansson and Morberg, 1995a)

Some of the results from these studies are summarised in Table 4.3.1, for instance Olah (1976) in a study on the effect of ocular magnification on the measurement of trabecular bone volume and density, found that there was no variation in measurements of trabecular bone volume made at × 25 and × 400, while measurements of trabecular bone density made at the two different magnifications varied by up to 30%.

Table 4.3.1 Variability in Histomorphometry.

Author	Parameter Measured	Parameter Assessed	Variability (%)	Parameter Assessed	Variability (%)
Birkenhenhäger-Frenkel *et al.*, 1976	Trabecular Volume Osteoid Coverage (%)	Serial - Sections	88 54	inter - observer	3 23
Olah 1976	Trabecular Volume Trabecular Density (%)	Mag. x 25 - x 400	no variation 30		
Delling *et al.*, 1980	Volume Measurement Coverage Measurement (%)	intra - observer Serial - Sections	1.7 4.1 no variation	inter - observer	12 100
Keller and Young, 1987	Ingrowth (%)	reproduc - ibility	5%		
Johansson and Morberg 1995a	Bone Area Bone to Metal Contact (%)	100 µm 50 µm	57 [11.57] 40 [12.12] 56 [10.18] 39 [9.60]	30 µm 10 µm	55 [10.18] 31 [9.54] 54 [9.97] 30 [8.98]
Johansson and Morberg 1995b	Bone Area Bone to Metal Contact (%)	Longitud-inal Section	53 [9.37] 34 [9.64]	Transverse Section	51 [15.71] 30 [11.10]

Figures in square parentheses are standard deviations

Bone Ingrowth

Klawitter *et al.*, (1976) discussed the conversion of planar to volumetric data when considering longitudinal sections through cylindrical implants using Equation 4.3.4, where A_1-A_3 are the area fractions as indicated in Figure 4.3.1. They used a rather unusual technique to quantify bone ingrowth by cutting out portions of micro-radiographs and weighing them.

$$\text{Volume}\,(\%) = \frac{16A_1 \times 8A_2 \times A_3}{25} \times 100 \qquad (4.3.4)$$

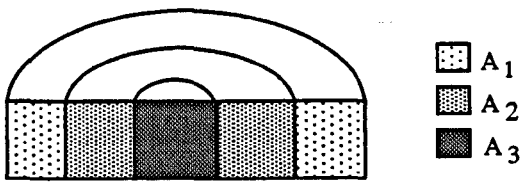

Figure 4.3.1 Definition of area fractions for Equation 4.3.4

More usually, authors evaluated the percentage of bone ingrowth either manually using a point counting technique (Eggli *et al.*, 1988; Martin *et al.*, 1993; Moroni *et al.*, 1994) or with the aid of an image analyser (Holmes, 1979; 1986; Keller and Young, 1987; Shors *et al.*, 1987; Ohgushi *et al.*, 1992; Dhert *et al.*, 1994). Keller and Young, (1987) used image analysis to study bone ingrowth in porous coatings while Holmes (1979) and Frayssinet *et al.*, (1993) studied ingrowth in macro-porous ceramics. Keller and Young, (1987) found that their technique had a reproducibility of 5% (i.e., measurements made on the same specimen were within 5% of each other). Analysis was generally performed at magnifications between × 8 and 50.

Bone Coverage

Bone coverage or bone surface is a measurement of the amount of contact between the implant and host tissue. This was assessed manually by Maxian *et al.*, (1993, 1994) using a linear intercept technique. Frayssinet *et al.*, (1993) used fully automated image analysis to determine the bone implant interface whereas other authors have reported the use of image analysis in conjunction with either a light pen to trace the interfaces (Keller and Young, 1987; Dhert *et al.*, 1994) or an automated method of image digitisation (Birkenhäger Frenkel *et al.*, 1980; Klein *et al.*, 1983b; Dallant *et al.*, 1987). Stea *et al.*, (1995) also used image analysis to study the thickness of hydroxyapatite coatings and bone on-growth. Analysis was generally performed at magnifications of × 100 - 200.

Apposition Rate

A number of authors have used fluorochrome labels to assess the apposition rate (i.e., the rate of bone ingrowth or bone turnover) within and around porous implants (Klein *et al.*, 1983b; Ohgushi *et al.*, 1992; Ouhayoun *et al.*, 1992; Bloebaum *et al.*, 1994; Lin *et al.*, 1994b). The apposition rate of bone is commonly measured using Equation 4.3.5 where D is the measured distance between labels, n is the number of measurements and t the time interval between administration of the labels.

$$\text{Apposition Rate } (\mu\text{m day}^{-1}) = \frac{\sum_{x=1}^{x=n} (D)_x}{n.t} \qquad (4.3.5)$$

However, due to stereological effects (i.e., the relative orientation of label to plane of section) a correction factor is required as the measured distance (D) (Figure 4.3.2) may not be the true distance (d) between the labels.

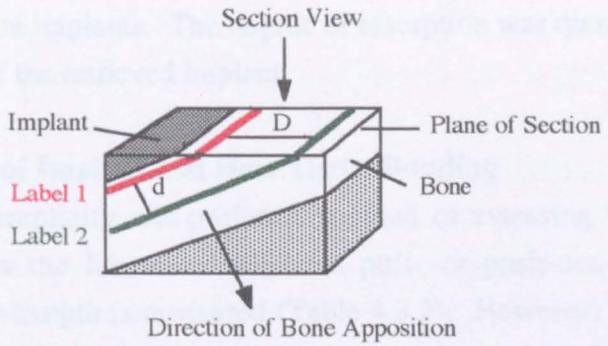

Figure 4.3.2 Stereological effects of specimen sectioning

Assuming the plane of section has a minimum angle of 15° from the "label line" as resolving the difference between the two labels in a plane of section with an angle less than 15° would be impossible (Frost, 1976) the apposition rate may be calculated as:

$$\text{Apposition Rate } (\mu\text{m day}^{-1}) = \frac{\mathbf{0.74} \sum_{x=1}^{x=n} (D)_x}{n\,t} \qquad (4.3.6)$$

Furthermore, when calculating apposition rates it should be remembered that discontinuous bone deposition will have occurred at various points within the specimen, leading to variations in "apposition rate" from point to point and that this phenomenon will be more marked with increasing lengths of time between the administration of labels (Tam *et al.*, 1980).

Care must be taken when processing fluorochrome labelled tissue as aqueous based sodium or phosphate buffered formalin has a detrimental effect on the intensity of fluorochrome labels, whereas formal alcohol leaves the label intact (Frost, 1969).

Implant Resorption

Assessment of resorption has been carried out with or without the use of image analysis, by measurement of the cross sectional area of a similar specimen or measuring specimen density prior to implantation and comparing this with estimates of area or density as a function of the cross sectional area after implantation (Eggli *et al.*, 1988, Klein *et al.*, 1983a, Keller and Young, 1987). Resorption rates have been assessed by comparison of the cross sectional areas (Eggli *et al.*, 1988) or coating thicknesses (Maxian *et al.*, 1993) of different specimens implanted for varying lengths of time.

Radio-opacity has also been used to indicate the degree of resorption (Klein *et al.*, 1983 b) and Renooij *et al.*, (1985) employed Sr-85 labelling of porous tricalcium phosphate and hydroxyapatite implants. The degree of resorption was quantified by the reduction in radioactivity of the retrieved implant.

4.3.3.4 Strength of Implant and Host Tissue Bonding

For reasons of simplicity, the preferred method of assessing the implant/host tissue bond reported in the literature has been pull- or push-out testing, in which the interfacial shear strength is measured (Table 4.3.2). However, several authors dispute the suitability of this method for assessing the strength of a bond between implant and host tissue (Steinemann, 1986; Gross *et al.*, 1987; Black, 1989; Lin *et al.*, 1992; Pröbster *et al.*, 1994). They believe that results from this method are either erratic (as a result of misalignment between the direction of loading and the interface) or misleading, especially when comparing materials with varying surface roughness (due to measurement of the forces necessary to overcome both bone bonding and mechanical interlock). These authors promote tensile type tests, in which the main axis of loading is perpendicular to the implant/tissue interface. However, implants have to be specially designed with "gripping facilities" and the technique has generally only been assessed on dense implants implanted transcortically, as the gripping of porous implants and bone without damage can prove difficult (notable exceptions being Gross *et al.*, 1987 and Lin *et al.*, 1992).

Dhert *et al.*, (1991) and Kangasniemi *et al.*, (1994) demonstrated that the different test methods could not be compared by testing a series of implants in an identical anatomic site by pushout and tensile testing. The significantly lower values for tensile tests as compared with shear tests (2.81±0.99 cf. 13.3±2.1 MPa for hydroxyapatite and 0.36±0.38 cf. 15.3±2.7 MPa for fluorapatite) indicate that the contribution of mechanical interlock to pushout results is quite considerable (Table 4.3.3). Similarly, investigators using tensile tests do not report increased fixation for rougher specimens (Gross *et al.*, 1987; Pröbster *et al.*, 1994; Kangasniemi *et al.*, 1994) compared with reports from pushout tests (Bobyn *et al.*, 1980; Saha *et al.*, 1987; Maxian *et al.*, 1993; Hayashi *et al.*, 1994).

There have been several finite element studies into the boundary conditions of pushout testing in order to identify the most important parameters to reduce test variability (Dhert *et al.*, 1992; Orr *et al.*, 1995). Assuming a cylindrical specimen with uniaxial alignment between the direction of loading and the specimen interface, the most important parameters were found to be clearance between hole and implant, the modulus of the implant and the degree of bone in- or on-growth. The thickness of surrounding tissue was reported to have a small contribution while the dimensions of the specimen made little difference. Therefore, while pushout testing may not be the best method for assessment of absolute values of bond strength it is the more practical method and may be used as a comparative test with which to assess the relative bond strengths of a series of specimens.

One of the most important considerations when performing these tests is the assessment of the interface area. This was performed by most authors by measurement of implant dimensions before surgery and/or after test piece preparation. However, errors may be introduced as a result of specimen chipping or resorption during surgery. In order to overcome this problem some authors have suggested that measurement of the bone/implant contact area should be made and used to calculate the bone strength (Kiefer *et al.*, 1986; Gross *et al.*, 1987), but this may not be practicable where an interconnected porous material is under investigation, due to difficulties in the identification of the pore surfaces that constitute part of the interfacial area; besides it is the behaviour of the implant as a whole which is of more interest.

Table 4.3.2 Some push-out tests performed on hydroxyapatite in the literature

	Specimen Details	Specimen Size (mm) **CHV** (mm min^{-1})	Implant Site	Time *in Vivo* (weeks)	Interfacial Shear Stress (MPa)			
		Surface Pore Size (μm) →			20-50	50-200	200-400	400-800
Bobyn *et al.*, 1980	Porous Surfaced Co-Cr alloy	4.5 Ø; 91 **0.5**	Trans-cortical femur Dog	4 8 12	3.5 [1.1] 6.7 [1.1] 8.6 [0.7]	9.3 [1.2] 17 [1.4] 15 [1.3]	8.4 [1.4] 16 [0.9] 17 [1.5]	7.7 [1.2] 10 [1.5] 14 [3.2]
		Surface Roughness (μm) →			106		45	
Kiefer *et al.*, 1986	Rough Surfaced Ti alloy	5 Ø; 251 **1.0**	Femoral epiphysis Sheep	13	3.6 [0.3]		4.2 [0.9]	
		Surface Roughness (μm) →			1.27-1.52	3.81	1000-200 pores	
Saha et al 1987	Rough Surfaced Ti alloy	5-6 Ø;61 **25.4**	Trans-cortical femur Dog	23	1.04 [0.32]	3.17 [0.81]	11.54 [2.96]	
					HA coated smooth titanium			
Geesink *et al.*, 1988	HA Coated Ti alloy	4.5 Ø; 91 **?**	Femoral trans-cortical Dog	6 13 26 52	49.1 [2.3] 54.8 [2.6] 63.9 [1.7] 61.2 [2.4]			
			Composition →		"HAGlass"		PHB+40% HA	
Tanner *et al.*, 1990	HA + Bioglass or PHB*	2.4 Ø; 51 **3.0**	Femoral diaphysis Rabbit	4 13 26	11.59 [3.14] 20.65 [7.50] 19.29 [6.27]		1.53 [2.04] 6.87 [1.16] 8.44 [2.66]	
		Surface Roughness (μm) →			Ti only, 4.5-5.0		HA coated, 7.8-9.0	
Dhert *et al.*, 1991	Rough Ti HA Coated Ti	5.0 Ø; 71 **0.5**	Femoral Humeral trans-cortical Goat	12 F 25 F 12 H 25 H	7.4 [5.1] 9.6 [5.0] 6.7 [2.0] 7.5 [3.9]		13.3 [2.1] 17.3 [6.1] 11.1 [5.2] 13.3 [6.0]	
					70% Porous HA with 200μm pores			
Ueta 1992	Porous HA	3.0 Ø; 51 **?**	Femoral condyle Rabbit	2 4 6 8	2.68 [0.36] 4.46 [0.36] 4.23 [0.67] 4.39 [0.25]			

Table 4.3.2 Continued over page.

Table 4.3.2 Continued.

	Specimen Details	Specimen Size (mm) **CHV** (mm min^{-1})	Implant Site	Time *in Vivo* (weeks)	Interfacial Shear Stress (MPa)	
			Coating Finish →		"Smooth"	"Rough"
Maxian *et al.*, 1993	HA Coated Ti	4.8 Ø; 20l **10**	Femoral trans-cortical Rabbit	4 12	2.526 [0.166] 3.517 [0.160]	3.484 [0.616] 6.244 [0.282]
			Surgical Technique →		2-3 mm Gap	Press fit
Maxian *et al.*, 1994	"Rough" HA Coated Ti	4.8 Ø; 20l **10**	Femoral trans-cortical Rabbit	2 4 12	1.83 [0.22] 1.87 [0.24] 3.30 [0.70]	2.0 [0.4] 2.3 [0.4] 3.2 [0.5]
					Max	
Lin *et al.*, 1994a	HA Coated Co-Cr-Mo	5 Ø; 2.5l **5.4**	Femoral trans-cortical Dog	6 12	18.5 37.5	
			Surface Roughness (μm) →		3.4 [0.5]	8.4 [1.8]
Hayashi *et al.*, 1994	HA Coated Ti	6 Ø; 13l **0.5**	Femoral trans-cortical Dog	4 12	5.8 [2.1] 5.7 [1.6]	8.3 [3.0] 13.3 [6.0]
			Coating Finish →		HA Coated	Porous Ti
Salkeld *et al.*, 1995	HA Coated Porous Ti	4.8 Ø; 18l **1.27**	Femoral trans-cortical Dog	3 6 12 26	13.05 [3.76] 17.32 [3.10] 17.72 [7.98] 24.44 [5.81]	9.78 [2.82] 11.57 [5.18] 14.75 [3.24] 15.47 [4.03]
			Coating Finish →		Smooth	Grooved
Kla-witter *et al.*, 1995	HA Coated Carbon	6 Ø; 18l **?**	Femoral trans-cortical Dog	3 6 4	5.16 [1.93] 4.08 [1.51]	6.12 [3.10]

Figures in square parentheses are standard deviations

Table 4.3.3 Some tensile tests performed on hydroxyapatite in the literature

	Specimen Details	Specimen Size (mm) **CHV** ($mm\ min^{-1}$)	Implant Site	Time *in Vivo* (weeks)	Interfacial Shear Stress (MPa)			
			Implant Shape →		Cylindrical*		Rectangular	
Gross *et al.*, 1987	Glass-ceramic	4 x 4 x 8l	Femoral trans-cortical Rabbit	4	1.17 [0.2]			
				8			2.39 [0.2]	
		4 Ø; 8l		12	1.95 [0.5]		1.59 [0.2]	
		Cylindrical* Implant Orientation →			Distally		Proximally	
	Glass-ceramic	4 Ø; 8l	Femoral distal Rabbit	4	1.04 [0.2]		0.74 [0.3]	
				8			1.78 [0.4]	
				12	0.97 [0.08]		0.62 [0.1]	
		Cylindrical* Implant, Oriented Distally, Surface Roughness (μm) →			0.06	10	28	52
	Glass-ceramic	4 Ø; 8l	Femoral distal Rabbit	12	0.82 [0.08]	0.97 [0.08]	0.96 [0.07]	1.11 [0.11]
		?						
					14% porous HA with <2 μm Pores			
Lin *et al.*, 1992	Porous HA	4 Ø; 8l Semi-Cylindrical	Tibial diaphysis Rabbit	2	0.717 [0.286]			
				4	1.375 [0.627]			
				8	1.534 [0.544]			
				16	1.594 [0.715]			
		2.5×10^{-3}						
		Surface Roughness (μm) →			HA 10 [0.7]	HA 3.4 [0.8]	Ti 4 [1]	
Kangas-niemi *et al.*, 1994	HA Coated Ti	5 Ø; 3l	Femoral trans-cortical Goat	6	0	0	0	
				12	2.81 [0.99]	3.98 [0.90]	0.04 [0.07]	
		0.1		24	1.17 [1.35]	1.86 [1.86]	0	
		Surface Roughness (μm) →			63	101 Pores	175 Pores	103	109 #
Pröbster *et al.*, 1994	Coated or Grooved# Ti alloy	4 Ø; 8l	Femoral distal epiphysis Rabbit	24	1.55 [0.22]	2.81 [0.11]	3.08 [0.68]	2.52 [0.28]	3.20 [0.48]
		1							

Figures in square parentheses are standard deviations

*Flattened on one side.

4.3.3.5 Compression Strength of Implant Pre- and Post-Implantation

The use of compression testing to evaluate the mechanical properties of cancellous bone is well documented (Section 3.4). It would seem logical then to apply this technique to candidate synthetic bone materials in the as received and post-implantation (with ingrown bone) condition. This technique has been adopted by Holmes *et al.*, (1984) in the study of bone ingrowth into hydrothermally converted corals. Holmes *et al.*, observed that the compressive moduli and ultimate strengths of specimens after six months in a cancellous bone site (0.16GPa, 24.9 MPa) were significantly higher than similar specimens tested as received (0.02-0.06GPa, 4.1 MPa). Martin *et al.*, (1993) reported compressive yield stress and modulus to increase linearly with time (from 4 to 52 weeks *in vivo*) for specimens implanted in a cortical bone defect but found no correlation between mechanical properties and bone ingrowth. Unfortunately they did not give details of the compression strength of implants before implantation. Trécant *et al.*, 1994 have also reported the use of this technique to assess implant integrity before and after implantation. They found that the compressive strength of 50% porous blocks of hydroxyapatite (60%) and tricalcium phosphate (40%) increased from 2.6 ± 0.3 MPa before testing to 5.9 ± 1.7 MPa after one week in rabbit femurs and 6.8 ± 1.1 MPa after three weeks in dog femurs. However, the authors did not state whether or not the implants were placed in cortical or cancellous sites, and the implants were fixed in 80% ethyl alcohol before testing.

4.4 Summary

It is clear that both *in vitro* and *in vivo* testing can provide valuable information about the performance of a material if care is taken in the interpretation of the results. However, there are a number of "operating" parameters which can considerably alter both the *in vitro* and the *in vivo* behaviour of "hydroxyapatite". These parameters may be classified into two groups, specimen parameters and host parameters. Examples of specimen parameters include chemical stoichiometry, crystallinity, the architecture of the pore structure (where specimens are porous) and the surface morphology. Typical host parameters would include the cell line or animal species and the culture conditions or the implantation site and surgical technique.

The degree of variation in the reported results can be partly blamed on the wide range of basic "operating parameters" adopted by different researchers, which has resulted in much confusion. There is an apparent lack of understanding, characterisation and control of many of these variables.

Histomorphometric techniques for evaluation of bone ingrowth, coverage and apposition rate are well developed, although previous studies that have demonstrated that the results are subject to variability of up to 100% due to parameters such as section thickness, inter-section variation and operator dependence.

Lack of standardisation in the mechanical characterisation of retrieved implants has also resulted in an inability to directly compare the results of different experiments.

CHAPTER 5

CHARACTERISATION OF POROUS HYDROXYAPATITE

5.1 Introduction

Porous hydroxyapatite (HA) implants offer the potential for osseous defect repair and much work has been performed to investigate the *in vivo* and *in vitro* response of this material. However, in conjunction with the biological assessment of a material it is also important to characterise fully its physical, chemical and mechanical properties to aid understanding and control of any exhibited bio-response. In this thesis a commercially available porous hydroxyapatite, Endobon®, was examined. The main feature of the material is the preservation of the open macro-porous structure of bovine cancellous bone. This chapter details the investigation which was made into the chemical, structural and mechanical properties of this material.

5.2 Materials

The material selected for this study is a commercially available porous hydroxyapatite registered by Merck GmbH., (Darmstadt, Germany) as Endobon®. The material is produced by the sequential defatting, pyrolysis and sintering of cancellous bone, which is obtained from the distal and proximal ends of bovine femora and humeri. This method allows the removal of the organic component of cancellous bone, while preserving the trabecular structure, and hydrothermally converting the bone mineral and amorphous inorganic components within cancellous bone into hydroxyapatite. The final product is a porous hydroxyapatite with a three dimensional interconnecting network of pores (Figure 5.2.1).

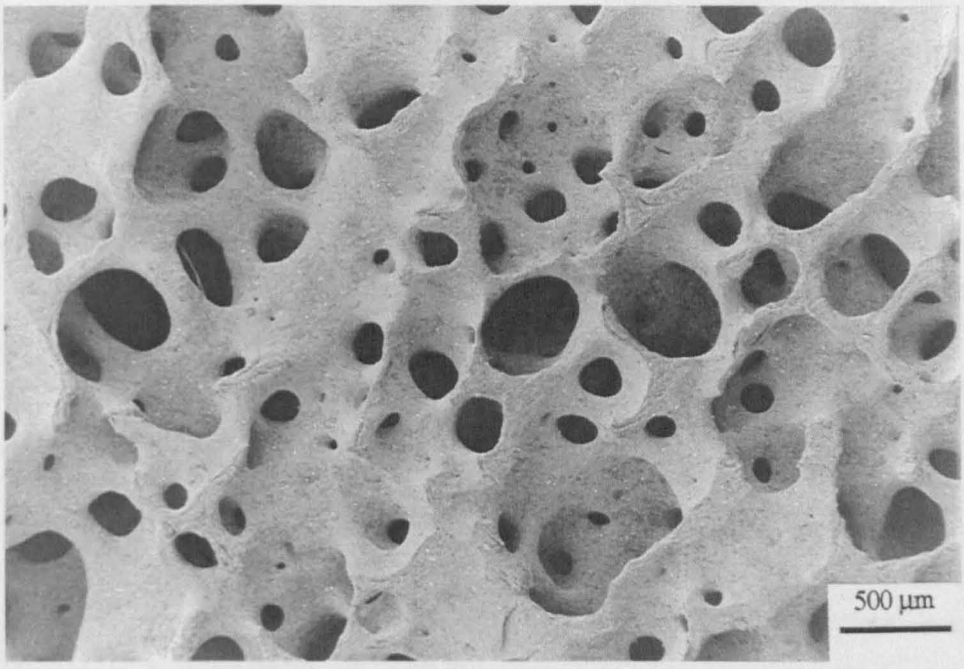

Figure 5.2.1 Typical macrostructure of a hydrothermally converted porous hydroxyapatite specimen.

5.2.1 Production of Porous Hydroxyapatite

The following section describes in general terms, the methods used by Merck GmbH., to produce hydrothermally converted porous hydroxyapatite from bovine cancellous bone.

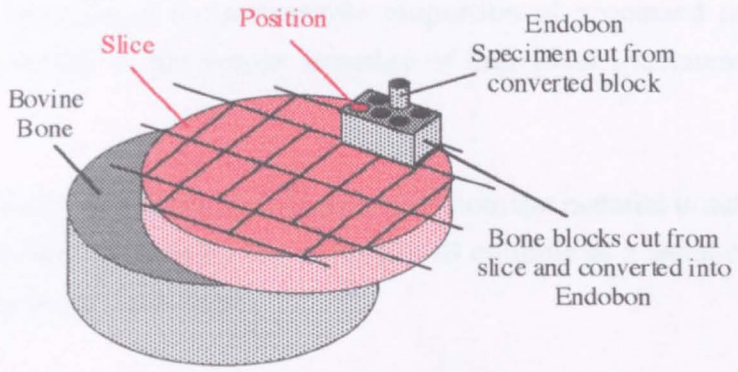

Figure 5.2.2 Diagram of specimen origin

De-Fatting. The distal and proximal ends of femora and humeri are sawn into 25x25x75 mm long rectoids (Figure 5.2.2). These blocks are then placed in a pressure vessel supplied with de-ionised water and pressurised to 1.8 atmospheres, at a temperature of 110°C for 2 hours. This process is repeated three times, with fresh water. The bone blocks are then removed from the pressure vessel and dried slowly.

Pyrolysis. The bone blocks are then placed in a furnace with a reducing atmosphere and heated to 700°C in order to carburise any remaining organic material. When this process is complete the furnace is flushed with oxygen and the carburised material is allowed to "burn off". The blocks are then cooled and carefully removed from the furnace. The blocks now consist of pure mineral and are fragile due to lack of sintering. They may be considered as a cancellous structured "green body" composed of 100 nm particles.

Acid Clean. The material has a high Ca:P ratio as a result of CaO formation on the material surfaces during the oxygen burn off proceedure. The blocks are therefore dipped in citric acid in order to dissolve out this phase. Excess acid is then removed with de-ionised water and the blocks are dried.

Sintering. The dried blocks are heated to 1250°C at a ramp rate of 5°C min^{-1} and held at temperature for 3 hours, before cooling at a ramp rate of 5°C min^{-1} in the furnace.

Cutting and Inspection of Morphology. Specimens are hand cut using a water cooled diamond band saw for rectangular/square cross-sectioned specimens and a diamond tipped, water cooled trephine for circular cross-sectioned specimens (Figure 5.2.2). During cutting, the regularity and density of the specimen architecture is assessed (i.e. the porous structure) and any overly anisotropic or dense regions are removed. This

results in the rejection of a considerable proportion of processed material. After cutting, the regularity of the porous structure of individual specimens are inspected once again.

Autoclaving. To ensure minimal CaO contamination, the material is autoclaved. If the CaO level is too high (> 1 wt%), the material will crumble as a result of an associated volume increase in the CaO phase.

Porous hydroxyapatite specimens produced using this method will be refered to as Endobon specimens in the rest of this thesis.

5.2.2 Specimen Variability

Initial studies of the first batch of 44 Endobon specimens (designated Batch O_M), received from Merck in early October 1992, indicated a significant variability in pore orientation and porosity. The apparent density of these specimens was found to range from 0.4 - 1.3 $g.cm^{-3}$ (Figure 5.2.3).

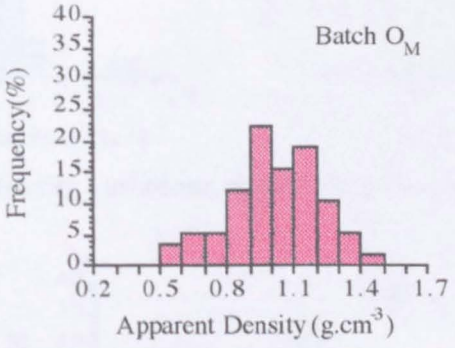

Figure 5.2.3 Variation of apparent density in Batch O_M.

To reduce variability in further batches of samples, a labelling protocol was adopted by Merck, enabling the location of the region in the bone from which the specimens were cut. This was achieved with the identification of the bone type (humeral, femoral), the slice number and the block position (Figure 5.2.2). Subsequently, four batches were received that had been labelled and segregated on the basis of their differing appearance and contrast on X-radiographs (Table 5.2.1) - the individual trabeculae of these materials, and hence their anisotropy, being clearly visible on a suitably exposed X-ray plate.

Table 5.2.1 Batch classifications as indicated by Merck (Darmstadt, Germany).

Batch	Structure	X-Ray Contrast	No.of Specimens
A_M	Epiphyseal	High	52
B_M	Epiphyseal	Low	100
C_M	Metaphyseal	High	35
D_M	Metaphyseal	Low	98
X_M	"High Density"	–	42

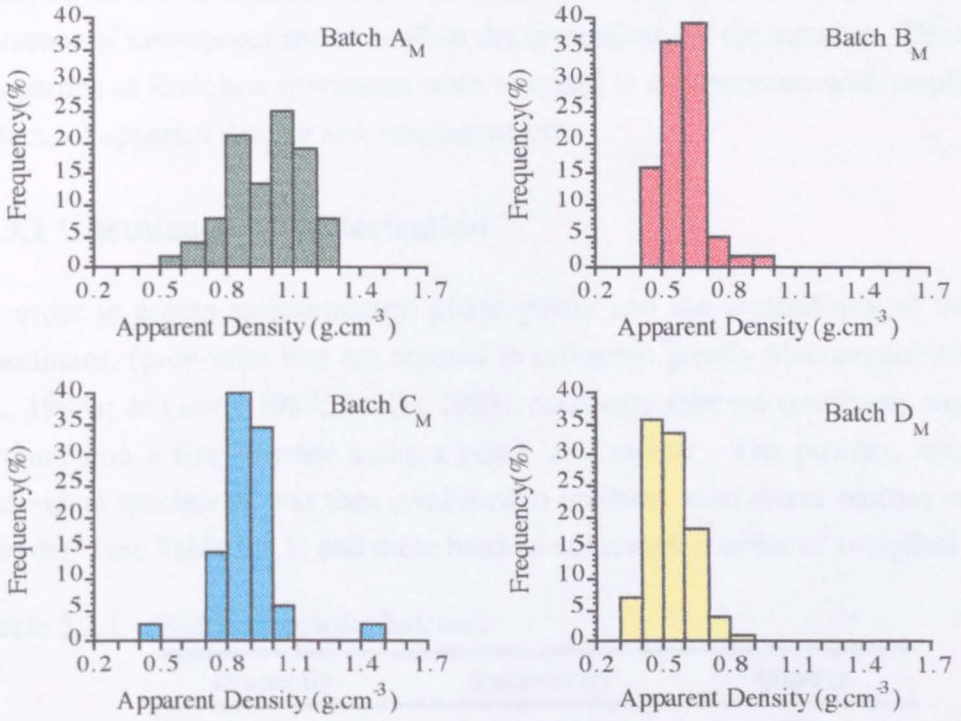

Figure 5.2.4 Apparent density variations within batches selected from X-radiographs

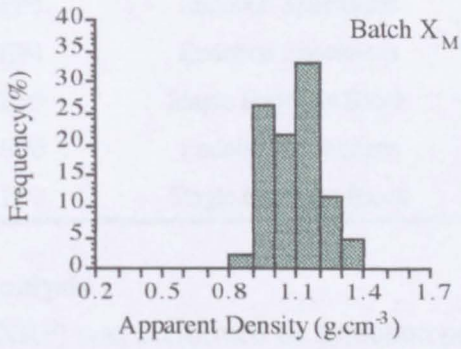

Figure 5.2.5 Additional high density specimens.

However, as can be seen from Figure 5.2.4, the apparent density ranges within the batches were still broad, with little density variation between the batches. Therefore, it was necessary to redefine the batches into three distinct density groups and to obtain an additional batch of high density specimens (Figure 5.2.5).

5.3 Methods of Characterisation of Endobon

The characterisation of Endobon was carried out in three parts: chemical analysis, structural classification and mechanical testing. Chemical analysis was performed to ensure that the material was composed of hydroxyapatite. The variation in apparent density mentioned in the Section 5.2 resulted in the requirement for a comprehensive analysis of the macrostructure. The microstructure was investigated to assess the presence of micropores and to confirm the crystallinity of the material. The mechanical properties of Endobon specimens were assessed in compression with emphasis on the effects of apparent density and macrostructure.

5.3.1 Chemical Characterisation

In order to assess stoichiometry, phase purity and the crystallinity of the Endobon specimens, (properties that are reputed to influence greatly biocompatibility, Klein *et al.*, 1983a; de Groot, 1987; Bruijn, 1993), randomly selected specimens were carefully ground into a fine powder using a pestle and mortar. The powder, resulting from individual specimens, was then combined to produce seven distinct batches of "Endobon powder" (see Table 5.3.1) and these batches underwent a series of analytical tests.

Table 5.3.1 Endobon powder batches.

Powder ID	Specimen ID	Quantity
EP1	Endobon Blocks	20g
EP2	Endobon Blocks	20g
EP3	Endobon Specimens	10g
EP4	Endobon Specimens	10g
EP5	Single Endobon Block	5g
EP6	Endobon Specimens	5g
EP7	Single Endobon Block	6g

5.3.1.1 Elemental Analysis

X-ray fluorescence (XRF) was performed on Endobon powder samples to determine the value of the calcium to phosphor us ratio (Ca:P) of the ceramic. The work was performed at Ceram Research (Stoke on Trent, England) where samples were dried at 110°C before ignition at 1200°C. The Ca:P Ratio was calculated using equation 5.3.1.

$$\text{Ca:P Ratio} = \left(\frac{\text{wt\% of CaO}}{\text{wt \% of } P_2O_5}\right) \times \left[\left(\frac{A_r\, P_2O_5}{2(A_r\, P)}\right) + \left(\frac{A_r\, CaO}{A_r\, Ca}\right)\right] \times \left(\frac{A_r\, P}{A_r\, Ca}\right) \qquad (5.3.1)$$

Where A_r = Relative Atomic Mass. Specimens were also analysed for magnesium, sodium, strontium, aluminium, silicon, zinc, barium, tin, zirconium, iron, chrome, lead, copper, titanium, manganese and potassium using both XRF and inductively coupled plasma spectroscopy (ICP). ICP was performed at Medac (Uxbridge, England) where samples were digested in HCl and H_2O_2.

5.3.1.2 X-Ray Diffraction

X-ray diffractometry was carried out on Endobon powder (EP) 1-4 using a Siemens D-5000 X-ray diffractometer in flat plate geometry with graphite monochromated Cu-K_α radiation. Data were acquired from 5-110° 2θ, with a step size of 0.02° at 12 s per step. The diffraction patterns obtained by this method were then compared with ASTM standard patterns for hydroxyapatite on the EVA version 3.04 data base.

The crystal structure was refined using the Rietveld method with the Generalised Crystal Structure Analysis System (Larson *et al.*, 1990) program. The starting model used in refinement was based on the single crystal structure, as determined by Kay *et al.*, 1964 (Figure 2.2.1). Parameters such as the unit cell dimensions were refined before the structural parameters were varied. Specific attention was paid to the *a*- and *c*- axis lengths, the unit cell volume, the hydroxyl oxygen site [O(H)] site occupancy (theoretical value = 0.5), the [O-P-O] angles and the [Ca(2)-O(H)] and [Ca(2)-Ca(2)] bond lengths (*d*), the latter of which was used to calculate the hydroxyl channel radius, (r_c), using equation 5.3.2.

$$r_c = \frac{d\,[Ca(2)\text{-}Ca(2)]}{2} \tan\frac{\pi}{6} \qquad (5.3.2)$$

These values were of particular interest, as an increase in r_c and a higher O(H) site occupancy indicates the presence of carbonate when in conjunction with an increase in unit cell volume and *a*-axis length. In contrast, an increase in *c*-axis length tends to indicate the formation of oxide ions (reported at temperatures in excess of 1450°C as a result of H_2O loss). The values of the [O-P-O] angles (θ_i) were used to calculate the tetrahedral distortion index ($^aD_{ind}$), as in equation 5.3.3. This value, which is a measure of the PO_4 moiety, may be used to assess the extent of relaxation in the crystal structure and indicates the likelihood of carbonate substitution at this site. Lower values (< 5) denote a more regular tetrahedral environment.

$$^aD_{ind} = \frac{\sum_{i=1}^{i=6} (\theta_i - 109.17)^2}{6} \qquad (5.3.3)$$

5.3.1.3 Fourier Transform Infrared Spectroscopy

Fourier transform infrared spectroscopy (FT-IR) allowed the detection of expected ionic groups, such as hydroxyl and phosphate, as well as adsorbed water and other ionic groups, such as carbonate. Infrared spectroscopy was carried out on EP powders 1-4, using a Nicolet 800 System FTIR spectrometer, fitted with a photo-acoustic sampler, at a resolution of 4 wave numbers, operating from 4000 to 400 cm^{-1}. Prior to the detection of each powder, the specimen chamber of the photo-acoustic sampler (PAS) was purged with helium gas and dried using magnesium perchlorate. The signal generated by the PAS resulted from the detection of expansions in the gas surrounding the sample. The expansions in the gas being caused by the heating of the sample as a result of exposure to IR radiation.

5.3.2 Density Characterisation

5.3.2.1 Apparent Density

Apparent density, as defined when applied to cancellous bone, describes the open and closed porosity of a structure, i.e., the value obtained when including the volume of the pores as well as the trabeculae. Apparent density was calculated by dividing the weight of the specimen (W_{dry}), measured on a digital balance accurate to 0.0001g (Ohaus, model AP250D), by the specimen bulk volume calculated from the specimen length (l) and radius (r), measured using a micrometer, as follows.

$$\text{Apparent density} = \frac{W_{dry}}{\pi l r^2} \tag{5.3.4}$$

In order to determine whether the assumption that the Endobon specimens were perfectly cylindrical would lead to unacceptable levels of accuracy, a group of specimens were randomly selected and their apparent densities calculated as described in equation 5.3.4 and using Archimedes' principle. This process involved weighing a specimen dry (W_{dry}), submersed (W_{sub}) and saturated (W_{sat}) in de-ionised water, the apparent density being given by:-

$$\text{Apparent density} = \left(\frac{W_{dry}}{(W_{sat} - W_{sub})}\right)\rho_{H_2O} \tag{5.3.5}$$

where, ρ_{H_2O} = Density of deionised water. In order to ensure that water fully penetrated all the open porosity of the specimens, they were left under vacuum in de-ionised water for 30 minutes before weighing submerged and saturated. Both types of

measurement were repeated at least twice for each specimen and on different days to check repeatability.

5.3.2.2 Real Density

Archimedes' principle was used to determine the real density of Endobon specimens, i.e., the density of the individual struts, as an indication of the extent of closed porosity present in a structure, where:

$$\text{Real density} = \left(\frac{W_{dry}}{(W_{dry} - W_{sub})}\right)\rho_{H_2O} \qquad (5.3.6)$$

The accuracy of this method was checked with the use of helium pycnometery. This was carried out on specimens with a wide range of apparent densities, using a Micromeretics AccuPyc 1330, at Micromeretics Ltd., Bedfordshire, England.

5.3.3 Microscopy of Endobon Specimens

Scanning electron microscopy (SEM) and optical microscopy (OM) were performed on a variety of whole, sectioned, embedded, polished and etched "as-received" Endobon specimens, in order to study both the macro- and microstructure. Both techniques were used qualitatively and quantitatively, in conjunction with image analysis.

5.3.3.1 Preparation of "As Received" Specimens for Microscopy

Embedding

Specimens were cleaned by ultrasonication in acetone for 5 minutes. They were then placed in 25mm diameter embedding moulds (Struers, Glasgow, Scotland) and held under vacuum in a Epovac (Struers, Glasgow, Scotland) for 30 minutes to ensure a high vacuum. Epofix epoxy resin (Struers, Glasgow, Scotland) was then mixed 15:2 by volume with hardener and, if required, dark blue dye was mixed into the epoxy resin for contrast in darkfield optical microscopy. The resin was then introduced into the moulds under vacuum, which ensured penetration to the centre of the specimens. The resin impregnated specimens were then left to cure overnight.

Sectioning

Specimens were sectioned after embedding to avoid brittle fracture during the cutting process. Embedded specimens were sectioned into approximately 1mm thick slices using an Accutom-2 (Struers, Glasgow, Scotland) fitted with a Bakerlite bonded

diamond blade (Struers, Glasgow, Scotland) and running at 2000 RPM. The line pressures before and after the blade contacted the specimen were noted and the pressure change (ΔP) calculated. The feed was then adjusted until ΔP = 0.1-0.2 bar, which resulted in a feed rate of approximately 0.2 mm s^{-1}. After sectioning, specimens were re-embedded in 25mm moulds (Struers, Glasgow, Scotland) for ease of handling.

Grinding and Polishing

This proce dure was performed on an Abramin (Struers, Glasgow, Scotland). A water-lubricated 125 grit wheel was used to expose and to level off section surfaces. Further grinding was then performed on resin bonded diamond wheels with sequentially finer particle sizes (63, 30 and 10 μm) at a pressure of 20N for 5-10 minutes, or until scratches were removed. Polishing was performed under DP-Blue lubrication (Struers, Glasgow, Scotland) on cloth covered polishing wheels with 3 and 1 μm diamond paste (Struers, Glasgow, Scotland). Care was taken to clean specimens thoroughly between wheel changes (with the use of an ultrasonic bath) to reduce particulate cross-contamination, especially when polishing. After polishing, sections were ready for study under the optical microscope.

Etching

Selected sections were etched to reveal the grain structure, with an aqueous 5% phosphoric acid solution. Sections were placed in high sided petri dishes and the acid solution was added drop-wise to the surface of the section. Etching was stopped 30s after addition of the first acid drop to the surface, by flushing with distilled water.

Gold or Carbon Coating of Sectioned and Whole Specimens

This technique was performed on sections or specimens for scanning electron microscopy. Sections or specimens were cleaned in acetone, mounted on cleaned stubs with carbon cement or conductive tape and a conductive track drawn from the section, or specimen surface to the base of the epoxy block or specimen (i.e., in contact with the conductive stub), they were then left to dry overnight. A sputter coater (Balzers, Milton Keynes, England) was used to coat the sections before viewing. Sections were usually gold coated, but when energy dispersive X-ray analysis was performed, sections were carbon coated.

The macro-structures of implanted specimens, sectioned for histology, were also studied. Sections of these specimens were prepared using the Exakt cutting-grinding technique, which is detailed in Chapter 6, Section 6.3.4.1.

5.3.3.2 Optical Microscopy

All optical microscopy was performed using an Axioskop microscope (Carl Zeiss, Welwyn Garden City, England) capable of bright field (BF), dark field (DF), polarised and differential interference contrast (DIC) illumination in both reflected and transmitted light. Embedded sections of "as-received" specimens under reflected BF illumination and histological sections under transmitted BF illumination were both studied at magnifications of ×12.5. These images were transmitted directly from the microscope to an image analyser via a video link and were used for the quantification of macropore size, orientation and morphology as a function of apparent density (see Appendix). Micrographs of sections of "as-received" specimens taken at magnifications of × 100-500 under reflected DF illumination were used to study qualitative aspects of Endobon microporosity, such as the shape and distribution of micropores within the Endobon struts.

5.3.3.3 Electron Microscopy

Electron microscopy was carried out using JEOL 6300 series scanning electron microscopes. Sections and whole specimens were studied at a range of magnifications using an accelerating voltage of 10-20 keV. Microporosity was studied on polished sections in the unetched condition at magnifications of × 500 or × 2000. Grain size studies were made on etched and polished sections at magnifications of × 2000. Micrographs of these specimens were taken for processing on an image analyser (see Appendix). The macroporosity of whole specimens was studied qualitatively at magnifications of × 20.

5.3.4 Image Analysis

Image analysis was performed using a Quantimet 570 image analyser system, which consisted of a high resolution video camera linked to an analogue to digital converter, and microprocessor. It was also possible to link the camera directly to the Axioscope microscope (Carl Zeiss, Welwyn Garden City, England) enabling direct microstructural quantification. Analysis was performed using the QUIC menu system, with which it was possible to perform basic processing on images "acquired" by the video camera and displayed on the computer screen. By manipulation of black, grey and white levels it was possible to enable the computer to "detect" a series of "features" that required analysis. A series of pre-defined parameters, such as "feature" area, length, aspect

ratio, roundness and orientation, could then be selected and calculated for the individual identified features. It was also possible to measure the total "field" area and perimeter, where the field is the sum of all the identified features. Calibration was performed by imaging a feature of known dimension (such as a micrometre bar on a SEM micrograph, or a graticule under the microscope) and setting the pixel : μm calibration factor appropriately.

Details of the methods used for the preparation and detection of images can be found in the appendix. Methods for the determination of various macroscopic and microscopic features are as follows.

5.3.4.1 Macropore Size

The equivalent circular diameter (MP_{cd}) of the individual pores was calculated from the measured "area" (Equation 5.3.7). However, although acceptable for equiaxed pores, this method was not appropriate for elliptical or elongated pores. Therefore pore lengths (MP_l) and breadths (MP_b) were also measured, where the pore length is the dimension of the longest axis, and pore breadth the dimension of the shortest axis.

$$MP_d = \left(\sqrt{\frac{Area}{\pi}}\right) \times 2 \qquad (5.3.7)$$

5.3.4.2 Macropore Shape and Anisotropy

Macropore shape was assessed by calculating the aspect ratio (from the length and breadth) of individual pores.

Measurements of macropore orientation and the longitudinal and transverse intercepts were combined to assess specimen anisotropy. Individual pore orientations were measured by the image analyser and expressed as an angle of deviation from the horizontal of the longest axis of the pore. The longitudinal and transverse intercepts of the individual pores were also measured by the image analyser, where the longitudinal intercept was the maximum intercept length through a pore made by a horizontal line and the transverse intercept was the maximum intercept length through a pore made by a vertical line. The values of longitudinal and transverse intercept length and orientation were the plotted on two polar plots and anisotropy assessed in the longitudinal and transverse direction as described by Whitehouse and co-workers (Whitehouse *et al,* 1971; Whitehouse, 1974a and b; Whitehouse and Dyson, 1974) and Hodgskinson and Currey (1990 a and b).

5.3.4.3 Macropore Connectivity

The number of distinct macropores per section was calculated and used to assess the connectivity of the macro-porosity within the structure as described by Hodgskinson and Currey (1990 a and b).

5.3.4.4 Grain Size

The equivalent circular diameter (G_d) of the individual grains was calculated from the measured area of each grain (equation 5.3.8). Unlike macropores, grains were generally equiaxed and therefore it was not necessary to measure both length and breadth.

$$G_d = \left(\sqrt{\frac{Area}{\pi}}\right) \times 2 \qquad (5.3.8)$$

5.3.4.5 Micropore Size

As a result of the large variation in micropore size, it was necessary to perform two sets of measurements at magnifications of $\times 500$ and 2000 for each specimen. The equivalent circular diameter (μP_d) of both sets of micropores was calculated from individual measured pore areas (Equation 5.3.9). However, the larger micropores tended to be oval in shape, so the lengths (μP_l) and breadths (μP_b) of these micropores were also measured.

$$\mu P_d = \left(\sqrt{\frac{Area}{\pi}}\right) \times 2 \qquad (5.3.9)$$

5.3.5 Compression Testing

Preliminary compression testing was performed using a floor standing Instron 6025 Universal testing machine using a 1 KN load cell. Further compression testing of as-received Endobon and implanted specimens was performed using an Instron 4464 bench-top test machine, fitted with a 2 kN load cell, using test templates created on Series IX Automated Testing System 1.26 (Instron, High Wycombe, England). All compression testing was performed using a specially designed jig that allowed specimens to be tested in Ringers solution at 37°C, (Figure 5.3.1). Specimens were

placed on the lower platen before addition of sufficient physiological fluid to cover the specimen. A pre-load of 0.005 kN was then applied with a crosshead velocity of 0.05 mm s^{-1}. The test was then switched to computer control. Load was applied axially to the specimen with a crosshead velocity of 0.001 mm s^{-1}. The test was recorded electronically with a sample rate of 0.5 points s^{-1}.

Figure 5.3.1 Compression testing assembly for testing of specimens under physiological conditions.

Failure usually occured via brittle fracture during the colapse plateau region of behaviour (Figure 3.3.1). Where this did not occur, testing was aborted before specimens reached the densification stage (Figure 3.2.3). Ultimate compressive stress (UCS) was defined as the maximum compressive stress recorded during the test, where compressive stress (σc) was calculated as in Equation 5.3.9. Compressive modulus (Ec) was determined from the slope of the linear-elastic region of the stress/strain plot

$$\sigma_c = \frac{\text{Load (N)}}{\pi\, r^2} \qquad (5.3.9)$$

where r = radius of specimen in mm.

5.4 Results

5.4.1 Chemical Characterisation

5.4.1.1 Chemical Analysis

Results of XRF and ICP spectroscopy are shown in Tables 5.4.1-5.4.3. The calcium to phosphor us ratios for the individual powder batches were calculated from XRF results (Table 5.4.1). With the exception of EP2, the Ca:P ratio was found to be in excess of the theoretical value (1.67), indicating either CaO contamination or phosphate defficiency.

Table 5.4.1 Calcium : Phosphor us ratios

	EP1	EP2	EP3	EP4	EP5	Theoretical
CaO	55.6	55.4	55.2	55.3	55.4	56.84
P_2O_5	41.8	41.8	41.7	41.6	41.7	43.16
Ca:P	1.68	1.67	1.68	1.68	1.68	1.67

Endobon was found to contain significant and consistent levels of magnesium and sodium. Strontium was detected at levels of 200-600 ppm and aluminium levels varied from 30 - 150 ppm. Silicon, zinc and barium impurities were all detected at levels of around 100 ppm. Specimens were also analysed for tin, zirconium, iron, chromium, lead, copper, titanium, manganese and potassium. Tin, zirconium and iron were detected at levels of less than 25 ppm, the other elements were present at levels of less than 10 to 0.5 ppm (Tables 5.4.2 and 5.4.3).

Table 5.4.2 Results of XRF (Figures quoted are oxide weight percentage of total ash).

(wt%)	CaO	P_2O_5	MgO	Na_2O	Al_2O_3	SiO_2	SrO	ZnO	BaO
EP1	55.6	41.8	1.00	0.67	<0.02	<0.02	0.03	0.03	0.02
EP2	55.4	41.8	0.86	0.68	<0.02	<0.02	0.03	0.02	0.02
EP3	55.2	41.7	1.06	0.76	<0.02	<0.02	0.08	0.02	0.02
EP4	55.3	41.6	0.80	0.55	0.12	0.03	0.06	0.02	0.02
EP5	55.4	41.7	0.85	0.58	0.20	0.18	0.08	0.02	0.02

Table 5.4.3 Results of ICP (Figures quoted as a percentage of total sample.)

(%)	Mg	Na	Al	Si	Sr	Zn	Ba
EP1	0.57	0.69	0.003	0.01	0.020	0.017	0.015
EP2	0.49	0.66	0.003	0.01	0.022	0.015	0.013
EP3	0.59	0.77	0.003	0.01	0.060	0.013	0.011
EP4	0.46	0.60	0.016	0.01	0.039	0.015	0.013
EP6	0.48	0.67	0.007	0.01	0.044		

Carbon and hydrogen analysis was also performed (Table 5.4.4). The detected levels of H were approximately 50% less than the theoretical value of 0.20 wt% (see Appendix), indicating that dehydroxylation occurred during the sintering process. There was some variation in the levels of carbon present.

Table 5.4.4 Carbon and hydrogen analysis results.

Element	EP1	EP2	EP3	EP4	Theoretical
C	0.09	0.03	0.04	0.09	-
C	0.07	0.03	0.07	0.09	-
H	0.12	0.14	0.10	0.11	0.20
H	0.09	0.10	0.11	0.15	0.20

5.4.1.2 X-Ray diffraction

Agreement between standard patterns for hydroxyapatite (EVA version 3.04) and the reflection peaks obtained from X-ray diffraction of all powdered Endobon specimens was consistent in all specimens (Figure 5.4.1). However a small peak at 37.4° was also present, indicating some CaO contamination (Figure 5.4.1b). The peaks were narrow indicating high crystallinity, which was consistent with the findings of concurrent SEM work (Section 5.4.3). Attempts to perform full refinement of the data failed in all but two cases (Table 5.4.5), as a result of the inability to model the crystal structure accurately due to the considerable ionic substitutions occurring in the lattice. However, it was possible to determine the unit cell parameters (Table 5.4.6).

Table 5.4.5 Results of Rietveld refinement of Endobon powders.

ID	Ca(2)-O(H) Length (nm)	O(H) Occupancy	Ca(2)-Ca(2) Length (nm)	Channel Radius R_c (nm)	Distortion Index D_{ind}
EP5	0.2390 [3]	0.604	0.415 [4]	0.1198	1.89
EP7	0.2414 [3]	0.495	0.415 [4]	0.1197	7.08

Numbers in square parenthesis are standard deviations on last significant figure.

Table 5.4.6 Unit cell parameters for Endobon powders.

ID	a-axis (nm)	c-axis (nm)	Unit Cell Volume (nm^3)
EP1	0.9426 [3]	0.6890 [2]	0.5301
EP2	0.9419 [1]	0.6883 [1]	0.5288
EP3	0.9422 [1]	0.6886 [1]	0.5294
EP4	0.9432 [2]	0.6894 [2]	0.5308
EP5	0.9421 [1]	0.6886 [1]	0.5294
EP7	0.9417 [1]	0.6886 [1]	0.5288
Theoretical	0.9423	0.6875	0.5286

Numbers in square parenthesis are standard deviations on last significant figure.

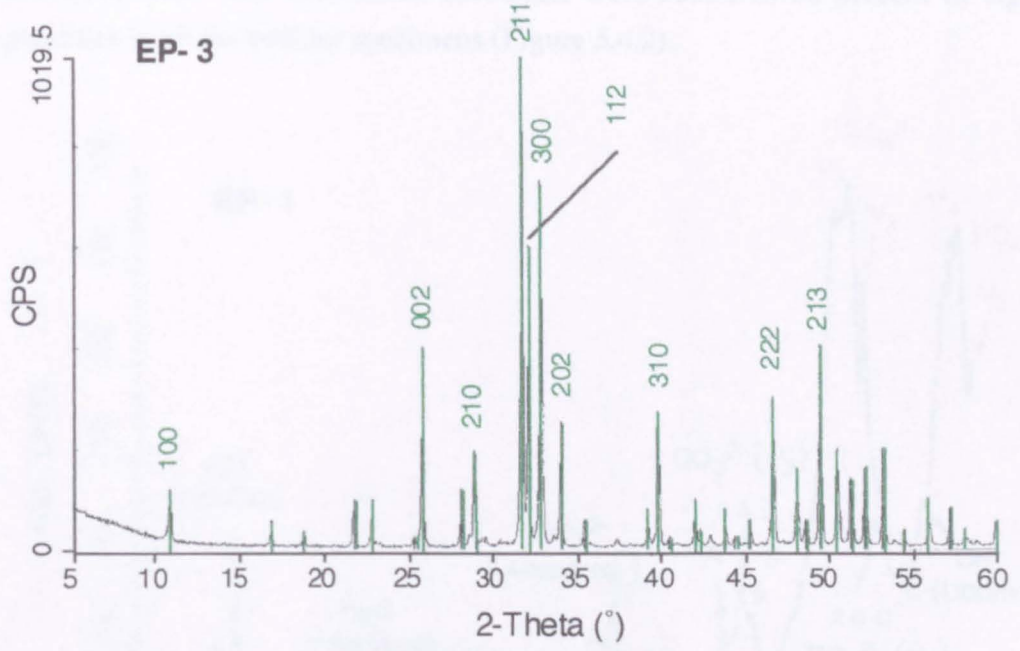

(a)

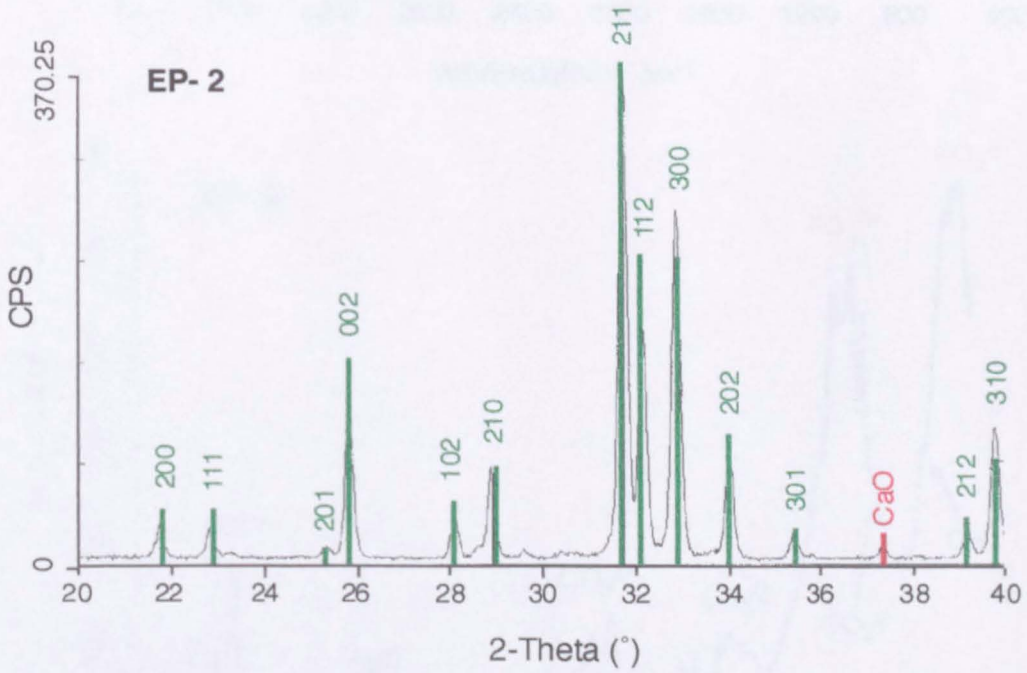

(b)

Figure 5.4.1 Typical XRD patterns for Endobon powders, (a) full diffraction pattern for EP-3 and (b) expanded portion of pattern for EP-2, demonstrating some CaO contamination.

5.4.1.3 Infra Red Spectroscopy

Adsorbed water and substituted carbonate were found to be present in significant quantities in all the powder specimens (Figure 5.4.2).

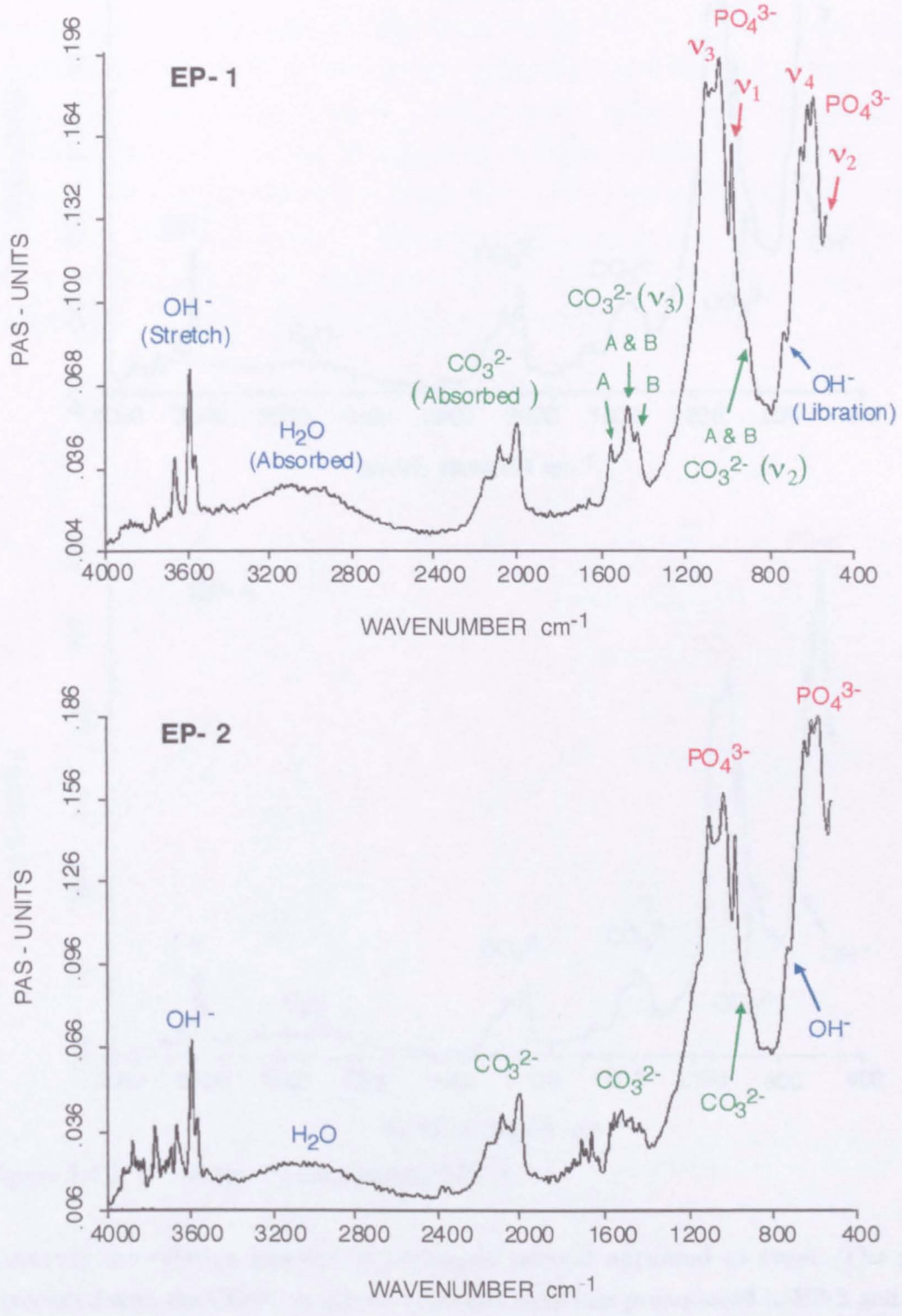

Figure 5.4.2 Continued over page.

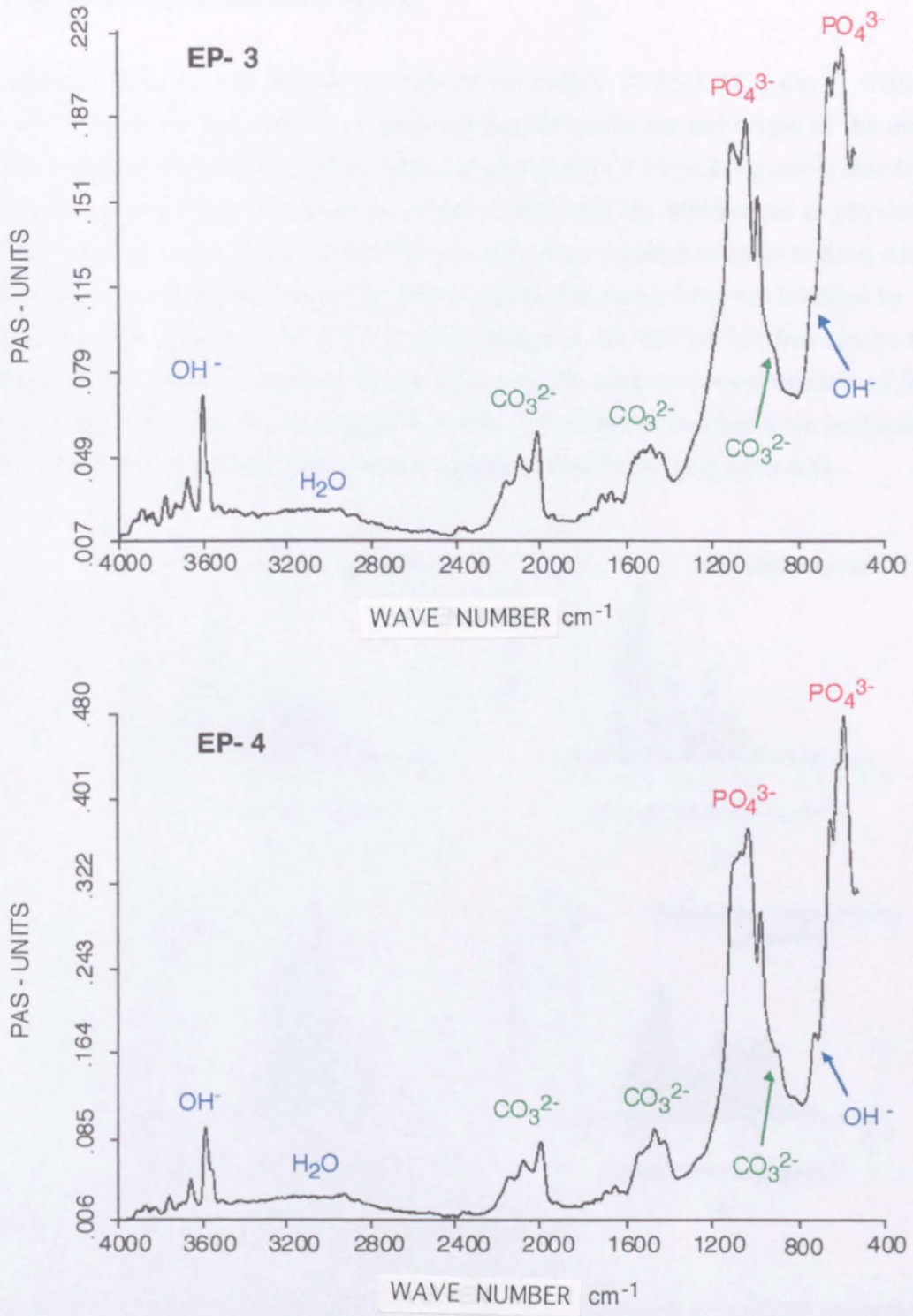

Figure 5.4.2 FT-IR spectra for powders EP1-4.

However the relative amount of carbonate present appeared to vary. The peaks associated with the CO_2^{3-} ν_3 vibration modes were less pronounced in EP-2 and EP-3 and those corresponding to the Type B carbonate substitution appeared weaker when compared with the peaks in spectra obtained from powders EP-1 and EP-4.

5.4.2. Density Characterisation

Apparent density was found to vary considerably (0.35-1.44 g.cm^{-3}) within the population of 350 specimens, a result which reflects the natural origin of the material. Humeral specimens had a slightly lower mean density (0.65 [0.21] g.cm^{-3}) than those of femoral bone (0.80 [0.25] g.cm^{-3}), possibly reflecting the differences in physiological loading in life. An extra set of dense specimens was required in order to have sufficient specimens for characterisation and implantation; but these were not labelled by Merck with the bone origins. The density distributions of the various batches can be seen in Figure 5.4.3. Endobon batches for the *in vivo* work were composed entirely of femoral and high density specimens (Figure 5.4.3 d). The implant batches were reclassified as in Table 5.4.7 to produce three distinct groups of specimens (Figure 5.4.4).

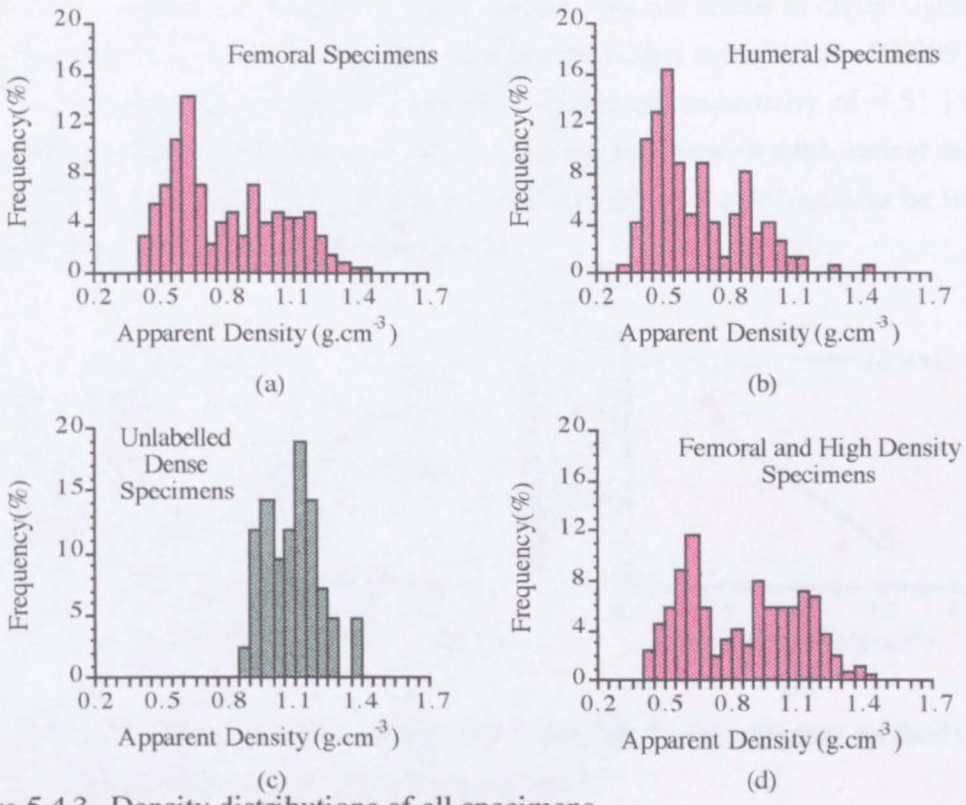

Figure 5.4.3 Density distributions of all specimens.

Table 5.4.7 Density results of batches selected for characterisation and implantation.

Apparent Density (g.cm^{-3})	Batch B	Batch C	Batch A
Range	0.51 - 0.68	0.86 - 0.98	1.09 - 1.38
Mean [Standard Deviation]	0.62 [0.03]	0.92 [0.03]	1.18 [0.06]
Population	48	27	48

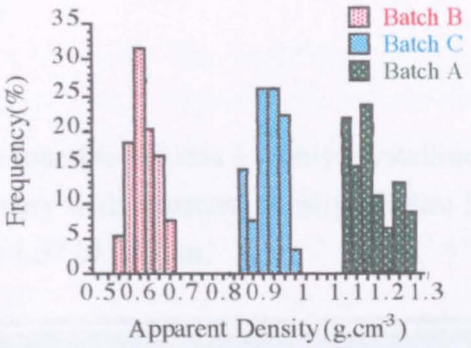

Figure 5.4.4 Density distributions of specimens in Batches B, C and A.

As can be seen from Figure 5.4.5 agreement between the dry and wet methods of density measurement was good. The discrepancy between the "wet" and "dry" results of low density specimens tended to be greater, however difficulties were experienced in keeping these specimens saturated. Real density was not found to differ significantly through out the population of Endobon specimens, with a mean value of 3.009 [0.038] $g.cm^{-3}$, which is consistent with a constant closed microporosity of 4.51 [1.21] % (assuming Endobon to be composed of pure hydroxyapatite with a theoretical density of 3.151 $g.cm^{-3}$, Barralet, 1995). However, the real density was found to be inversely related to the apparent density (Figure 5.4.5b).

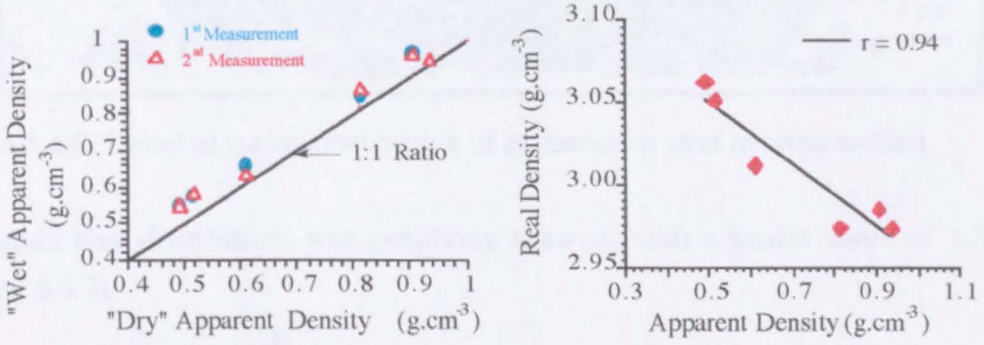

(a) (b)

Figure 5.4.5 Relationship between (a) "wet" and "dry" measurement methods and (b) Real and apparent densities of Endobon specimens.

The gas porosimetry results are detailed in Table 5.4.8. The trend between the real and apparent density was not observed with these results.

Table 5.4.8 Gas porosimetry results.

Apparent Density	1.170	0.921	0.621	mean
Real Density $g.cm^{-3}$	3.044 [0.006]	3.034 [0.008]	3.040 [0.015]	3.039 [0.005]

Numbers in square parenthesis are standard deviations.

5.4.3 Microstructure

Grain Size

Endobon specimens were found to possess a highly crystalline, equiaxed grain structure which did not appear to vary with apparent density (Figure 5.4.6). The average grain size (G_d) was found to be 1.57 [0.78] μm.

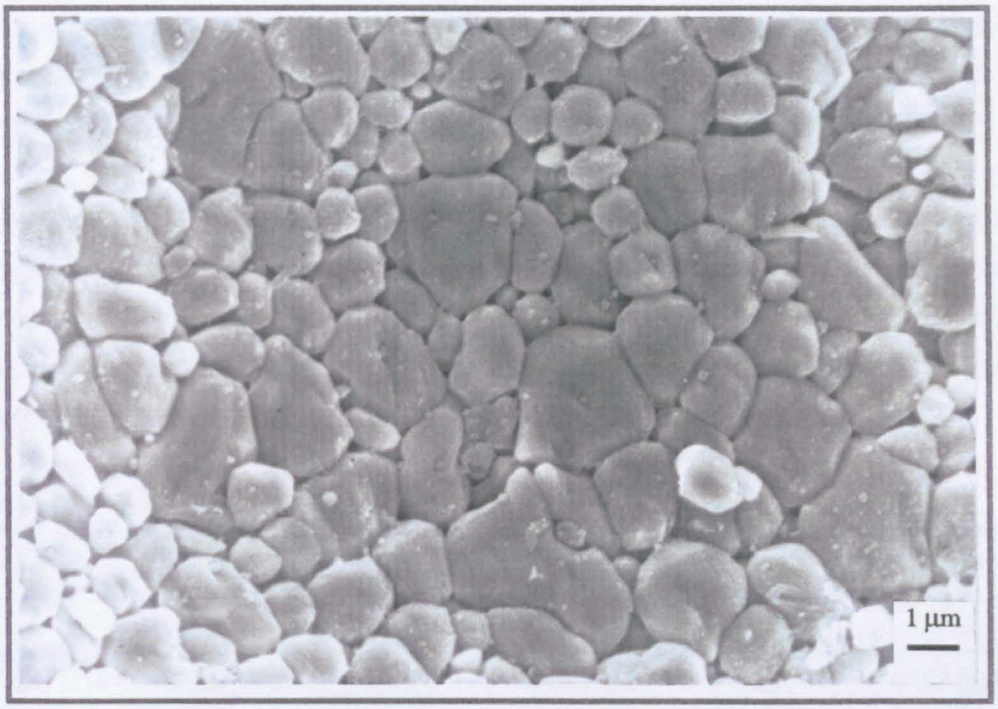

Figure 5.4.6 Detail of the microstructure of an Endobon strut in cross section.

The grain size distribution was positively skewed, with a modal value of 1.35 μm (Figure 5.4.7).

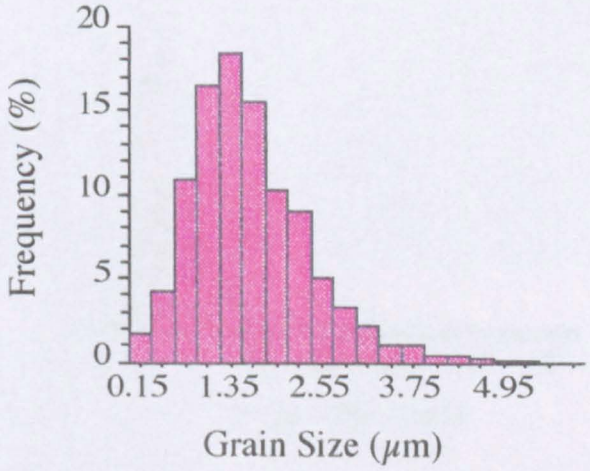

Figure 5.4.7 Frequency distribution of grain size.

Micro-Porosity

The microporosity could be classified into two groups:

- **Micropores <3 μm in size.** These were isolated circular pores, randomly distributed throughout the ceramic struts, occasionally positioned within grains, but more usually located at grain boundaries and triple points. (Figure 5.4.9)
- **Micropores >3 μm in size.** There were two distinct groups of pores in this size range, the larger pores (typically 10 μm long) were elliptical and aligned longitudinally with the ceramic struts (Figure 5.4.10), while the smaller pores (3-5 μm) were randomly oriented and irregular in shape. Both types appeared to be interconnected and more numerous in the centre of the struts (Figure 5.4.11).

Image analysis of the relative areas covered by two the types of micro-pores in a polished, sectioned strut are detailed in Table 5.4.9. The frequency distribution of the micro-pore size is illustrated in Figure 5.4.8. It is evident that although the < 3 μm pores are more numerous, the > 3 μm pores provide a greater contribution to the volume fraction of porosity.

Table 5.4.9 Image analysis of micropores

Micropore Group	Magnification of Analysis (×)	Mean Micropore Size (μm)	Micropore Size Range (μm)	Modal Micropore Size (μm)	Calculated Microporosity (%)
All	**2000**	**1.4 [1.2]**	**0.1 - 14.5**	**0.8**	**17.93 [6.09]**
<3 μm	2000	1.2 [0.6]	0.1 - 3.0	0.8	5.73 [0.69]
>3 μm	2000 and 500	6.8 [2.3]	3.0 - 14.5	n/a	12.20 [5.51]

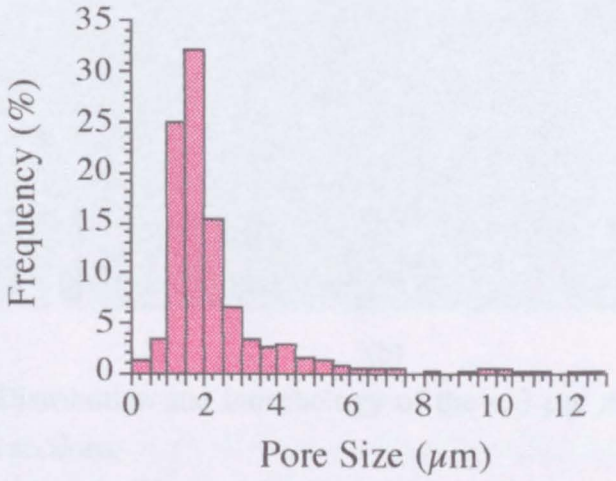

Figure 5.4.8 Frequency distribution of micro-pore size.

(a)

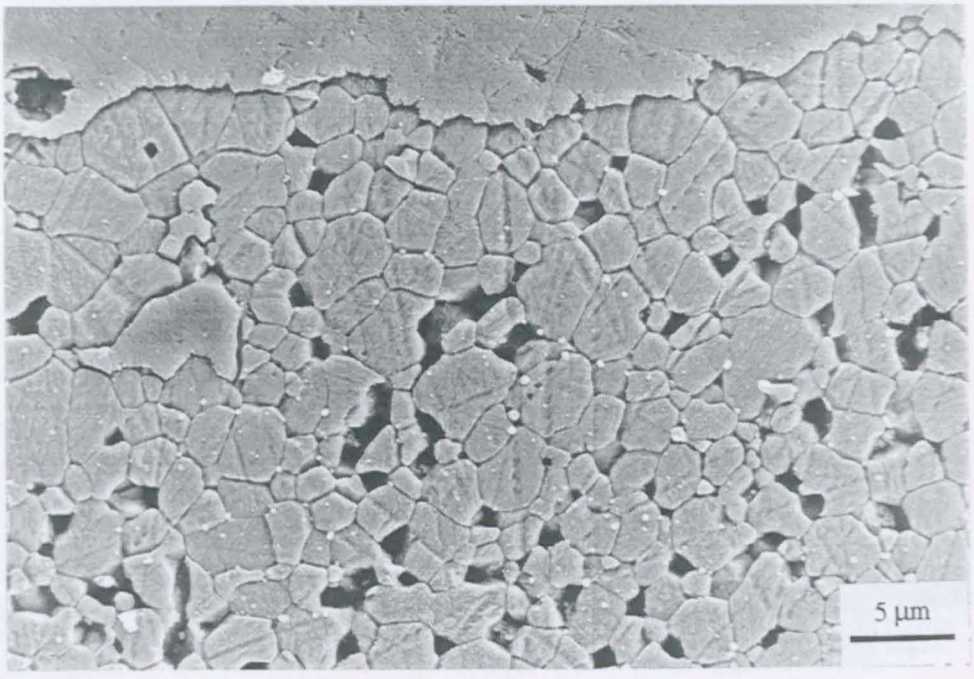

(b)

Figure 5.4.9 Distribution and morphology of the < 3 µm micropores in (a) polished and (b) etched sections.

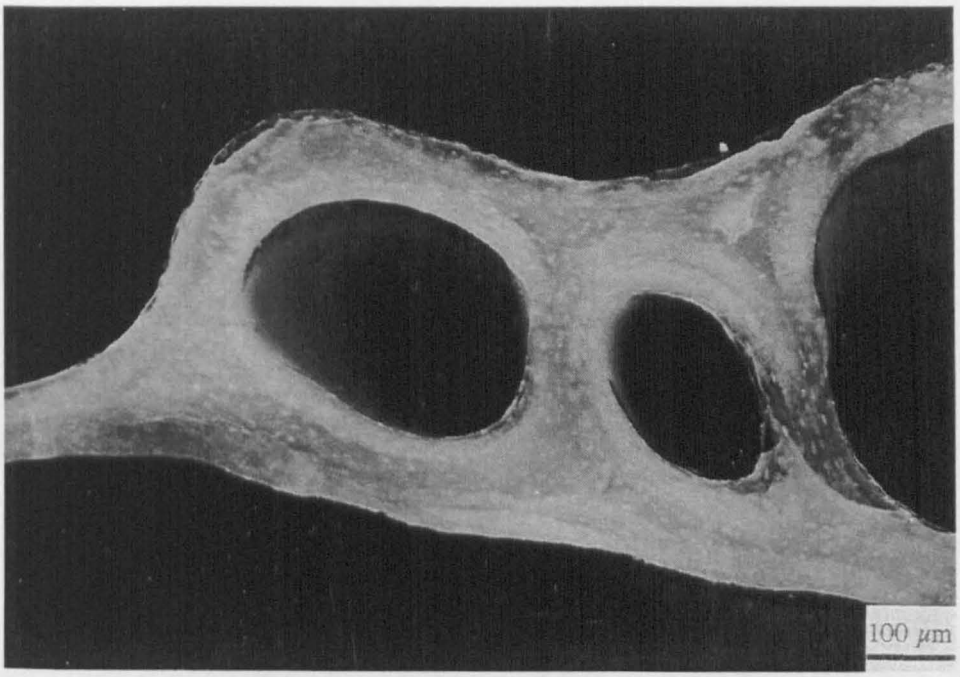

(a)

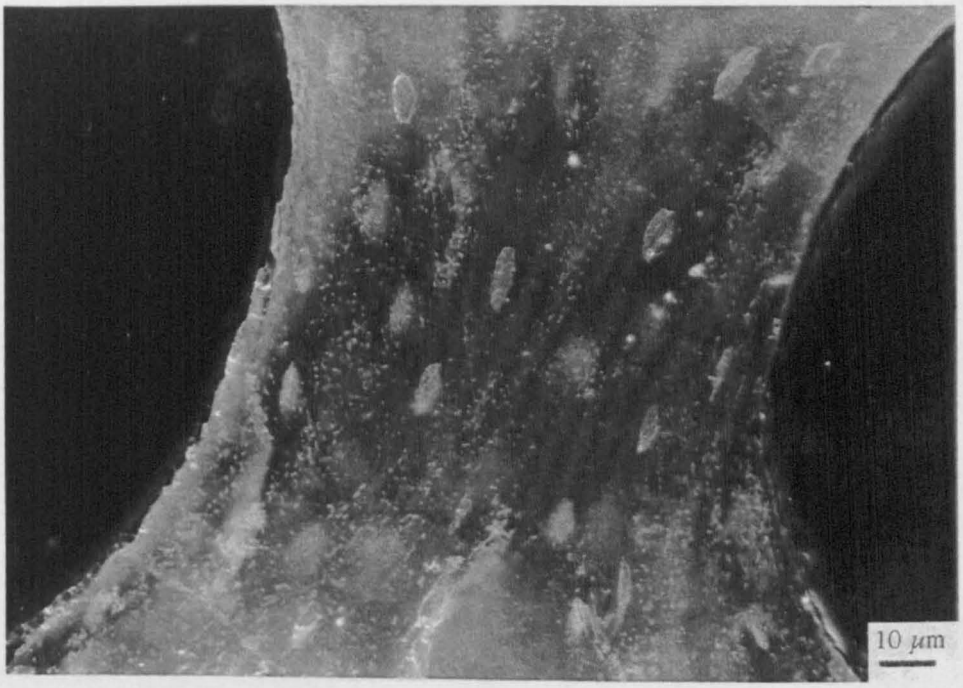

(b)

Figure 5.4.10 Darkfield illumination of polished thick sections of Endobon, demonstrating the alignment of large micropores within the ceramic struts at (a) low (× 100) and (b) high (× 500) magnification.

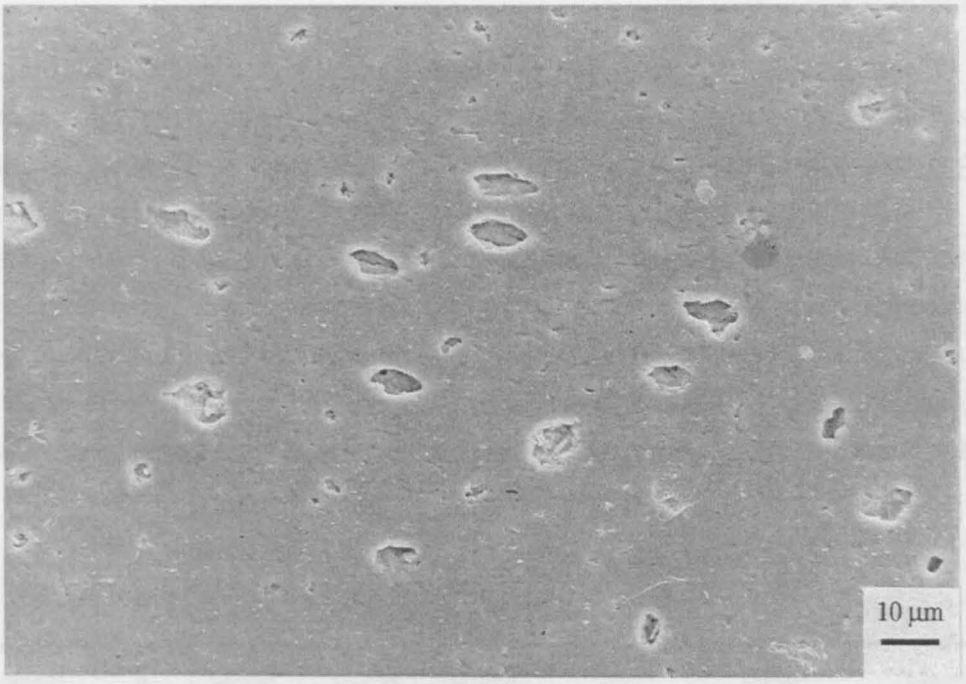

(a)

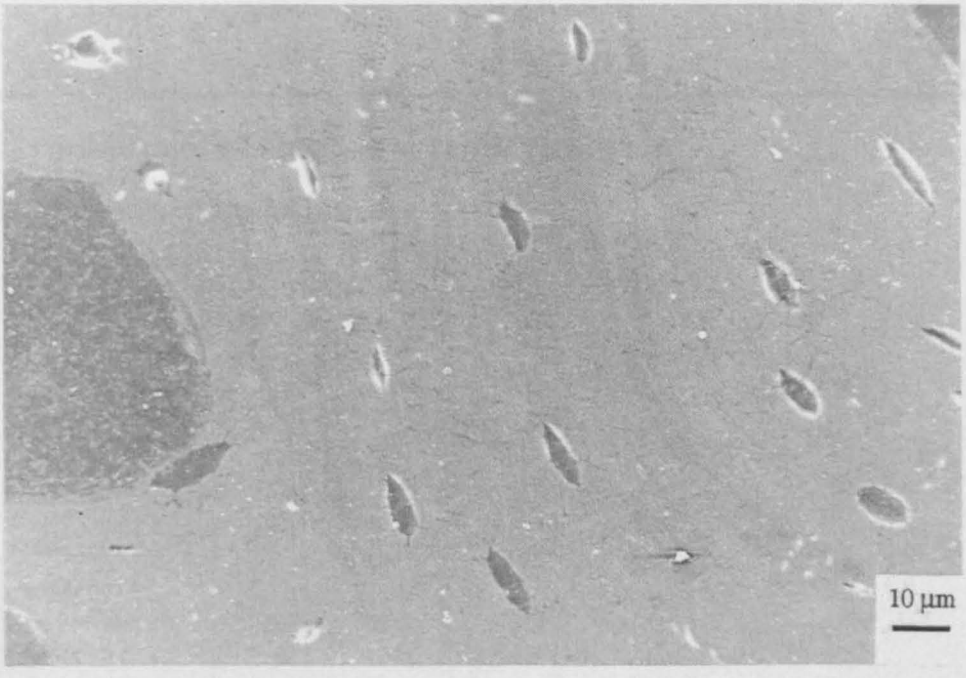

(b)

Figure 5.4.11 Comparison of (a) "10 µm" micropore size and morphology within an Endobon ceramic strut and (b) osteocyte lacunae within trabecular bone.

5.4.4 Macrostructure

No significant variation in macrostructure was noted between specimens with similar densities, which originated from either the humerus or femur. The features of the macrostructure, such as mean pore size, aspect ratio and connectivity were dependent on both the apparent density (Figure 5.4.12) and the degree of isotropy (Figure 5.4.13) of the specimen. It was impossible to distinguish between the individual structural effects of apparent density and isotropy, as the degree of anisotropy appeared to be related to the apparent density and was highly variable, however when studying specimens from the three density batches some trends in the size, shape and connectivity of pores became apparent and will be disscussed below (Table 5.4.10).

Table 5.4.10 Image analysis of macropores.

Batch	n	Modal ECD*	Modal Length	Modal Breadth	Size Range	Mean Aspect Ratio	Mean Connectivity
B	192	1080	630	430	90-2600	2.15 [0.63]	0.66 [0.39]
C	74	320	560	250	60-1050	1.81 [0.53]	0.06 [0.03]
A	253	265	390	310	50-1850	1.51 [0.34]	0.03 [0.01]

All sizes in μm, standard deviations in square parentheses.

* ECD = Equivalent circular diameter.

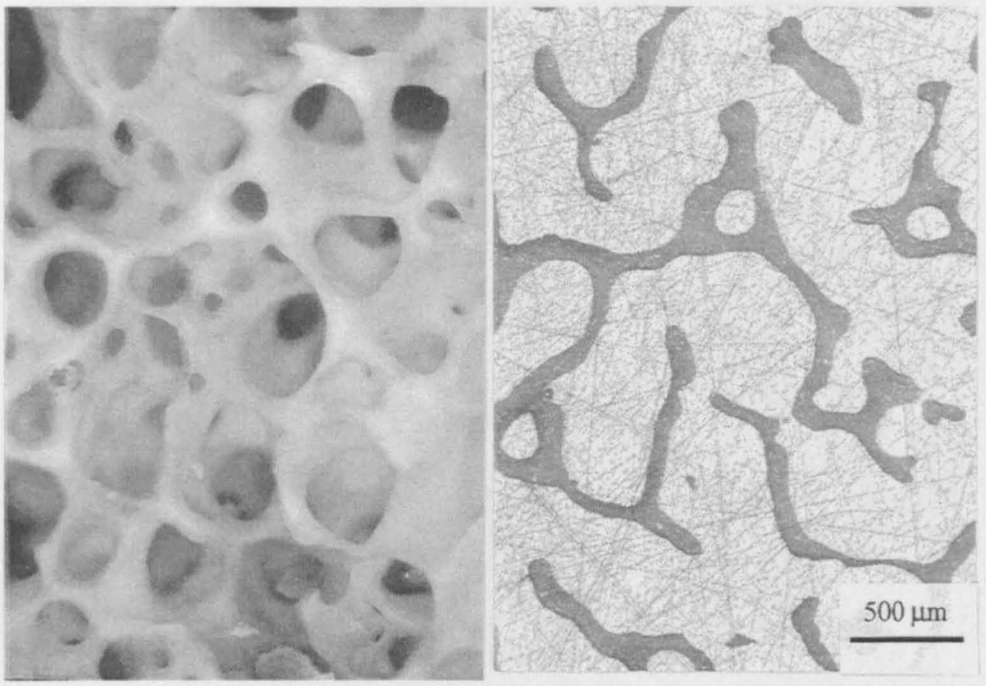

(a)

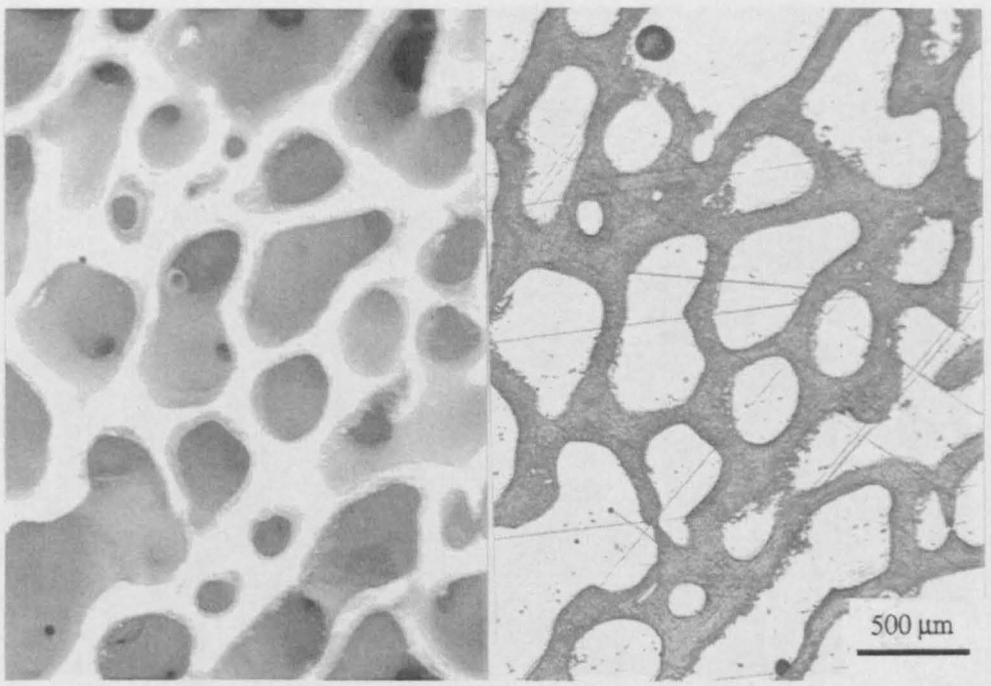

(b)

Figure 5.4.12 Optical micrographs demonstrating the effects of density variation on macrostructure in isotropic specimens (a) 0.64 g.cm^{-3} (b) 1.32 g.cm^{-3}.

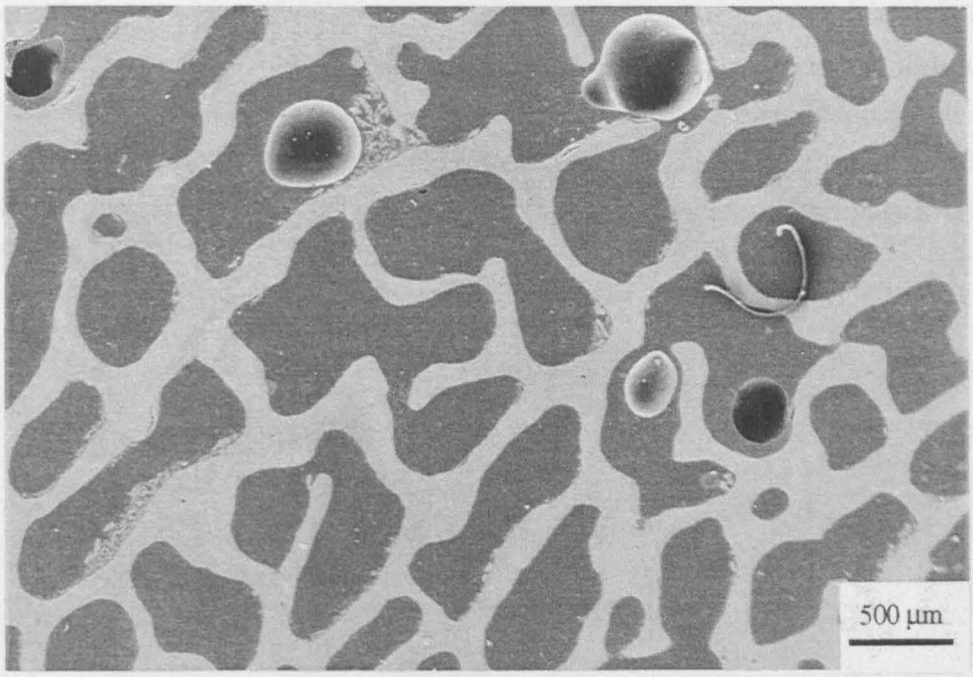

(a)

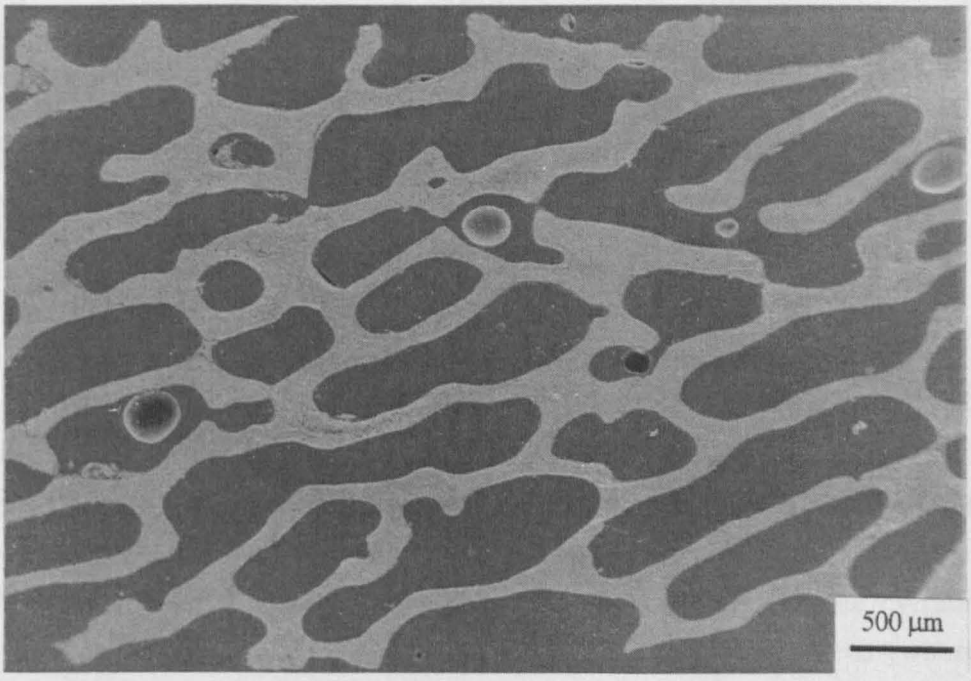

(b)

Figure 5.4.13 Scanning electron micrographs demonstrating the effects of anisotropy on the macrostructure of specimens with similar densities (a) 1.32 g.cm^{-3} (b) 1.14 g.cm^{-3}.

Pore size

When considering the size of macropores within specimens from batches A, B and C (Table 5.4.10, Figure 5.4.14), it can be seen that the mean and modal pore sizes increased with decreasing density. Batch B specimens were also found to possess broader size ranges than the other batches (Figure 5.4.14a). This effect was particularly noticeable for the pore lengths (Figure 5.4.14b) but less distinct for the pore breadths (Figure 5.4.14c).

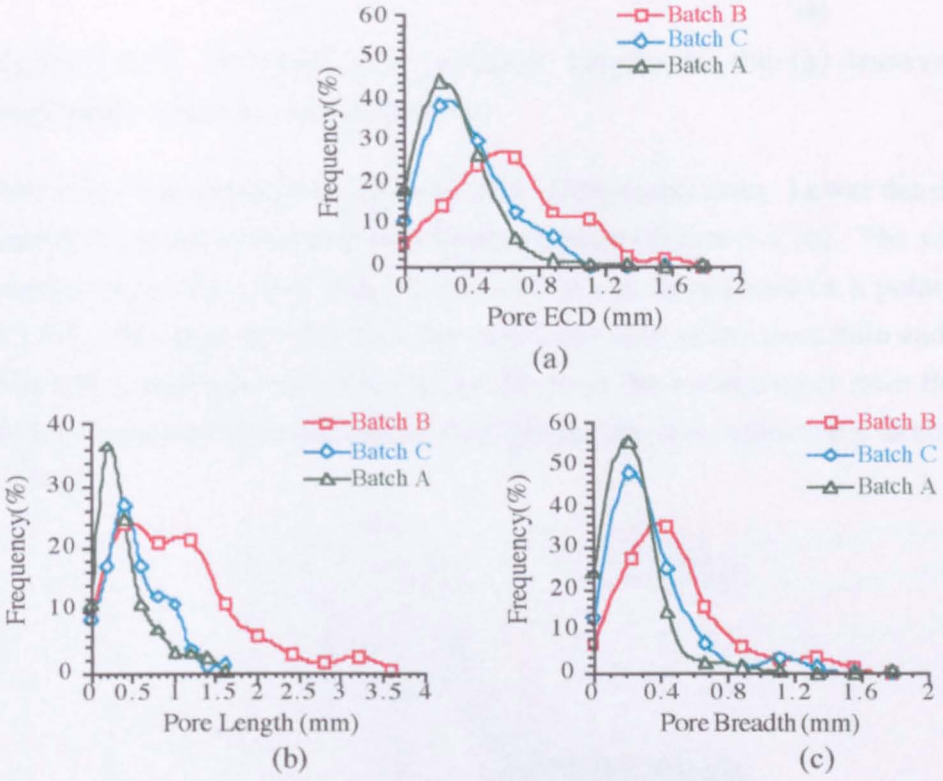

Figure 5.4.14 Variations in Endobon pore (a) ECD, (b) length and (c) breadth.

Anisotropy and Pore Shape

The degree of anisotropy exhibited by specimens from each batch in the longitudinal and transverse directions was assessed by measurement of the pore intercept lengths and pore orientations parallel to and perpendicular to the long axis of the cylindrical specimen, respectively, and plotting the results against pore orientation (where an orientation of either 0° or 180° indicates a pore aligned with the long axis of the cylindrical specimen) as in Figure 5.4.15. These plots show that all specimens are transversely isotropic (Figure 5.4.15a). However in the longitudinal direction Batch B specimens are highly anisotropic (Figure 5.4.15b).

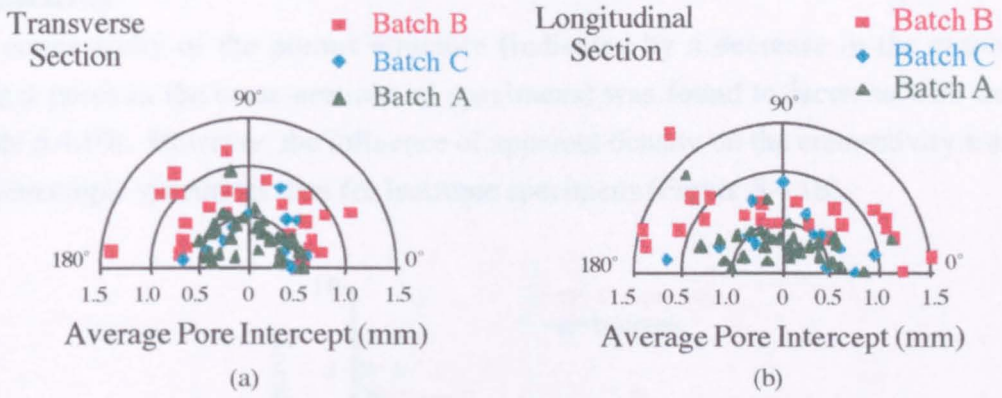

Figure 5.4.15 Average pore intercept lengths in the (a) transverse and (b) longitudinal direction, with orientation.

Pore shape was assessed by measurement of the aspect ratio. Lower density specimens tended to possess pores with higher aspect ratios (Figure 5.4.16). The variation in the orientation of the pores with the aspect ratio is represented in a polar plot (Figure 5.4.17). This demonstrates the relationship between pore aspect ratio and alignment in Batch B specimens, such that the variation in the mean aspect ratio throughout the batches indicated that lower density specimens are more anisotropic in structure (Table 5.4.10).

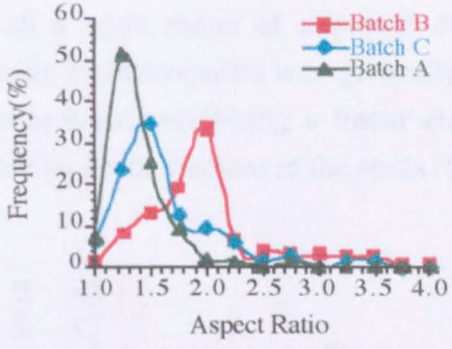

Figure 5.4.16 Frequency distribution of Endobon macro-pore aspect ratios

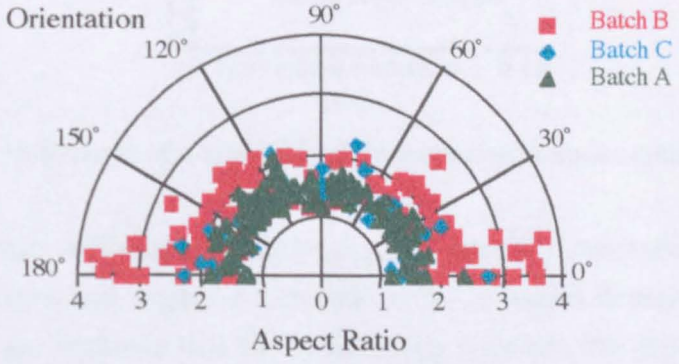

Figure 5.4.17 Variation in Endobon macro-pore aspect ratio with orientation.

Connectivity

The connectivity of the porous structure (indicated by a decrease in the number of distinct pores in the cross-sections of specimens) was found to decrease with density (Table 5.4.10). However, the influence of apparent density on the connectivity was less for anisotropic specimens than for isotropic specimens (Figure 5.4.18).

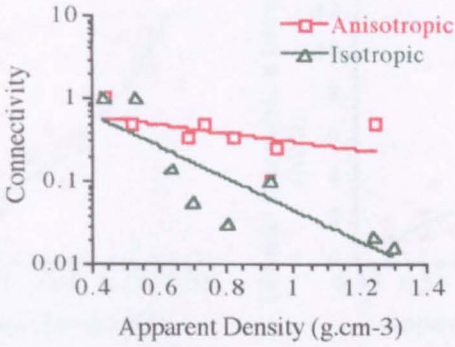

Figure 5.4.18 Variations in connectivity with anisotropy and apparent density.

5.4.5 Mechanical Characterisation

Endobon specimens with a wide range of apparent densities were selected for mechanical testing. Porous hydroxyapatite was generally found to fail in a manner typical of an elastic-brittle foam, exhibiting a linear elastic region followed by a collapse-plateau dominated by brittle fracture of the struts (Figure 5.4.19).

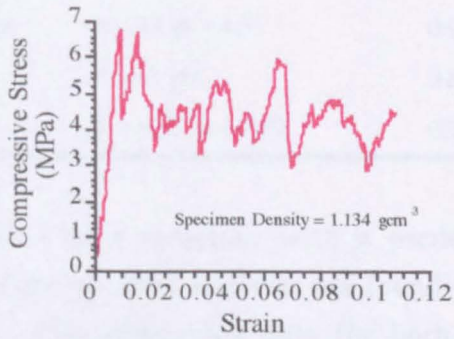

Figure 5.4.19 Behaviour of a typical Endobon specimen under compression.

However, the exact deformation behaviour and specific mechanical properties of individual specimens was highly dependent on the apparent density (Figure 5.4.20). Figure 5.4.20 a and b shows that the relationship between the apparent density and ultimate compressive stress, in the range of densities tested, could be described by

either an exponential (Figure 5.4.20a) or a quadratic (Figure 5.4.20b) relationship, as proposed by Ryskewitch (1953) and Gibson (1985; 1988) respectively. Regression analysis of the two relationships (Table 5.4.11) indicated that the quadratic equation was more accurate at describing the experimental data, with a confidence level of 81% as opposed to 77% for the exponential equation.

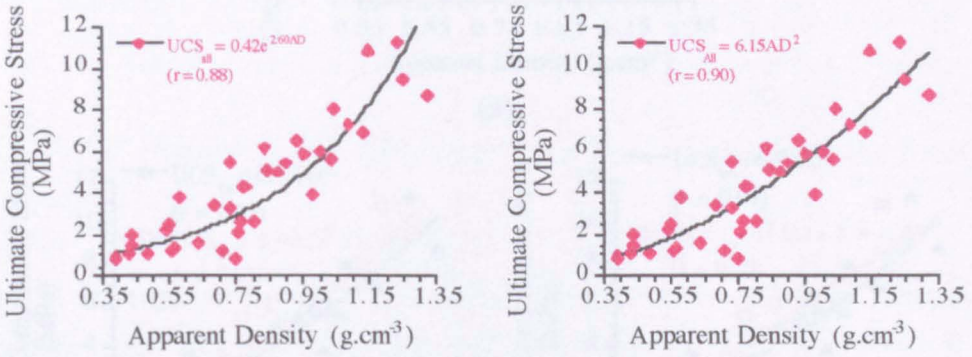

Figure 5.4.20 (a) Exponential and (b) power relationships between the UCS and apparent density of Endobon specimens

Table 5.4.11 Relationships between mechanical properties and apparent density.

Data	Equation	r	Equation N°
All UCS data	$\sigma = 0.42\ e^{2.6\rho}$	0.88	(5.4.1)
All UCS data	$\sigma = 6.2\ \rho^2$	0.90	(5.4.2)
Isotropic UCS data:	$\sigma = 6.7\ \rho^2$	0.91	(5.4.3)
Anisotropic UCS data:	$\sigma = 5.9\ \rho^2$	0.91	(5.4.4)
Anisotropic UCS data:	$\sigma = 11\ \rho - 4.3$	0.90	(5.4.5)
Isotropic E_c data:	$\sigma = 1.1\ \rho^2$	0.84	(5.4.6)
Anisotropic E_c data:	$\sigma = 0.85\ \rho - 0.10$	0.75	(5.4.7)

Anisotropy was exhibited as a structure with a predominance of struts in the longitudinal direction of the cylinder and was not found to have a marked effect on UCS (Figure 5.4.21a). The segregated data for both isotropic and anisotropic specimens could be described by quadratic equations (Figure 5.4.21b, Table 5.4.11). However, Gibson (1985; 1988) predicted that specimens exhibiting the structure of an anisotropic open foam, tested in the longitudinal direction should be linearly related to the apparent density. This linear relationship was also found to be applicable to the data (Figure 5.4.21c, Table 5.4.11).

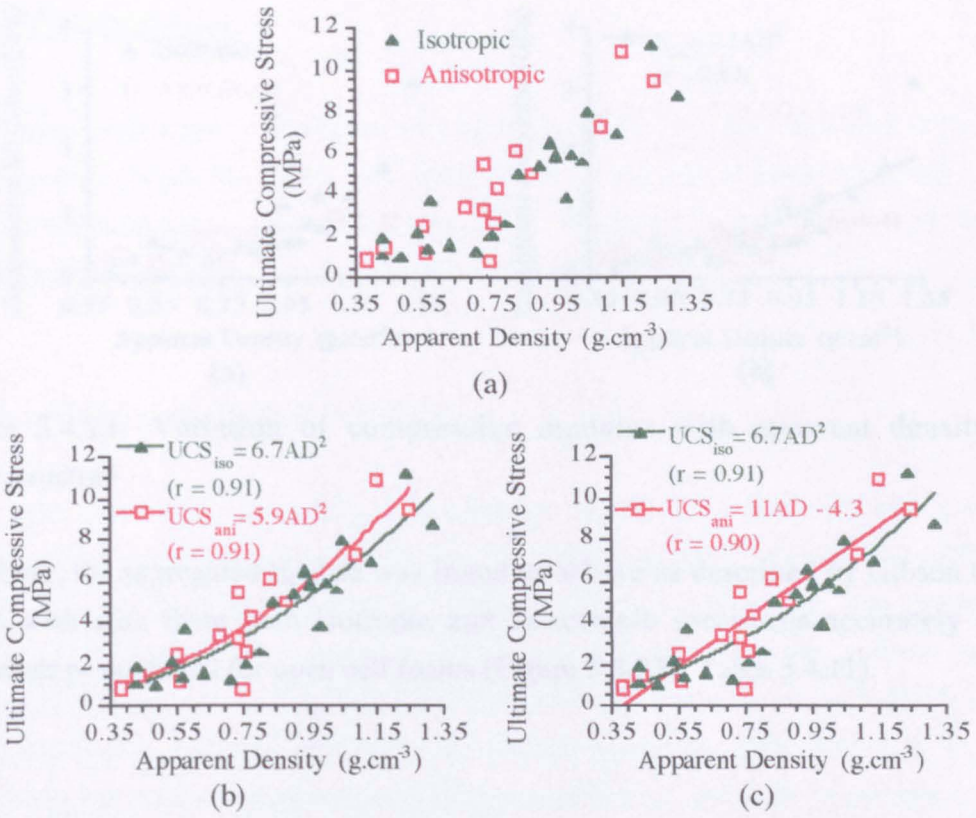

Figure 5.4.21 Variation of ultimate compressive stress with apparent density and macrostructure

The compressive modulus (E_c) was also found to be strongly related to the apparent density (Figure 5.4.22). As with the UCS the relationship between E_c and apparent density could be accurately described by a quadratic relationship, as predicted by Gibson (1985; 1988) for an isotropic open foam.

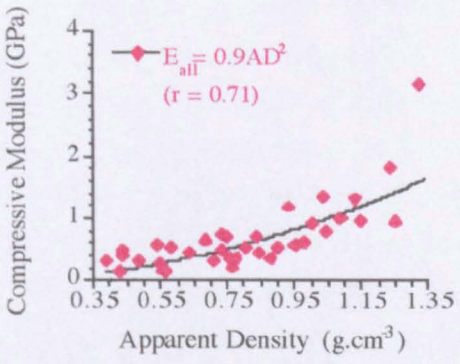

Figure 5.4.22 Variation of compressive modulus with apparent density

However, unlike the UCS, the effect of anisotropy on E_c was more apparent, with a trend towards a reduced value of E_c for anisotropic specimens at higher apparent densities (Figure 5.4.23a).

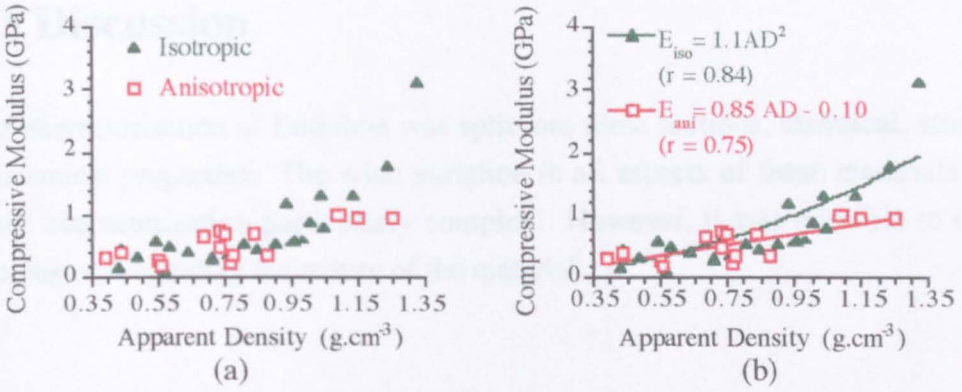

Figure 5.4.23 Variation of compressive modulus with apparent density and macrostructure

Moreover, the segregated E_c data was found to behave as described by Gibson (1985; 1988) with data from both isotropic and anisotropic specimens accurately fitting relationships predicted for open cell foams (Figure 5.4.23b, Table 5.4.11).

5.5 Discussion

The characterisation of Endobon was split into three sections, chemical, structural and mechanical properties. The wide variation in all aspects of these materials properties made characterisation particularly complex. However, it was possible to draw some conclusions regarding the nature of the material.

5.5.1 Chemical Characteristics

In order to obtain sufficiently large powder "batches" for full analysis, a number of specimens were randomly selected and crushed to provide 7 distinct powder batches, EP1-EP7. As a result of subsequent analysis it was clear that there was variation in the levels of some ionic impurities (notably aluminium and carbonate) within each batch. Only two powders were successfully refined using Rietveld analysis (EP5 and EP7), notably these powders were composed of single specimens (20x20x40 mm blocks), it is therefore possible that the pooling of specimens may have led to mixing of powders with significant enough differences to contribute to the refinement difficulties. Unfortunately as a result of the minimal amount of powder obtained from the single blocks ICP was not performed on these powder specimens.

Hydroxyapatite and bone mineral are known to accommodate a considerable range of lattice substitutions (Posner, 1969; Le Geros and Le Geros, 1993), therefore, due to the biological origin of the precursor material, it was expected that Endobon hydroxyapatite would contain some level of ionic substitution. However, the extent of ionic impurities detected were far in excess of the levels reported in the literature for commercially available and laboratory produced synthetic hydroxyapatite powders where a typical maximum level of a single ionic species is 0.3 wt% (Peelen *et al.*, 1978; Denissen *et al.*, 1980a; Driessen *et al.*, 1982). Analysis of impurity levels assessed using XRF (Table 5.4.2) and ICP (Table 5.4.3) indicated that magnesium and sodium impurities were consistently present at levels of 0.52 and 0.68 wt% respectively. These ions, which have been reported to substitute for calcium (Le Geros and Le Geros, 1993), are found in natural bone mineral and the levels of magnesium and sodium present in Endobon agree well with the reported levels of 0.44-0.55 wt% and 0.70-0.80 wt% for magnesium and sodium in bone-mineral (Mc Connel, 1973; Driessens, 1983; Aoki, 1991; Le Geros and Le Geros, 1993). Sodium substituted in the lattice is not believed to affect the dimensions of the unit cell, while magnesium substitutions have been reported to lead

to reductions in both the a and c axis length (Le Geros and Le Geros, 1993). This was not found to be true for the Endobon powders and no obvious trend was noted between the axis dimensions and the level of magnesium or sodium present (Figure 5.5.1a).

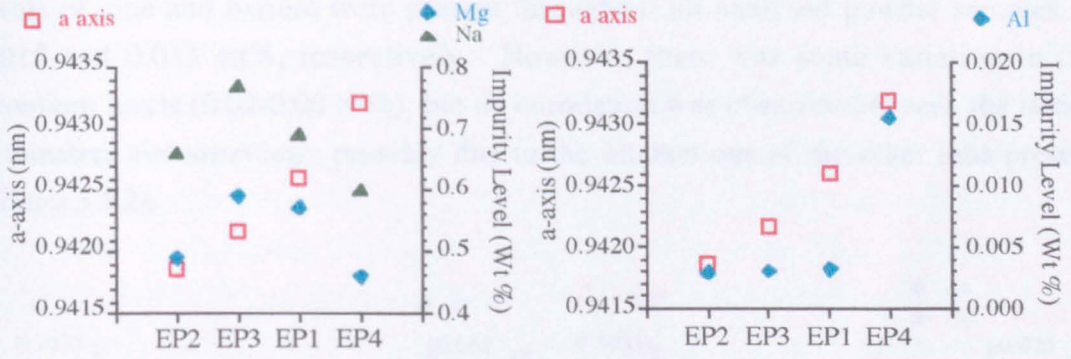

Figure 5.5.1 Variation in a-axis length with, (a) magnesium and sodium, and (b) aluminium impurity levels for powders EP1-4

Generally, the unit cell dimensions calculated from XRD data for all powders (Table 5.4.6) were shorter in the a-axis dimension and greater in the c-axis dimension than the theoretical values of 0.9423 and 0.6875 nm (JCPDS, 1980), with the exception of powders EP1 and EP4 which possessed greater dimensions in both the a and c-axis. However, a number of other cationic impurities were also detected, and in conjunction with suspected carbonate substitution, it is likely that the effects of individual ionic species were masked by the presence of other substituents, especially with such little variation in the levels of substituents from one sample to another.

Levels of alumina and silica in excess of 0.1 wt% were detected by XRF in some samples, however the variation in elemental silicon was not detected using ICP, the results of which indicated that silicon ions were present at a constant level of around 0.01%. Aluminium impurities were detected with ICP in two powder samples (EP4 and EP6) at levels of 0.016 and 0.007 %, compared with values of 0.003 % in the other samples. Aluminium ions substituted for calcium are reported to increase the length of the a-axis (Le Geros and Le Geros, 1993) and partial refinement of the XRD data for samples EP1-4 (Table 5.4.6, Figure 5.5.1b) indicated that the a-axis of EP4 (0.9432 nm) increased above the value of the other powders (0.9418-0.9426 nm). This suggests that the large variation in aluminium content was not a result of external powder contamination in powder samples EP4 and EP6, but that the aluminium present was substituted into the crystal lattice.

Traces of strontium, zinc and barium impurities were also detected (Table 5.4.3) and, as for magnesium and sodium, these ions have been reported to be present in trace quantities in bone mineral (Mc Connel, 1973; Le Geros and Le Geros, 1993). Similar levels of zinc and barium were present throughout all analysed powder samples of 0.015 and 0.013 wt%, respectively. However, there was some variation in the strontium levels (0.02-0.06 wt%), but no correlation was observed between the lattice parameters and strontium, possibly due to the interactions of the other ions present (Figure 5.5.2).

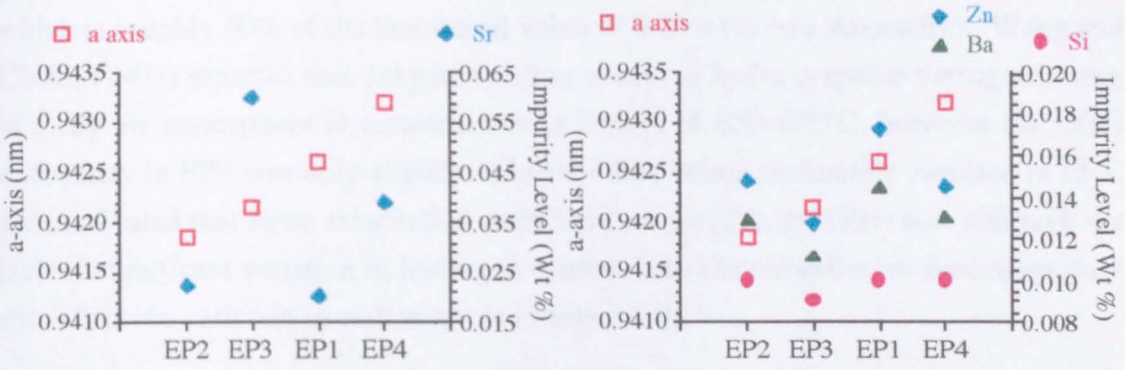

Figure 5.5.2 Variation in a-axis length with, (a) strontium, and (b) zinc, barium and silicon impurity levels for powders EP1-4.

The calcium to phosphor us ratios (Table 5.4.1), calculated from the results of the XRF analysis are all greater than the theoretical value for hydroxyapatite of 1.67. Considering the levels of ionic substituents present that are known to substitute for calcium, notably magnesium, sodium and strontium (Posner, 1969; Le Geros and Le Geros, 1993), this result suggests that there may have been considerable loss of phosphate groups. However, the presence of a small peak at 37.4° in the XRD pattern indicates that there is some CaO present, which is more likely to be the source of the elevated Ca:P ratio.

The amount of carbon detected within the Endobon powder specimens was considerably less than is normally detected in bone mineral, which has been reported at levels of 1.6 - 8 wt% (Aoki, 1991; Mc Connel, 1973; Driessens, 1980; Le Geros, 1992). This is most likely due loss of carbonate during the sintering process, which occurs at elevated temperatures in a dry air atmosphere (Knowles *et al.*, 1994; Barralet, 1995). The carbon content of powder samples EP1-4 was found to be dependent on the Ca:P ratio (Figure 5.5.3a) and the c-axis length (Figure 5.5.3b) which may indicate that Endobon-hydroxyapatite undergoes B type carbonate substitution (Le Geros *et al.*,

1968). Furthermore, the results of the successful refinement of EP7 indicated that there was considerable strain in the region of the phosphate tetrahedra, with a high value of 7.075 for the distortion index, Knowles *et al.*,(1994) reported values of 3-5 for material sintered between 1025-1225°C . However, successful refinement of EP5 determined that the O(H) occupancy was elevated (0.604 compared to a theoretical value of 0.5 (Knowles *et al.*, 1994) and 0.495 for EP7) and the distortion index was calculated as 1.89 suggesting that the region surrounding the phosphate tetrahedra is relaxed. This finding indicates that the OH site may have undergone substitution in preference to the PO_4^{3-} site. Furthermore, Hydrogen levels were stable at between 0.11-0.13 wt%, which is roughly 50% of the theoretical value of 0.20 wt% (see Appendix). Wang and Chaki, (1993) reported that dehydroxylation occurs in hydroxyapatite during sintering in a dry air atmosphere at temperatures in excess of 850-900°C, however the O(H) occupancy in EP7 was only slightly reduced while being moderately elevated in EP5. This indicated that some substitution must have occurred at the O(H) site, although the lack of significant variation in hydrogen content between the different specimens does not reflect the variation in carbon levels (Table 5.4.4).

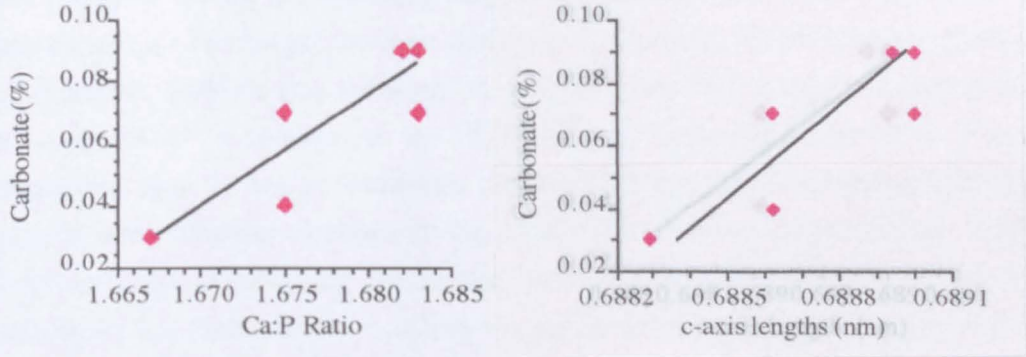

Figure 5.5.3 Variation in (a) Ca:P ratio and (b) c-axis with carbonate level for powders EP1-4

Hence, these two sets of apparently conflicting XRD refinement results suggest that both A and B type carbonate may be occurring. This conclusion is confirmed by the FT-IR spectra as the range of peaks between 1400-1550 cm^{-1} in the FT-IR spectra of EP 1-4 indicate the presence of A and B type carbonate (Figure 5.4.2). Similar behaviour has been previously reported by Vignoles (1984) and Barralet (1995) in systems with far greater levels of carbonate substitution. Vignoles proposed that B type substitution only occurred after all the A sites were filled with carbonate (requiring 4 wt% carbonate) while Barralet proposed that A and B sites were filled in equal proportions until half the A sites were filled (requiring 2.45 wt% carbonate), from this

point he suggested that only B type substitution occurred. Since B type substitution has been observed in Endobon powders with carbonate contents of 0.04-0.09 wt% Barralets' mechanism seems the most suitable for description of the current data. However, the improved definition of the B type peaks in the FT-IR spectra for EP1, EP3 and EP4 suggest that carbonate is present primarily on the type A site at very low carbonate contents (>0.05 wt%) and B type substitution only occurs in the Endobon powder with higher levels of carbon content, as it becomes energetically favourable for both types of substitution to occur simultaneously.

These results imply that during the production of Endobon from bovine cancellous bone, the natural apatite precursor was not converted to pure hydroxyapatite, but retained most of the ionic substituents found in bone mineral. The lack of significant levels of elements such as potassium might be expected as a result of the hydrothermal defatting procedure, during which some ions, weakly bound to the defective crystal surfaces, or present in the amorphous fraction of the inorganic element of bone, may have been leached out. Bone apatite is believed to be primarily B-type carbonate substituted (Le Geros and Le Geros, 1993). Loss of CO_3^{2-} from PO_4^{3-} sites is likely to have occurred during the sintering stage of production (Knowles *et al.*, 1994) and the reduced levels of hydrogen indicate that OH^- is also being lost (Wang and Chaki, 1993) it is therefore possible that substitution of CO_3^{2-} into OH^- site occurs during this stage and some CO_3^{2-} is retained in the PO_4^{3-} site. Differences in the level of carbonate substitution may be due to variations in the amount of organic material removed from material with differing densities in the hydrothermal defatting procedure. This would lead to irregular atmospheric conditions during pyrolysis and sintering, where sintering atmosphere has been shown to affect the composition of the final product (Wang and Chaki, 1993; Barralet, 1995). The variation in levels of cationic substitutions could result from natural irregularities in the mineral content of individual bones as a result of environmental changes (such as diet, lifestyle and age) within the different sources of bovine bone (Rey, 1990).

5.5.2 Structural Characteristics

5.5.2.1 Micro-Structure

Endobon was found to possess a highly crystalline structure, this is in disagreement with the findings of Saalfeld *et al.*, (1994) who proposed that Endobon contained an amorphous fraction. This was due to an increase in pH observed in water containing

Endobon specimens, which was interpreted as the dissolution of an amorphous phase from the specimens. The results of the XRD on EP1-4 indicated that there was some CaO contamination within the specimens, it is likely that the increase in pH observed by Saalfeld *et al.*, (1994) was due to the dissolution of this phase.

The grains were generally equiaxed in shape with a modal grain size of 1.35 μm. This represents a significant change from the starting material, which would have been composed predominantly of poorly bonded bone mineral, with a plate or rod like morphology, approximately 2.5-5 × 20-35 × 40-50 nm or 2.5 × 5 × 25 nm respectively (Le Geros and Le Geros 1993; Posner 1978a). The change in size and morphology can be explained by considering the high interfacial energy possessed by a ceramic with nm sized acicular grains. By increasing the grain size and changing the grain morphology to a more equiaxed shape, the internal surface to volume ratio would be reduced, so decreasing the surface energy of the body.

5.5.2.2 Micro-Porosity

Using Archimedes' principle and gas porosimetry, Endobon specimens were found to have a real density of 3.01 - 3.04 $g.cm^{-3}$, which equates to 95-96 % of the theoretical density of hydroxyapatite (3.151 $g.cm^{-3}$, Barralet 1995), i.e. 4-5 % of closed microporosity. However, inspection of etched and polished cross sections of Endobon specimens indicated that the microporosity within the struts was, on average, 18 %. It was also apparent that the porosity fell into two groups; spherical pores < 3 μm, and irregularly shaped or elliptical pores > 3 μm. The fraction of the smaller (< 3 μm) pores agreed well with the value of porosity detected using conventional methods (≈ 6%). Whereas, the fraction of the larger micro-pores was ≈ 12 %. This result indicates that the discrepancy between the direct observation and absorption techniques, results from the loss of the contribution by the larger (> 3 μm) pores. Such a result would be expected if the larger micro-pores were inter-connected with each other and the macro-porosity, leading to water intrusion within the interconnected pore network, while the smaller micro-pores would remain isolated within the ceramic struts (Smith 1994).

The location of < 3 μm pores on triple points and within grains indicates that they were formed during the sintering process, as a result of grain growth and coalescence respectively. In this case, the pores would be expected to be isolated from both each other and the external surface. Conversely, the size and alignment of the 10 μm elliptical pores suggest that these pores may be preserved osteocyte lacunae from the original microstructure of the bone, which are of a similar size, shape and distribution

in mature cancellous bone (Revell, 1986; Williams and Warwick, 1989). The irregularly shaped and randomly distributed 3-5 μm pores may be sections through preserved canaliculi, which in life provide a means of connection between the lacunae and the inter-trabecular spaces in living bone (Baud, 1968).

5.5.2.3 Macro-Porosity

Structural variation within individual bones due to the different loading conditions, and the effect of structural variation on the mechanical properies, are well documented (Wolff, 1870; 1892; Goldstein, 1987; Rice *et al.*, 1988; Hodgskinson and Currey, 1990a and b; Snyder and Hayes, 1990). Whitehouse and co-workers (1971; 1974 a and b, 1974) studied the structure of cancellous bone within the human verebra and femur and reported a series of different structural types. Similarly variation in structure from the bones of one individual to another have also been studied and found to depend on a series of interrelated parameters such as age, health, weight and activity (Currey, 1984). In order to reduce specimen variability resulting from the inherent variation in bone, Endobon blocks were screened for structural irregularity following conversion to HA and after the final product is cut from the converted blocks. However, as can be seen from Figure 5.4.3, there was still a considerable variation in the apparent density of the material. While all specimens exhibited similar basic structural characteristics to an open foam, with a three dimensional interconnecting network of struts and pores, some specimens also exhibited varying degrees of anisotropy which was particularly marked in low density specimens. This structural variation was reflected by changes in the macro-pore size, shape, orientation and connectivity.

As expected the modal value of macropore equivalent circular diameter decreased with increasing apparent density (Figure 5.4.14a), however it was also evident that the lower density Batch B specimens had a broader range of macropore equivalent circular diameters than the other batches. This result may reflect the two populations of anisotropic and isotropic pores, furthermore, the distribution of Batch B pore lengths was bi-modal (Figure 5.4.14b), while the distribution of pore breadths was mono-modal for all specimens with less variation in the modal value from batch A-B. These results indicated that a minimum modal pore size was maintained in the transverse direction for all bone structures, either isotropic or anisotropic (Figure 5.4.14c).

Anisotropy was found to be characterised by a variation in pore shape from round to elliptical, and the alignment of the long axis of the pores with respect to the long axis and transverse axis of the cylindrical specimen. More anisotropic structures possessed

pores with higher aspect ratios and more uniform alignment. The variation in the average aspect ratio throughout the batches reflected the tendency of lower density specimens to be anisotropic in structure, i.e. for pore shape to be less equiaxed. This trend was also evident in the increased average angle of pore orientation (60°), which indicated that the pores of Batch B specimens were more closely aligned with the long axis of the cylindrical specimens, as compared to Batches C and A, both of which had average orientations of 45°. When considering Wolffs law (1870; 1892), which states that bone will remodel to meet its physical requirements with the minimum safe weight, it is not surprising that the low density material tended to be anisotropic as uniaxial loading will result in the production of lower density structures than isotropic loading to the same magnitude. This phenomenon was demonstrated by Whitehouse and Dyson, (1974) in the study of trabecular structure in the human femoral head. They found that open anisotropic structures predominated in low stress regions, while denser isotropic structures developed where stresses were elevated.

The connectivity of a porous implant is believed to play an important role in encouraging tissue ingrowth (Eggli *et al.*, 1988). Both the apparent density and the anisotropy appeared to affect this parameter. In anisotropic specimens, an increase in density resulted in an increase in the thickness of struts, rather than the number of struts. Hence in this case, connectivity was more strongly affected by the degree of anisotropy than the apparent density. Conversely, in isotropic specimens, connectivity was highly influenced by apparent density, where an increase in density was reflected by an increase in the number of struts (and hence the distinct number of pores in a cross section), rather than an increase in the thickness of the struts.

5.5.3 Mechanical Characteristics

In this investigation, an exponential relationship between ultimate compressive stress (UCS) and apparent density (Ryshkewitch, 1953) gave a significantly lower R value when compared to application of a quadratic relationship, which has been proposed for isotropic open engineering foams and isotropic cancellous bone (Gibson, 1985; Gibson and Ashby, 1988; Rice *et al.*, 1988). This finding is in agreement with the findings of Duckworth (1953) who studied Ryshkewitch's relationship using a number of porous ceramic systems and reported that the relationship became inaccurate for systems with > 50% porosity. Furthermore, specimens exhibited similar behaviour to an elastic

brittle foam (Gibson and Ashby, 1988), with a linear elastic region at low strains, followed by a collapse plateau due to failure of the individual struts by brittle fracture. The ability of the data for anisotropic specimens to fit both quadratic and linear UCS relationships (5.1.21, Table 5.4.11), but to exhibit the predicted foam-like behaviour when considering the E_c, (Figure 5.4.23, Table 5.4.11), may be due to misalignment of the cell walls, and differences in cell wall thickness. From a study of specimen cross-sections, it is evident that the proportion of struts that were aligned with the long axis of the cylinder varied considerably from specimen to specimen (Figure 5.4.13), although cell walls in high density, anisotropic specimens were thicker than comparative isotropic specimens. It is also possible that a slight change in the modelled and real structure of the anisotropic structures could account for this behaviour. The two different quadratic and linear relationships proposed for isotropic and longitudinally aligned anisotropic foams were due to variations in the modelled geometry and expected deformation behaviour (Gibson and Ashby, 1988), where anisotropic structures were considered as open honeycombs with uniformly aligned cells (Figure 5.5.4a). However, in bone, the anisotropic cells range from aligned to staggered (Figure 5.5.4b) depending on the position and function of the bone.

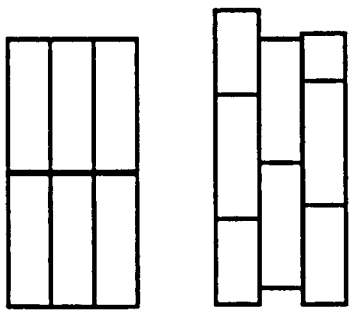

Figure 5.5.4 A simplified diagram of a longitudinal section through (a) Gibson and Ashby's model (1988) and (b) a more realistic model of anisotropic cancellous bone.

In isotropic foams, Gibson and Ashby (1988) modelled the failure mode as the brittle fracture of transverse cell edges at strut junctions, while in anisotropic specimens, failure was due to the buckling and fracture of the longitudinal cell walls. Misalignment of the cell walls from the direction of loading would result in failure of anisotropic specimens by brittle fracture of the longitudinal cell walls at junctions with transverse struts, this effect would be more pronounced in structures such as in Figure 5.5.4b and buckling would be inhibited by the staggered transverse struts. Furthermore, Gibson (1985) stated that only low density anisotropic hydroxyapatite specimens composed of thin struts would be expected to fail by buckling and fracture, as in higher

density anisotropic specimens, buckling becomes more difficult as a result of the thicker struts and failure will occur by brittle fracture initiated at defect sites on the strut surfaces and at junctions with transverse struts. Similarly, Gibson and Ashby (1988) modelled the linear elastic region in isotropic foams as the elastic bending of transverse cell edges on application of a compressive load, while in anisotropic specimens, the linear elastic region corresponded to the compression of the longitudinal cell walls when a load is applied in the longitudinal direction. The accuracy of this model will depend principally on the alignment of the longitudinal cells or pores as both models contain the longitudinally aligned struts.

CHAPTER 6

IN VITRO PERFORMANCE OF POROUS HYDROXYAPATITE

6.1 Introduction

The osteogenic nature of synthetic, dense hydroxyapatite (HA) has led to great interest in its potential as a material for the augmentation of osseous defects. The similar use of low density HA, with its highly interconnected porosity, has also been advocated, particularly in cancellous applications where its structure more closely mirrors that of its host (Holmes *et al.*, 1984). Furthermore, this structure invites the ingrowth of bone into the implant presenting a more securely fixed and integrated repair. However, although much work has been performed on the osteogenic cell response to synthetic, dense HA or HA coatings, (Best *et al.*, 1995; de Bruijn, 1993) little work appears to have been carried out on porous HA, as regards the reaction of cells to both the HA and the extensive interconnected macro-porosity. The purpose of this study was to investigate the response of human osteoblast-like cells to Endobon *in vitro*, with particular emphasis on the migration of the cells though the three dimensional porous structure.

6.2 Culture Materials

6.2.1 Porous Hydroxyapatite

Rectangular blocks of Endobon (E. Merck, Darmstadt, Germany), with a mean apparent density of 0.73 [0.11] $g.cm^{-3}$, were supplied, with a square cross section with dimensions of approximately 15-20 × 15-20 × 40-45 mm. The cross section of these blocks was cut down to a side dimension of approximately 11 mm. Slices (approximately 1.5 mm thick) were sectioned from the blocks ,using a Accutom-2 (Struers, Glasgow, UK), to produce specimens with a square cross section with dimensions of approximately 11 × 11 mm, that would fit into 24-well culture plates with circular wells of 2 cm^2 cross sectional area. Slices were then weighed using an electronic balance (Ohaus, Cambridge, UK) and the dimensions taken from an average of 3 measurements on each side using a micrometer (Table 6.2.1). After measurement, the slices were washed in de-ionised water using a Sonorex TK-30 ultrasonic bath (Bandelin, Berlin, Germany), for 3 sets of 5 minutes, with a change of water each time. Slices were then allowed to air dry, before being autoclaved at 68.95 kPa pressure for 10 minutes.

Table 6.2.1 Details of Endobon Slices

Slice ID Number	Mass (g)	Thickness (mm)	Top Surface Area (mm^2)	Apparent Density ($g.cm^{-3}$)
1	0.2464	1.87	131.0	1.00
2	0.1491	1.92	106.1	0.73
3	0.1474	1.68	132.4	0.66
4	0.1540	1.83	131.5	0.64
5	0.1323	1.59	109.3	0.76
6	0.0855	1.59	106.7	0.50
7	0.1278	1.63	133.6	0.59
8	0.1130	1.32	112.2	0.76
9	0.1162	1.10	127.9	0.82
10	0.1039	1.21	109.3	0.79
11	0.1223	1.37	125.8	0.71
12	0.1102	1.34	110.6	0.75
13	0.1313	1.30	127.8	0.80
14	0.1089	1.28	124.6	0.67
15	0.0957	1.33	104.8	0.69
16	0.0950	1.31	103.3	0.70

6.2.2 Culture Reagents

6.2.2.1 Culture Medium

All cells were cultured in 1 ml of culture media prepared by mixing the following reagents in the relevant quantities under sterile conditions at room temperature. Once combined, the medium was sterilised by filtration through 0.2 μm cellulose acetate filters (Sartorius, Sutton, UK) into sterile 20 ml bottles and stored at -20°C. This medium is hereafter referred to as DMEM+10% FCS.

Reagent	Supplier	Quantity	Comments
Dulbecco's modified Eagle's medium (DMEM)	Gibco, Paisley UK	500 ml	With 1000g.l^{-1} glucose
10% Foetal Calf Serum (FCS)	Gibco, Paisley UK	50 ml	
1 M $C_5H_{10}N_2O_3$ Solution (HEPES)	Gibco, Paisley UK	10 ml	Buffer
Non-Essential Amino acids (NEAA)	Gibco, Paisley UK	5 ml	Glutamine free
10 000 units Penicillin and 10 000 μg Streptomycin per ml Solution	Gibco, Paisley UK	5 ml	In Saline
200 mM Glutamine Solution	Gibco, Paisley UK	5 ml	In Saline
L-Ascorbate acid	Sigma, Poole UK	75 mg	

6.2.2.2 Balanced Salt Solution

Earles balanced salt solution (EBSS) was prepared by mixing the following reagents in the relevant quantities.

Reagent	Supplier	Quantity	Comments
Earles Balanced Salt Solution (EBSS)	Gibco, Paisley UK	1 Packet	$NaHCO_3$ Free
1 M $C_5H_{10}N_2O_3$ Solution (HEPES)	Gibco, Paisley UK	20 ml	Buffer
De-Ionised water		980 ml	

The reagents were combined, in a volumetric flask at room temperature and sterilised by filtration through 0.2 μm cellulose acetate filters (Sartorius, Sutton, UK) into sterile 500 ml bottles.

6.2.2.3 Phosphate Buffered Solution

Phosphate buffered solution (PBS) was prepared by dissolving one PBS tablet (Sigma, Poole, UK), in 200ml of de-ionised water. Once prepared, the PBS had a pH of 7.4 and contained 0.01 M phosphate buffer, 0.0027 M potassium chloride and 0.137 M sodium chloride. The prepared PBS was sterilised by autoclaving at 68.95 kPa pressure for 10 minutes.

6.2.2.4 Trypsin Solution

A 0.25% Trypsin solution was prepared by combining Trypsin (Sigma, Poole, UK) with PBS (prepared as above) supplemented with 20mM HEPES.

6.2.3 Cell Lines

Two types of cell source were used in this investigation. A pilot study was performed with human osteosarcoma cells (HOS TE-85), ECACC number 87070202, isolated from a tumour obtained from a 13 year old female. These cells have been shown to exhibit certain osteoblast-like characteristics (Tremollieres *et al.*, 1992; Clover and Gowen, 1994). However, the immortalised behaviour of this cell line alters some aspects of its behaviour, particularly that associated with growth regulation i.e., proliferation and alkaline phosphatase activity, which renders them unsuitable for studies into these aspects of osteoblastic function (Hassager *et al.*, 1992; Clover and Gowen, 1994). In this study passage numbers **10-12** were used.

The main investigation was conducted with primary human osteoblast-like cells (HOb) isolated from the trabecular bone of adult femoral heads, removed during total hip replacement (Di-Silvio 1995). These cells, when grown in monolayer, have been shown to form mulitlayers , on confluence, with nodular formation at approximately 21 days, and mineralization at 28 days (Di-Silvio 1995). These cells have been fully characterised and have been used without loss of phenotype upto passage 19 (Di-Silvio). In this study passage numbers **15-18** were used.

6.3 Methods

6.3.1 Culture of Cells on Porous Hydroxyapatite Slices

6.3.1.1 Sub-Culture and Passage of Cells

The cells used in this study had all been stored frozen at -176°C in a suspension of 90% foetal calf serum (FCS) and 10% dimethylsulphoxide (DMSO). In order to ensure a viable culture, cells were washed, sub cultured and passaged, before being seeded on the hydroxyapatite slices.

Frozen cells in 90% FCS, 10% DMSO were removed from the liquid nitrogen bank and thawed rapidly (in 2 minutes) to 37°C.

Immediately on thawing, the cell suspension was diluted with 5ml of DMEM + 10% FCS, pelletted by centrifugation for 5 minutes at 2000 rpm and the supernatant aspirated. 15-20 ml of fresh DMEM+10% FCS was then added to the cells (there were approximately 10^7 cells frozen in suspension), which were flushed through a Pasteur pipette to separate the cells into a homogenous single cell suspension. The cell suspension was then pipetted into a sterile 75 cm^2 square area, flat bottom culture flask (Falcon, Oxford, UK.), which was incubated in a 37°C, 5% CO_2, 95% humidity, air atmosphere.

Once the cells had proliferated to form a confluent layer on the bottom of the flask, they were harvested by trypsinisation for seeding on the porous hydroxyapatite. The DMEM+10% FCS was aspirated, 5 ml of phosphate buffered saline (PBS) was added and the flask returned to the incubator for 2 minutes. The PBS was then changed and the culture incubated for a further 2 minutes. A 2 ml solution of 0.25% Trypsin in PBS and HEPES buffer was then added and the flask gently tilted to and fro to ensure complete coverage of the cells on the bottom of the flask; any excess fluid was removed. The cells were viewed using phase contrast microscopy (Olympus, London, UK.) until they became detached. 3 ml of DMEM+10% FCS was then added immediately and the cells were removed from the flask surface using a plastic cell scraper (Falcon, Oxford, UK.). The cell suspension was flushed using a plugged Pasteur pipette in order to re-suspend the cells and any remaining cell aggregates were then removed by passing the resultant cell suspension through a 70 μm pore, cell sieve (Falcon, Oxford, UK.).

6.3.1.2 Measurement Of Cell Concentration

The volume of the final cell suspension was measured with a pipette. 50 µl of 0.4% Trypan Blue solution (Sigma, Poole, UK.) was then added to 50 µl of cell suspension. The mixture was then placed in the central chamber of the haemacytometer, which had a known volume of 10^{-4} ml. Unstained cells that appeared within the measure grid were counted (C_v) and the viable cell concentration (C_c), of the original cell suspension was given by:

$$C_c = C_v \times 2 \times 10^4 \text{ cells.ml}^{-1} \qquad 6.2.1$$

Cell viability (%) was calculated using:-

$$\text{Cell Viability} = \frac{Cv}{Ct} \times 100 \qquad 6.2.2$$

where C_t is the total number of cells (dead or alive) that appeared within the measure grid of the haemacytometer.

The original suspension was then diluted to the appropriate cell density (2×10^4, 4×10^4 or 8×10^4 cells.cm^{-2}), where a final cell concentration of 1.6×10^5 cells.ml^{-1} gave a cell density of 8×10^4 cells.cm^{-2} when plated out in a 24 well plate (wells of 2 cm^2 area, excluding cell walls). After dilution, the suspensions were flushed using a Pasteur pipette to ensure DMEM+10% FCS and cells were fully mixed before seeding of cells on hydroxyapatite slices.

6.3.1.3 Determination of Cell Density for Culture on Porous Hydroxyapatite

Human osteogenic sarcoma (HOS TE-85) cells were re-suspended in DMEM + 10% FCS at cell concentrations of 4×10^4, 8×10^4 and 1.6×10^5 cells.ml^{-1}. Six Endobon slices were placed in circular tissue culture wells (Falcon, Oxford, UK.) with a surface area of 2 cm^2 and 1 ml of cell suspension was added to each slice. Two slices were seeded with each concentration to produce cultures with starting cell densities as indicated in Table 6.3.1. Slices of each cell density were incubated for 24 hours and 72 hours in a 37°C, 5% CO_2, 95% humidity air atmosphere. After culture, cells were prepared for scanning electron microscopy.

Table 6.3.1 Details of specimens cultured with HOS cells

Slice ID Number	2	5	8	13	11	12
Time *in vitro* (Days)	1	1	1	3	3	3
Cell Density (cells.cm^{-2})	2×10^4	4×10^4	8×10^4	2×10^4	4×10^4	8×10^4

6.3.1.4 Culture of Human Osteoblast-like Cells on Porous Hydroxyapatite

Human osteoblast-like (HOb) cells were cultured in DMEM + 10% FCS. Ten Endobon (E. Merck, Darmstadt, Germany) slices were placed in circular tissue culture wells (Falcon, Oxford, UK) with a surface area of 2 cm^2. A cell suspension was prepared with a concentration of $1.6x10^5$ cells.ml^{-1}, 1ml of which was added to each well. Cells were incubated on the slices as indicated in Table 6.3.2, in a 37°C, 5% CO_2, 95% humidity air atmosphere. The culture medium was changed every 2-3 days. After culture, cells were prepared for light microscopy and scanning and transmission electron microscopy.

Table 6.3.2 Details of specimens cultured with HOb cells

Slice ID Numbers	1 & 3	4 & 6	7 & 9	10 & 14	15 & 16
Time *in vitro* (Days)	1	4	7	14	21
Cell Density (cells.cm^{-2})	$8x10^4$	$8x10^4$	$8x10^4$	$8x10^4$	$8x10^4$

6.3.1.5 Fixing of Cultures

A 1.5% solution of glutaraldehyde (Robinson and Gray 1990a, Sabatini *et al.*, 1963) buffered in 0.1 M sodium cacodylate (pH 7.2-7.4) was used to primary fix all cultures. The buffer was produced in a 0.2 M strength by dissolving 4.28g of sodium cacodylate (Agar, UK.) in 100 ml of de-ionised water and adding 12.5 M hydrochloric acid (BDH, Poole, UK.) drop-wise to the solution until the pH was lowered to between 7.2 and 7.4. A 3 % solution fixative was produced by the dilution of 25% glutaraldehyde (Agar, UK.) with de-ionised water. These reagents were prepared in advance and stored at 4°C. The buffered fixative was then made up as required by mixing equal volumes of 0.2 M sodium cacodylate buffer with 3% glutaraldehyde solution to produce a 1.5% glutaraldehyde buffered in 0.1 M sodium cacodylate (pH 7.2-7.4). Care was taken to ensure that the mixture had warmed up to room temperature before use (Robinson and Gray 1990a).

Primary Fixation

The cultures were transferred to a new well of the 24 well plate (Falcon, Oxford, UK.) taking care to keep the slices "cell side up". 1ml of EBSS was carefully pipetted down the side of each well [not directly on the slices] and the plate replaced in the incubator for five minutes. This process was repeated a total of three times. The EBSS was aspirated and replaced with 2 ml of 1.5% glutaraldehyde, buffered in 0.1 M sodium cacodylate (pH 7.2-7.4). The cultures were fixed for 3 hours at room temperature, after

which the fixative was removed and replaced with 1ml of 0.1 M sodium cacodylate buffer (pH 7.2-7.4). At this stage the under sides of the specimens were marked with a soft lead pencil for future reference. The specimens were then stored overnight at 4°C and one whole slice from each time point was processed for scanning electron microscopy (SEM). The second slice was divided in two, one half processed for transmission electron microscopy (TEM) and the other for light microscopy (LM).

6.3.2 Scanning Electron Microscopy

6.3.2.1 Preparation for Scanning Electron Microscopy

After primary fixation, cultures were washed twice in 0.1 M sodium cacodylate buffer (pH 7.2-7.4) and dehydrated using a graded alcohol series (30%, 40%, 50%, 60%, 70%, 90% and 96% industrial methylated spirits (BDH, Poole, UK.)) with three changes at 100 % ethyl alcohol (BDH, Poole UK) containing Na_2SO_4 (BDH, Poole, UK.). Specimens were transferred to glass jars, and washed twice as before, but in 100% acetone (BDH, Poole UK).

Specimens were desiccated using a Balzers CO_2 critical point dryer (Milton Keynes, UK.). The temperature of the critical point dryer chamber was then cooled to 17°C and pressurised before slowly replacing the air within the chamber with CO_2. When this proce dure was complete, the acetone was carefully drained off, making sure to keep the meniscus between the gaseous and liquid CO_2 above the slices in the specimen boat. Once all the acetone had been drained, the chamber was isolated for 45 minutes. The gas was then vented off and the chamber resealed. The temperature was then raised at a rate of 6°C.min^{-1} to 42°C. The pressure was then reduced by slowly venting the CO_2 from the chamber. The specimens were then removed, mounted on SEM stubs with the use of carbon tabs (Agar, UK.) and sputter coated with gold for a period of 2-6 minutes using a Balzers High Vacuum sputter coater (Milton Keynes, UK.).

6.3.2.2 Scanning Electron Microscopy of Cultures

This examination was performed using a JOEL WINSEM 6300 series field emission electron microscope, which enabled the use of low accelerating voltages (typically 1-5 keV), minimising the damage to the cells. Micrographs were taken at magnifications of × 20, to 3000 using Ilford FP4 Plus, 120 film (Agar, UK).

6.3.3. Transmission Electron Microscopy

6.3.3.1 Preparation for Transmission Electron Microscopy

Specimens for TEM were fixed as described in section 6.3.1.5 and stored at 4°C. Post-fixation was carried out directly before dehydration and processing through to resin.

Post-Fixation of cultures for TEM

The cultures were washed twice in 0.1 M sodium cacodylate buffer (pH 7.2-7.4) and then subsequently post fixed in 2 ml of a 1% osmium tetroxide solution (Agar, U.K.) buffered with 0.1 M sodium cacodylate (pH 7.2-7.4), which was carefully pipetted down the side of the well, and left for 1 hour at room temperature. The cultures were then washed twice in 2 ml of de-ionised water.

Processing Through to Resin for TEM

Specimens for TEM were dehydrated using a graded alcohol series (70%, 90% and 96% industrial methylated spirits (BDH, Poole, UK.)) with three changes at 100 % ethyl alcohol (BDH, Poole UK), dehydrated with Na_2SO_4 (BDH, Poole, UK). Specimens were transferred to glass jars and allowed to incubate for a further 30 minutes in 100% ethyl alcohol (BDH, Poole UK) at room temperature. An epoxy resin was prepared, based on a recipe proposed by Spurr (1969) but modified (Kayser, 1995) to increase hardness and pot life (Table 6.3.3).

Table 6.3.3 Embedding resin modifications.

Ingredient	Standard Recipe (g)	Modified Recipe (g)
Vinyl Cyclohexene Dioxide (ERL - 4206)	10	10
Diglycidyl Ether of Polypropylene Glycol (DER 736)	6	4
Nonenyl Succinic Anhydride (NSA)	26	26
Dimethylaminoethanol (S-1)	0.4	0.2

After 30 minutes the absolute ethanol was aspirated and a 1:1 mixture of the modified Spurr's resin and 100% ethyl alcohol (BDH, Poole UK) was introduced. The specimens were left uncovered overnight in a specimen rotator which allowed the alcohol to evaporate. The resin was aspirated and replaced with fresh resin which was allowed to infiltrate the specimens for a further 24-72 hours. Disposable embedding moulds (Agar, UK.) were prepared by filling a third of the mould with resin and allowing the resin to cure at 60°C for 18 hours. The specimens were placed in the moulds, cell side up, on the pre-cured resin (Figure 6.3.1a), vacuum infiltrated for 3 hours with fresh resin and cured at 60°C for a minimum of 18 hours.

Preparation of Resin Blocks for Microtomy

Once hardened (Figure 6.3.1b), blocks were sawed in the longitudinal direction of the specimen (Figure 6.3.1c), into 0.5 mm thick sections. The sections were then trimmed using a razor blade and cut into 2-3 mm square fragments, such that each fragment contained a piece of cultured porous hydroxyapatite slice (Figure 6.3.1d). At this point, some fragments were additionally treated with a 50% aqueous solution of orthophosphoric acid for 30-60 minutes, in order to dissolve the ceramic,thereby improving the sectioning properties of the fragment (Figure 6.3.1e). All fragments were washed in de-ionised water in an ultrasonic bath and cleaned with polypropylene. A few drops of fresh resin were pipetted into clean polyethylene capsules, taking care to ensure no air bubbles were introduced. The fragments were transferred to the capsule and allowed to sink to the bottom with the cultured surfaces oriented perpendicular to the axis of the capsule (Figure 6.3.1f). More resin was added until the capsules were two-thirds full and the whole assembly placed under vacuum for 2 hours before being placed, uncapped, in an oven at 60°C for at least 18 hours to cure.

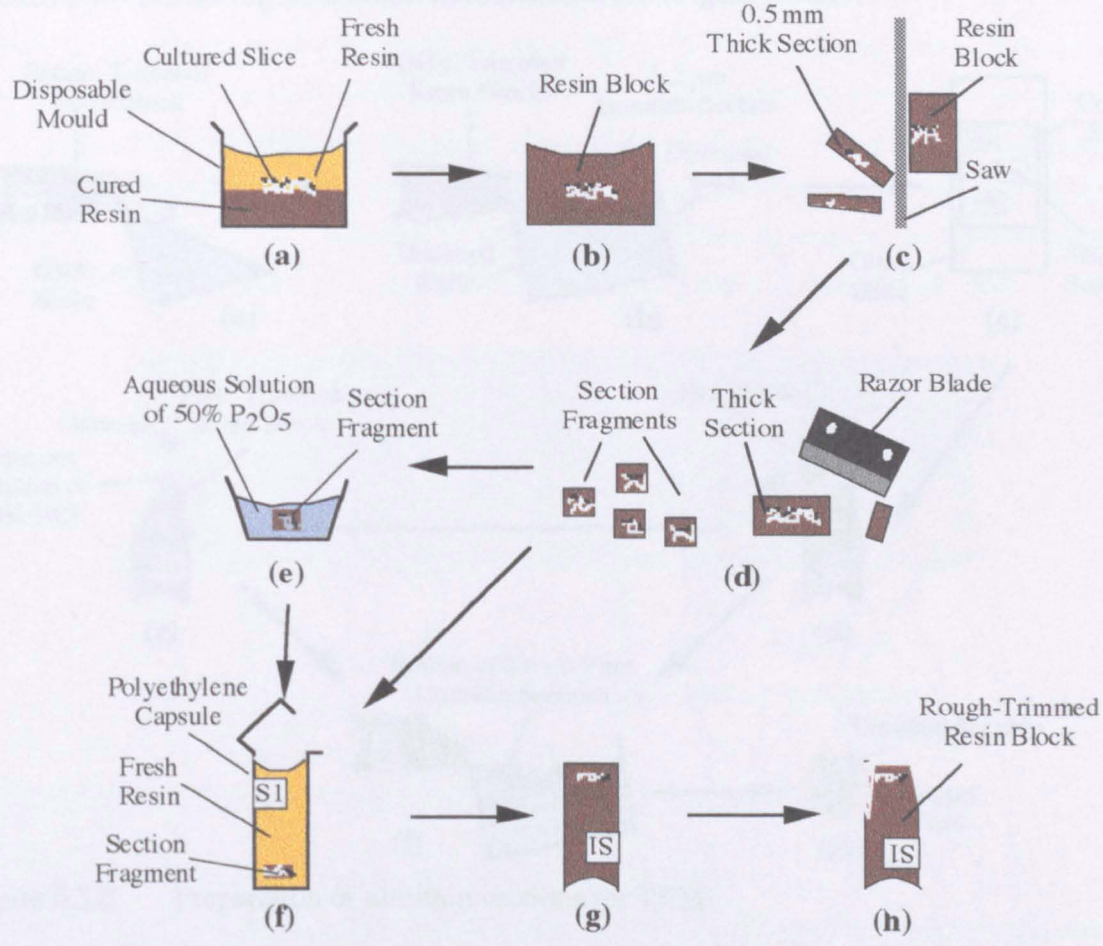

Figure 6.3.1 Embedding of slices and preparation of resin blocks for microtomy.

The hardened, cylindrical blocks were then trimmed down with a hack saw (Figure 6.3.1g) and if necessary further trimming was performed with a razor blade. The blocks were then ready for thin sectioning with an ultramicrotome (Figure 6.3.1h).

Preparation of ultra-thin sections for TEM

The blocks were mounted on a LKB Ultratome III (LKB, Sweden) and the ceramic exposed by sectioning the resin with a glass knife. Once the surface of the ceramic had been exposed (indicated by shattering of the glass blade), a Diatome diamond knife (Reichert, UK) was fitted and 1-2 μm "semi-thin" sections made. The sections were floated out on de-ionised water (Figure 6.3.2b), collected and transferred to drops of water on glass slides and placed on a hot plate at 60-70°C. As the water evaporated, the sections spread and adhered to the slide, once dry they were then stained with a 1% Toluidine Blue solution (Raymond A Lamb, London, UK.) in 1% Borax (BDH, Poole, UK.) (pH 11) at, 60-70°C. After 3-5 minutes excess stain was rinsed off and the sections were allowed to dry. Samples were then mounted in Canada balsam (Agar, UK.) prior to viewing with bright field illumination (Figure 6.3.2c).

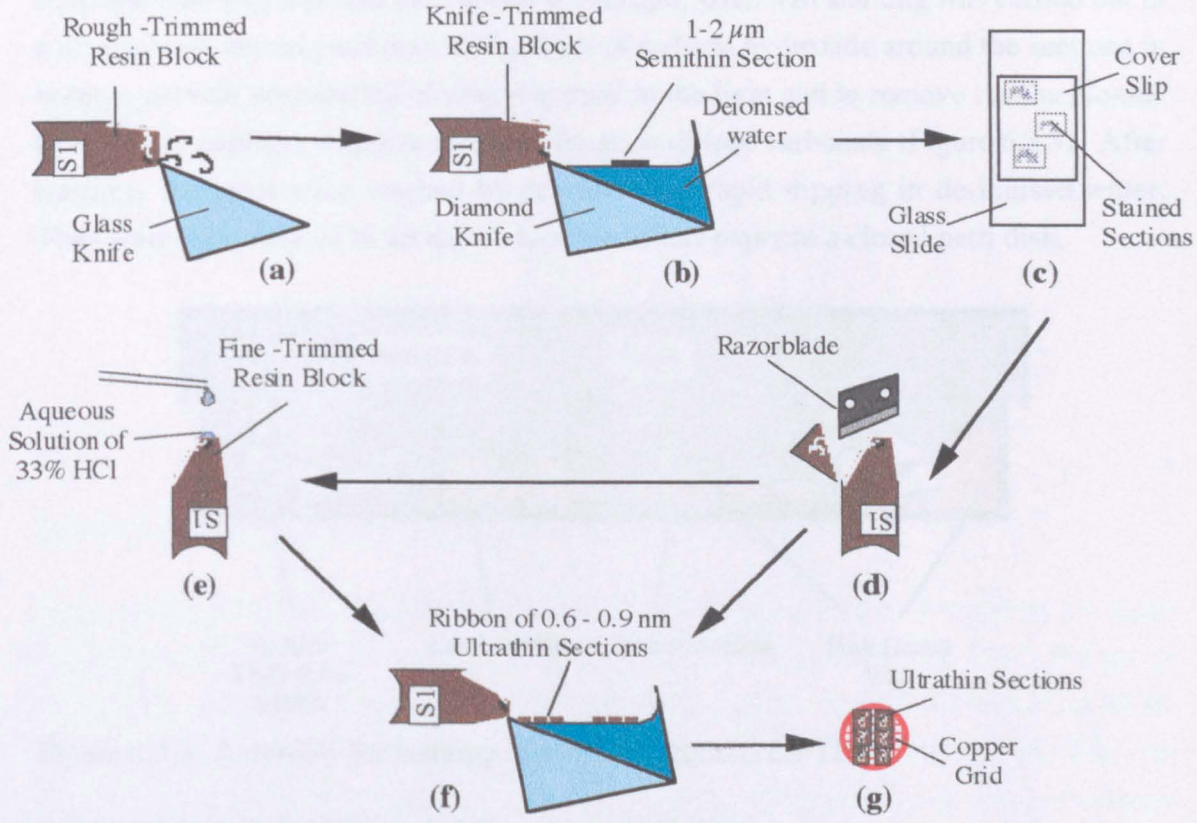

Figure 6.3.2 Preparation of ultrathin sections for TEM.

Once an area of interest had been identified, each block was trimmed using a razor blade to between 0.1-0.5 mm^2 to enable high quality sections to be obtained. After

levelling of the surface, "ultra-thin" (60-90 nm) sections either were cut directly from razor blade-trimmed sections (Figure 6.3.2.f), or in certain instances,some of the razor blade-trimmed blocks containing fragments that had not been treated with orthophosphoric acid during block preparation (Figure 6.3.1e), were surface-treated with a drop of 33% hydrochloric acid solution for 1-2 minutes to remove the ceramic to a depth of 1-2 μm (Figure 6.3.2e). Sectioning of fragment-treated and surface-treated blocks was much smoother than ceramic containing blocks. Ribbons of sections were produced rather than single sections, which were much easier to handle. As with "semi-thin" sections, the "ultra-thin" sections were compressed during cutting, this was remedied by grouping ribbons with a hair probe, and then expanding the sections by exposing them to chloroform vapour. The ribbons or single sections were collected on cleaned copper grids that were covered with a support film and the assembly placed ribbon side up on clean,hardened filter paper in a petri dish to dry. The sections were double stained (Echlin, 1964) first with 2% aqueous uranyl acetate (BDH, Poole, UK.) for 10 minutes and then with Reynolds' lead citrate for a further 10 minutes (Reynolds, 1963). Staining was achieved by floating the grids specimen side down on drops of stain that had been pipetted onto dental wax (Agar, UK). All staining was carried out in a blacked out, closed petri dish with pellets of sodium hydroxide around the sections in order to prevent degradation of uranyl acetate in the light and to remove carbon dioxide from the atmosphere, so preventing precipitation of lead carbonate (Figure 6.3.3). After staining, the grids were washed by repeated and rapid dipping in de-ionised water. They were then allowed to air dry on hardened filter paper in a closed petri dish.

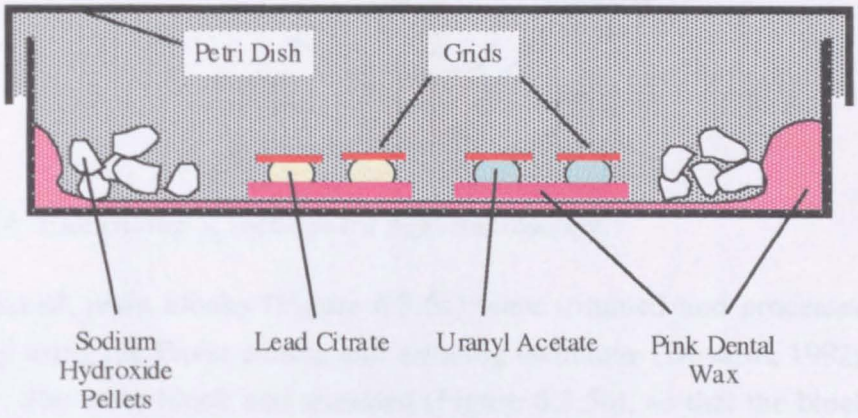

Figure 6.3.3 Assembly for staining of ultrathin sections for TEM.

6.3.3.2 Transmission Electron Microscopy of Cultures

This was performed on a Philips TEM-CM12 transmission electron microscope using an accelerating voltage of 80 keV. Micrographs were taken at magnifications of $\times$3000 to 30 000 using Kodak 4489 EM film (Agar, UK)

6.3.4 Light Microscopy

6.3.4.1 Preparation for Light Microscopy

After primary fixation, cultures were washed twice in 0.1 M sodium cacodylate buffer (pH 7.2-7.4) and dehydrated using a graded alcohol series (70%, 90% and 96% industrial methylated spirits (BDH, Poole, UK.)) with three changes at 100 % ethyl alcohol (BDH, Poole UK), dehydrated with Na_2SO_4 (BDH, Poole, UK.). Specimens were transferred to glass jars and allowed to incubate for a further 30 minutes in 100% ethyl alcohol (BDH, Poole UK) at room temperature. The ethanol was then aspirated, replaced with hard grade London White resin (LR Co. Basingstoke, UK) and the specimens infiltrated overnight. The resin was changed and the specimens left to infiltrate for a further 24 hours. Disposable embedding moulds (Agar, UK.) were prepared by mixing 1-2 drops of hard grade LR White accelerator, (LR Co. Basingstoke, UK) with 10 ml of hard grade LR White resin, and then filling a third of each of the moulds with the mixture and allowing it to cure. The slices were removed from the resin in which they had been infiltrated and placed in the prepared moulds on the pre-cured resin, cell side up. 20 ml of fresh hard grade LR White resin was mixed with 3 drops of hard grade LR White accelerator and added to the moulds. Hardening took approximately 5-10 minutes and was carried out on ice to protect the cultures as the reaction was highly exothermic (Figure 6.3.4).

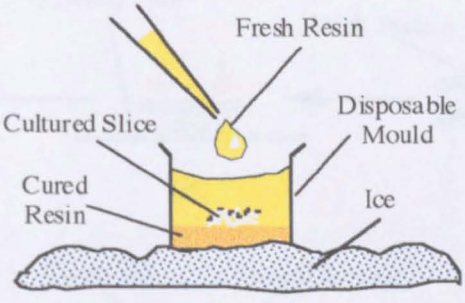

Figure 6.3.4 Embedding of sections for light microscopy.

Once hardened, resin blocks (Figure 6.3.5a) were trimmed and processed for light microscopy using the Exakt cutting and grinding technique (Donarth, 1982; Rohrer *et al.*, 1992). The resin block was trimmed (Figure 6.3.5b), so that the block could be sectioned transversely with an Exakt diamond band saw (Medenex, Bath UK.) to produce thick (100-200 μm) plane parallel sections (Figure 6.3.5c) and the section thickness measured with a micrometer. The sections were mounted with Technovit 7210 VCL precision adhesive (Medenex, Bath UK.) on Plexiglas slides (Medenex, Bath UK.) with the use of an Exakt vacuum-adhesive system (Medenex, Bath UK.), which ensured plane parallelism between the bonded and top surfaces of the section (Figure

6.3.5d). After polymerisation of the glue by blue wavelength light, the combined slide, glue and section thickness was measured and the slide and glue thickness calculated. The slides were placed in an Exakt microgrinding system (Medenex, Bath UK.), consisting of a vacuum attachment that retained the slide, adjustable weights which controlled the grinding pressure and a water lubricated, diamond coated, circular grinding plate (Figure 6.3.5e). Adjustment of a micrometer attached to gold contact points allowed grinding to be stopped when the section had reached a predetermined thickness (calculated from the measured section thickness and the slide+glue thickness). Finer grinding was achieved with a series of polishing papers beginning with 800 grit (Medenex, Bath UK.) which has an average particle size of 22 μm and finishing with 4000 grit (Medenex, Bath UK.), which has an average particle size of 5 μm (Figure 6.3.5f). Fine grinding was usually complete when sections had reached a thickness of 10-20 μm. Sections were stained with a 1% Toluidine Blue (Sigma, Poole UK.) solution in 1% Borax (Sigma, Poole UK.) (Figure 6.3.5.g).

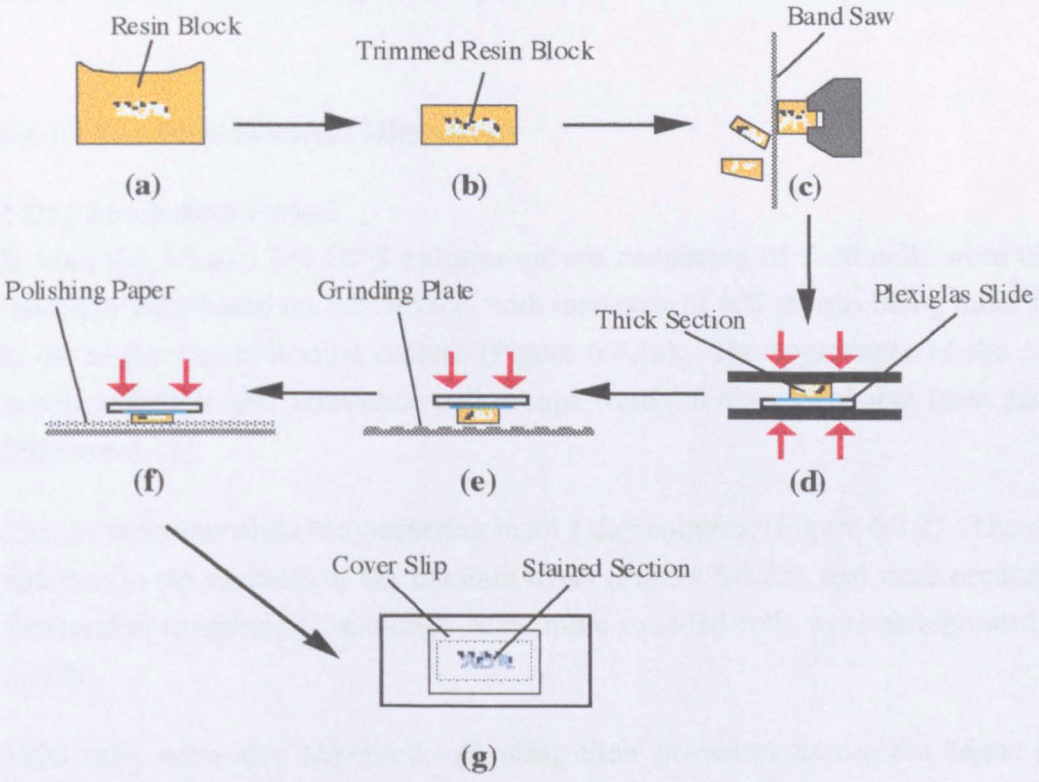

Figure 6.3.5 Preparation of sections for light microscopy.

6.3.4.2 Light Microscopy of Cultures

This was performed on a Zeiss Axioskop microscope (Carl Zeiss, Oberkochen LTD. Welwyn Garden City, UK) with a transmitted light source. Micrographs were taken at magnifications of × 50 to 400.

6.4 Results

6.4.1 Culture Trials with Human Osteoblast Sarcoma Cells

Human Osteoblast Sarcoma (HOS) cells were successfully raised at concentrations of 4.0×10^4, 8.0×10^4 and 1.6×10^5 cell.ml^{-1} on porous hydroxyapatite slices for periods of 1 and 3 days (Table 6.4.1), with no instances of infection (or accelerated cell death) at either time point. Toxic response was not observed.

Time *In Vitro* (Days)	Cell Densities (cell.cm^{-2}) 2×10^4	4×10^4	8×10^4
1	1/2 HOS	1/4 HOS	1/8 HOS
3	3/2 HOS	3/4 HOS	3/8 HOS

Table 6.4.1 HOS culture specimen parameters.

6.4.1.1 Scanning Electron Microscopy

1 Day Incubation Period

In both the 1/2 and 1/4 HOS cultures groups consisting of 5-20 cells were observed randomly distributed on the surface, with instances of cell groups being more frequent in the higher concentration culture (Figure 6.4.1a). The appearance of the 1/8 HOS culture varied in that individual cell groups were not distinguishable from each other (Figure 6.4.1b).

Cell division was observed occurring in all 1 day cultures, (Figure 6.4.2). The cells had attached to the surfaces of the ceramic struts (Figure 6.4.2a), and were predominantly flattened in morphology, although some more rounded cells were also present (Figure 6.4.2b).

HOS cells were also observed extending their processes across the edges of some macropores (Figure 6.4.3a) and appeared to be bridging some of the smaller (50-100μm) macropores (Figure 6.4.3b).

The cells appeared to adhere in preference on the un-machined, smoother macropore surfaces rather than the cut surfaces of the hydroxyapatite slice which were almost uninhabited by cells (Figure 6.4.4a).

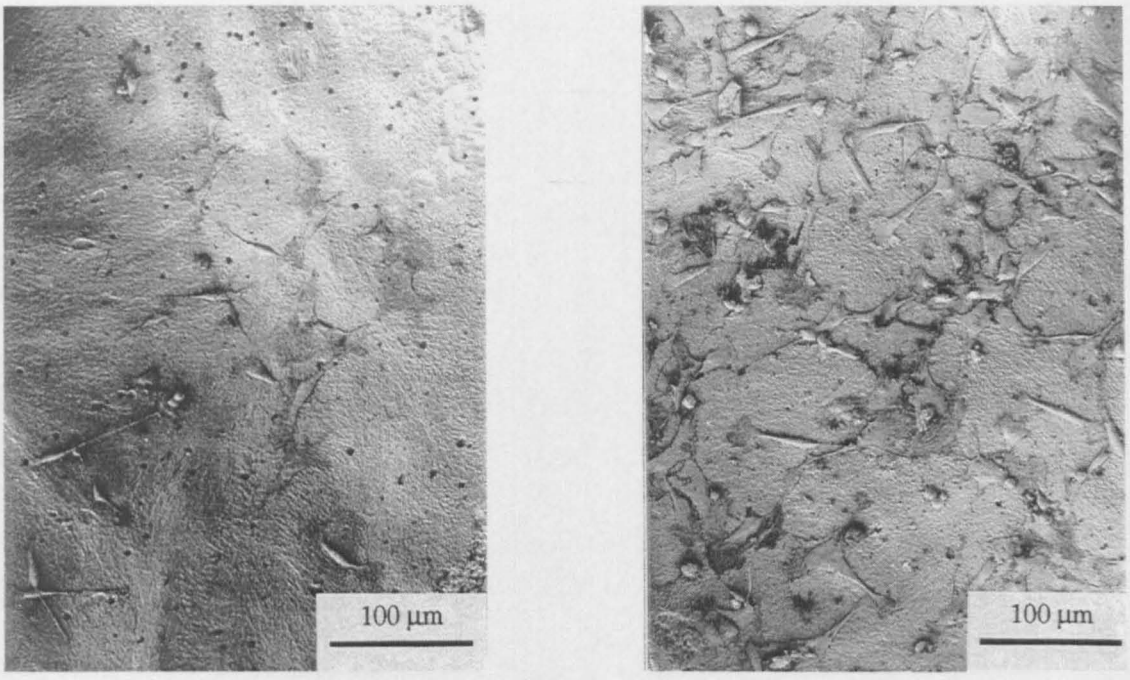

(a) (b)

Figure 6.4.1 Distribution of cells on: (a) 1/2 HOS and (b) 1/8 HOS cultures.

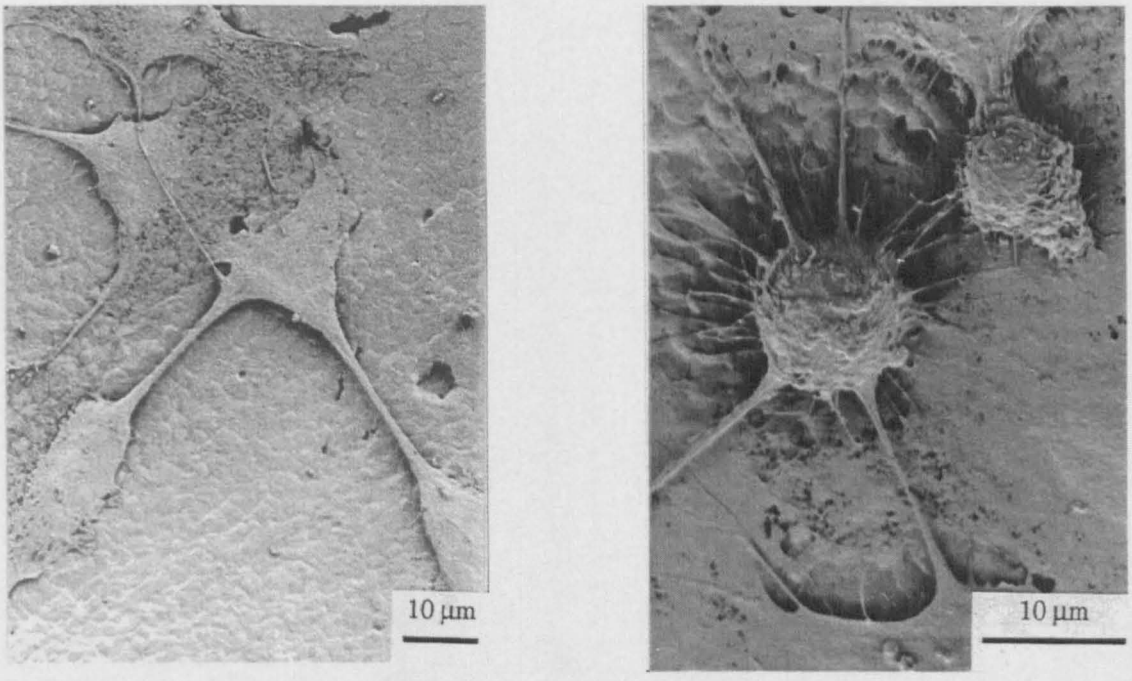

(a) (b)

Figure 6.4.2 Dividing HOS cells after 1 day *in vitro* demonstrating: (a) Flattened and (b) rounded morphologies.

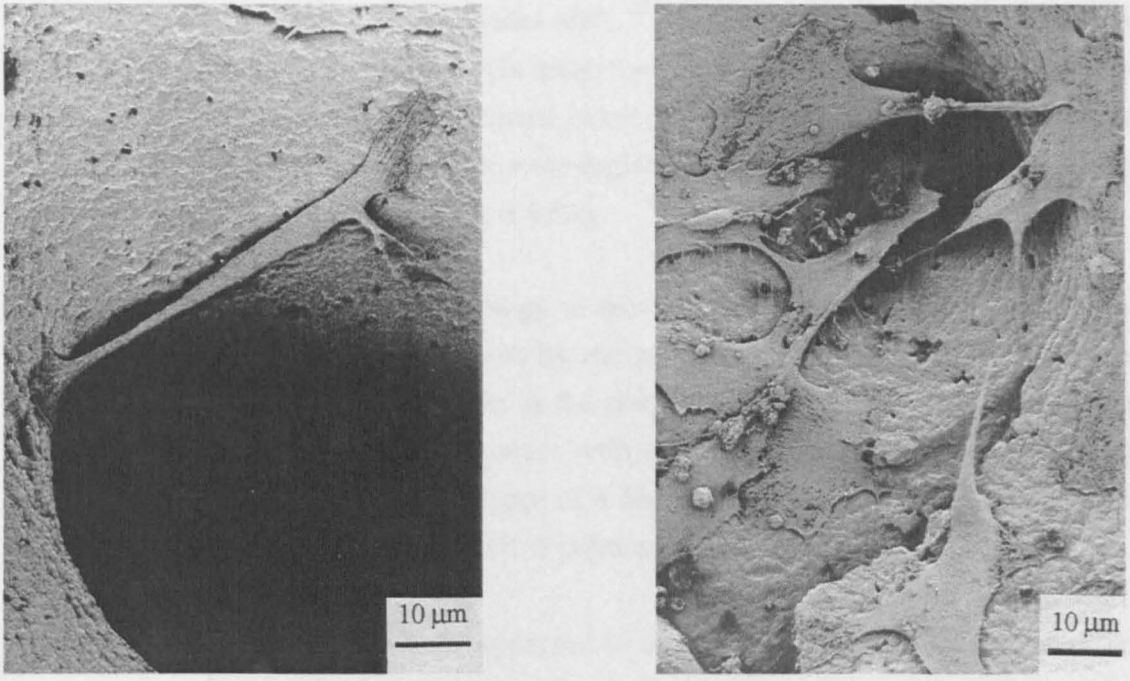

(a) (b)

Figure 6.4.3 HOS cells after 1 day in culture: (a) Single cell bridging and (b) a group of cells invading small macropores.

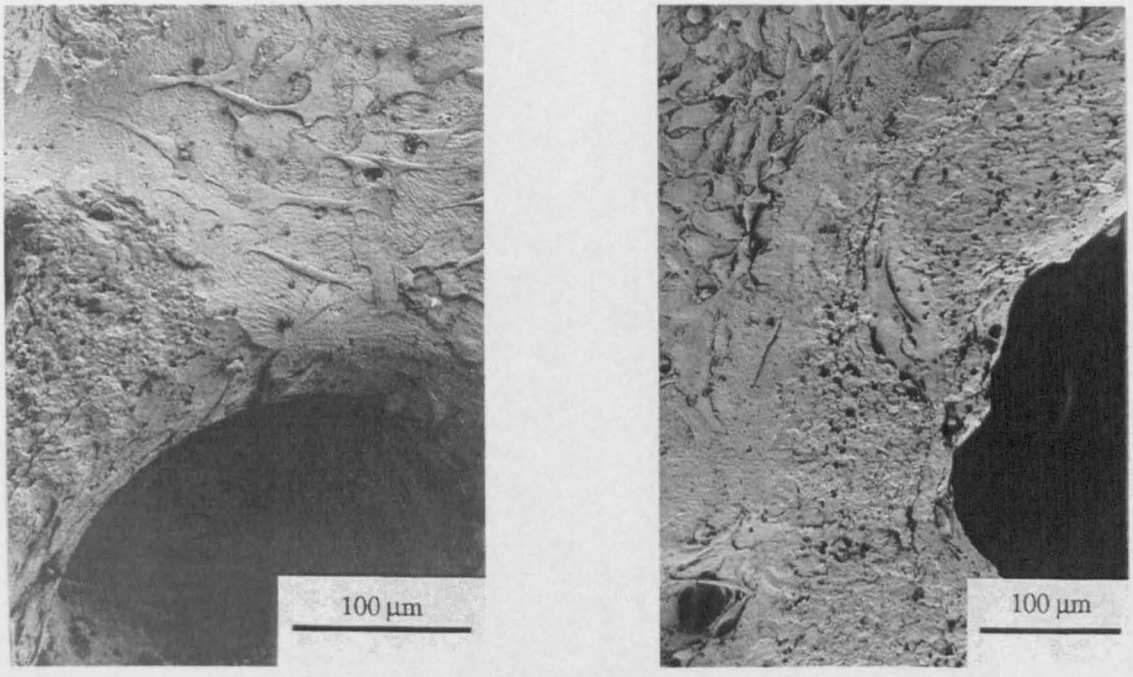

(a) (b)

Figure 6.4.4 HOS cells demonstrating a preference for the smoother pore surfaces after incubation for: (a) 1 day and (b) 3 days.

3 Day Incubation Period

Considerable cell division was evident after 3 days incubation, cells had achieved mono-layer confluency over the visible macropore surfaces in the 3/8 HOS culture and appeared to be migrating into the internal pores (Figure 6.4.5b). However, in both the 3/2 and 3/4 HOS cultures, there were some regions in which the substrate could still be clearly seen beneath the cells (Figure 6.4.5a).

There was a variation in the morphology of the cells in 3 day cultures. Non-confluent cells, "isolated" from their neighbours by the substrate in 3/2 and 3/4 HOS cultures were flattened (Figure 6.4.6a), while in the confluent regions present in all cultures, where cells were in continuous contact with each other, cells were more usually rounded. Moreover, there was evidence of a fibrous extra-cellular substance in some particularly dense regions of the 3/8 HOS culture (Figure 6.4.6b).

As in the 1 day cultures the cells appeared to adhere in preference on the smoother macropore surfaces, this phenomenon was more pronounced as a result of the contrast in appearance between the highly populated macropore surfaces and the cut edges (Figure 6.4.4b).

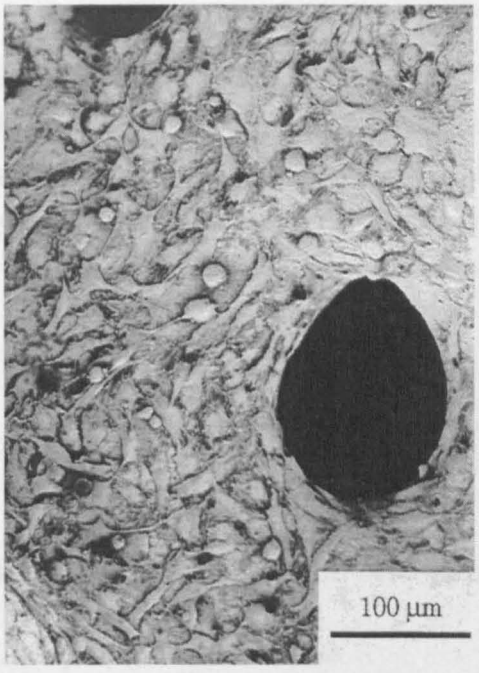

(a)

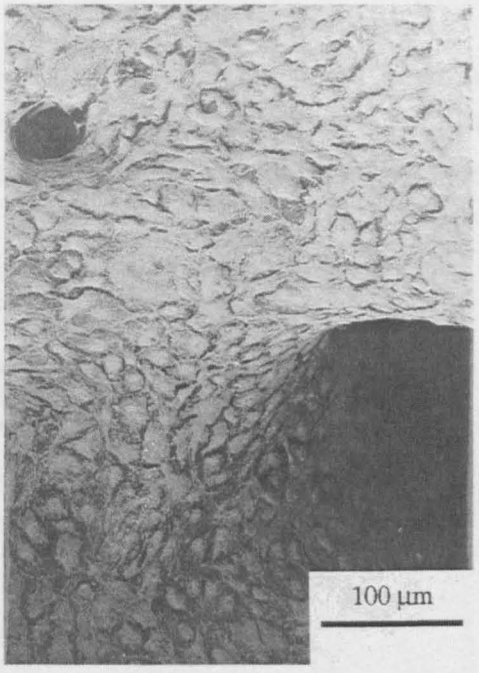

(b)

Figure 6.4.5 Distribution of cells on: (a) 3/4 HOS and (b) 3/8 HOS cultures.

(a)

(b)

Figure 6.4.6 Variation in cell morphology (a) 3/4 HOS and (b) 3/8 HOS cultures.

6.4.2 Culture of Human Osteoblast Cells

Human Osteoblast (HOb) cells were successfully incubated on all porous hydroxyapatite slices at a concentration of 1.6×10^5 cell ml^{-1} for periods of 1, 4, 7, 14 and 21 days with no instances of infection (or accelerated cell death) at either time points. Toxic response was not observed.

Cell Density.	Time *In Vitro* (Days)				
(cell.cm^{-2})	1	4	7	14	21
8×10^4	1/8 HOb	4/8 HOb	7/8 HOb	14/8 HOb	21/8 HOb

Table 6.4.2 HOb culture specimen parameters.

6.4.2.1 Scanning Electron Microscopy

1 Day Incubation Period

Observations for 1/8 HOb cells were identical to that of the 1/8 HOS cells, cells were evenly distributed over the smooth pore surfaces (Figure 6.4.7a) and had a flattened morphology (Figure 6.4.7b).

4 Day Incubation Period

Observations for 4/8 HOb cells were similar to that of the 3/8 HOS cells, with formation of confluent mono-layers and migration of cells into the porous structure (Figure 6.4.8a). However, unlike HOS cells some areas of surface ceramic were still visible allowing the close contact between the cells and macropore surface to be studied. There appeared to be a diffuse organic deposit associated with the ceramic surfaces in close proximity to cells and cell processes (Figure 6.4.8b). Extra-cellular matrix was observed in proximity to cells throughout the culture (Figure 6.4.9a), as was the production of vesicle-like spheroids (Figure 6.4.9b). Cells also appeared to be colonising the rough surfaces of some of the machined edges, where they demonstrated a preference for rough surfaces with crevices (Figure 6.4.9c).

7 Day Incubation Period

Globular deposits, associated with the extra-cellular matrix were detected in the 7/8 HOb cell cultures (Figure 6.4.9.d). These cultures exhibited confluent multi-layers of cells on the uppermost smooth pore surfaces, and in-filling of smaller macropores and the formation of sheets of confluent cells was observed (Figure 6.4.10a). These sheets (Figure 6.4.10b) bridged the larger macropores, a process hereafter referred to as capping.

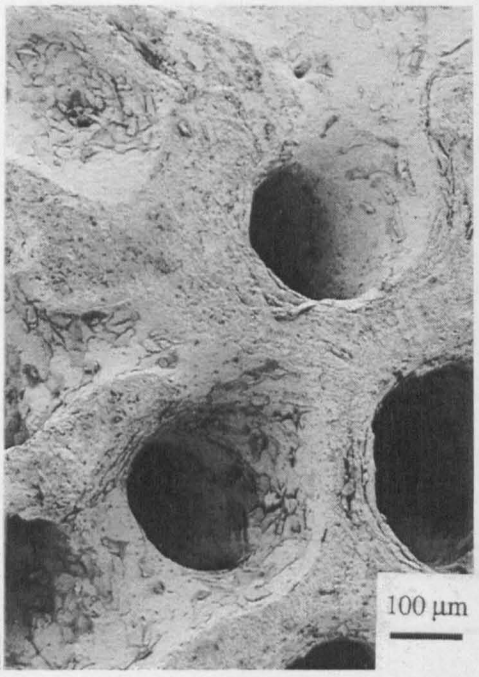

(a)

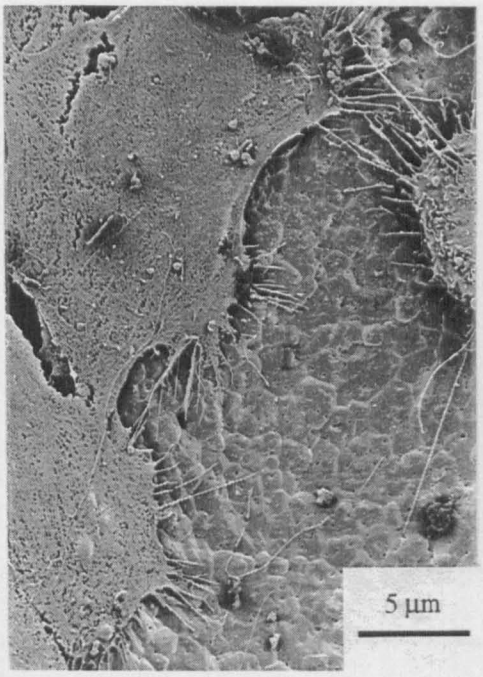

(b)

Figure 6.4.7 (a) Distribution and (b) morphology of 1/8 HOb cells.

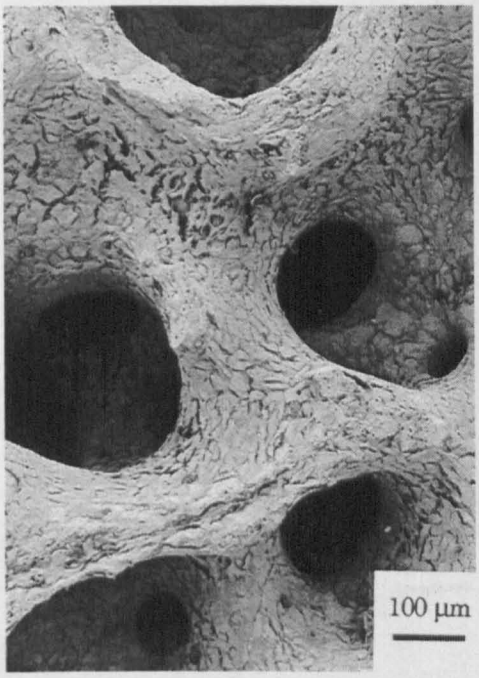

(a)

(b)

Figure 6.4.8 (a) Confluent mono-layer on upper pore surfaces of 4/8 HOb cultures and (b) ceramic surface in proximity to cells and cell processes in 4/8 HOb cultures.

(a)

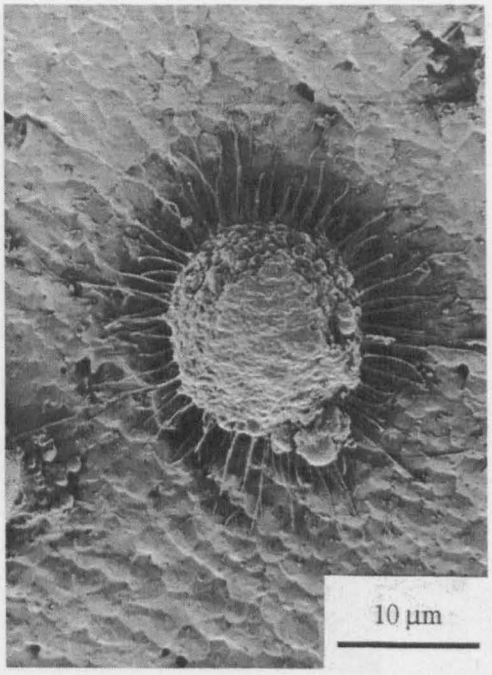

(b)

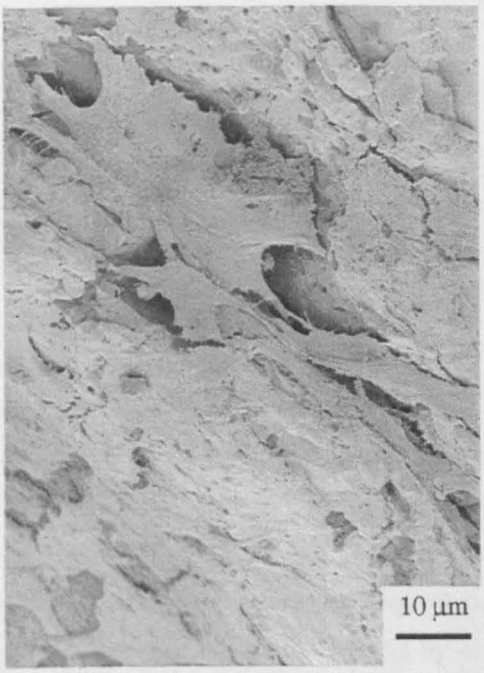

(c)

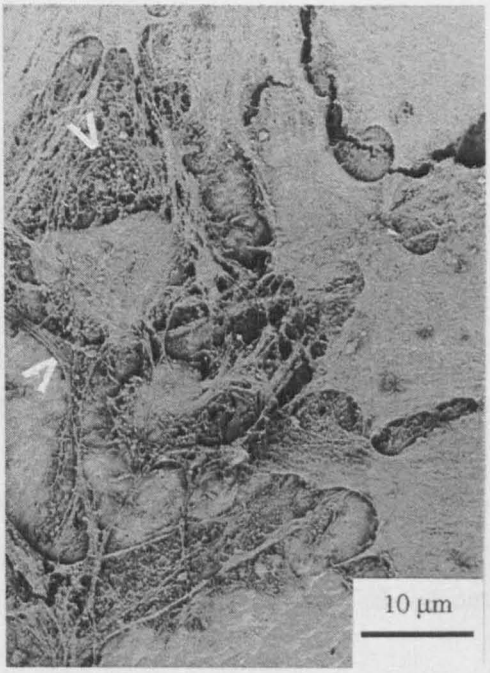

(d)

Figure 6.4.9 Production of (a) extra-cellular matrix and (b) extra-cellular vesicles, and (c) colonisation of cells on a machined surface in 4/8 HOb cultures (d) granules associated with the extra-cellular matrix in a 7/8 HOb culture.

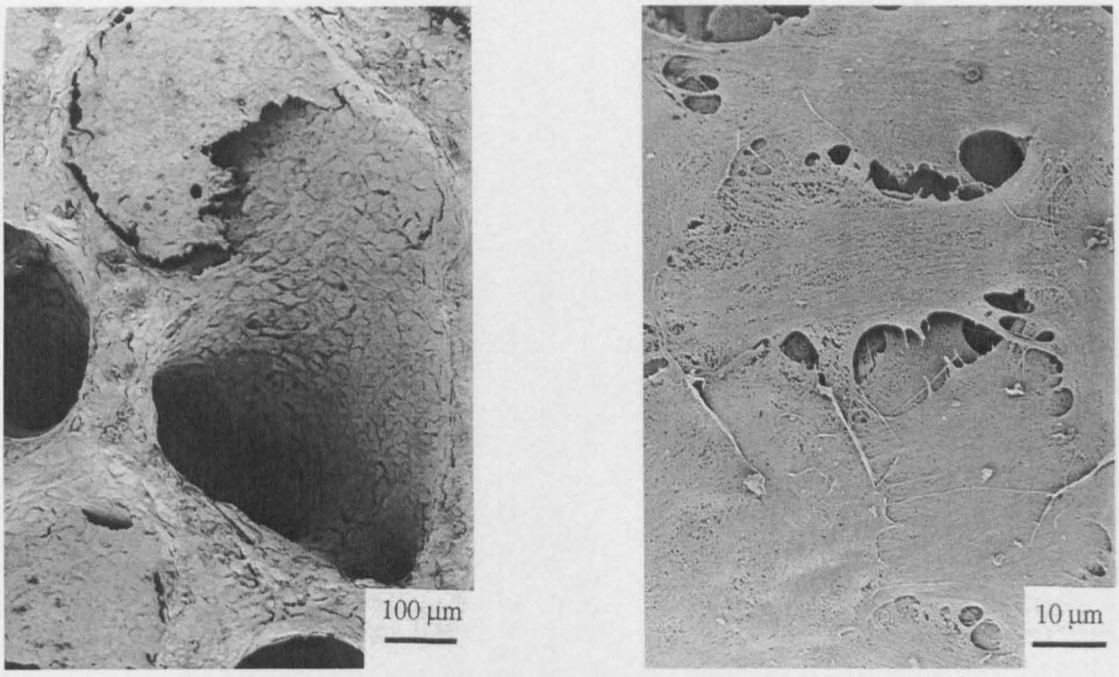

(a) (b)

Figure 6.4.10 (a) Example of cellular capping and (b) typical appearance of a cap upper surface in 7/8 Hob cultures.

14 Day Incubation Period

The regularity of the macropore capping increased on the 14/8 HOb cultures, as did the size of the capped pores (Figure 6.4.11).

Views of "sections" of the confluent cell caps on the ceramic surfaces at the edges of cell caps were obtained as a result of cap tearing during the dehydration process due to cellular shrinkage. It was clear from these views that the caps were made of cell multi-layers (Figure 6.4.12a). Incomplete caps were observed on the larger pores which demonstrated that caps were formed by the apposition of cells from the pore edges into the centre (Figure 6.4.12b). There was extensive production of extra-cellular matrix by cells on the pore surfaces (Figure 6.4.13a) and cell caps. However, some of the cut surfaces were still un-colonised by cells (Figure 6.4.13b).

21 Day Incubation Period

At this time point the regularity of cell capping continued to increase (Figure 6.4.14a) and there was extensive production of fibrous extra-cellular matrix on the upper surfaces, especially between the cells comprising the cell caps (Figure 6.4.14b).

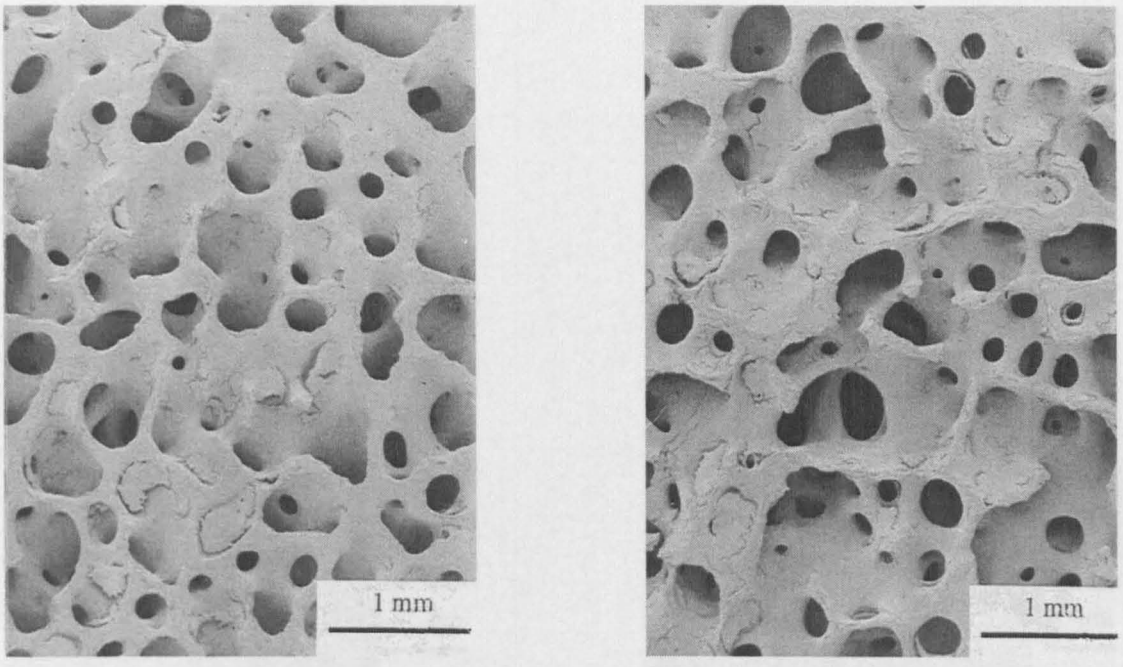

(a) (b)

Figure 6.4.11 Frequency of macropore capping at (a) 7 and (b) 14 days.

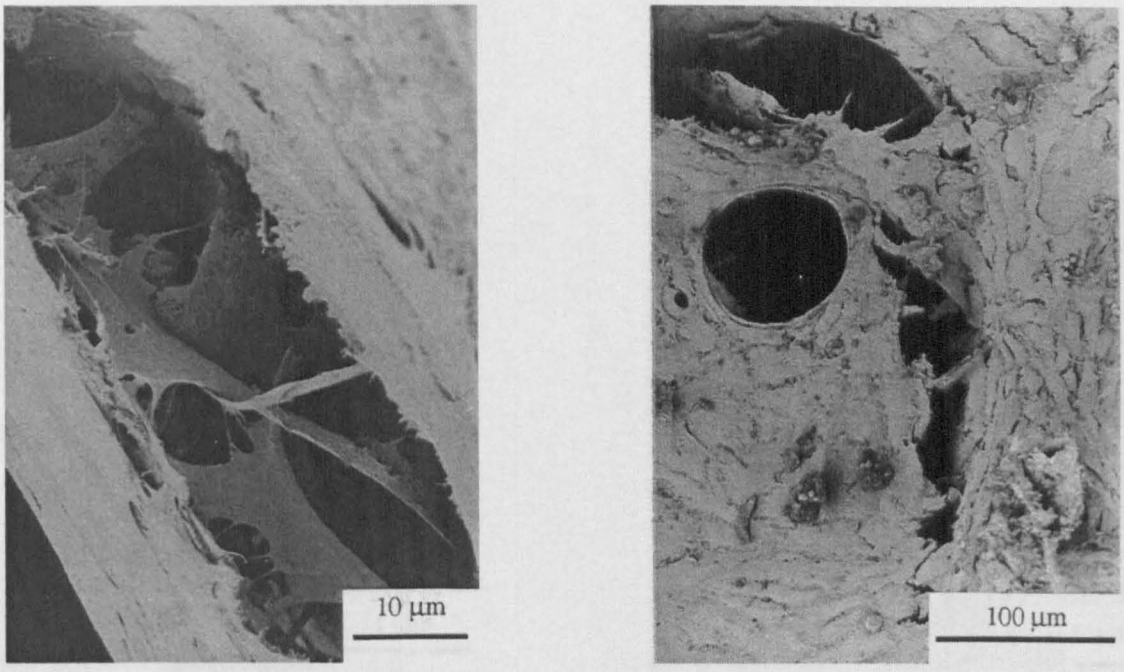

(a) (b)

Figure 6.4.12 (a) "Sectioned" cell multi-layer, (b) an incomplete cell cap, after 14 days incubation.

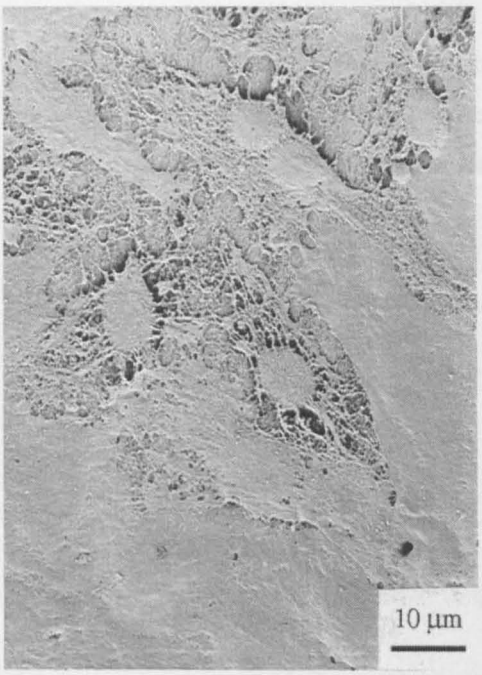

(a)

(b)

Fiure 6.4.13 (a) Extensive extra-cellular matrix formation on a confluent cell multi layer and (b) cell-free cut surfaces after 14 days incubation.

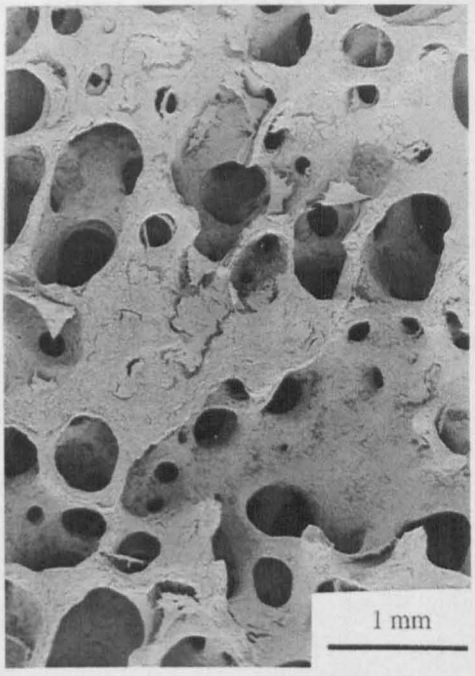

(a)

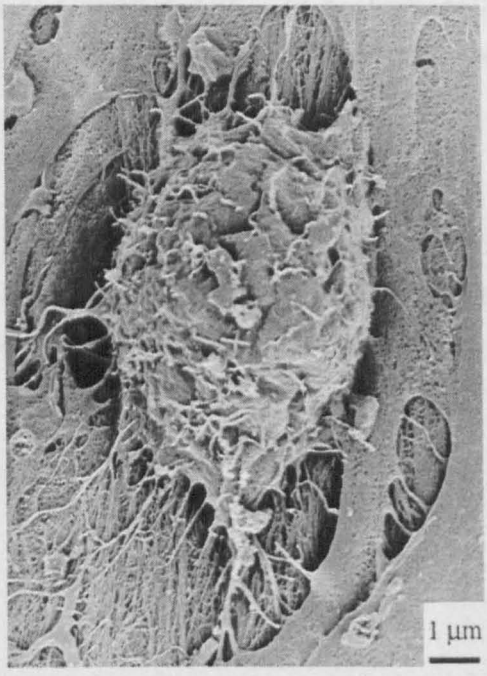

(b)

Figure 6.4.14 (a) Frequency of cellular capping, and (b) detail of extracellular matrix prodution around one cell, after 21 days incubation.

6.4.2.2 Transmission Electron Microscopy

Using transmission electron microscopy to study both decalcified and undecalcified sections it was evident that the general morphology of cells did not alter with time in culture (Figure 6.4.15) and that normal cellular activity was not inhibited by the presence of the ceramic (Figure 6.4.16). Cell multi-layers were detected on specimens that had been incubated for 7 days (Figure 6.4.15a) and occassionally surfaces devoid of cellular activity in the plane of the section were coated with an electron dense layer (Figure 6.4.17).

Studies of the cell/HA interfaces on both decalcified and undecalcified sections demonstrated the close relationship between the cells and the HA surface. The cells were observed in direct contact with the Endobon and appeared to mould themselves to fit the morphology of the surface (Figure 6.4.18).

Surface roughness of the Endobon appeared to affect the bulk morphology of cells, those proliferating on the machined rough surfaces took on a more rounded appearance and did not appear to be well attached (Figure 6.4.19a). Similarly cells in crevices appeared to form 3 dimensional networks (Figure 6.4.19b), which correlated with the in-filling of small macropores observed using SEM (Figure 6.4.3b). In contrast, cells attached to the smoother macropore surfaces had a more flattened morphology and appeared well attached (Figure 6.4.19c).

TEM examination confirmed that the caps were composed of cell multi-layers (Figure 6.4.20). Cap multi-layers (Figure 6.4.20a) and surface multi-layers (Figure 6.4.15b) also appeared to possess layers of extra cellular matrix between the cells. This matrix was also occasionally observed between cells and the Endobon pore surface (6.4.21).

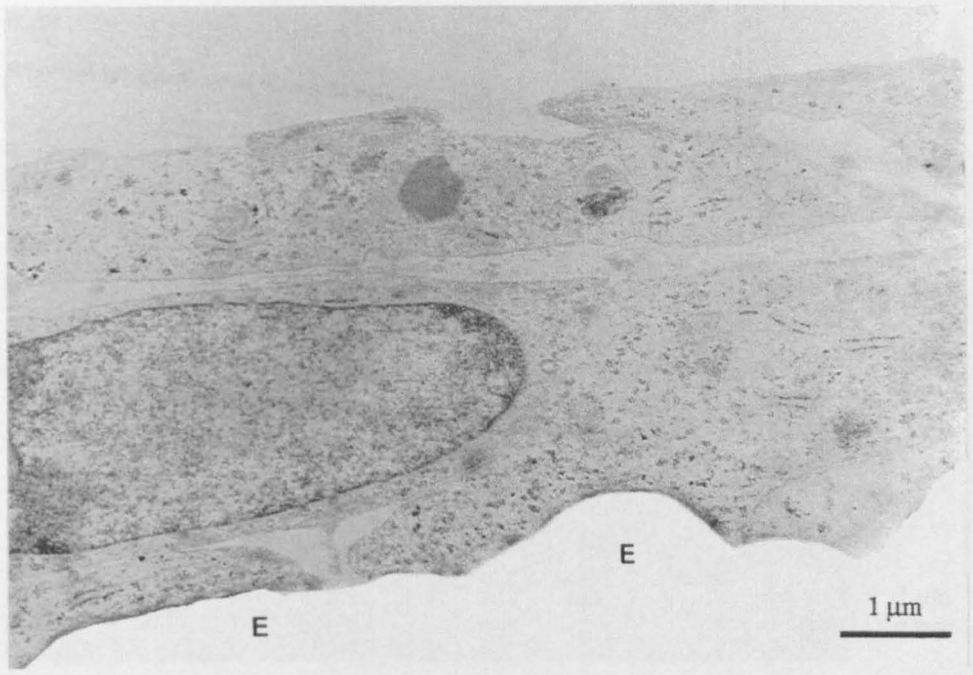

(a)

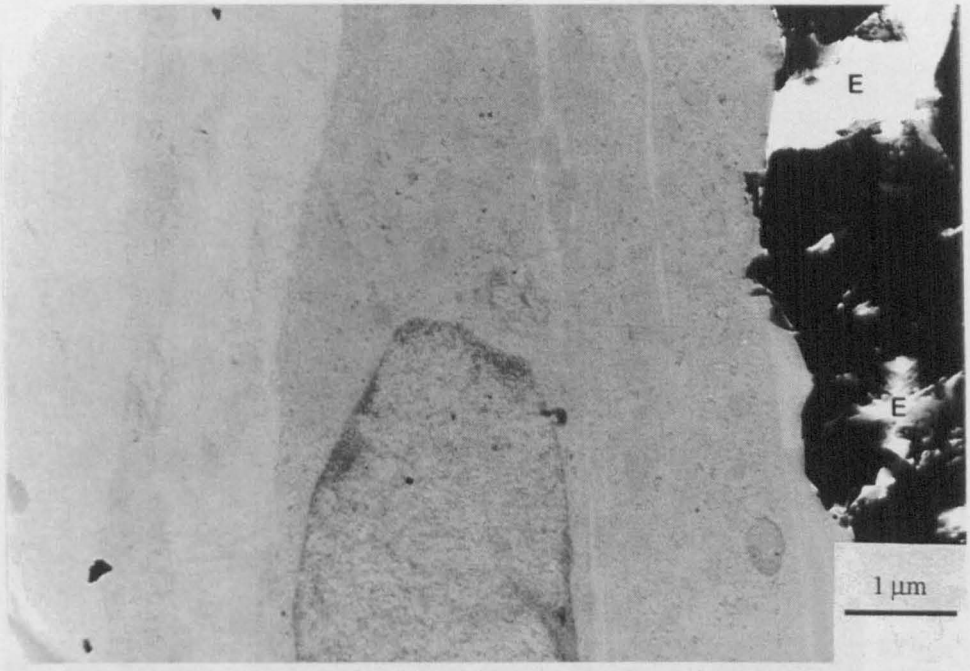

(b)

Figure 6.4.15 Morphology of HOb cells on the surface of an Endobon macropore after (a) 7 and (b) 21 days in culture.

(E = Endobon)

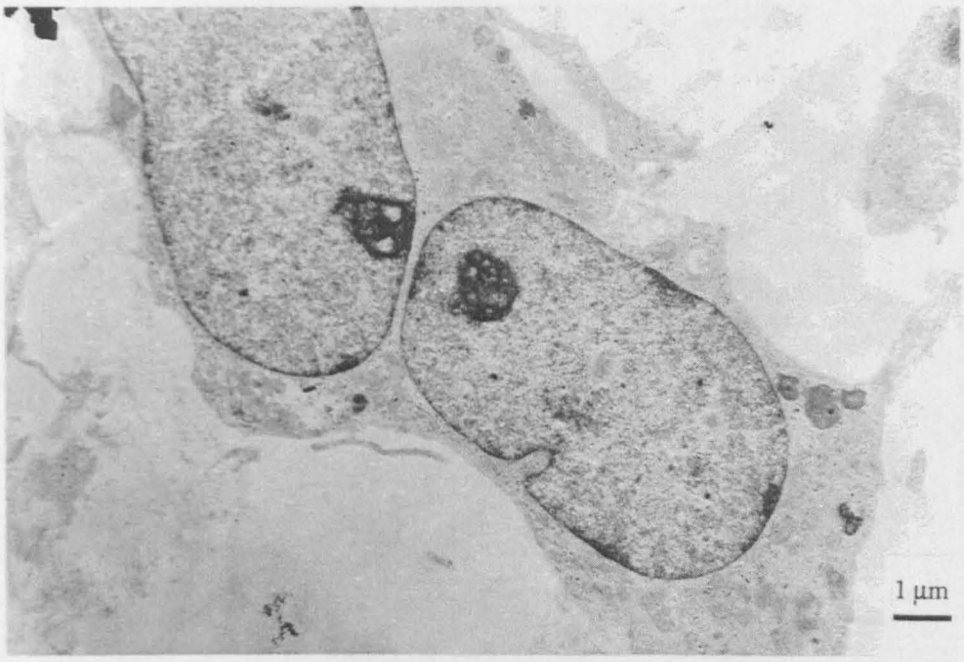

Figure 6.4.16 Cell division occurring within a 14 day HOb culture.

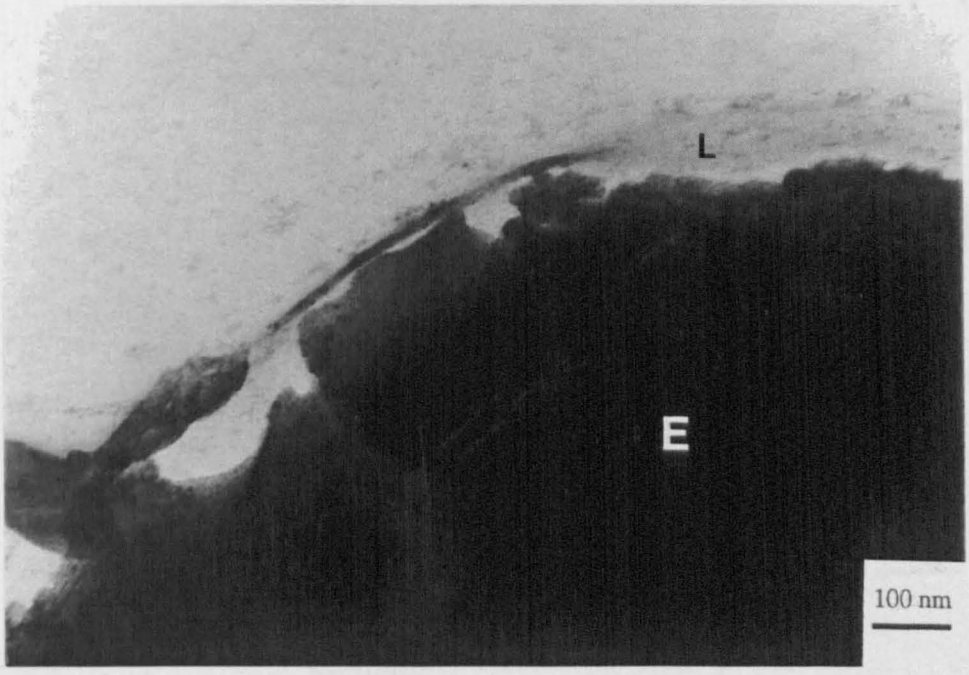

Figure 6.4.17 Electron dense layer on Endobon surface in a 21 day HOb culture.
(L = Electron Dense Layer, E = Endobon)

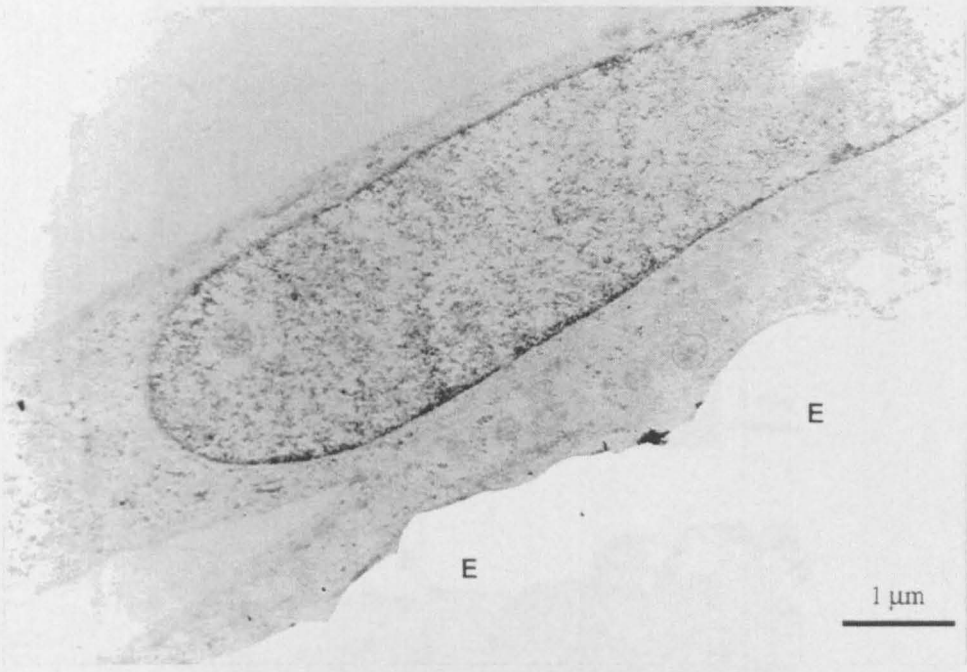

(a)

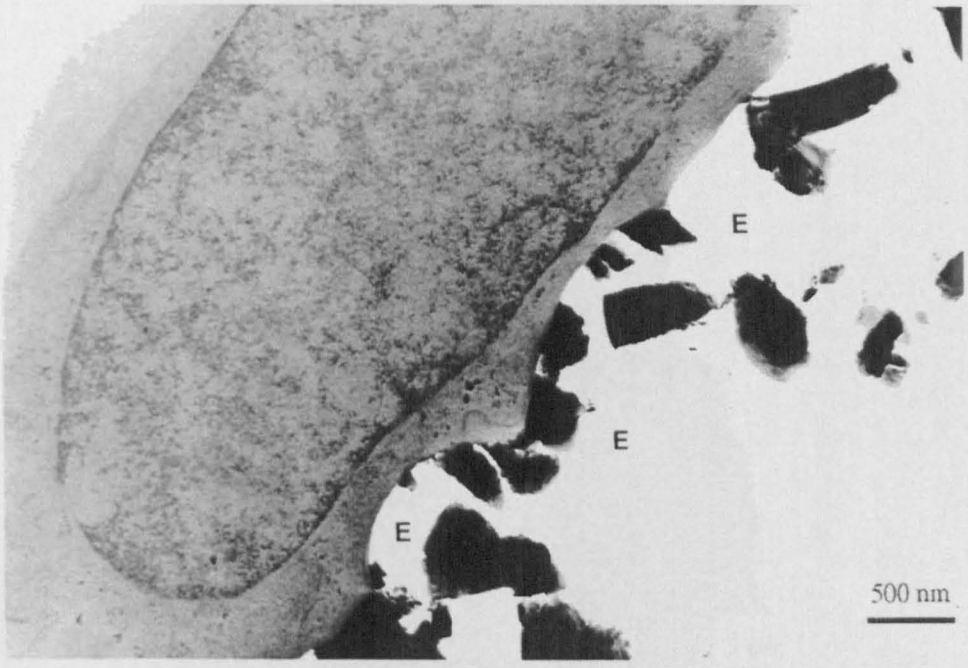

(b)

Figure 6.4.18 HOb cells following the morphology of the Endobon macropore surfaces after incubation for (a) 7 and (b) 14 days. (E = Endobon)

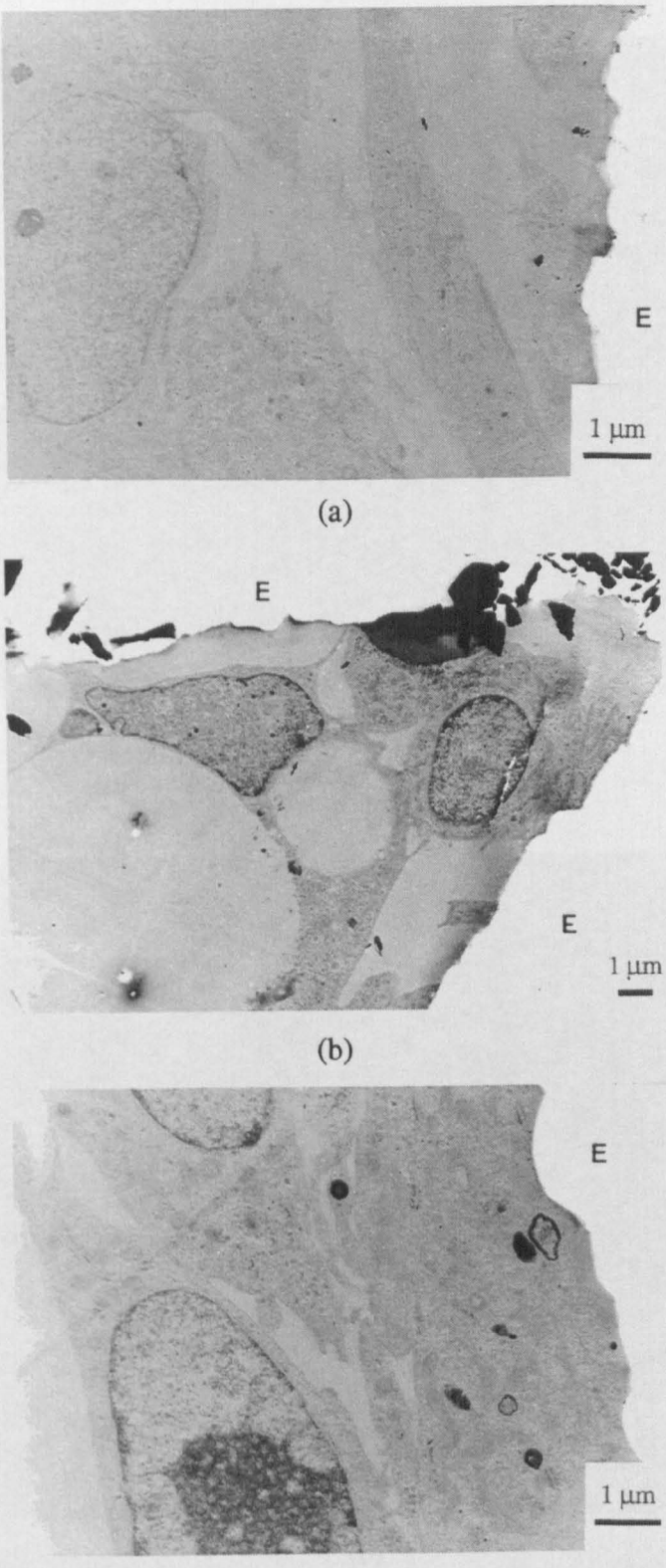

Figure 6.4.19 HOb cells after 14 days incubation on a variety of Endobon surfaces demonstrating differing cell morphologies, (a) rough surface, (b) crevice and (c) flat surface. (E = Endobon)

(a)

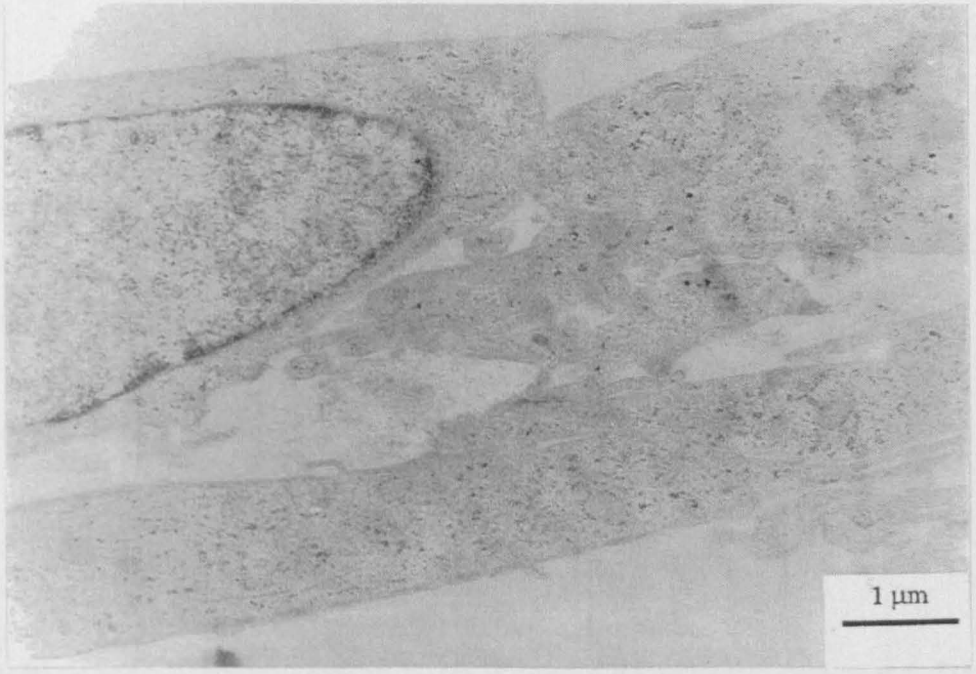

(b)

Figure 6.4.20 Sections through cell caps in HOb cultures incubated for (a) 14 and (b) 21 days.

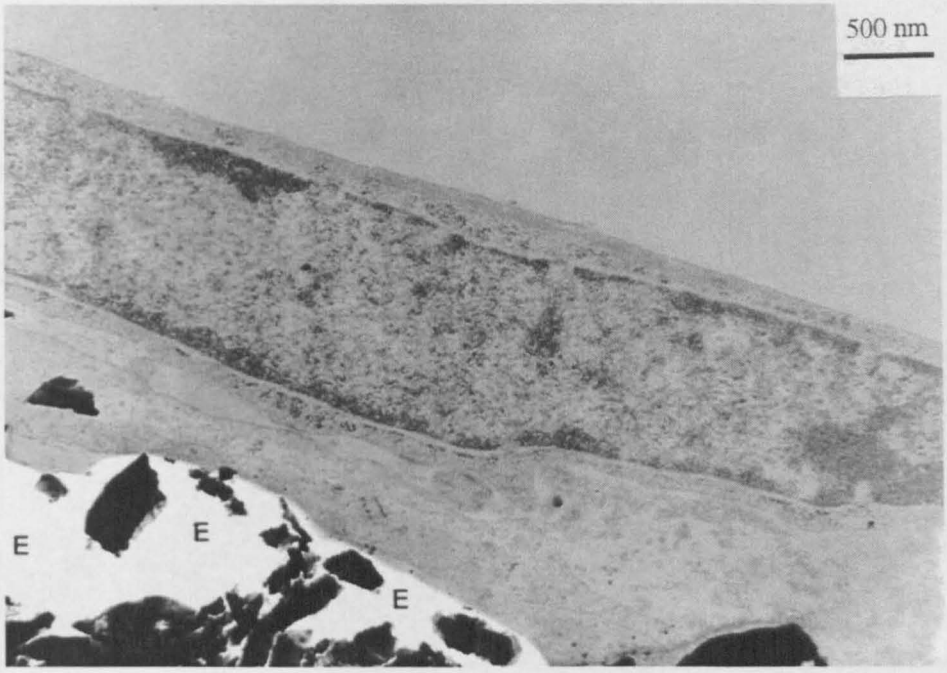

Figure 6.4.21 Extra cellular matrix between HOb 14/8 cell and Endobon surface.
(E = Endobon)

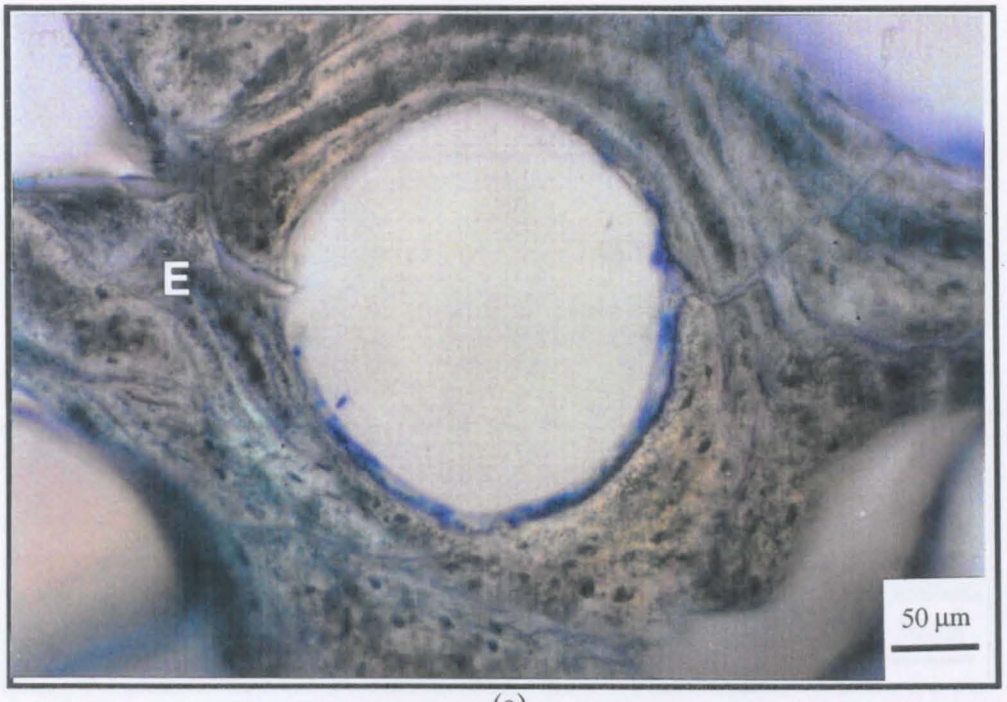

(a)

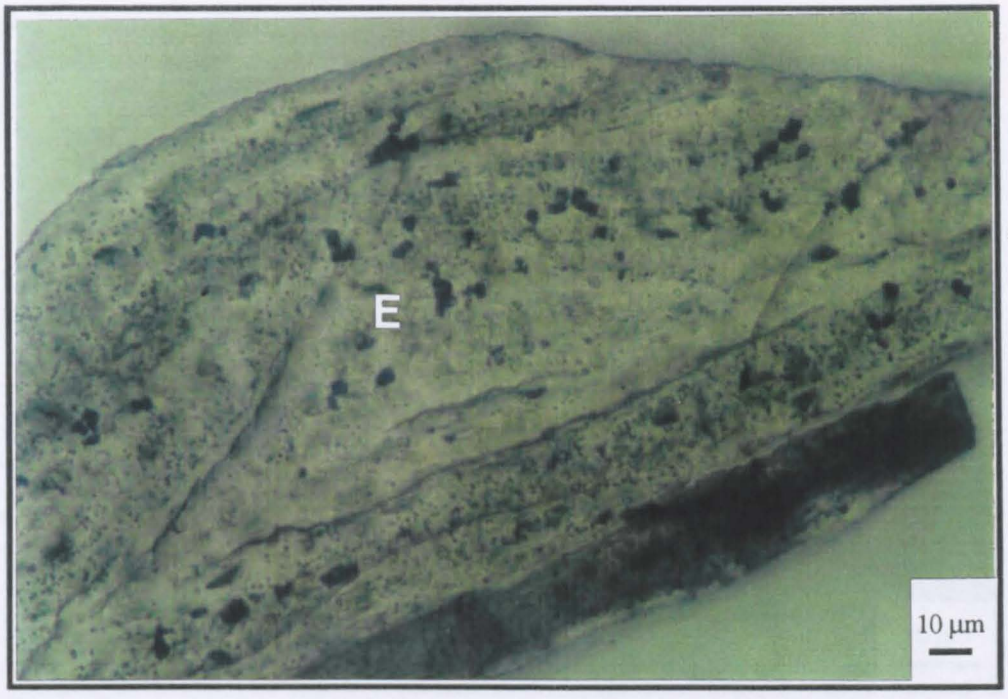

(b)

Figure 6.4.22 Cells proliferating (a) on the inner surfaces of the macro-pores and (b) within the ceramic struts of Endobon specimens after 7 days *in vitro*.

(E = Endobon)

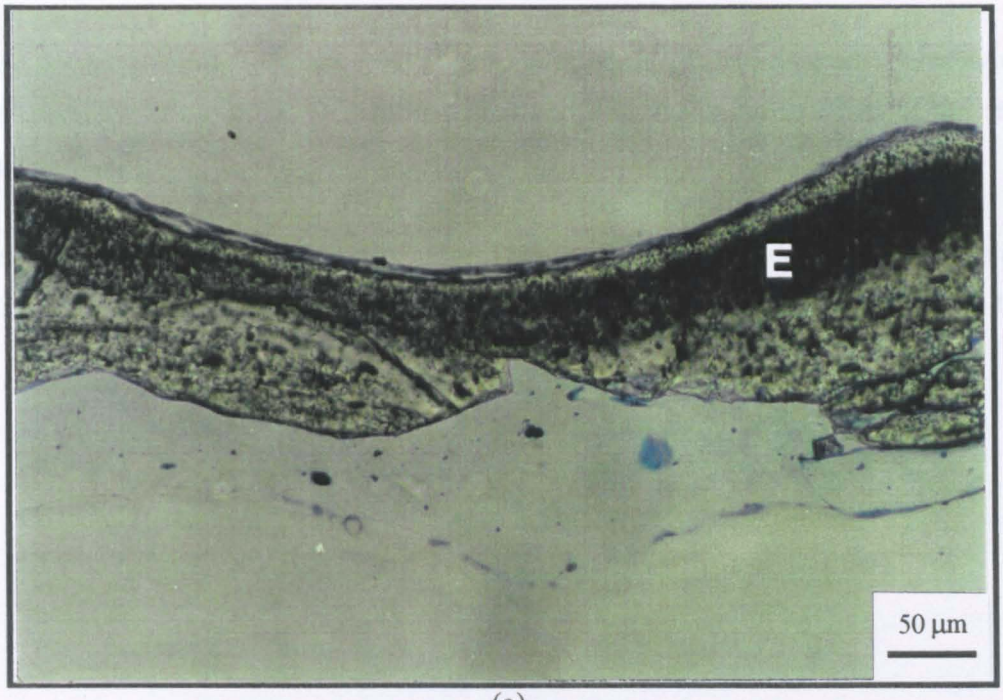

(a)

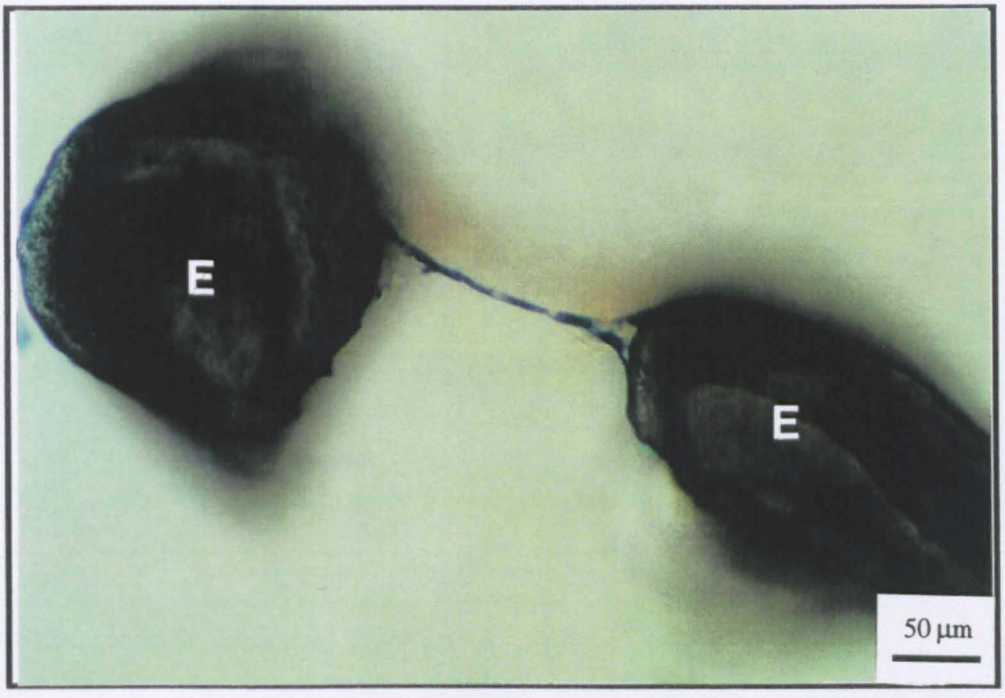

(b)

Figure 6.4.23 (a) Cells mutilayers on the smooth surfaces of the Endobon and (b) cell capping over the upper macro-pores of Endobon specimens after 7 days *in vitro*.
(E = Endobon)

6.4.2.3 Optical Microscopy

Thick sections through the ceramic slices revealed that cells were proliferating on the inner surfaces of the pores (Figure 6.4.22a) and within the dense struts of the ceramic (Figure 6.4.22b).

Extensive cell multilayering was evidient on the upper surfaces of all cultures over 7 days old (Figure 6.4.23a) and sections through cell caps were observed in 14 and 21 day cultures (Figure 6.4.23b).

6.5 Discussion

Previous assessments of the behaviour of porous hydroxyapatite *in vitro* have often employed the use of "standard" transformed cell lines, which are often derived from human sarcoma, foetal or animal tissue, as a result of the ease of attainment, the characterisation available in the literature and the ability of the cells to retain their phenotype irrespective of the passage. Such a cell line, TE-85, was used in an initial pilot study on Endobon to ascertain the correct cell density. However, for assessment of the *in vitro* performance of Endobon, an un-transformed mature human osteoblast-like cell line was used, as the immortal characteristics of the transformed and sarcoma cells have been reported to effect some aspects of osteoblastic behaviour such as proliferation and alkaline phosphatase activity (Clover and Gowen, 1994). The mature human osteoblast-like cell line used in this work, has previously been characterised, and shown to exhibit osteoblast-like behaviour under the incubation conditions employed in this study (Di-Silvio, 1995).

6.5.1 Acid Treatment of Blocks for TEM

Three different routes were employed for the processing of ultra-thin sections for TEM (Figure 6.5.1).

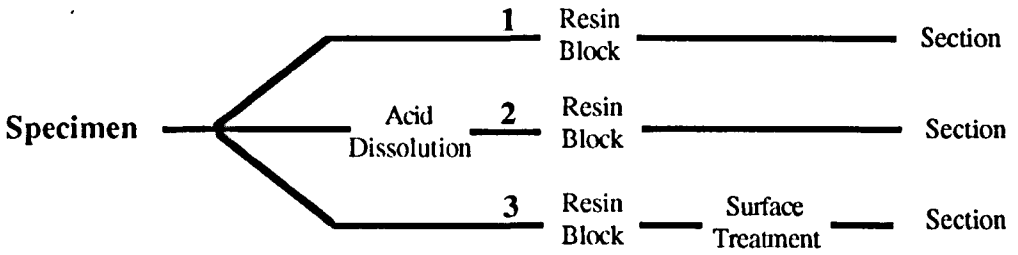

Figure 6.5.1 Processing routes summarised.

This was due to problems encountered as a consequence of the direct sectioning of a polycrystalline ceramic (Figure 6.5.1 route 1). Sectioning was problematic, with the production of single sections which tended to stick to the knife. Furthermore, study of these sections revealed that many of the cells were found to be obscured by ceramic debris, produced as a result of fragmentation of the ceramic during sectioning. Washing of the ultra-thin sections in 50% hydrochloric acid for 2-3 minutes was found

to remove all the debris, however the integrity of the resin deteriorated. Moreover, fragmentation of the ceramic during sectioning invariably led to scoring of the resin embedded cells. Attempts were made to orient blocks in the ultramicrotome so that the cell layer would be cut before the ceramic, but as a result of the random position of cells on and in the porous ceramic some portion of the resin embedded cells was always scored. Therefore, some fragments were decalcified by treatment with orthophosphoric acid for periods of 30-60 minutes to dissolve away the ceramic before embedding in resin blocks (Figure 6.5.1 route 2). Sectioning was smoother (ribbons of sections were produced rather than single sections, which were easier to handle) and section integrity was good. However, as noted by Stevens *et al.*, (1990) subsequent staining (with both toluidine blue and TEM stains) was poor. Location of the cell/ceramic interface was also difficult during examination of these blocks. Treating the surface of trimmed resin blocks with a 33% hydrochloric acid solution for 1-2 minutes, before cutting of ultrathin sections, was found to be a more successful approach (Figure 6.5.1 route 3). This treatment only removed the ceramic to a depth of 1-2 μm, which was adequate to cut 5-10 ultra-thin sections, and as a result of the reduced length of exposure to the acid, staining was not affected, moreover, a clear ceramic/cell interface was preserved.

Table 6.5.1 Relative effectiveness of different processing routes.

Processing Route	Sectioning Properties	Resin Integrity	Stain Intensity	HA Debris	Scores in Resin	HA Interface
1	×	√	≈	×	×	√
2	√	×	×	√	√	×
3	√	√	≈	√	√	√

× Bad, ≈ Acceptable, √ Good

6.5.2 Culture Trials with Human Osteoblast Sarcoma (TE-85) Cells

As a result of the high degree of porosity, it was necessary to carry out a series of trial cultures to determine a suitable cell "density", where density refers to the number of cells per unit area assuming the cells are seeded on a flat surface. High density cultures, where the cells are rounded and multi-layered have been advocated by Hunter *et al.*, (1995) as these conditions are believed to be most like the *in vivo* environment and necessary for the production of a bone-like matrix. Faucheux *et al.*, (1994) carried out a series of *in vitro* experiments on Endobon, they used a cell density of

approximately 0.6×10^4 cells.cm^{-2} and placed 2 mm thick, 15.4 mm diameter Endobon specimens which were placed on an agarose layer within the cell culture dish to prevent migration of the cells from the specimen to the dish. In this study culture trials were seeded with cell densities of 2×10^4, 4×10^4 and 8×10^4 cells.cm^{-2} with the specimens being placed directly on the tissue culture plastic and incubated for periods of 24 and 72 hours. There was no evidence to suggest cell migration had occurred at either time point, thus the agarose was considered unnecessary.

The irregular dispersion of cells on the macropore surfaces of the specimens seeded with cell densities of 2×10^4 (HOS 1/2) and 4×10^4 (HOS 1/4) compared to the 8×10^4 (1/8 HOS) culture suggested that the latter cell concentration was more appropriate for the homogenous seeding of cells. Hunter *et al.*, (1995) demonstrated that a flattened morphology indicates that cells are well attached to a surface, therefore the predominantly flattened morphology of cells after incubation for 1 day on the Endobon was encouraging. Equally, the degree of cell division and possible production of a collagenous extra-cellular matrix after incubation for 3 days was promising, as this cell line has been reported to exhibit similar behaviour to osteoblast-like cells (Tremollieres *et al.*, 1992, Kyeyune-Nyombi *et al.*, 1989).

6.5.3 Culture of Human Osteoblast-Like Cells

As expected, the behaviour of the HOb cells at 1 and 4 days was similar to that of the HOS cells at 1 and 3 days incubation, except that cell coverage in some areas of the 4 day HOb culture appeared less dense than for the 3 day HOS culture, with regions of ceramic visible at some points. This agrees with the observations of Clover and Gowen, (1994) who reported increased proliferation in TE85 HOS cells when compared to primary HOb cells.

The activity of cells in the proximity of macropores was similar to that observed in the HOS cultures (Figure 6.4.3). This behaviour has previously been reported by Bagambisa and Joos, (1990) who studied the phenomenological behaviour of osteoblasts on 60-70% porous and dense hydroxyapatite. These authors suggested the cells migrated across macropores by the extension of long processes across the pore, that these processes attached to the opposite side and that the cell cytoplasm then flowed into the processes; so resulting in the spanning of pores by cell bodies. Bagambisa and Joos, (1990) also reported the capping of macropores (Figures 6.4.10;

6.4.11) and suggested that this was achieved by a similar mechanism to single cell bridging. From the SEM observations made on Endobon this would seem to be true. The arrangement of cells in the incomplete caps in Figure 6.4.12b indicate that the pores are bridged by successive additions of cells to the cap edge and cell processes can be seen extending across the void.

One of the most striking observations made on both types of culture was the appearance of the cells to avoid the machined surfaces of the ceramic slices, which possessed a greater degree of surface roughness. Even after 14 and 21 days of culture, when all other upper surfaces were covered in cell multi-layers regions of the cut surface were still exposed. In section, cells in direct contact with the smooth ceramic had a flattened, fibroblast like appearance, consistent with a well attached morphology, and were observed moulding to the ceramic surface (Figure 6.4.18). This observation was in distinct contrast to that of the cells on the rough surfaces, which were rounder and appeared to have less points of contact (Figure 6.4.19). This variation in behaviour suggests that the osteoblast-like cells migrated away from the rough surfaces to the smoother strut walls, where they were able to form more attachments, confirming the premise that the ability of a cell to attach to a surface defines the bioactivity of the surface (Bagambisa and Joos, 1990; Doherty *et al.*, 1994; Hunter *et al.*, 1995).

Once confluency was reached,multi-layers were formed on the surfaces and cells in the upper multi-layers (i.e. not in contact with the ceramic) and within the cap multi-layers became more rounded. Extra-cellular matrix was identified within the cell layers (and occasionally at the cell/substrate interface), often in the proximity of rounded cells. Production of extra-cellular matrix seemed particularly intense in the 14 and 21 day cultures (Figure 6.4.20), this agrees with the findings of Faucheux *et al.*, (1994) who reported a slackening of cell division at 10 days with production of extra-cellular matrix instead. Similar results were also reported by Di-Silvio (1995) in work using the same cell line as this study.

Evidence of cell growth in the interior of the macropores from 7 days, would suggest that cells migrated into the interior of the ceramic, as well as producing confluent multi-layers over the uppermost surfaces and capping the macropores. However the sporadic nature of this internal colonisation, particularly deep within the ceramic, may indicate that this cellular activity resulted from some cells being washed into the interior of the ceramic during seeding. Alternatively, the variable nature of the ceramic structure could have lead to "direct" and "convoluted" pathways for cell migration, resulting in

the variable instances of internal colonisation. Faucheux *et al.*, (1994) also reported internal colonisation of Endobon specimens.

Mineralisation of the extra-cellular matrix was not conclusively determined, although the production of matrix vesicles was detected in cultures from 4 days onwards, where matrix vesicles are believed to be closely associated with the mineralisation process, (Anderson *et al.*, 1980; Landis, 1981). Globular deposits, similar in morphology to the "crystals" reported by Courteney-Harris *et al.*, (1995) and the "granules" reported by Landis, (1981) were detected in 7 day cultures. However, most studies report conclusive evidence of calcification to occur in primary cell cultures between 21 and 28 days of incubation (Courteney-Harris *et al.*, 1995; Di-Silvio, 1995).

Unlike many other studies of hydroxyapatite *in vitro* the visible surfaces of the ceramic did not appear to be completely coated with adsorbed proteins or inorganic precipitates (Bagambisa and Joos, 1990; Serre *et al.*, 1993; de Bruijn, 1993). There was an indistinct deposit visible in the vicinity of cells and cell processes (Figure 6.4.8b), and an organic layer was detected on some surfaces where cells were not apparent in the section (Figure 6.4.17). This deposit may have been a form of adhesion protein secreted by cell processes which have subsequently moved (Bagambisa and Joos, 1990; Hunter *et al.*, 1995).

CHAPTER 7

IN VIVO PERFORMANCE OF POROUS HYDROXYAPATITE

7.1 Introduction

Having established that Endobon is able to support the proliferation of human osteoblast-like cells. *In vivo* studies were performed to assess the biocompatibility of Endobon when placed in an osseous environment. Much work has been conducted into the *in vivo* response of dense hydroxyapatite and hydroxyapatite coated implants (Denissen *et al.*, 1980b; Dhert *et al.*, 1991; Maxian *et al.*, 1993), with few studies into the behaviour of porous hydroxyapatite *in vivo*. Many investigations which do assess porous hydroxyapatite fail to study the effects of variations in porosity on the bone ingrowth and implant integrity.

This chapter details an investigation into the histological response to chemically similar porous hydroxyapatites (Endobon) with different degrees of porosity. Histomorphometric and biomechanical studies are also performed to assess the effect of bone ingrowth on the mechanical behaviour and fixation of the porous hydroxyapatite implants with time *in vivo*.

7.2 Materials

7.2.1 Porous Hydroxyapatite Implants

Specimens were supplied in the form of cylinders with a mean diameter of 0.458 [0.006] cm and a mean length of 0.876 [0.040] cm (Figure 7.2.1). On receipt, apparent densities were calculated for all Endobon specimens. (Chapter 5, Sections 5.2.2 & 5.3.2) In order to reduce int -implant variability, Endobon specimens for implantation were restricted to those of "femoral origin" only. Specimen selection for implantation was then limited further to those that fell within three distinct apparent density groups (Table 5.4.7). The groups were designated Batch A, C and B after the radio-opaque classifications initially given to the specimens by workers at Merck. (Chapter 5, Section 5.2.2). All specimens were filed down to a length of 0.655 [0.058] mm with a diamond file and heat sterilised before implantation. The average densities and density distributions for the selected implants for implantation are given in Table 7.2.1 and Figure 7.2.2, respectively.

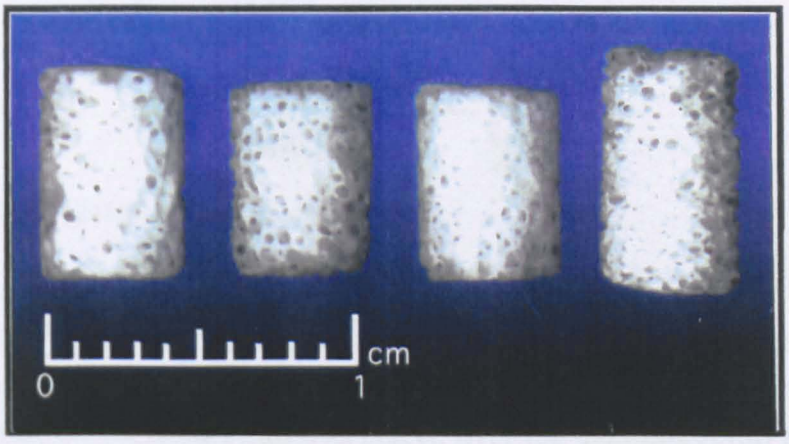

Figure 7.2.1 Typical Endobon specimens, centre specimens filed for implantation.

Table 7.2.1 Densities of implant batches ($g.cm^{-3}$).

	Batch B	Batch C	Batch A
Density Range	0.51 - 0.68	0.86 - 0.96	1.09 - 1.29
Mean [Standard Deviation]	0.61 [0.04]	0.90 [0.03]	1.18 [0.06]
Population	39	10	28

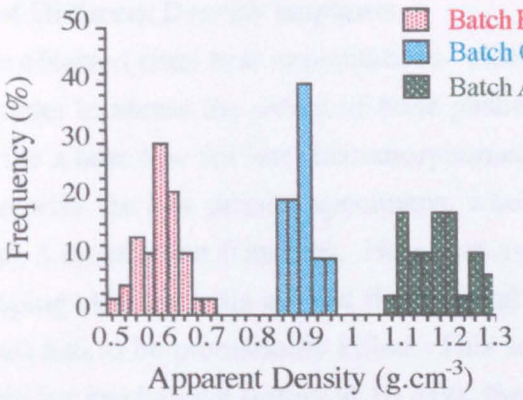

Figure 7.2.2 Density distribution of Endobon implants.

7.2.1.1 Sterilisation of Implant Specimens

15ml glass test-tubes were cleaned and degreased using Hibiscrub and acetone in an ultrasonic bath, rinsed with de-ionised water and dried at 70°C. Specimens were placed inside the test tubes, the ends of which were then sealed with aluminium foil (see Figure 7.2.3).

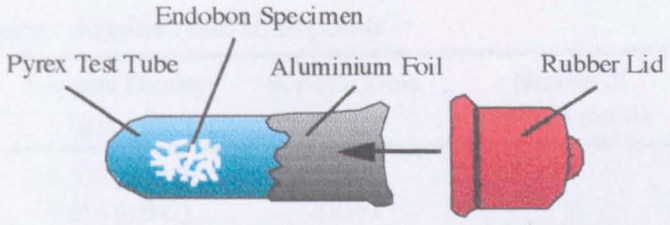

Figure 7.2.3 Implant sterilisation assembly.

Sterilisation was performed by placing the assembly into a clean furnace, which was then ramped at a rate of 5°C per minute up to 200°C and held at temperature for 40 minutes. The specimens were then allowed to cool to room temperature in the furnace. Once cool, a tight fitting rubber cap was placed over the aluminium foil to protect it whilst in transit to the operating theatre.

7.2.2 Animal Model

All implantations were carried out on 6 month old New Zealand White rabbits of mixed sex. Implants were placed in the distal end of the right femur. This site was selected as it presented the largest volume of load bearing cancellous bone within the animal. After operation animals were isolated in a recovery room overnight. They were subsequently kept in open pens in groups of 5-6 and allowed full use of the knee.

7.2.2.1 Time Points of Different Density Implants

Zero time points were obtained from trial implantations. Histology was also performed at this time point in order to assess the extent of bone pushed into the implant during the operation,to provide a base line for later histomorphometry. The most exhaustive, study was carried out with the low density specimens, where implants were initially scheduled for 5 weeks, 3 months and 6 months. However, as a result of problems with some animals developing skin necrosis around the external wound site (not near the implant), these animals had to be prematurely killed. This action resulted in a number of specimens available for mechanical testing at 10 days, therefore low density 10 day histology animals were added to the schedule. Two animals from different low density time points independently died at three weeks of natural causes (one had a lung infection, the other appeared healthy), and these were assigned as an extra histology time point. Having resolved the problem with the skin necrosis (detailed later), there was only one fatality in the other density implant groups. However, two implants were excluded from mechanical testing as a result of infection at the site of implantation resulting in pathological arthritis.

Table 7.2.2 Implant densities and time points.

Apparent Density ($g.cm^{-3}$)	Survival Time	Number of intact retrievals
0.507 [0.104]	0/0	3
0.614 [0.042]	10/365	9
0.666 [0.024]	3/52	2
0.598 [0.040]	5/52	9
0.902 [0.036]	5/52	9
1.222 [0.049]	5/52	9
0.614 [0.056]	3/12	7
1.174 [0.064]	3/12	9
0.610 [0.039]	6/12	8
1.169 [0.046]	6/12	10

Where:

10/365 = 10 days
3/52 = 3 weeks
5/52 = 5 weeks
3/12 = 3 months
6/12 = 6 months

In Vivo.

Numbers in square parenthesis are standard deviations.

7.3 Methods

7.3.1 Implantation Procedure

All implantation operations were carried out at the Royal Free Hospital School of Medicine, Hampstead. Trial implantations were carried out under the supervision of visitors from E. Merck, in order that the surgeons became familiar with the equipment and procedures before beginning the project. During this it was discovered that Endobon specimens should be of a maximum length of 6-7 mm to reduce the amount of bleeding from the marrow cavity. It was also recommended that implants, when fitted, should sit below the subchondral plate. All operations were carried out by the same two surgeons.

(a)

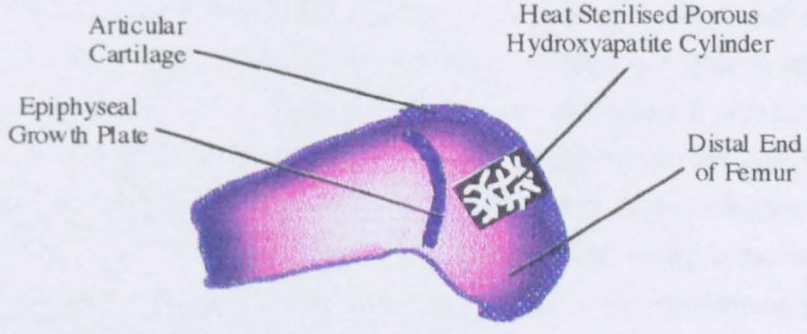

(b)

Figure 7.3.1 Position of Implant within the distal end of the femur (a) magnetic resonance image from a retrieved knee (b) schematic diagram identifying key points.

Initially there was concern that specimens with very low apparent densities would crumble during the press fitting stage of the operation. However, this was not found to be a problem during a trial implantation during which specimens with an apparent density of 0.514 $g.cm^{-3}$ survived the process intact. Implantations were carried out in the following manner:-

7.3.1.1 Location of Implant Site

An approximately 40 mm long medial skin incision was made centred over the femoral condyle. This incision was oriented in a vertical direction for the resting rabbit. Loose dissection was used to release the skin from the underlying soft tissue and to reduce post operative adhesions. The joint capsule was incised parallel to the patella on the lateral side. The knee was extended and with gentle manual pressure the patella was dislocated medially and the knee again flexed.

In three operations the skin was incised on the lateral side to enable easier observation of the wound. However in all three cases, severe skin necrosis developed and the rabbits had to be terminated prematurely.

7.3.1.2 Removal of Bone Plug to Create Hole For Implant

The desired position was marked using a stainless steel hammer and circular punch, thus cutting through the cartilage to the sub-chondral plate. A hole approximately 6 mm in depth was drilled using a 4.5 mm external diameter, diamond tipped trephine and a compressed air powered drill (Figure 7.3.2a). During drilling, the centre of the hollow trephine was kept lubricated with sterile saline fed through the drill and the hole depth was monitored using the millimetre graduations on the side of the trephine. The trephine was removed with the drill running in reverse and sometimes the plug of bone would be removed with the trephine, but more usually it required separate removal. The punch, which had three internal spines, was reintroduced into the trephined hole using gentle taps with the hammer. The trabecular bone at the base of the hole was fractured using a sharp twist of the punch, which was then withdrawn, removing the piece of bone. The depth of the hole was checked using a measuring rod with millimetre graduations and if less than 6 mm deep, at the shallowest point, then bone removal with the punch was repeated, with or without further drilling as required.

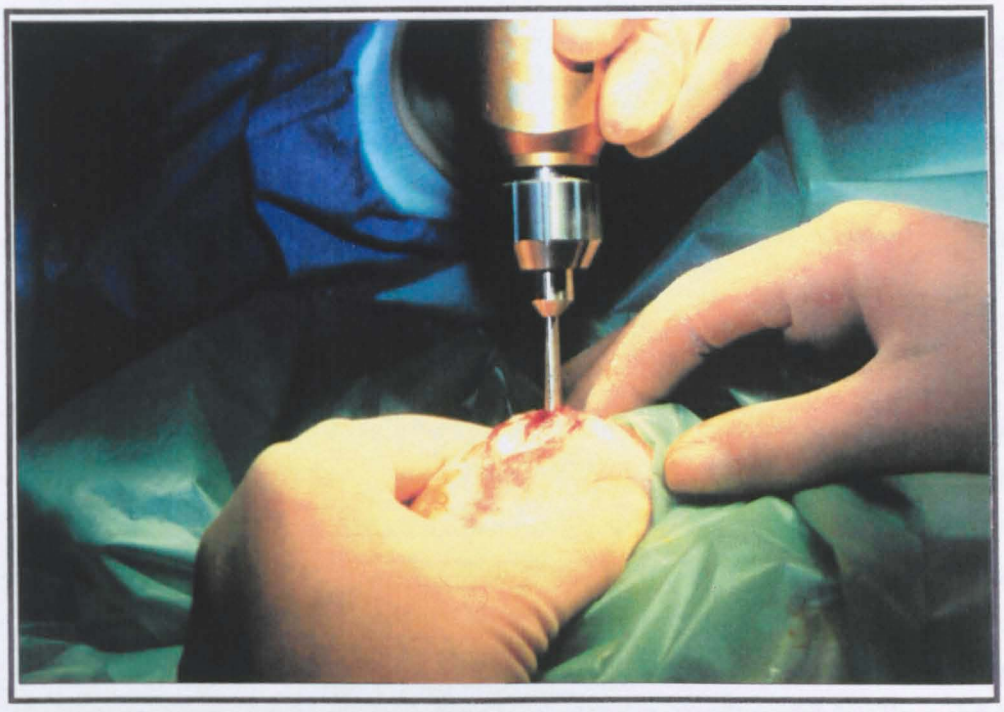

(a)

(b)

Figure 7.3.2 Implantation proce dure: (a) drilling of defect (b) inserted specimen.

7.3.1.3 Specimen Implantation

The Endobon specimen was gently tapped into the defect using a metal tipped nylon rod and a hammer, where the nylon end was against the implant and metal end presented to the hammer. When in position the surface of the implant was shaped to fit in with the profile of the surrounding articular surface using the side of the nylon rod. Any debris or fractured pieces of Endobon were washed away with sterile saline (Figure 7.3.2b).

7.3.1.4 Closing Up

The knee was then straightened, the patella relocated and the capsule sutured using interrupted sutures. The skin incision was initially closed with either interrupted sutures or skin clips. Later this proceedure was revised to reversed interrupted sutures, where the knot fell on the inside of the wound after stitching. The latter method was used as this prevented unravelling, or pulling out of stitches or skin clips, which resulted in tears in the skin (especially with the skin clips) making subsequent resuturing difficult. Initially there was also some difficulty with healing and in some cases the wound became necrotic and rabbits had to be terminated prematurely. This result was found to be due to a poor tolerance to silk sutures by the rabbits, which was remedied in later operations by the use of Vicryl sutures on the external medial wound and PDS monofilament sutures on the internal lateral wound. No further complications were then experienced.

7.3.2 Fluorochrome Labelling

Rabbits selected for labelling were injected subcutaneously in to the loose skin at the back of the neck on three consecutive days of each designated week. (Table 7.3.1)

Table 7.3.1 Fluorochrome labelling protocols

Label	Concentration	Dosage	Days Injected After Operation		
			10/365 B	5/52 B	5/52 A and C
Tetracycline	20 mg ml $^{-1}$	0.5 mg kg $^{-1}$	6,7	6,7,8	13,14,15
Calcein Blue	50 mg ml $^{-1}$	0.2 mg kg $^{-1}$	-	14,15,16	-
Alizarin Red	30 mg ml $^{-1}$	0.5 mg kg $^{-1}$	-	21,22,23	-
Calcein Green	30 mg ml $^{-1}$	0.5 mg kg $^{-1}$	-	28,29,30	20,21,22

10/365 = 10 days and 5/52 = 5 weeks *in vivo*.

7.3.3 Retrieval of Implants

Implants were retrieved after periods of 10 days, 3 weeks, 5 weeks, 3 months and 6 months. Rabbits were terminated by injecting an overdose of anaesthetic (Hyprorm/Diazepam) and the distal end of the right femur was dissected out. In some cases the left femur and left and right patellae were also removed. The appearance of surrounding tissue, the extent of healing undergone at the site of implantation, the mobility of the joint and any other abnormalities were noted.

7.3.3.1 Bone Dissection and Storage

After termination, the distal end of the operated femur was completely removed and all soft tissue was stripped from the bones. Specimens for histology were trimmed and placed immediately in formal alcohol fixative (70% ethanol). Specimens for mechanical testing were wrapped in cotton swabs soaked in deionised water and stored, frozen at -20°C. Deionised water was used rather than Ringers solution or sterile saline, as the latter two have been reported to have a dehydrating effect when in contact with frozen bone (Wall *et al.*, 1970).

7.3.3.2 Location of Implants Post-Retrieval

Radiographs

In order to properly locate the implants to aid the accurate dissection for histological and mechanical specimens,radiographs of the distal end of the operated rabbit femora were taken in two directions (longitudinally and transversely). The settings for correct exposure were: 50 kV and 30 mA for 0.25 s. However implants from Batch B (low apparent density) were difficult to image due to insufficient contrast between the mineral of the surrounding trabeculae and the porous implant.

Magnetic Resonance Imaging

Magnetic resonance imaging (MRI) was adopted as an alternative to taking radiographs of Batch B implanted specimens. MRI images are built up as a result of the presence of hydrogen ions in soft tissue and blood. It was therefore necessary to soak the specimens in deionised water at 4°C for at least 48 hours before scanning to ensure a clear image. Specimens were then towel dried and placed in sample presentation coil. A low resolution preliminary scan was made to determine the relative position of the bones within the coil and the implant within the bone. Each scan consisted of a series of images of consecutive "slices" through the bones. The slices were constrained to be at least two millimetres apart to avoid signal interference, so it was important to ensure

that they intersected the implants correctly. A maximum of 50 slices could be made over the length of the presentation coil, allowing three bones to be scanned at once. When the bones were correctly aligned, a high resolution scan was initiated, which took 3-4 hours depending on the length of the echo time. Two scans were performed on the specimens, each with a different length of echo time (either 24 or 48 ms). This parameter affected the contrast of the image and thus the information it yielded. The two different echo times chosen resulted in scans which always showed the position of the specimen within the bone. However the shorter time produced the clearest images, which were found to show the precise position of the implant within the bone.

7.3.4 Histology

Histology was performed on at least two implants from each time and density point. Implants for histology were selected randomly from the group of surviving rabbits, except in cases where knees were "arthritic" or rabbits had been labelled subcutaneously with fluorochromes. All sections were prepared at the bone laboratories of the Histopathology Department at The Royal Free Hospital School of Medicine.

7.3.4.1 Section Preparation

The operated femora of the rabbits selected for histology from each time or density point were trimmed in a manner that left the distal condyle intact and then fixed in a 70 % dilution of ethanol and formaldehyde immediately after dissection of the femur from the rabbit. All femora, fluorochrome labelled and unlabelled,were fixed in formal alcohol for a period of 4 days. After fixation, the tissue was dehydrated and embedded in Technovit resin. The resin blocks were then processed through to semi-thin (5-10 μm) sections using the Exakt technique (Donarth, 1982; Rohrer *et al.*, 1992). A detailed description of this process is given in Chapter 6 (6.3.4.1). Sections were all cut parallel with the longitudinal axis of the implants, with the exception of the top and middle 6/12 sections, which were cut in the transverse direction (the bottom of these implants was sectioned longitudinally).

At least one section from each implant was stained with toluidine blue. Where animals had been labelled with fluorochromes, one section was left unstained for fluorescence microscopy.

7.3.4.2 Histology

Stained sections were studied with the use of a Zeiss Axioskop optical microscope. Sections were studied under normal, plane-polarised and λ-polarised transmitted illumination at a range of magnifications (×12.5-1000). After staining with toluidine blue, microscopic features appeared as indicated in Table 7.3.2.

Table 7.3.2 Colour of microscopic features after staining with toluidine blue.

Histological Feature	Colour
Osteoid seams	Light blue
Cement lines	Bright Purple
Calcification front	Dark, granular purple
Cell nuclei	Dark blue/purple
Cell Cytoplasm	Light blue
Endobon	Dark, granular grey

7.3.4.3 Histomorphometry

Histomorphometry was performed on micrographs taken at a magnification of × 25. A series of photographs were taken of each section. These photographs were then taped together to form a collage of the whole section (Figure 7.3.3a). Each collage was then split into 9 zones (Figure 7.3.3b). Histomorphometry was performed on each of the zones to build up a map of ingrowth variation within each section, as well as to obtain average values for the sections, as grouped in time and density points.

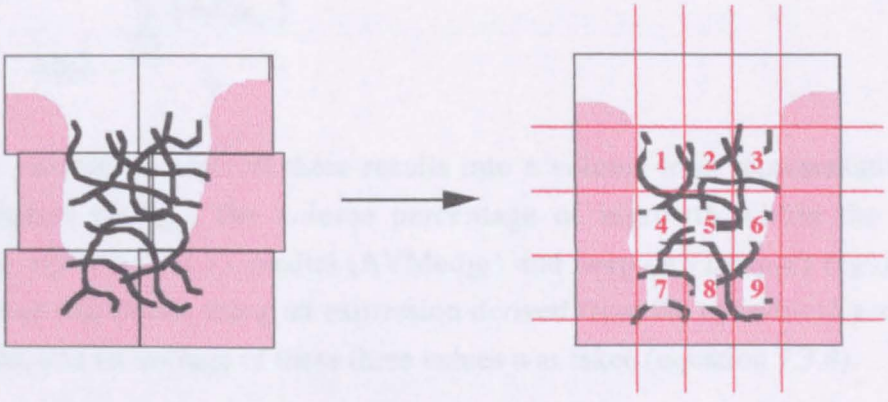

(a) (b)

Figure 7.3.3 (a) Collage of micrographs to give whole implant section.
(b) Histomorphometry zones.

Percentage of Bone Ingrowth

The percentage of bone ingrowth was measured for each zone with the use of a Weibel grid (Weibel and Elias, 1967), composed of 42 points, which was placed over the appropriate part of the collage (Figure 7.3.4).

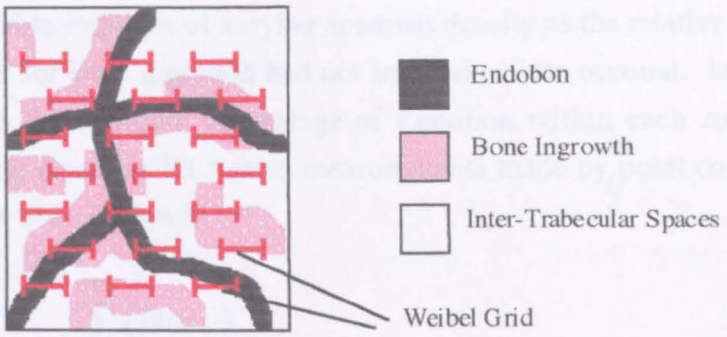

Figure 7.3.4 Measurement of bone ingrowth with a Weibel grid.

A "hit" for bone ingrowth (H_{BI}) was then scored where ever a point fell over an area of bone and the absolute percentage of bone ingrowth within the whole zone (AZ_{BI}) was calculated using equation 7.3.1.

$$AZ_{BI} = \frac{\sum_{i=1}^{i=42} (H_{BI\,i})}{42} \times 100 \qquad (7.3.1)$$

The absolute percentage of bone ingrowth within the whole section (AS_{BI}) was the mean of the values for the nine zones (equation 7.3.2). Similarly a value for the amount of ingrowth within the deep end of the section was given by the mean of zones 7-9 (Figure 7.3.3b).

$$AS_{BI} = \frac{\sum_{i=1}^{i=9} (AZ_{BI\,i})}{9} \qquad (7.3.2)$$

However, in order to convert these results into a volume term representative of the whole implant (AV_{BI}), the volume percentage of ingrowth within the superior ($AVSup_{BI}$, equation 7.3.3), medial ($AVMed_{BI}$) and deep ($AVDeep_{BI}$) regions of the section were calculated, using an expression derived from the cylindrical geometry of the implant, and an average of these three values was taken (equation 7.3.4).

$$AVSup_{BI} = \frac{4 \cdot (AZ_{BI\,1}) + (AZ_{BI\,2}) + 4 \cdot (AZ_{BI\,3})}{9} \qquad (7.3.3)$$

$$AV_{BI} = \frac{(AVSup_{BI} + AVMed_{BI} + AVDeep_{BI})}{3} \qquad (7.3.4)$$

These measurements were adequate for the comparison of the amount of ingrowth between different zones within the same implant, and different implants with the same apparent density. However, absolute values could not be used to compare the amount

of ingrowth within implants of varying apparent density as the relative amounts of pore space available for bone ingrowth had not been taken into account. In order to correct for this effect, the absolute percentage of Endobon within each zone (AZ_{HA}) was calculated using equation 7.3.5 from measurements made by the point counting technique adopted for the bone ingrowth.

$$AZ_{HA} = \frac{\sum_{i=1}^{i=x} (H_{HA_i})}{42} \times 100 \qquad (7.3.5)$$

The value obtained from equation 7.3.5 was then substituted into equation 7.3.6 and the absolute percentage of pore space available for bone ingrowth within each zone (AZ_{PS}) was calculated.

$$AZ_{PS} = 100 - AZ_{HA} \qquad (7.3.6)$$

The relative percentage of bone ingrowth within a zone (RZ_{BI}) was then given by equation 7.3.7.

$$RZ_{BI} = \frac{\sum_{i=1}^{i=x} (H_{BI_i})}{42} \times \frac{100}{AZ_{PS}} \qquad (7.3.7)$$

The relative percentage of bone ingrowth within the whole section (RS_{BI}) and whole implant (RV_{BI}) was calculated as before (equations 7.3.8 - 7.3.10).

$$RS_{BI} = \frac{\sum_{i=1}^{i=9} (RZ_{BI_i})}{9} \qquad (7.3.8)$$

$$RVSup_{BI} = \frac{4(RZ_{BI_1}) + (RZ_{BI_2}) + 4(RZ_{BI_3})}{9} \qquad (7.3.9)$$

$$RV_{BI} = \frac{(RVSup_{BI} + RVMed_{BI} + RVDeep_{BI})}{3} \qquad (7.3.10)$$

The accuracy of this method was verified by calculating the absolute volume percentage of Endobon within each implant (AV_E). This value was then converted into a calculated apparent density (AD_{calc}) using equation 7.3.11, where RD_{struts} is the real density of the struts.

$$AD_{calc} = AV_E \times \frac{RD_{struts}}{100} \qquad (7.3.11)$$

The values of calculated apparent density were then plotted against the values of measured apparent density (AD_{meas}).

Coverage of Bone Ingrowth

The coverage of the bone ingrowth on the implant surfaces within each zone was measured by placing a Merz grid (Merz and Schenk 1970) over the appropriate part of the collage (Figure 7.3.5).

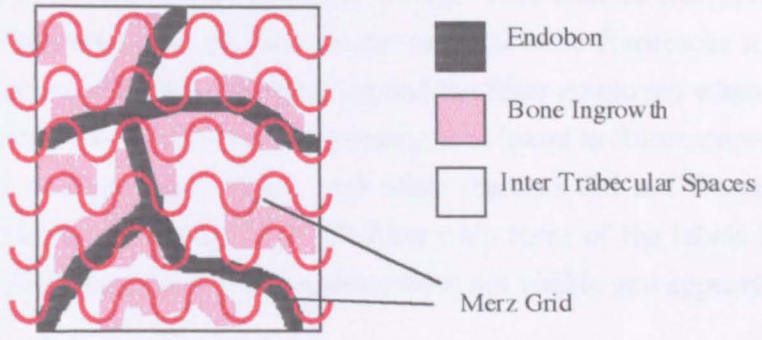

Figure 7.3.5 Measurement of bone coverage with a Merz grid.

A "hit" for bone coverage (H_{BC}) was scored where a line intersected a bone:Endobon interface. Similarly a hit for Endobon surface (H_{ES}) was scored where a line intersected either a bone:Endobon interface or a bone:trabecular space interface. The percentage of Endobon surface covered by bone ingrowth within the zone (Z_{BC}) was then given by equation 7.3.12 and the value of bone coverage for the whole section (S_{BC}) was calculated as the mean of all the zone values (equation 7.3.13).

$$Z_{BC} = \frac{\sum_{i=1}^{i=x} (H_{BC_i})}{\sum_{j=1}^{j=y} (H_{ES_j})} \times 100 \qquad (7.3.12)$$

$$S_{BC} = \frac{\sum_{i=1}^{i=9} (Z_{BC_i})}{9} \qquad (7.3.13)$$

As with the bone ingrowth, the area percentage of bone coverage for individual implants (A_{BC}) was calculated by determining the area percentage of coverage within the superior ($ASup_{BC}$, equation 7.3.14), medial ($AMed_{BC}$) and deep ($ADeep_{BC}$) regions of the section, using an expression derived from the cylindrical geometry of the implant, and taking an average of these three values (equation 7.3.15)

$$ASup_{BC} = \frac{4(Z_{BC1}) + (Z_{BC2}) + 4(Z_{BC3})}{9} \quad (7.3.14)$$

$$A_{BC} = \frac{(ASup_{BC} + AMed_{BC} + ADeep_{BC})}{3} \quad (7.3.15)$$

7.3.4.4 Apposition rates

Fluorochrome labels are bound to sites of active bone deposition shortly after administration (Teitelbaum and Nicholas, 1976). This enables identification of bone deposited at different points in time as the labelled bone fluoresces a characteristic colour dependent on the label administered and the filter employed when viewed under ultra-violet light (Table 7.3.3). Hydroxyapatite was found to fluoresce weakly with the FITC 02 filter and appeared white. All other features did not fluoresce and were therefore not visible. With the FITC 09 filter only three of the labels fluoresced, all other features (including the hydroxyapatite) were not visible and appeared black.

Table 7.3.3 Appearance of labelled bone under different filters.

Fluorochrome Label	Appearance under U.V. Light with FITC Filter 02	Appearance under U.V. Light with FITC Filter 09
Calcein Green	Green	Green
Alizarin Red	Red	Red
Tetracycline	Yellow	Orange
Calcein Blue	Blue	Not Visible

Apposition rates were measured using micrographs taken at magnifications of × 200 and × 400. As a result of often non-parallel labelled bands of bone due to discrepancies between the plane of section of the implant and the direction of bone apposition, it was necessary to calculate either an average value from several discrete measurements (Figure 7.3.6a) or a single continuous measurement made using a Quantimet 570 image analyser (Figure 7.3.6b). See Section 5.3.4. for details of the Quantimet 570 image analysis system.

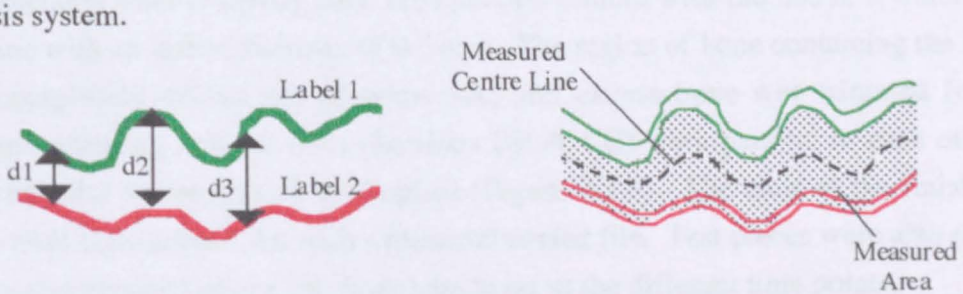

Figure 7.3.6 Measurement of apposition rate with (a) discrete measurements and (b) a continuous measurement.

Images for computer analysis were prepared in which specific regions between the leading edges of two labels were traced by an operator and centre lines were superimposed on the regions. Both the area within the region (shaded area in Figure 7.3.5, A_{AR}, in μm^2), and the length of the centre line, CL_{AR}, (in μm) were then measured and the apposition rate calculated as in equation 7.3.16.

$$\text{Apposition rate } (\mu m \text{ Day}^{-1}) = \frac{(A_{AR} \div CL_{AR})}{\text{Time (Days)}} \qquad (7.3.16)$$

7.3.5 Compression Testing

7.3.5.1 Preparation of test pieces

The precise position of the implants was located with the aid of magnetic resonance images (Figure 7.3.1) or X-radiographs (Figure 7.3.7).

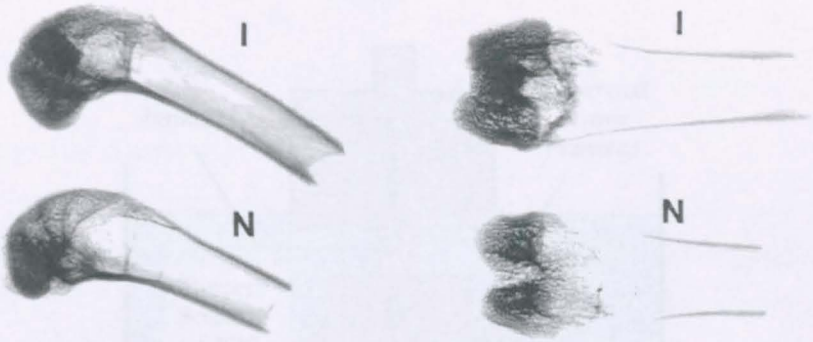

Figure 7.3.7 X-Radiographs taken for specimen location.

(I = Femur containing an Endobon implant; N = Non-operated femur)

The implants were removed from the operated femora with the use of a water cooled trephine with an inside diameter of 6.5 mm. The region of bone containing the implant was completely drilled out (Section AA) and excess bone was trimmed from the implant, ensuring that the ends (Sections BB & CC) were parallel to each other and perpendicular to the axis of the implant (Figure 7.3.8). The ends of the finished test piece were then ground flat with a diamond coated file. Test pieces were also prepared from non-operated femora, i.e. from pure bone, at the different time points.

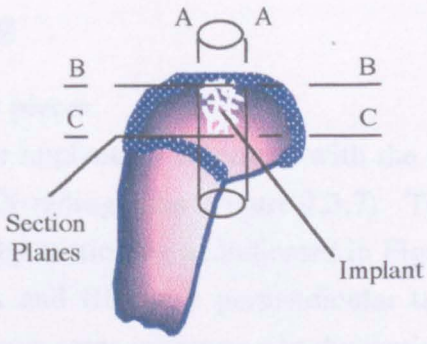

Figure 7.3.8 Dissection of integrated implants for compression testing.

7.3.5.2 Testing of specimens

All compression testing of biological specimens (i.e. those of integrated implants and those of pure bone) was carried out using an Instron 4464 bench top test machine fitted with a 2 kN load cell and test templates created on Series IX Automated Testing System 1.26. Testing was carried out with the use of a specially designed jig, which allowed the specimens to be evaluated in Ringers' solution at 37°C while load was applied axially to the specimens with a crosshead velocity of 0.001 mm s^{-1} (Figure 7.3.9).

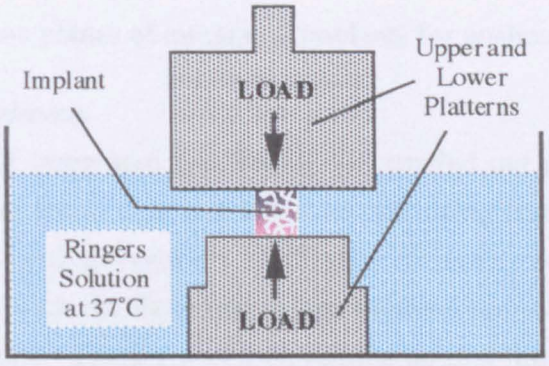

Figure 7.3.9 Test piece arrangement for compression testing of biological specimens.

As in Chapter 5, Section 5.3.5, test pieces were preloaded before testing was carried out under computer control. The results were recorded electronically and the ultimate compressive stress (UCS) was calculated as in equation 7.3.17. The compressive Modulus (E_C) was calculated from the slope of the linear region of the stress strain plot which corresponded to the initial region of elastic deformation during compressive loading (Figure 3.3.1).

$$UCS = \frac{L_{max}}{\pi r^2} \text{ (MPa)} \qquad (7.3.17)$$

Where L_{max} is the maximum load recorded during the test in N and r is the radius of the specimen in mm.

7.3.6 Push-Out Testing

7.3.5.1 Preparation of test pieces

The precise position of the implants was located with the aid of magnetic resonance images (Figure 7.3.1a) or X-radiographs (Figure 7.3.7). The test piece was prepared from the operated femora by sectioning as indicated in Figure 7.3.10, ensuring where possible that surfaces AA and BB were perpendicular to the axis of the implant. However, as there was always some inaccuracy in the cutting of the sections a jig was designed which was able to rotate in two directions allowing the longitudinal axis of the implant to be correctly aligned with the direction of applied force (Figure 7.3.11b).

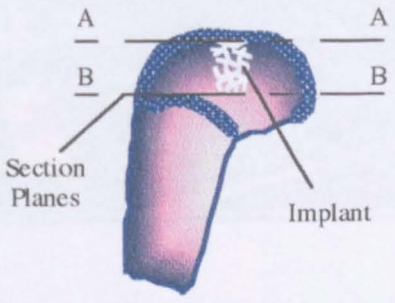

Figure 7.3.10 Section planes of integrated implants for pushout testing.

7.3.5.2 Testing of specimens

All push-out testing of integrated specimens was carried out using an Instron 4464 bench top test machine fitted with a 2 kN load cell using test templates created on Series IX Automated Testing System 1.26 (Figure 7.3.11a). Test pieces were gently clamped into position with the deep end of the implant centred over the hole in the pushout jig support plate. The jig was then rotated so that the superficial end of the implant was aligned with the push out pin (Figure 7.3.11b). Once suitably aligned, operation procedures were similar to those described for compression testing (Chapter 5, Section 5.3.5). Testing was performed with a crosshead velocity of 0.0083 $mm.s^{-1}$ and Ringers' solution at 37°C was pipetted onto the test pieces. The tests were recorded electronically with a sample rate of 10 points s^{-1}. The interfacial shear strength (ISS) was calculated using equation 7.3.18.

$$ISS = \frac{L_p}{\pi \emptyset l} \text{ (MPa)} \qquad (7.3.18)$$

Where L_p is the load required to dislodge the implant in N, Ø is the diameter of the implant and l the length of the implant in mm. Push out tests were also carried out on specimens "implanted" in slices of non-viable equine cancellous bone in order to

determine the apparent interfacial shear strength as a result of friction between the implant and surrounding tissue.

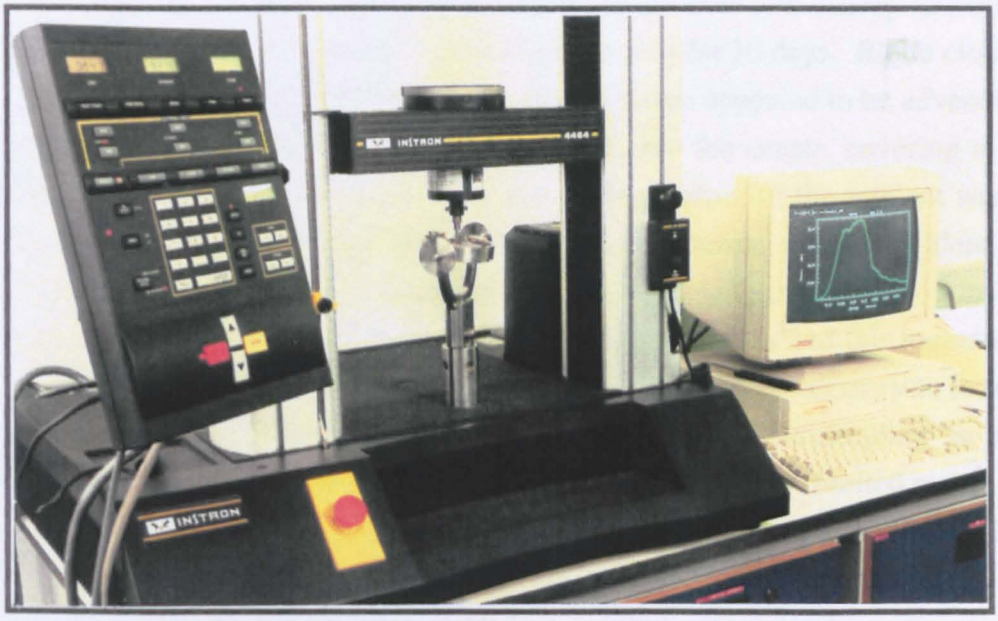

(a)

(b)

Figure 7.3.11 (a) Assembly for the pushout testing of implants and (b) close up of specimen in testing jig.

7.4 Results

After retrieval of the femora,individual ceramic struts were still clearly identifiable on the visible surface of all implants that had been *in vivo* for 10 days. Blood clotting was evident within the implant and some loose fibrous tissue appeared to be advancing over the implant surface from the edges of the defect into the centre, covering the rough ceramic surface. After 5 weeks *in vivo* the visible surface of the implant was coated with an opaque, smooth fibrous layer. The ceramic structure was still evident beneath this layer, although the internal blood clotting was no longer apparent. By 3 months the articular cartilage appeared fully healed over 50% of implants and this increased to 70 % after 6 months *in vivo*. X-radiographs or MRI images were necessary to locate these implants as the defect site was indistinguishable from the surrounding un-operated surface (Figure 7.4.1a). However, there were some instances of limited repair, usually associated with incorrect implant positioning, where ceramic struts protruded above the sub-chondral plate (Figure 7.4.1b),or infection.

(a) (b)

Figure 7.4.1 (a) Completed and (b) limited cartilage repair after 6 months *in vivo*.

7.4.1 Histology

Low density (Batch B) specimens were studied after 10 days *in vivo*. There was no evidence of bone regeneration within the centre of the macro-porous structure of the implant and only isolated areas of bone regeneration in the periphery of the implant, which did not appear to be in direct contact with the surrounding bone in the plane of

the histological section (Figure 7.4.2a). The site appeared to be recovering from the surgical insult, with significant regeneration of bone occurring from the deep end of the defect and limited regeneration occurring at the defect walls (Figure 7.4.2b). The interior of the implant contained a mixture of clotted blood and assorted cells. There was no conclusive evidence of osseo-inductive behaviour at this time point, as the isolated instances of regeneration in the periphery of the implant may have been due to osseo-conduction from the surrounding bone.

In all specimens the majority of bone ingrowth appeared to occur within the first 5 weeks and proceeded predominately from the distal end of the defect, in low density specimens the ingrowth penetrated approximately half the depth of the implant, with some integration from the walls of the defect (Figure 7.4.3a). However, the depth of penetration at this time point was reduced in the higher density specimens (batches C and A) (Figure 7.4.3b). The histological response to implants of all densities (batches B, C and A) after 5 weeks *in vivo* was similar. Fibrous encapsulation was not observed around the implants and there was evidence of the direct apposition of bone on the internal strut surfaces (Figure 7.4.4a). Cellular response was favourable with cells such as osteoblasts and osteocytes observed in close proximity to the implant surfaces (Figure 7.4.4b). Active areas of bone deposition, resorption (Figure 7.4.5a) and even remodelling (Figure 7.4.5b) were observed occurring within all implants that had been *in vivo* for at least 3 weeks. There was also some evidence of tissue integration within the ceramic struts (Figure 7.4.5a). From the fluorochrome labelling, it was evident that bone at the periphery of the implant was rapidly laid woven bone (Figure 7.4.6a), while the direct apposition of lamellar bone was observed on central, internal strut surfaces at 3 and 4 weeks (Figure 7.4.6b). However, any bone observed within the implant macropores (usually near the periphery) that had been deposited in the first two weeks was woven in nature (Figure 7.4.7a). The chronological ordering of the labels, from the implant surface to the bone surface, also demonstrated that the majority of ingrowth within the implants started at the strut surfaces and grew into the macro-pores suggesting osseo-inductive behaviour (Figure 7.4.7b).

At three months, bone had penetrated through-out the length of both Batch A and B implants (Figure 7.4.8a) and cartilage repair was also well progressed, particularly in high density specimens (Figure 7.4.8b). Active remodelling was still occurring, with revascularisation (7.4.9a) and invasion of bone marrow stroma in the distal implant macropores (Figure 7.4.9b). The importance of micro porosity became apparent as there was further evidence of vascular-, cellular- and osseo-integration, within the implant struts (Figure 7.4.10a). There was also an isolated instance of osteoclastic or

macrophagocytic activity within a high density specimen on a ceramic surface (Batch A), where ceramic particles were observed within the cell (Figure 7.4.10b).

At 6 months the macro-porous structure of low density (Batch B) specimens had been incorporated into the structure of the surrounding cancellous bone (Figure 7.4.11a). Bone ingrowth was more evenly distributed throughout the length of the implant and the degree of cellular activity had abated; seams of active osteoblasts were no longer prevalent, but had been replaced by quiescent "bone lining" cells (Figure 7.4.11b). There was also evidence of increased vascularity within the implants compared to those at 3 months as well as continued integration within the ceramic struts. There appeared to be more cellular activity in the high density specimens (Batch A), although again this was less than that at 3 months. The degree of vascularity was also increased in the high density specimens, however, there were two distinct developments in the appearance of the bone ingrowth within the macro-porous structure of the high density specimens. Remodelling appeared to have reduced the amount of ingrowth within the centre of one implant, leaving only the periphery of the implants fully integrated (Figure 7.4.12a). In contrast, the other implant prepared for histology was still fully integrated with bone which appeared to possess a structure similar to cortical bone (Figure 7.4.12b).

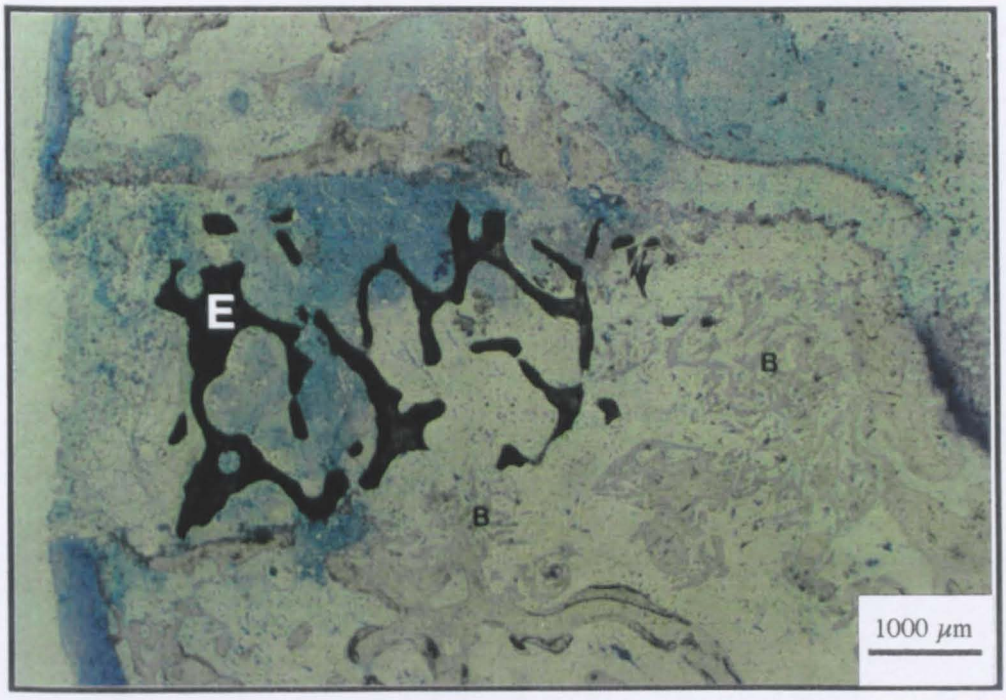

(a)

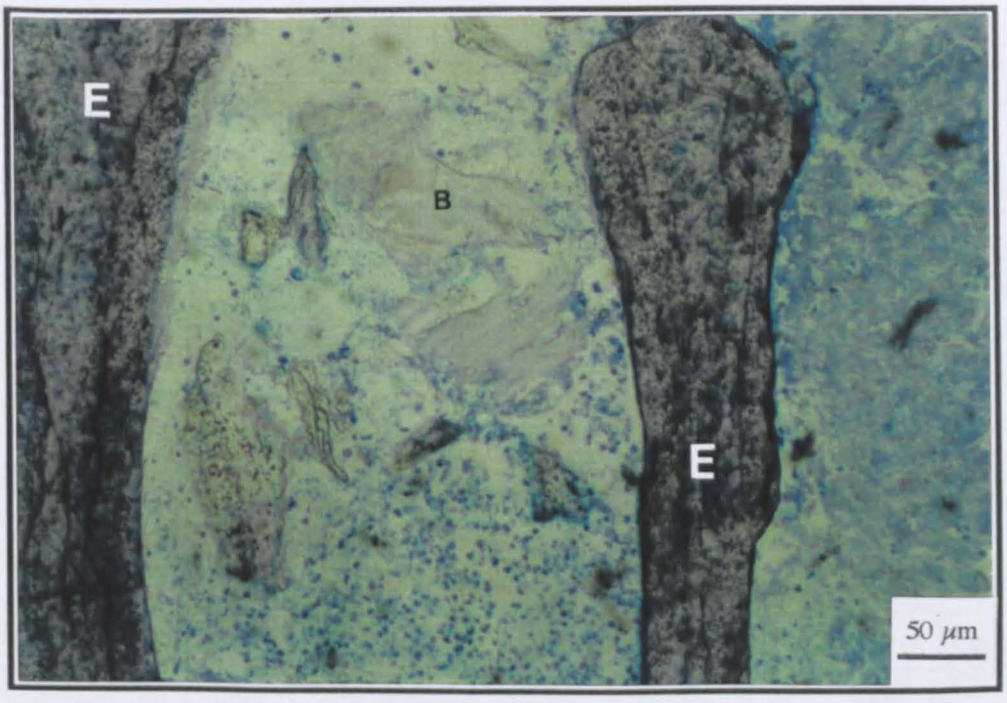

(b)

Figure 7.4.2 Histological appearance of low density (Batch B) implants after 10 days *in vivo*; (a) macroscopically (b) at periphery of implant.

E = Endobon Strut, B = New Bone

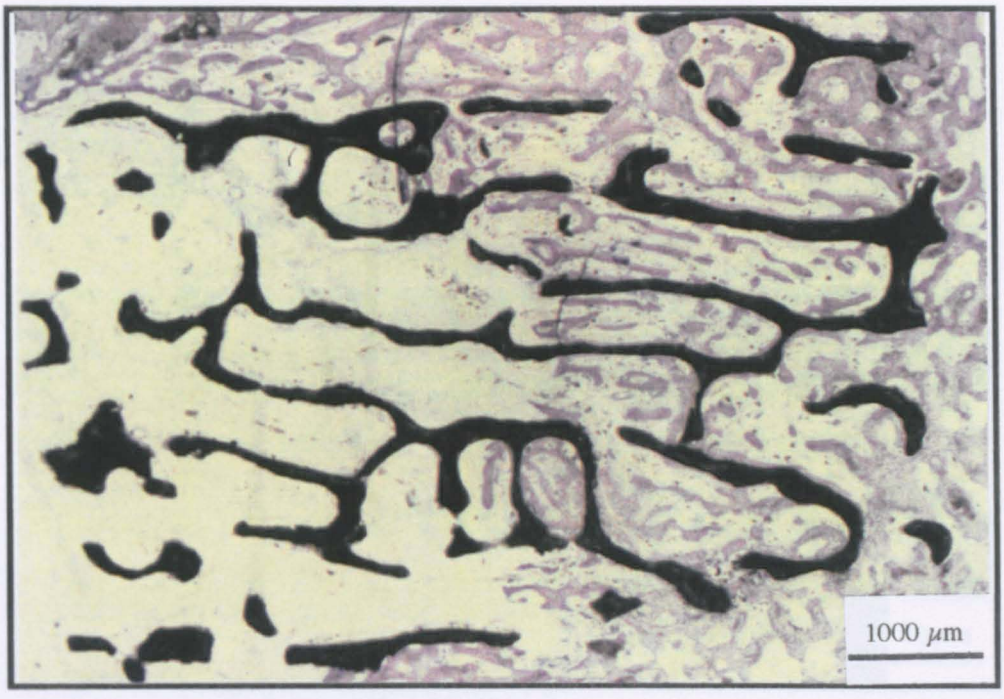

(a)

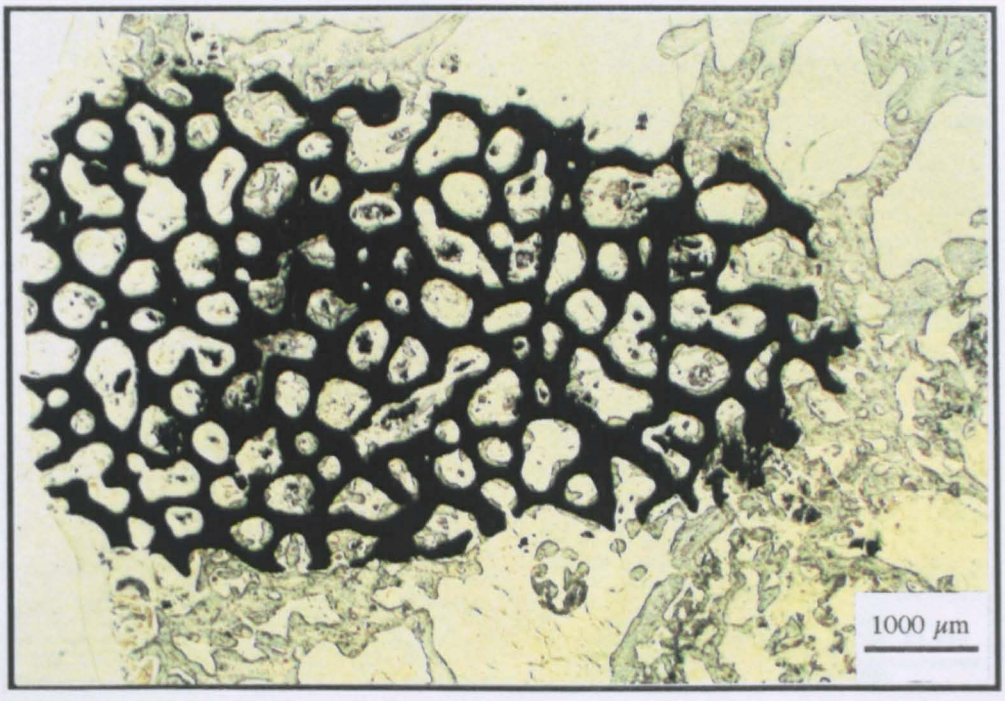

(b)

Figure 7.4.3 Integration of (a) low density (Batch B) and (b) high density (Batch A) implants after 5 weeks *in vivo*.

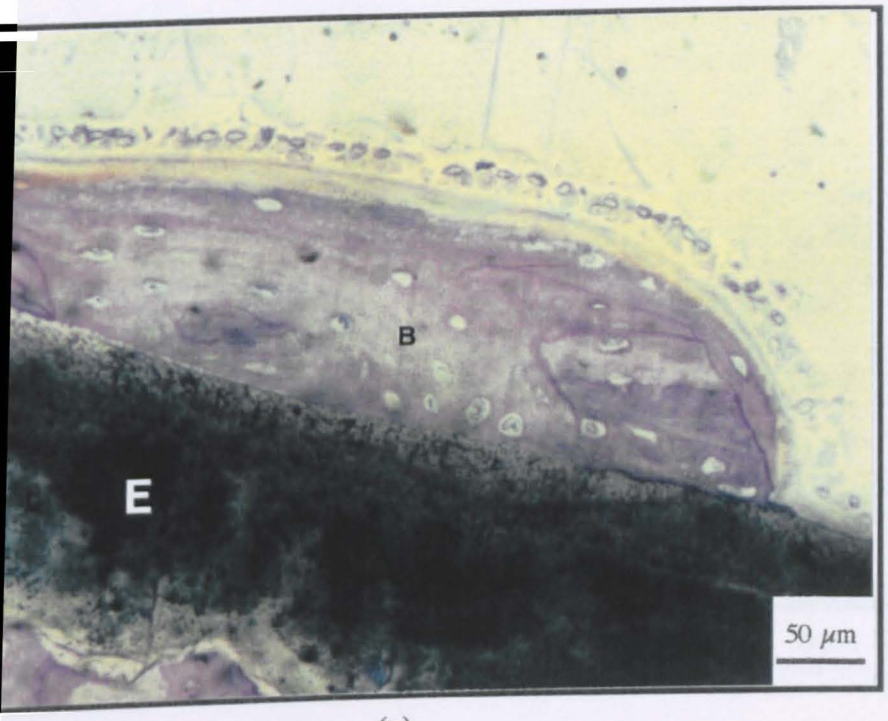

(a)

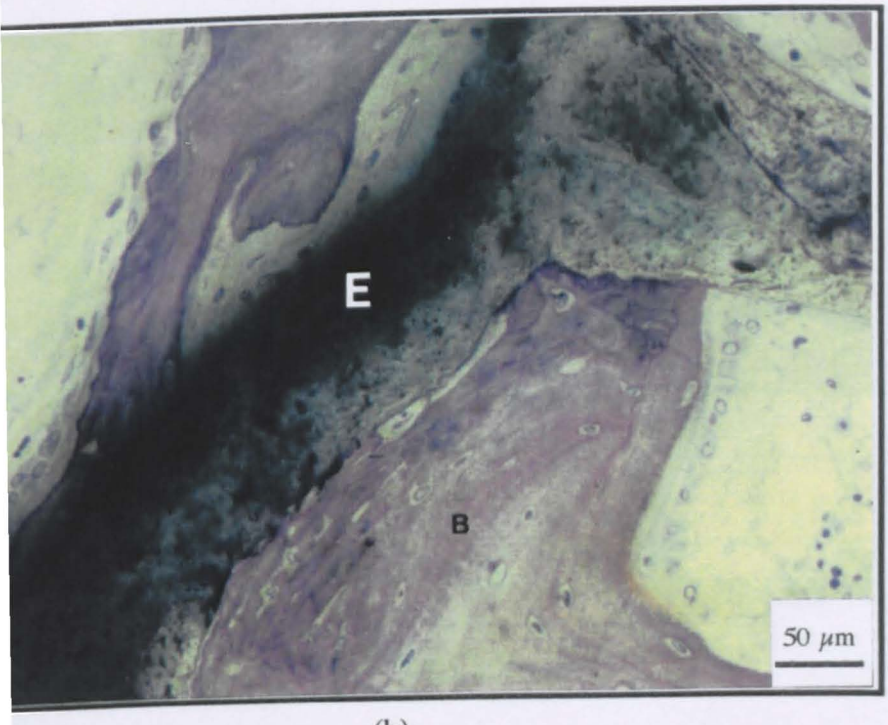

(b)

(a) Bone apposition and (b) cellular activity at the implant strut surfaces
ant after 5 weeks *in vivo*. (Batch B specimens.)
E = Endobon Strut, B = Cancellous Bone

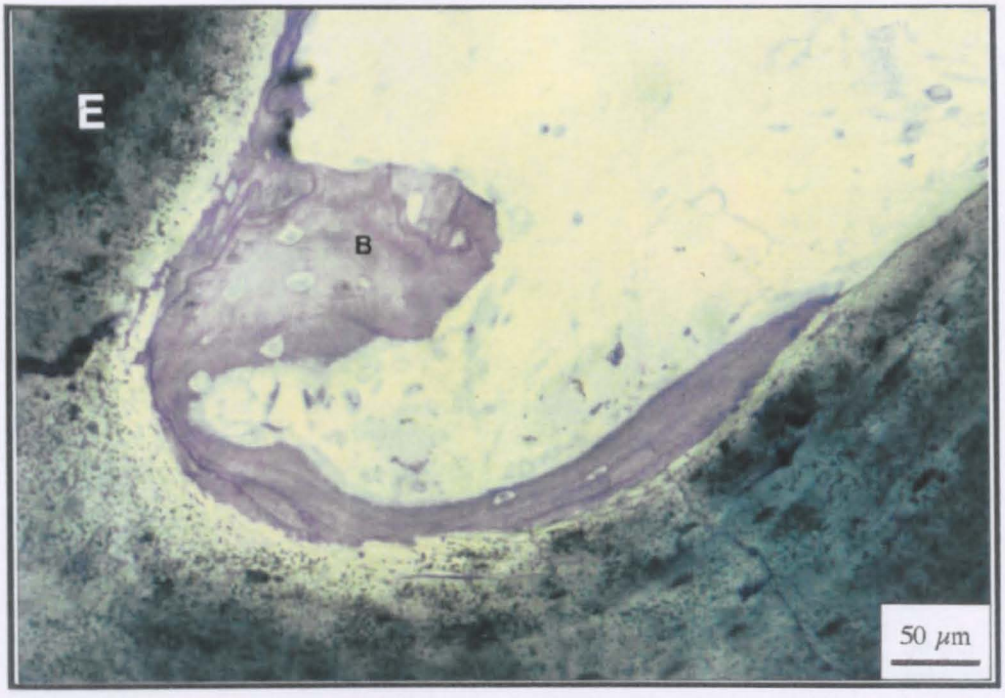

(a)

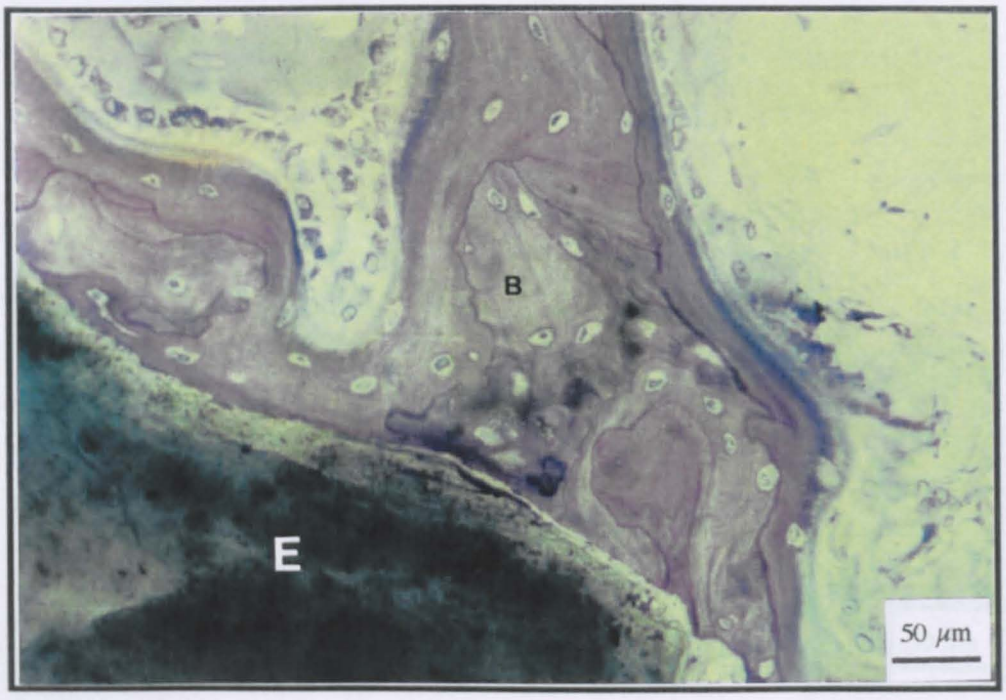

(b)

Figure 7.4.5 Bone (a) resorption and (b) remodelling occurring on internal implant strut surfaces after 5 weeks *in vivo*. (Batch B specimens.)

E = Endobon Strut, B = Cancellous Bone

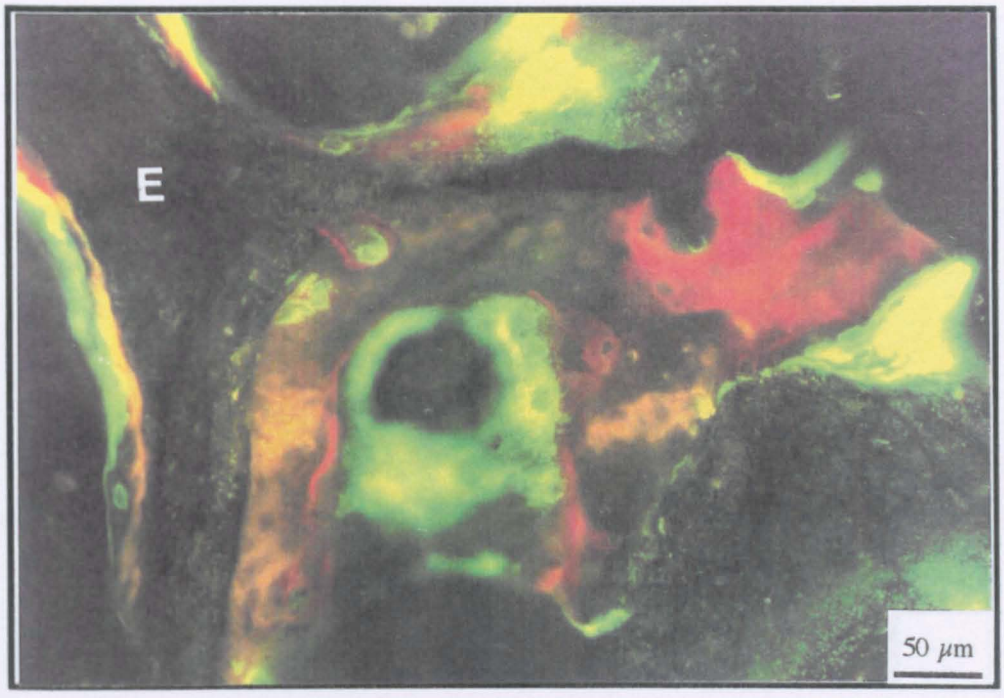

(a)

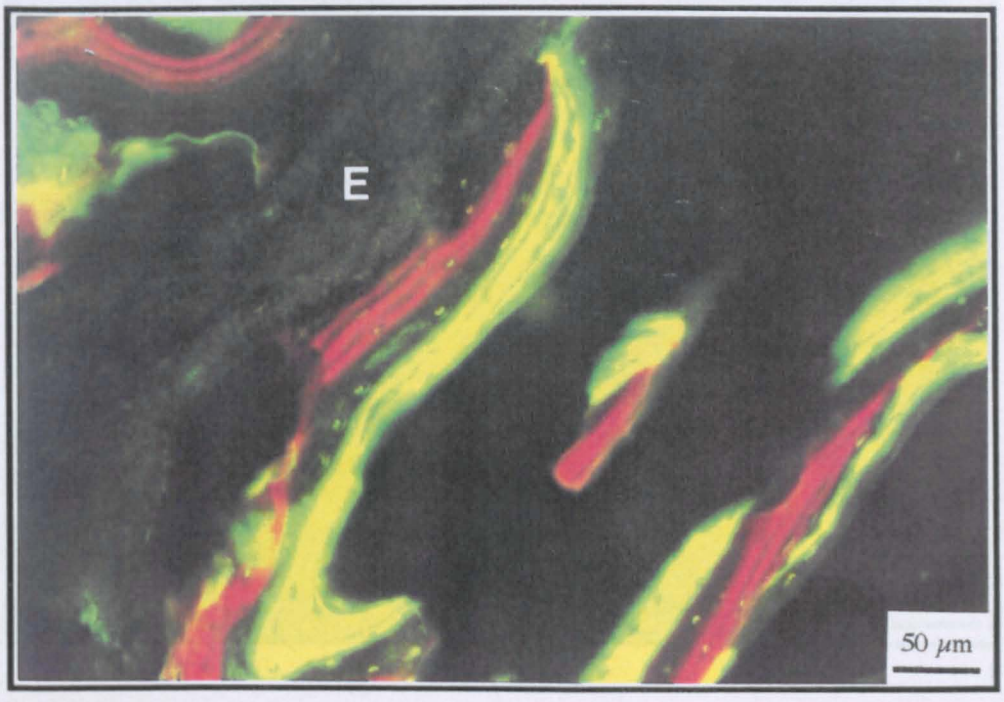

(b)

Figure 7.4.6 (a) Fluorochrome labelled bone demonstrating (a) woven bone at the periphery of an implant and (b) lamellar bone deep within the macroporosity of an implant. (Batch B specimen; orange = 1-2 weeks, red = 3-4 weeks, green = 4-5 weeks.)

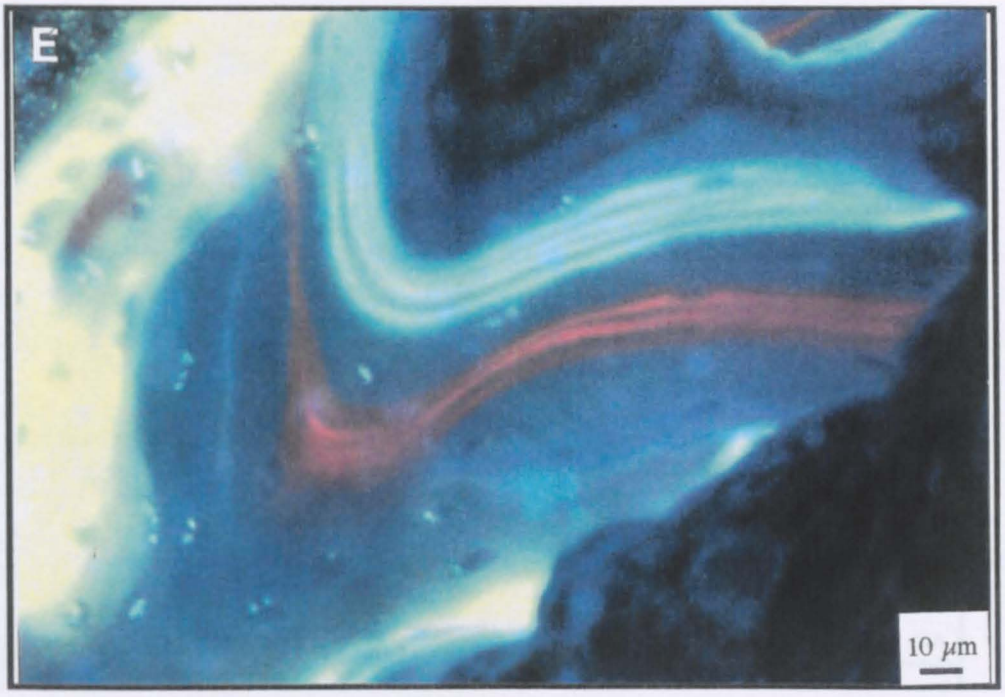

(a)

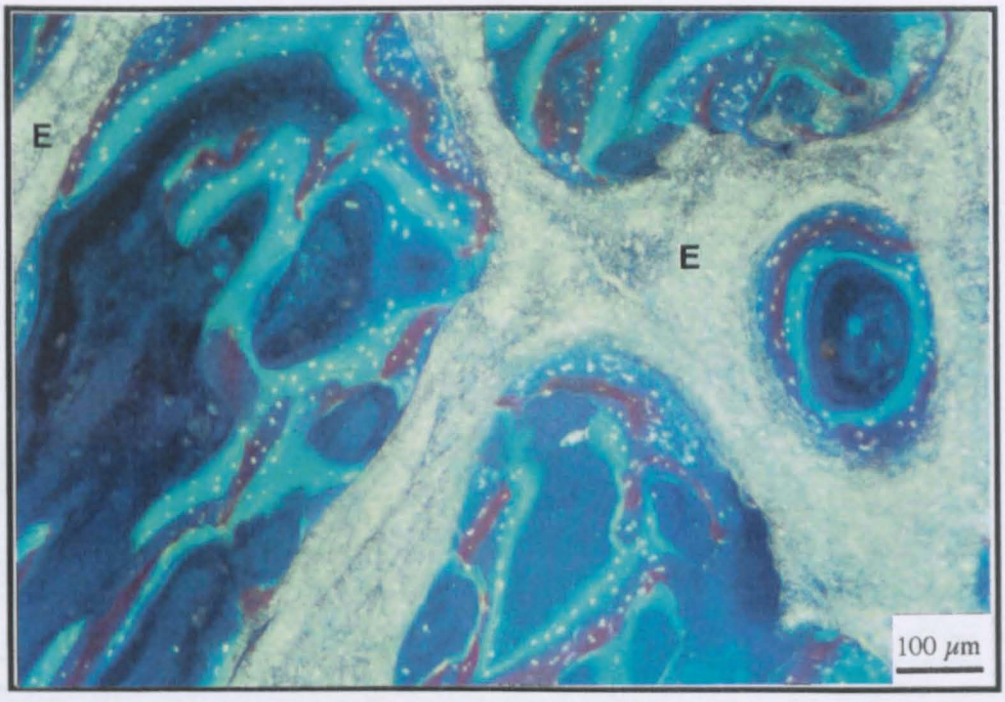

(b)

Figure 7.4.7 Fluorochrome labelled bone after 5 weeks *in vivo*, within low density implant macropores (a) near the periphery demonstrating woven bone deposited at 1-2 weeks (yellow) and lamellar bone deposited at 2-3 (blue), 3-4 (red) and 4-5 (green) weeks; (b) in the centre demonstrating direction of bone apposition on strut surfaces.

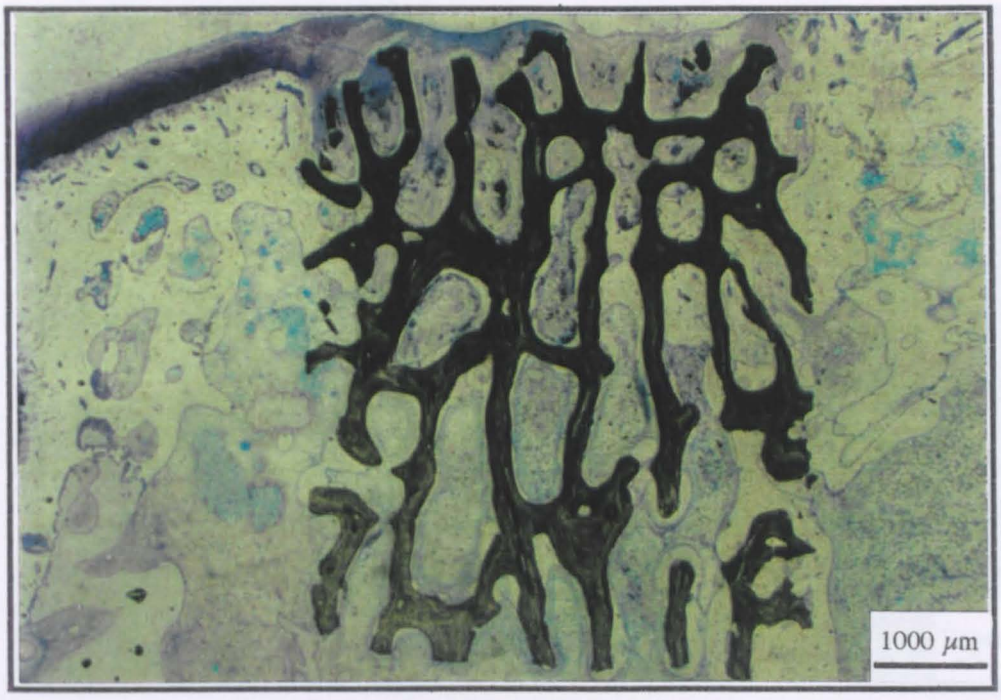

(a)

(b)

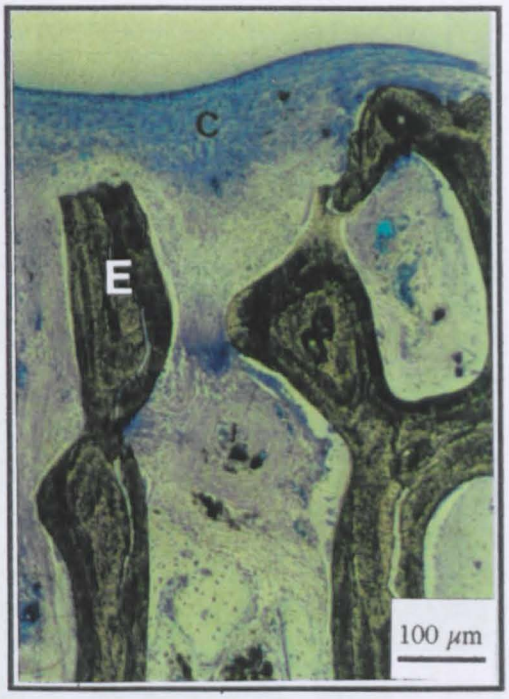

(c)

Figure 7.4.8 (a) Integration of bone within a high density (Batch A) implant after 3 months *in vivo*. Cartilage repair on upper surface of a (b) low and (c) high density (Batch A) implant after 3 months.

E = Endobon Strut, F = Fibrous Tissue, C = Fibro-Cartilage.

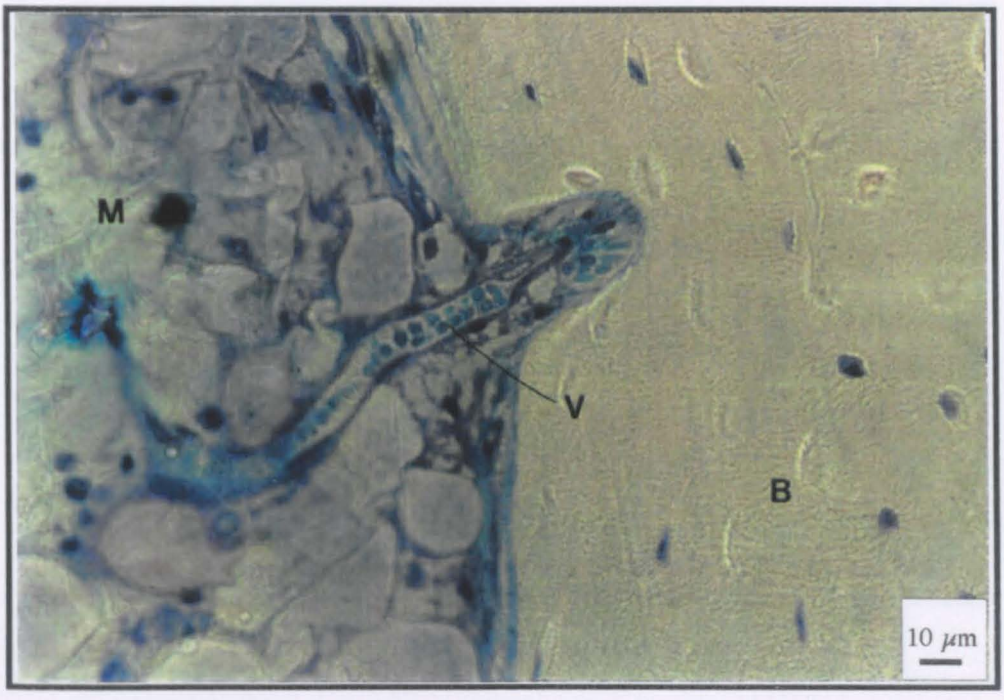

(a)

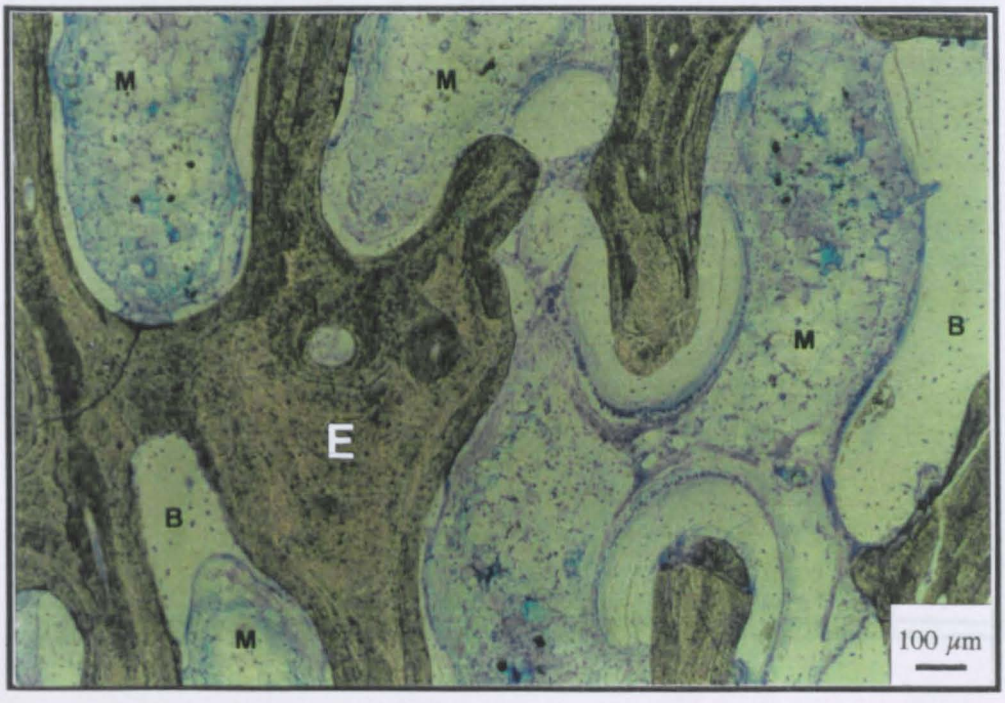

(b)

Figure 7.4.9 (a) Revascularisation and (b) invasion of marrow stroma, within an implant after 3 months *in vivo*. (Batch A specimen.)

V = Blood vessel, B = Cancellous Bone, M = Marrow, E = Endobon.

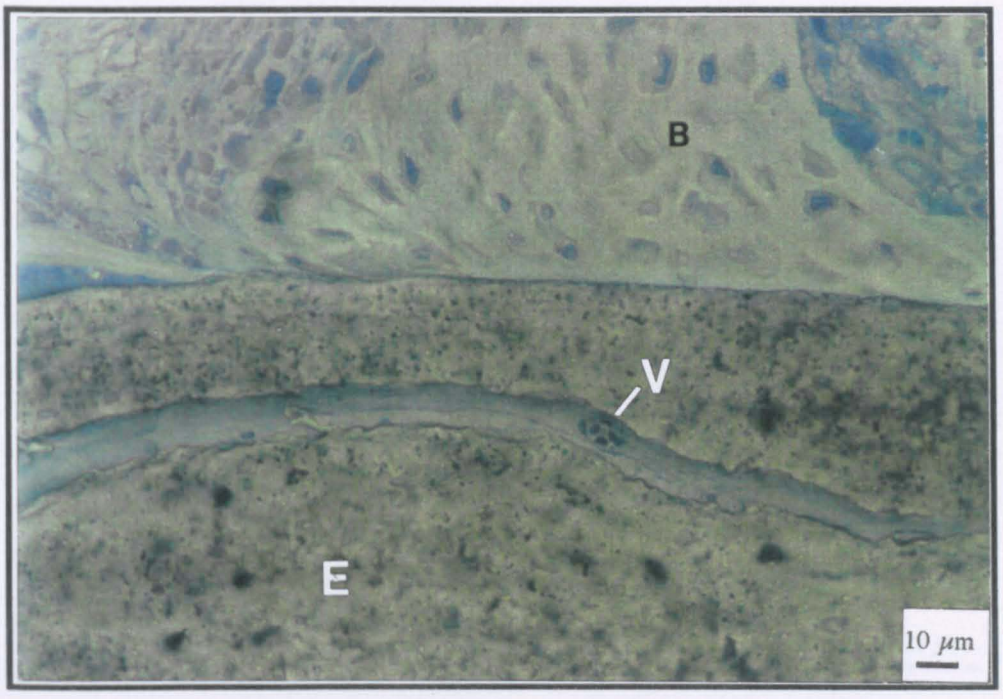

(a)

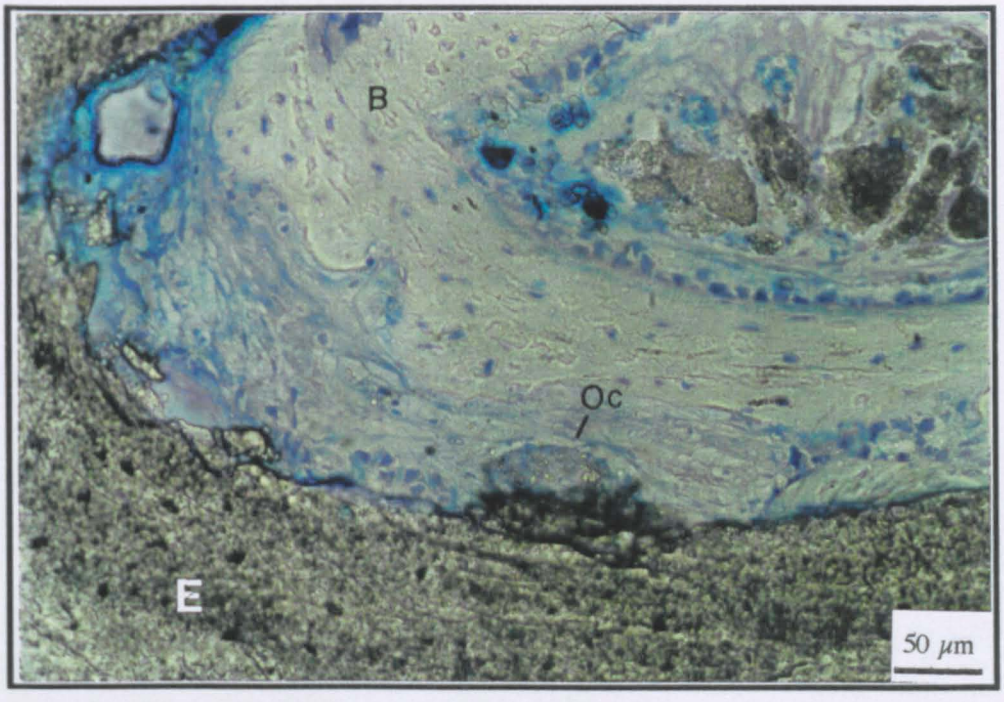

(b)

Figure 7.4.10 (a) Integration of bone within the microstructure of the ceramic struts. (b) Phagocytic activity on a strut surface within the centre of an implant. (Batch A specimens.)

V = Blood vessel, B = Cancellous Bone, E = Endobon Oc = Osteoclast.

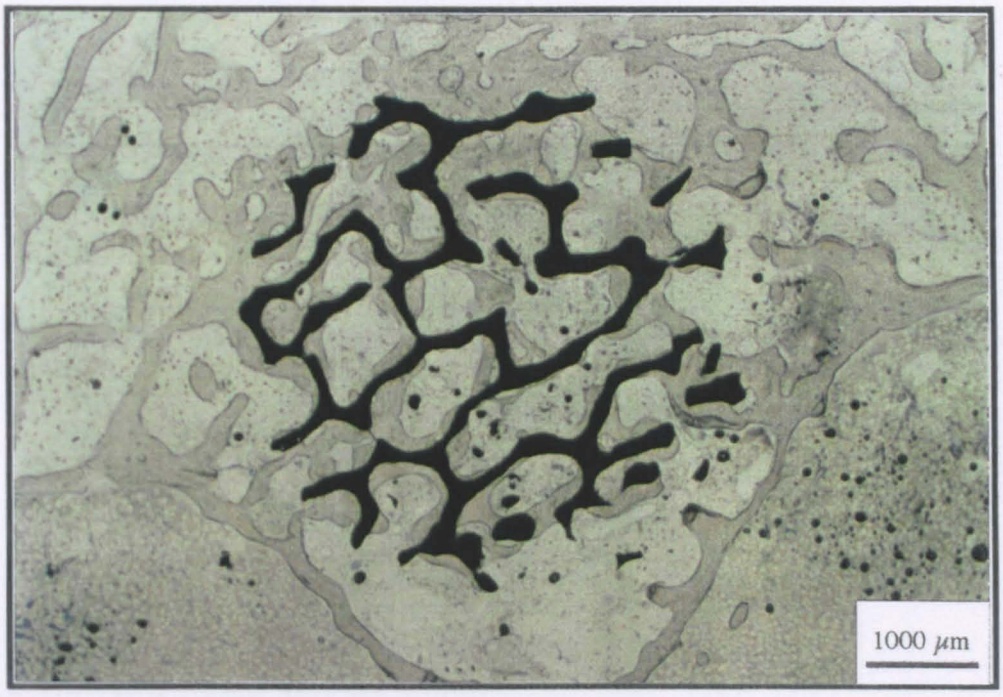

(a)

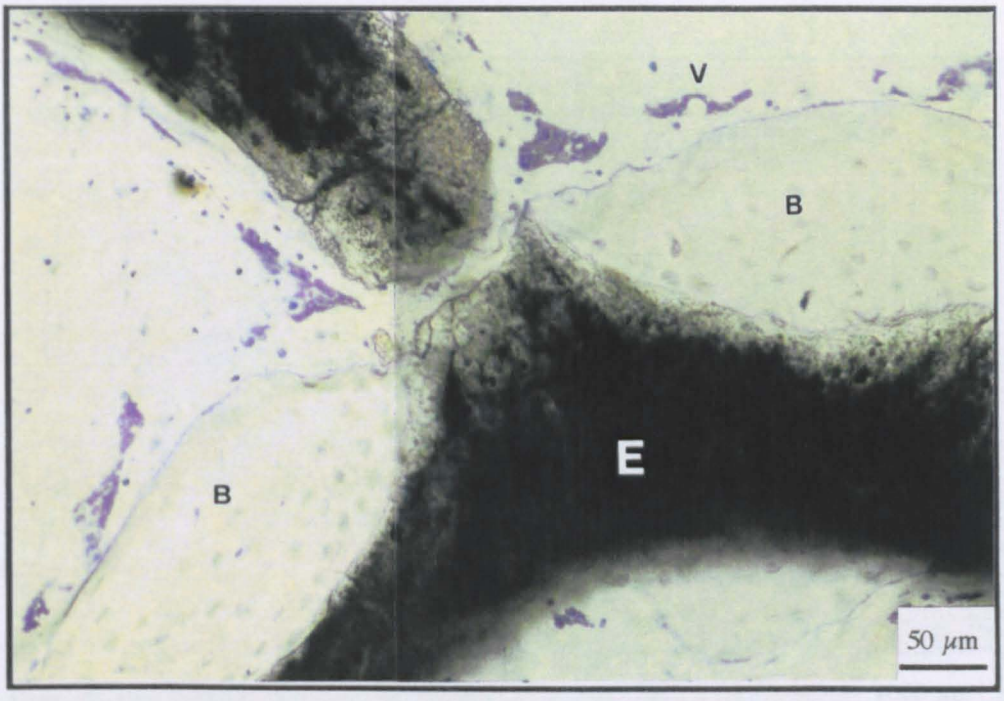

(b)

Figure 7.4.11 Histological appearance of low density (Batch B) implants after 6 months *in vivo*; (a) macroscopically (b) detail of vascularity and quiescent bone surfaces within central macropores.

V = Blood vessel, B = Cancellous Bone, E = Endobon.

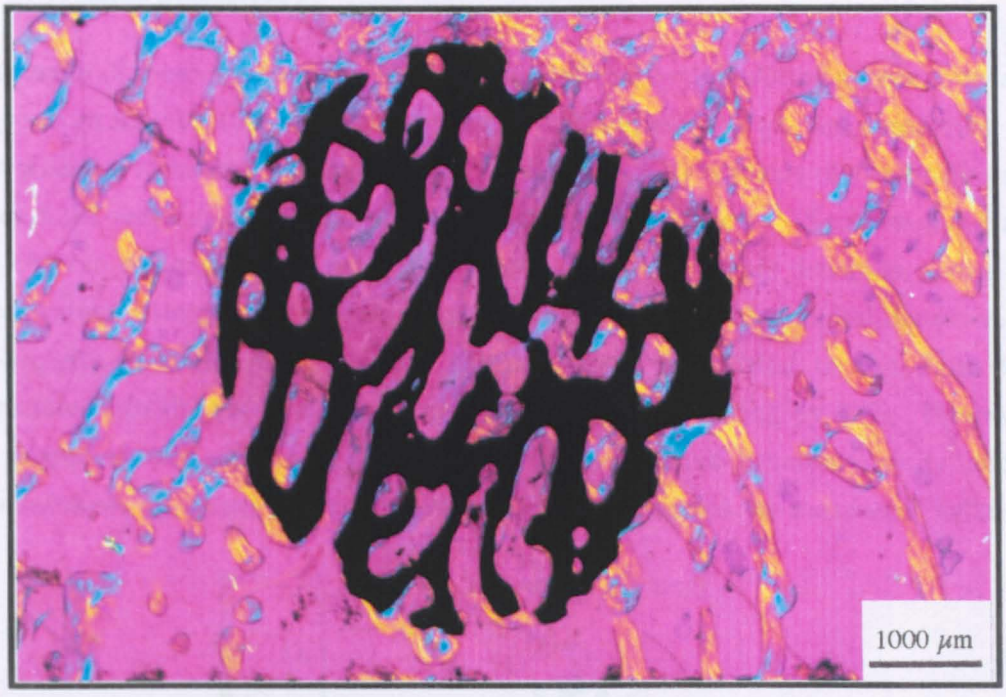

(a)

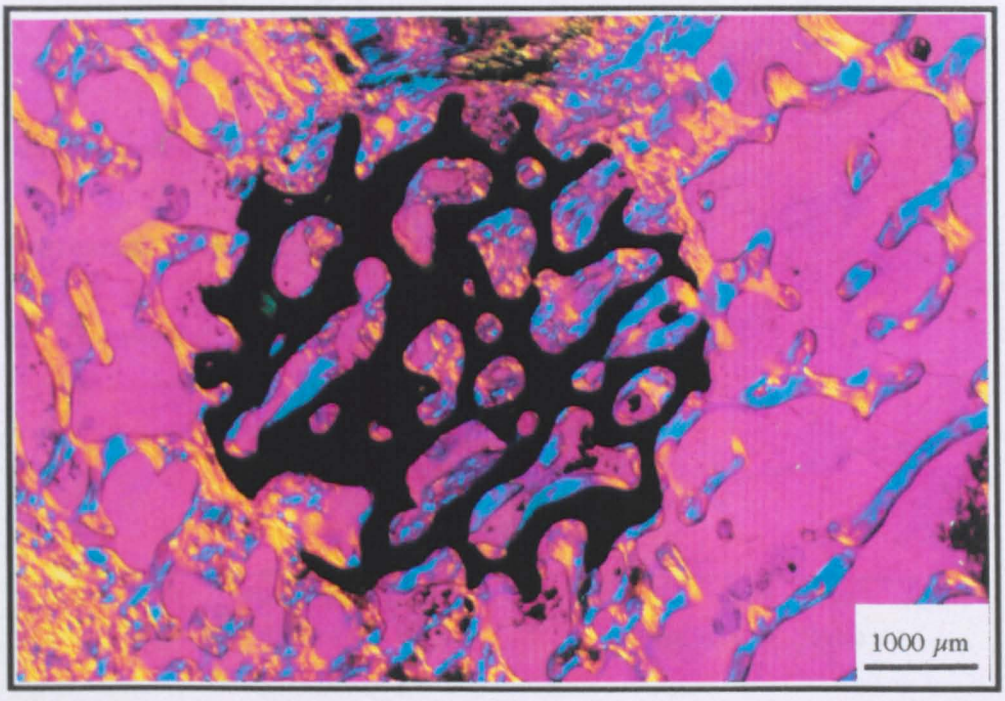

(b)

Figure 7.4.12 Macroscopic appearance of high density (Batch A) implants after 6 months *in vivo*; (a) remodelled (b) fully integrated.

7.4.2 Histomorphometry

The accuracy of the point counting method was verified by calculating apparent density (AD_{calc}) from the absolute volume percentage of Endobon (AV_E), and comparing the results with the measured apparent density (AD_{meas}). As a result of the findings in Chapter 5 the real density of the struts was taken as 2.58 $g.cm^{-3}$ (Sections 5.4.3 and 5.5.2). As can be seen from Figure 7.4.13, the calculated apparent densities, across the range of values tested, were generally greater than the measured apparent densities. A linear equation, constrained to pass through zero, was fitted to the data, and demonstrated that the point counting method was over-estimating by 14%. However, as the degree of over-estimation appears to be independent of apparent density, and to avoid confusion, all values quoted in this thesis are uncorrected "as-measured" values.

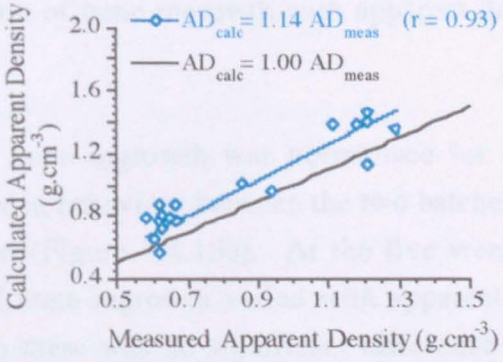

Figure 7.4.13 Verification of point counting method.

7.4.2.1 Percentage of Bone Ingrowth

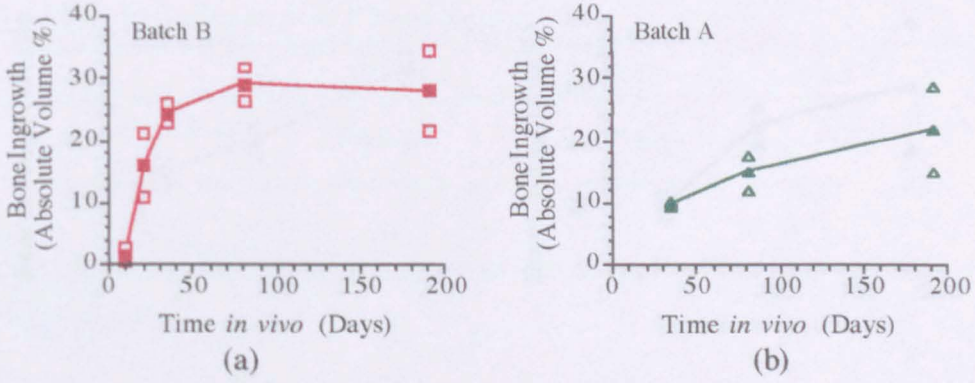

Figure 7.4.14 Variation of bone ingrowth within (a) Batch B and (b) Batch A implants.

Quantitative assessment of the volume of bone ingrowth within Batch B implants confirmed that the majority of the bone ingrowth occurred within the first five weeks

and was complete by 3 months (Figure 7.4.14a). The rate of bone ingrowth in the Batch A specimens was reduced in comparison to the rate of ingrowth in Batch B implants and continued to rise up to 6 months post-operatively (Figure 7.4.14b).

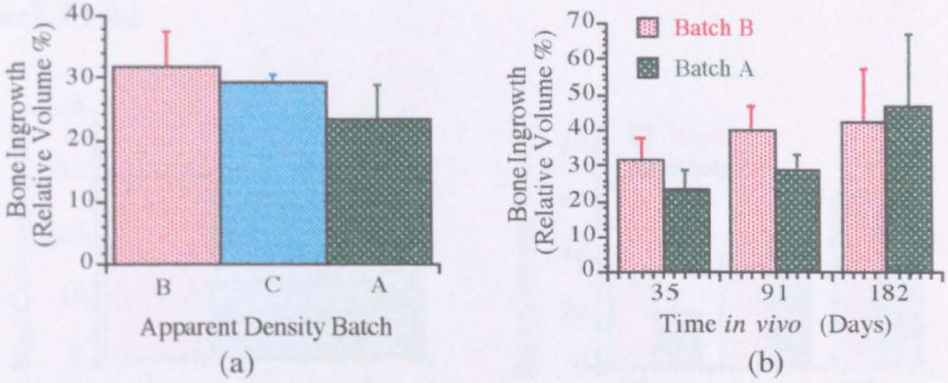

Figure 7.4.15 Variation of bone ingrowth with apparent density (a) at 5 weeks and (b) with time.

When the volume of bone ingrowth was normalised for available pore space for ingrowth the difference in behaviour between the two batches of implants with time *in vivo* was still apparent (Figure 7.4.15b). At the five week time point the relative volume percentage of bone ingrowth varied with apparent density (Figure7.4.15a), however by 6 months there was no significant difference between Batch B and A implants (Figure7.4.15b).

7.4.2.2 Bone Coverage of Implant Surfaces

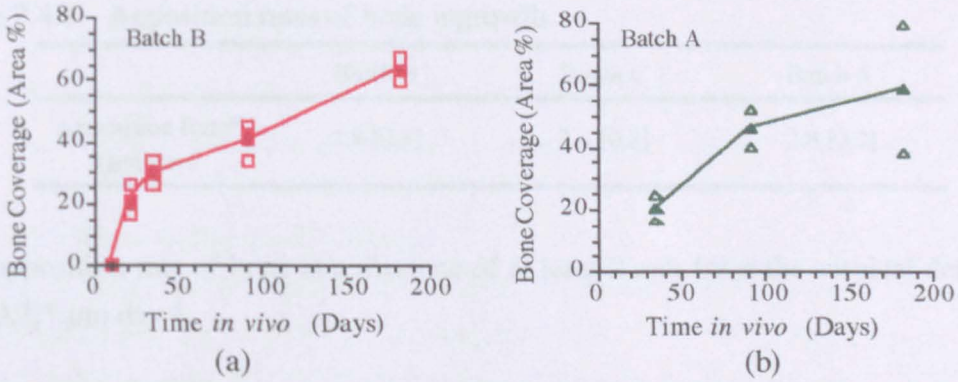

Figure 7.4.16 Percentage of bone coverage within (a) Batch B and (b) Batch A implants with time *in vivo*.

Unlike the bone ingrowth the bone coverage, or contact area between the implant and the bone ingrowth, continued to rise with time for both batch A and B implants, up to 6

months (Figure 7.4.16). Furthermore, the rate of coverage within the two systems appeared similar from 5 weeks to 6 months. At the five week time point the percentage of bone coverage varied with apparent density (Figure7.4.17a). However at 3 and 6 months there was no significant difference between Batch B and A implants (Figure7.4.17b).

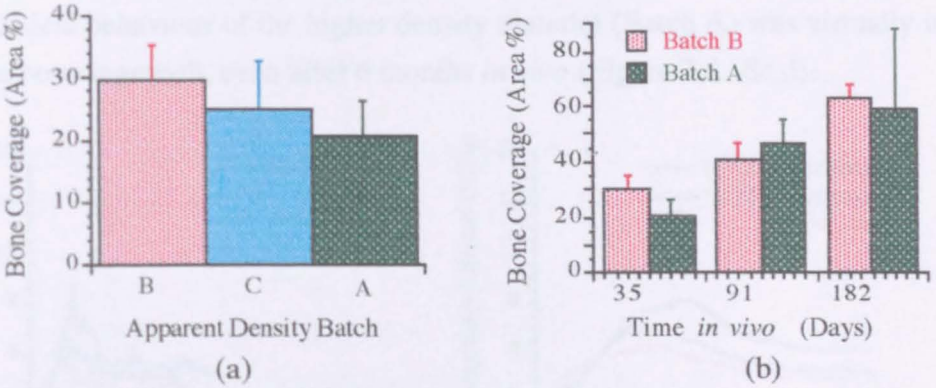

Figure 7.4.17 Variation of bone coverage with apparent density (a) at 5 weeks and (b) with time.

7.4.2.3 Apposition rates

Apposition rates were calculated for all 5 week implants during weeks 3-4 (Table 7.4.1). Determination of the apposition rates of bone deposited between weeks 1-2 and 2-3 in the Batch B specimens was not possible as a result of the predominance of woven bone and the convoluted nature of the bone seams laid down during these time periods, respectively.

Table 7.4.1 Apposition rates of bone ingrowth.

	Batch B	Batch C	Batch A
Apposition Rate* (μm/day)	3.8 [0.3]	3.4 [0.2]	2.8 [0.2]

The apposition rate of bone at a distance of at least 2 mm from the surgical defect was 3.1 [0.2]* μm.day^{-1}.

* Corrected for stereological effects.

7.4.3 Compression Testing

The mechanical behaviour of the low and medium density specimens (Batches B and C) altered significantly after 5 weeks *in vivo* (Figure 7.4.18c), with behaviour closer to that of the cancellous bone removed from the contra-lateral femur (Figure 7.4.18b), than the elastic-brittle behaviour displayed before implantation (Figure 7.4.18a). The mechanical behaviour of the higher density material (Batch A) was virtually unaffected by the bone ingrowth, even after 6 months *in vivo* (Figure 7.4.18c,d).

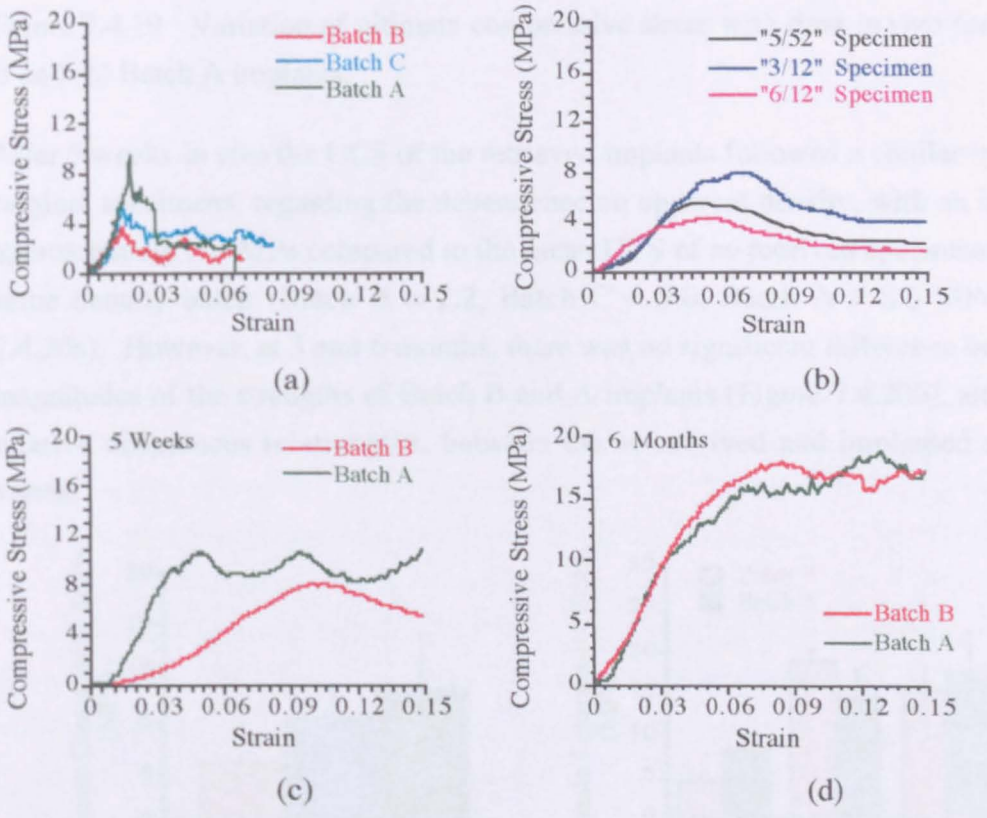

Figure 7.4.18 Compressive behaviour of (a) Endobon specimens, (b) cancellous bone and retrieved Endobon implants after (c) 5 weeks and (d) 6 months *in vivo*.

7.4.3.1 Ultimate Compressive Stress

At 10 days, there was no significant difference in the ultimate compressive stress (UCS) of implanted low density (Batch B) implants at 2.4 [0.8] MPa and as-received low density specimens at 2.5 [0.9] MPa. However, at 5 weeks, the UCS of implanted material increased significantly to 4.9 [2.1] MPa and continued to rise until 3 months *in vivo*, after which the value appeared to stabilise (Figure 7.4.19a). The UCS of high density (Batch A) implants also increased with time *in vivo* (Figure 7.4.19b), where as-received Batch A Endobon had a mean UCS of 8.6 MPa.

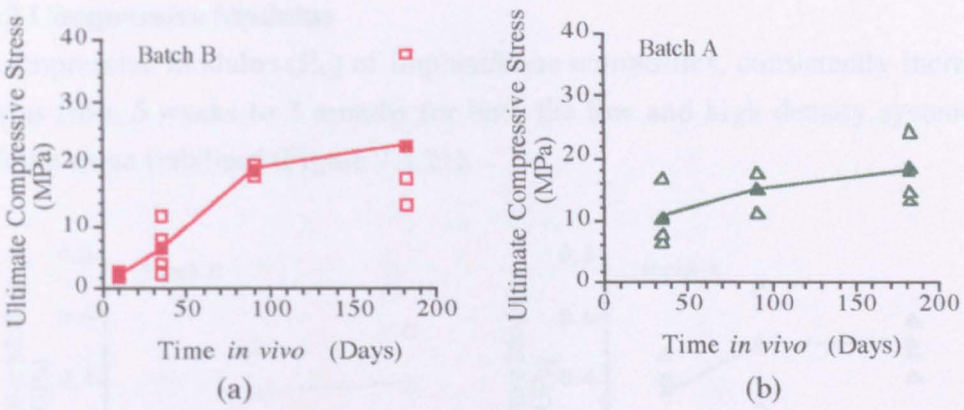

Figure 7.4.19 Variation of ultimate compressive stress with time *in vivo* for (a) Batch B and (b) Batch A implants.

After 5 weeks *in vivo* the UCS of the retrieved implants followed a similar trend to the original specimens, regarding the dependence on apparent density, with an increase of approximately 2-3 MPa compared to the mean UCS of as-received specimens from the same density batch (Batch B = 2.2, Batch C = 5.0, Batch A = 8.6 MPa) (Figure 7.4.20a). However, at 3 and 6 months, there was no significant difference between the magnitudes of the strengths of Batch B and A implants (Figure 7.4.20b), although the relative differences in strengths, between the as-received and implanted specimens varied.

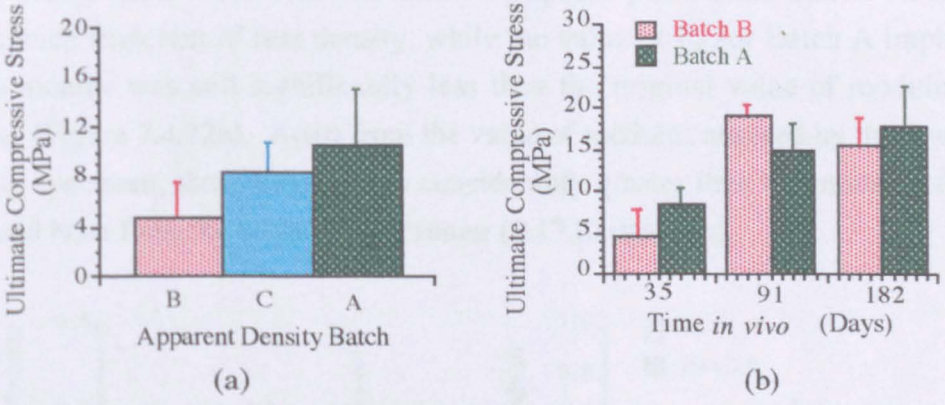

Figure 7.4.20 Variation of ultimate compressive stress with apparent density at (a) 5 weeks and (b) with time.

The UCS of high density (Batch A) implant/bone composites at all time points and low density (Batch B) implant/bone composites at 3 and 6 months was significantly greater than that of un-operated cancellous bone from the contra-lateral femur (6.0 [1.8] MPa).

7.4.3.2 Compressive Modulus

The compressive modulus (E_c) of implant/bone composites, consistently increased in modulus from 5 weeks to 3 months for both the low and high density systems, after which the value stabilised (Figure 7.4.21).

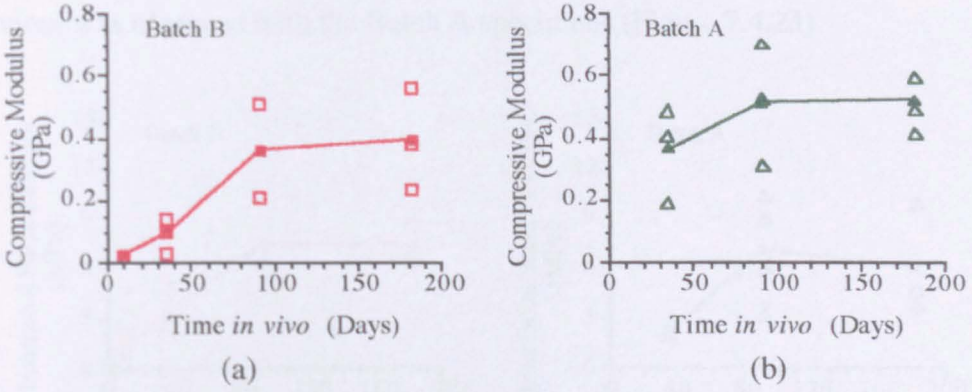

Figure 7.4.21 Variation of compressive modulus with time *in vivo* for (a) Batch B and (b) Batch A implants

Implants from all batches displayed a significant reduction (by 57-75%) in modulus after five weeks *in vivo* (Figure 7.4.22a) when compared to as-received Endobon of similar density (Batch B = 0.4 [0.1] GPa, Batch C = 0.8 [0.2] GPa, Batch A = 1.3 [0.4] GPa). However, at 3 and 6 months Batch B implants possessed a similar value of E_c to as-received Endobon of that density, while the value of E_c for Batch A implants at 3 and 6 months was still significantly less than the original value of modulus at that density (Figure 7.4.22b). Apart from the value of modulus attained by the 5 week, low density specimen, these values were considerably greater than the modulus of the un-operated bone from the contra-lateral femur (0.17 [0.04] GPa).

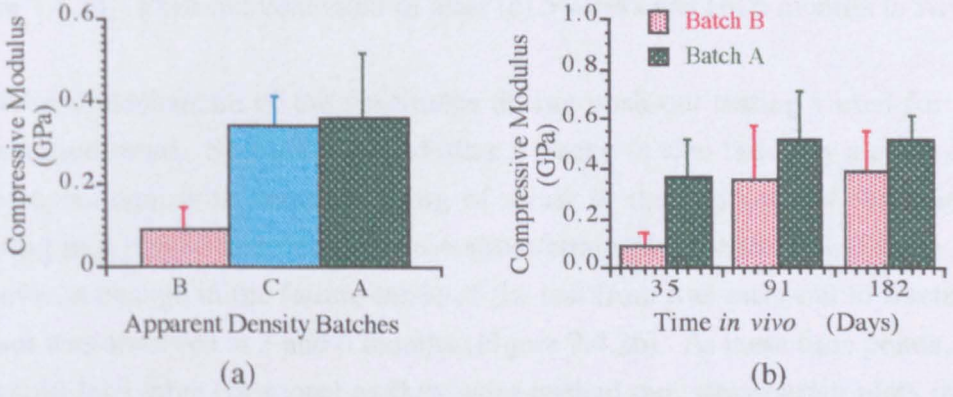

Figure 7.4.22 Variation of compressive modulus with apparent density at (a) 5 weeks and (b) with time.

7.4.4 Push-Out Testing

Pushout testing of Batch B implants at 10 days demonstrated that, despite the minimal amount of bony ingrowth, there was still some degree of "bonding". The shear strength increased with time up to 3 months, at which point a plateau was reached, similar behaviour was observed with the Batch A specimens (Figure 7.4.23).

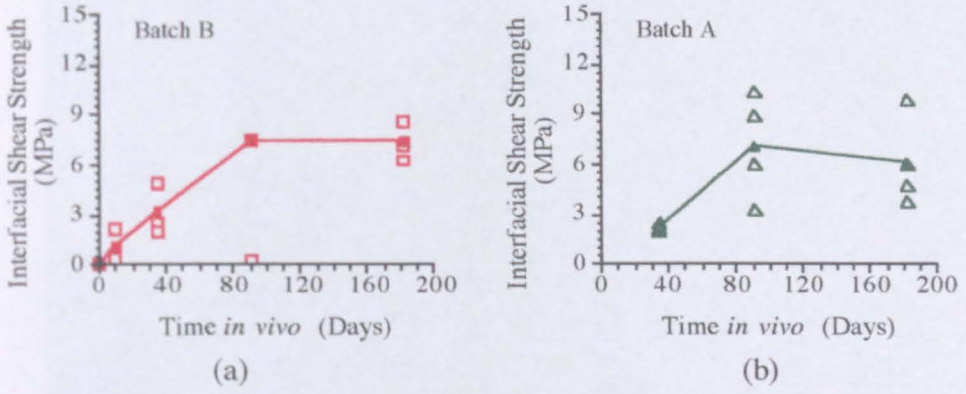

Figure 7.4.23 ISS with time *in vivo* for (a) Batch B and (b) Batch A implants.

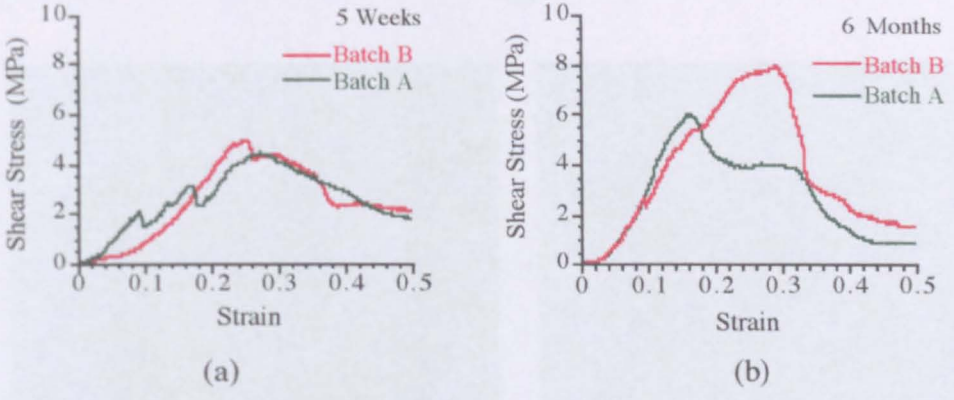

Figure 7.4.24 Push-out behaviour of after (a) 5 weeks and (b) 6 months *in vivo*.

The failure mechanism of the specimens during push-out testing varied for different implantation times. Specimens tested after 5 weeks *in vivo* failed by a clean extrusion of the specimen, with some crushing of struts at the end nearest the loading pin, resulting in a jagged appearance to the stress/strain plot for the test (Figure 7.4.24a). However, a change in the failure mode of the test from true push-out to fracture of the implant was observed at 3 and 6 months (Figure 7.4.26). At these time points, implants were split into three (or more) as they were pushed out, stress/strain plots for typical tests of this type are illustrated in Figure 7.4.24b, and demonstrate a sharper fall in load after failure. Study of sectioned portions of test pieces after failure indicated that

individual struts at or near the interface at all time points had sheared, leaving portions of ceramic in the surrounding bone (Figure 7.4.25).

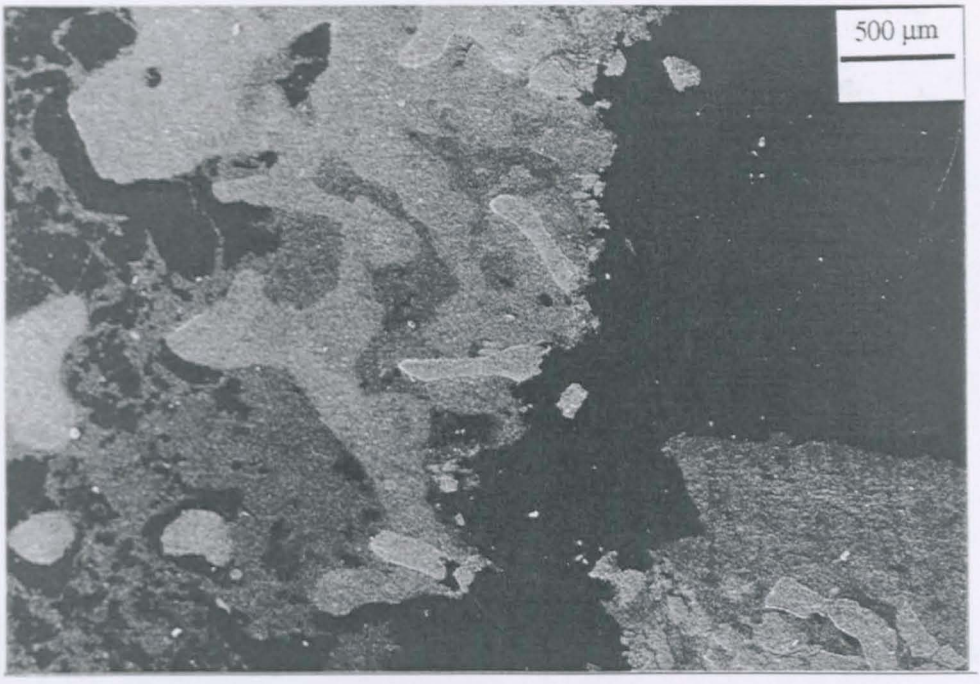

(a)

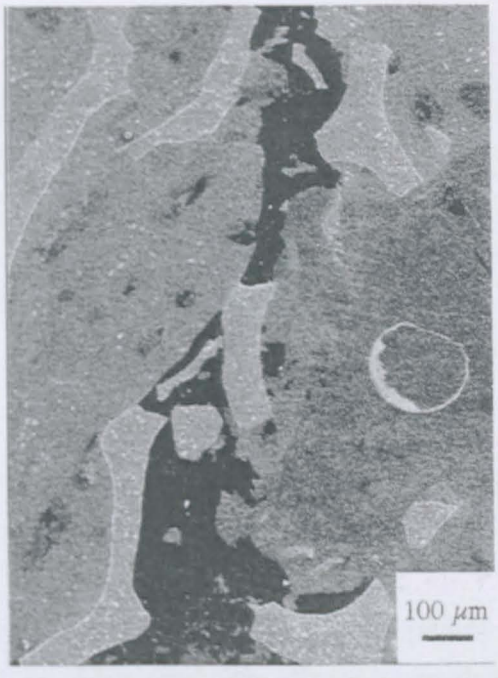

(b)

(c)

Figure 7.4.25 Polished section through push-out test pieces: (a) Upper portion of a 5 week implant. Failure of; (b) a strut, and (c) the bone ingrowth within a 3 month implant.

Figure 7.4.26 Variation of failure mode at (from left to right) 5 weeks, 3 and 6 months.

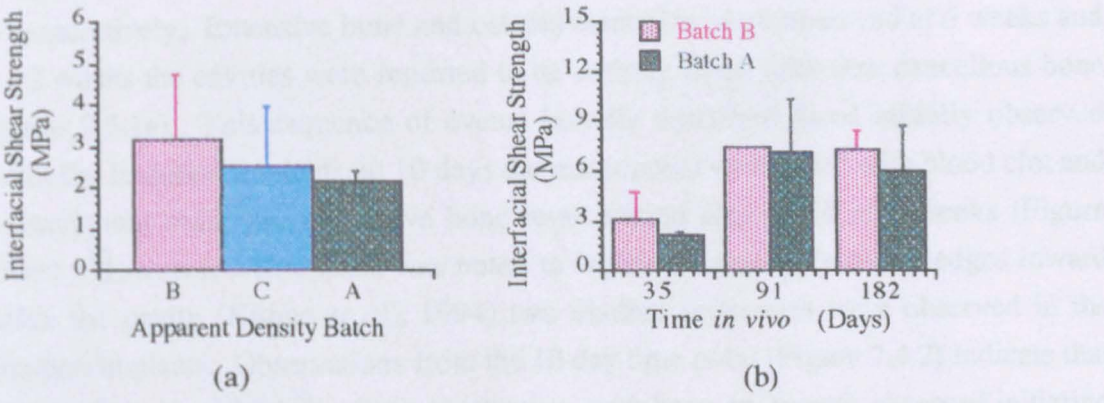

Figure 7.4.27 Variation of interfacial shear strength with apparent density (a) at 5 weeks and (b) with time.

As with the compression testing, apparent density was found to affect the push-out behaviour of the implants, where lower density implants possessed higher interfacial shear strength at 5 weeks (Figure 7.4.27a). However, this relationship between shear strength and apparent density was time dependent, with all Batch B and A specimens exhibiting statistically similar properties at 3 and 6 months (Figure 7.4.27b).

7.5 Discussion

The choice of implantation site has been shown to have a considerable effect on the perceived biological response to the implant (Dhert *et al.*, 1991; 1994). In this study implants were placed in the distal end of the femur, located in the centre of the patellar groove. This site was selected as it presented a large volume of load bearing cancellous bone, and ensured that the mechanical stimulation around the implant would encourage bone ingrowth and remodelling. This site also allowed the assessment of the ability of a stable bone/implant interface to be formed and maintained with mechanical loading across the interface.

7.5.1 Histology

Heimke (1990), proposed that, ideally, implants should induce a response similar to that of fracture healing, when placed in an osseous defect. Kühne *et al.*, (1994) observed a similar sequence of events occurring in the repair of empty defects in the femoral condyle(used as controls), where the cavities were initially filled with a blood clot and invaded by mesenchymal cells, osteoblasts and fibroblasts within the first two weeks post-operatively. Extensive bone and osteoid formation were observed at 6 weeks and by 12 weeks the cavities were reported to be entirely filled with new cancellous bone (Figure 7.5.1a). This sequence of events broadly described those initially observed within the Endobon implants, at 10 days the macropores were filled with blood clot and mesenchymal cells, and extensive bone regeneration was noted at 5 weeks (Figure 7.5.1c). However, where bone was noted to ingress primarily from the edges inward within the cavity (Kühne *et al.*, 1994) two distinct sequences were observed in the Endobon implants. Observations from the 10 day time point (Figure 7.4.2) indicate that bulk implants were initially osseo-conductive, with bone on-growth observed initiating from the defect walls towards the implant (as reported in the cavities by Kühne *et al.*, 1994). Labelling demonstrates that this bone is woven (Figure 7.4.6a), indicating accelerated deposition at the periphery of the implant. This result suggests that the primary purpose of the new bone is rapid fixation of the implant (as in the encapsulation of bone ends by callus in a fracture, Bourne, 1972). After this initial period, once bone on-growth and fixation had occurred, the Endobon appeared to induce the deposition of more ordered lamellar bone on its internal surfaces and within its pores (Figure 7.4.6b), thereby acting as a support for new bone and encouraging

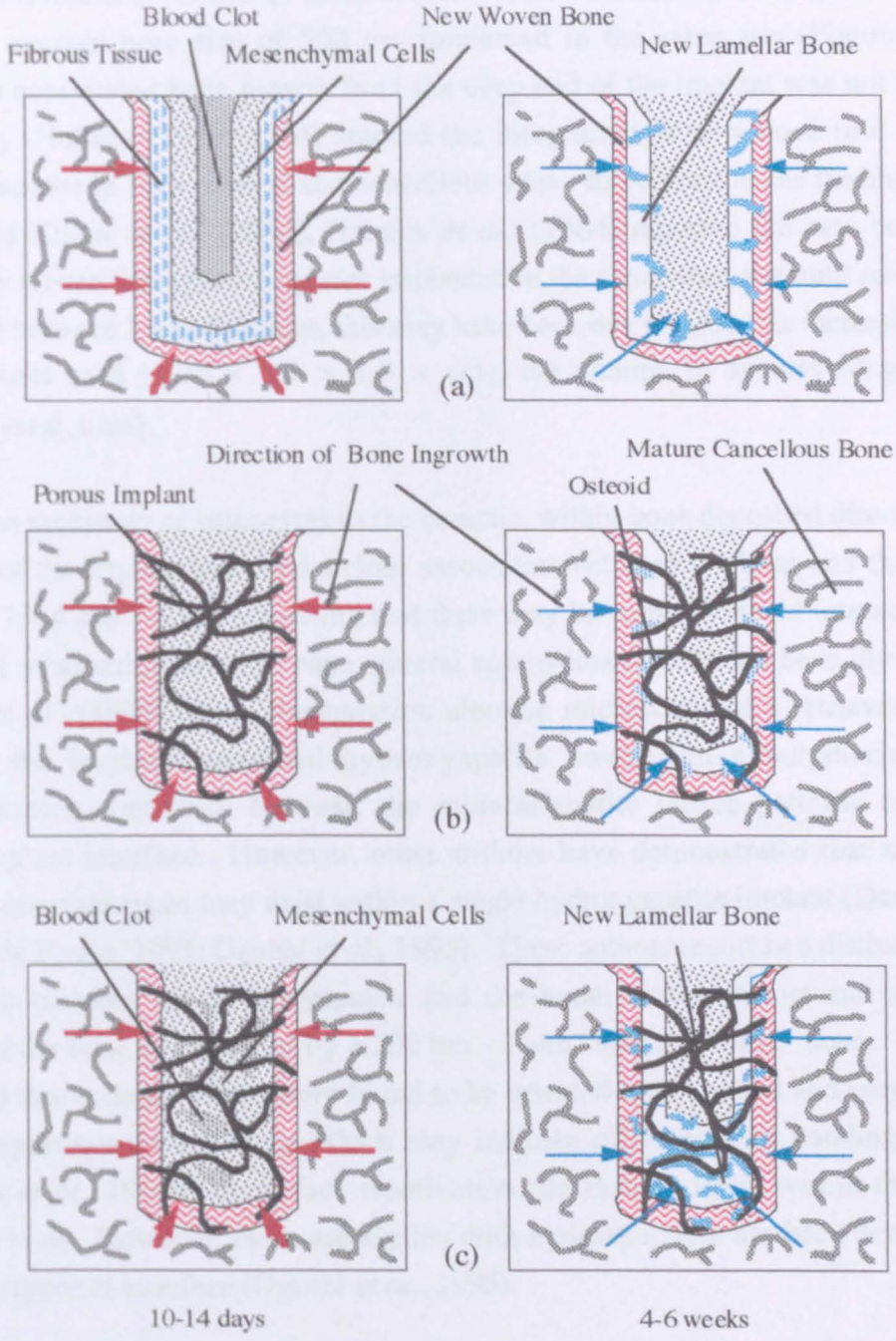

Figure 7.5.1 Schematic diagram of bone repair processes in: (a) An empty cavity (Kühne *et al.*, 1994) (b) Coralline hydroxyapatite (c) Endobon hydroxyapatite.

bone growth on its surfaces. Chronological order of labelled bone deposited on the internal macro-pore surfaces, from strut to bone surface indicated osseo-inductive behaviour within the internal macrostructure (Figure 7.4.7). This spontaneous deposition of bone appeared to advance from the deep end of the defect (Figure 7.4.3), i.e., from the most abundant source of potentially osteogenic cells. Kühne *et al.*, (1994)

observed a retarded version of these events within coralline-hydroxyapatite implants with an average pore size of 500 μm implanted in the same site (Figure 7.5.1b), although accelerated bone growth from the deep end of the implant was not reported. Similarly, Holmes (1979; 1984) studied the integration of new bone into coralline hydroxyapatite in both cortical and cancellous sites. In contrast to the findings of this work and Kühne *et al.*, (1994), Holmes *et al.*, (1984) reported the new bone to be primarily woven throughout implants implanted in the cancellous site,until remodelling occurred between 2 and 4 months, this may have been due to either the increased size of the implant used (1.25 × 1.0 × 1.0 × cm), the change in species (dog), or site (metaphyseal, tibia).

The close proximity of osteocytes to the ceramic, within bone deposited directly on the surface of the implant indicated a close association between the bone and the ceramic (Figure 7.4.4 and 7.4.5), suggesting that there may be some chemical interaction. An epitaxial relationship between bone mineral and hydroxyapatite has been illustrated by Doyle *et al.*, (1990) where transmission electron microscopy of a retrieved implant (where the implant contained hydroxyapatite powder in a polymeric matrix) demonstrated continuity between the mineral/apatite lattice patterns across the bone/implant interface. However, other authors have demonstrated that a series of distinct interface types may exist within a single hydroxyapatite implant (Davies *et al.*, 1991b; de Bruijn, 1993; Oguchi *et al.*, 1995). These authors report two distinct types of interface between the hydroxyapatite and the bone; direct contact and separation between the bone and implant by a 200 nm - 1 μm "electron dense" layer. They also reported that collagen fibres were found to be oriented both parallel and perpendicular to the hydroxyapatite surface which may indicate differences in bonding structure (Davies *et al.*, 1991b) or surface reactivation (de Bruijn, 1993) within the directly bonded bone. However, close association with hydroxyapatite has been demonstrated for both types of interface (Oguchi *et al.*, 1995).

The depth of implant position was found to have an important effect on the repair of the cartilage. The placing of implants above the sub-chondral plate tended to result in limited cartilage healing (Figure 7.5.2). From the appearance of histological sections it would appear that this is due to lack of strain-induced stimulation, as a result of the ceramic structure shielding the reparative fibrous tissue from the loading (Figure 7.4.8b). The *in vitro* response to mechanical loading was discussed by Burger and Veldhuijzen (1993) in a review of data on the effect of mechanical stimuli on organ cultures and isolated osteoblast-like or chondroblast-like cell cultures *in vitro*. These

authors suggested that the data demonstrated that compressive loading, of roughly physiological magnitude, resulted in accelerated matrix production while excessively high loading resulted in matrix resorption, indicating that cells have mechano-receptors. It was also apparent that a suitable load bearing substrate should be beneath the repairing cartilage. In the low density specimens, where large, initially empty, pores existed between the ceramic struts, little cartilage repair occurred (Figure 7.5.8b). Cartilage repair was found to be best directly above a thick strut, as very thin struts protruded above the surface (Figure 7.5.8c).

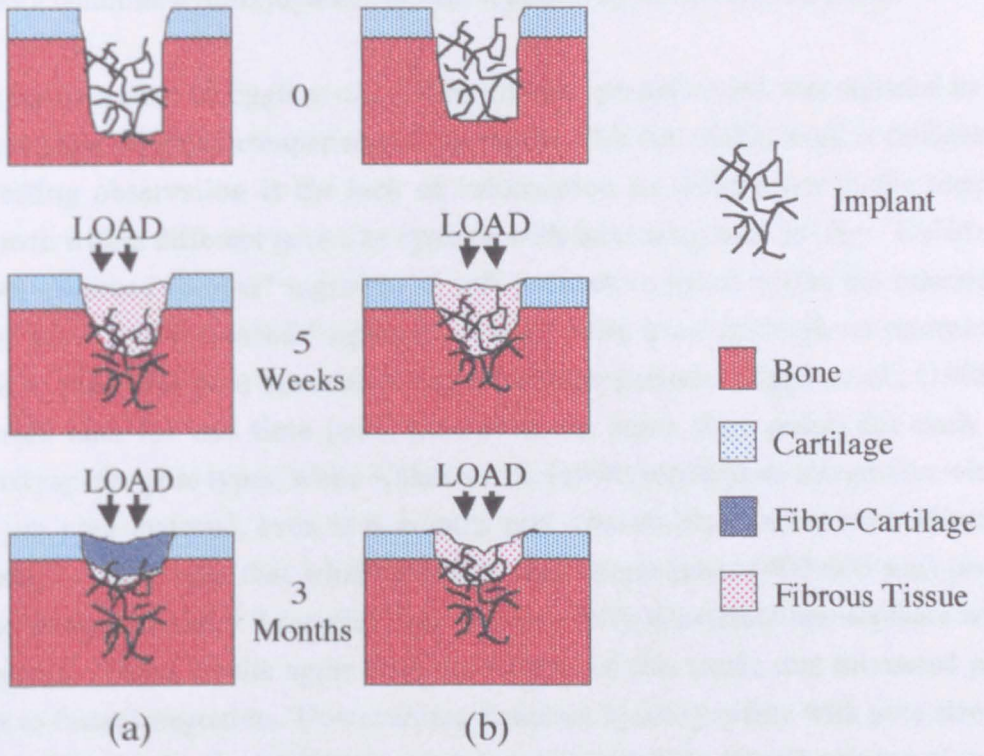

Figure 7.5.2 Schematic diagram of bone ingrowth and cartilage repair.

7.5.2 Histomorphometry

From the results of section 7.4.2 it is clear that the rate of osseointegration is strongly affected by the porous structure, and that the absolute degree of bone ingrowth is initially dependent on the pore size (Figures 7.4.14, 7.4.16, 7.5.4). A few studies have considered the pore size and inter-connectivity of porous implants and the effect upon bone ingrowth (Klawitter and Hulbert, 1971; Holmes, 1979; Holmes *et al.*, 1984; Uchida *et al.*, 1984; Eggli *et al.*, 1988; Daculsi and Passuti, 1990; Kühne *et al.*, 1994; Martin *et al.*, 1993. As in the early time points of this work (Figure 7.4.15), the majority of studies that compared hydroxyapatite implants with different porosity in the

same site (Uchida *et al.*, 1984; Daculsi and Passuti, 1990; Kühne *et al.*, 1994) found that the amount of ingrowth increased with increasing pore size. In contrast Eggli *et al.*, (1988) reported increased integration in hydroxyapatite implants with 50-100 μm pores compared to hydroxyapatite implants with 200-400 μm pores. This result was postulated to be due to reduced connectivity between the pores in the 200-400 μm pore material, a theory which had previously been proposed by Klawitter and Hulbert, 1971 and Holmes, (1979). This explanation was also proposed as the reason for the lack of integration within a 200 μm pore implant compared to the complete infiltration of a 500 μm pore coralline hydroxyapatite implant reported by Kühne *et al.*, (1994).

With the exception of Eggli *et al.*, (1988) little/no quantification was reported in any of these studies, so direct comparison of the results with that of this work is difficult. One interesting observation is the lack of information on differences in the amount of ingrowth within different pore size systems with increasing time *in vivo*. Uchida *et al.*, (1984) observed "denser" ingrowth of soft connective tissue within the material with larger pores and increased "ingrowth density" with time although no reference was made to the small pore material at extended time periods. Eggli *et al.*, (1988) only reported data for one time point (not even the same time point) for each of the hydroxyapatite pore types, while Kühne *et al.*, (1994) reported no integration within the 200 μm pore material, even at 6 months post-operatively. In contrast, Daculsi and Passuti, (1990) found that while implants with larger pores (400-600 μm) promoted faster integration, after 3 months bone had also fully penetrated the implants with 100 μm pores. These results agree with the finding of this work; that increased porosity leads to faster integration. However, for Endobon hydroxyapatite with pore sizes in the range of this study, the modal pore size does not affect the "final" volume of ingrowth at 6 months. Martin *et al.*, (1993) studied the change in ingrowth with time for 500 μm pore coralline hydroxyapatite. They reported an increase in relative bone volume up to 38% at 4 weeks, after which it fell to 35% at 3 months, 30% at 4 months and 17% at 1 year post operatively. This behaviour was not observed within the Endobon implants, furthermore Martin *et al.*, (1993) suggested that the trend may be due to "more porous implants....placed in longer-term animals", a fact which other authors believe should have had the opposite effect (Uchida *et al.*, 1984; Daculsi and Passuti, 1990; Kühne *et al.*, 1994). It is more likely that the observed loss of bone was due to implantation in a non-load bearing site, as Martin *et al.*, (1993) reported that although the amount of ingrowth decreased the mechanical properties remained stable between 8 weeks and 1 year.

Considering the results of the 5 week Endobon implants alone, the variation in the amount of bone ingrowth at 5 weeks as a function of the apparent density of the implant, could be explained by three possible mechanisms:

I Volume of bone ingrowth is attempting to replicate the original trabecular structure (implant structure dependent).

II Volume of bone ingrowth is dependant on the volume of space available for growth (pore size dependent).

III Bone ingrowth is mediated by the mechanical environment (implant structure dependent).

However considering the results of other time points another mechanism seems possible:

IV The volume of bone ingrowth at "early" time points is controlled primarily by morphology as a function of the speed with which cells can invade the structure (pore inter-connectivity dependent).

By considering the absolute volume fraction of bone together with the absolute volume fraction of implant, it is possible to study the total "structure" of the implant/bone system. This is somewhat elevated compared to the volume fraction occupied by non-operated bone (Figure 5.7.3) suggesting that mechanism **I** is not occurring.

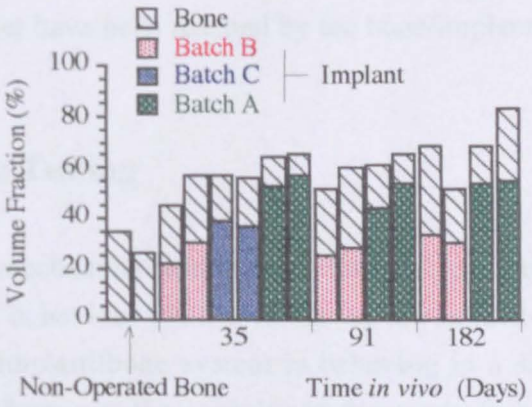

Figure 7.5.3 Absolute volume fractions of bone and Endobon.

The apposition rates calculated during week 3-4 within low density (Batch B) and medium density (Batch C) implants were somewhat elevated (3.8 $\mu m.day^{-1}$ and 3.4 $\mu m.day^{-1}$ respectively) compared to the apposition rate of un-operated bone 2-3 mm

away from the implant (3.1 μm.day^{-1}). However the apposition rate within the high density implants was reduced (2.8 μm.day^{-1}), which indicates that mechanism **IV** may be occurring at this time point. However, at 3 months the relative amount of ingrowth within Batch A specimens is still lower (Figure 7.5.4a), and it is unlikely that slower cellular invasion can be directly responsible for a variation in ingrowth at 3 months. Although Ogiso *et al.*, (1994) have reported that fibrous tissue can invade and colonise faster than osseous tissue, so inhibiting later bone deposition.

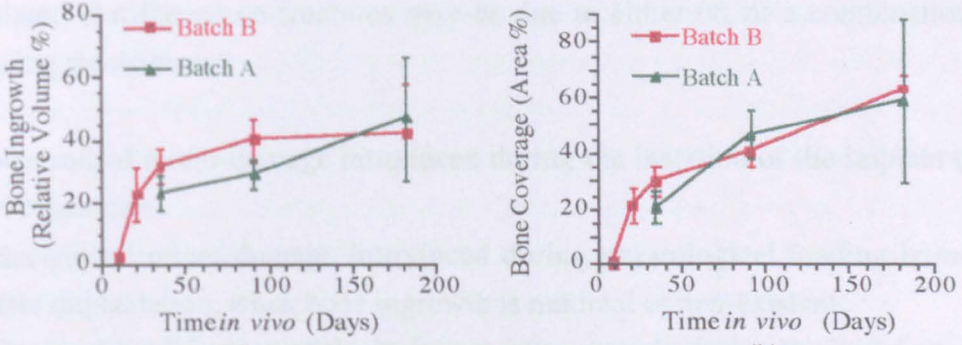

Figure 7.5.4 Variation in bone (a) ingrowth and (b) coverage with time.

The fact that the relative volume of bone ingrowth within implants from the two batches is similar at 6 months (Figure 7.5.4a), indicates that the final volume of bone ingrowth is controlled by the volume of space available for ingrowth (mechanism **II**). However, there was a large variation in the results of implants from this time period in both batches, and the continued rise in bone coverage up to 6 months indicates that equilibrium may not yet have been reached by the bone/implant system (Figure 7.5.4b).

7.5.3 Compression Testing

The alteration of the mechanical behaviour of the low and medium density specimens after implantation, to behaviour similar to that of the cancellous bone (Figure 7.4.18 c&d), indicates that implant/bone system is behaving in a similar manner to a well bonded composite. Moreover, the capacity of the newly formed bone to enhance the mechanical performance of the implant after implantation for 5 weeks, hence the ability of loads to be transmitted across the interface, demonstrates the intimacy of the bond between the implant and the bone. This increase in strength was also reported by Holmes *et al.*, (1984), who placed a porous coralline hydroxyapatite implant (500 μm) within a non-load bearing cancellous site. The ultimate compressive stress (UCS)

increased from 0.8-4.1 MPa (as-received porous ceramic) to 24.9 MPa (implant/bone composite after 6 months *in vivo*).

However, implantation appears to have had a deleterious effect on the compressive modulus (Figure 7.5.5b) which drops significantly for implants of all batches (e.g. after only 10 days *in vivo*, compressive modulus of batch B implants drops from 0.4 GPa to 0.02 MPa). Micro-fracturing within the ceramic struts was evident in the thin sections of all implants and may be responsible for the loss in mechanical integrity, however the incidence of fracture did not appear to increase with time *in vivo*. Hence, it was postulated that the micro-fractures may be due to either of, or a combination of the following mechanisms:

1 Mechanical micro-damage introduced during the insertion of the implant (tapping with hammer).
2 Mechanical micro-damage introduced during physiological loading immediately after implantation, when bone ingrowth is minimal or non-existent.
3 Chemical modification of the hydroxyapatite ceramic during the initial exposure to physiological solution.
4 Swelling and dissolution of the CaO contamination resulting in cracking of the struts as a result of exposure to aqueous based physiological solutions.

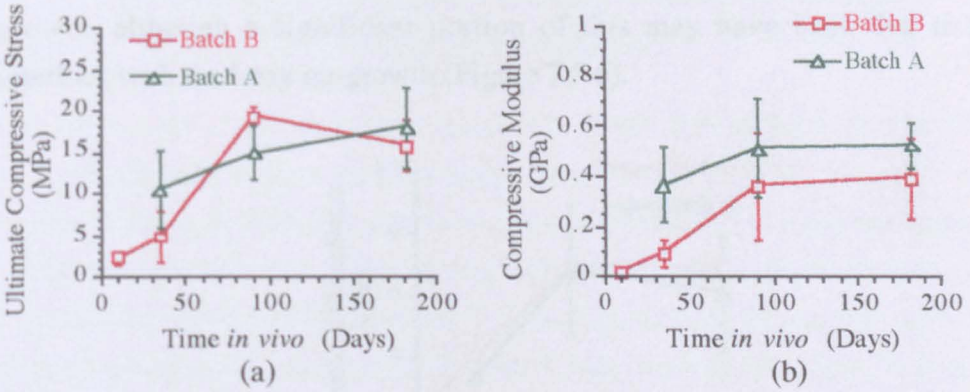

Figure 7.5.5 Variation in (a) ultimate compressive stress and (b) compressive modulus with time.

The apparent integration of blood vessels, osseous tissue and cells within cracks within the "dense" struts of the implanted Endobon, which is observed with increasing frequency after longer time *in vivo* (Figure 7.4.10a) may indicate that bone ingrowth is attempting to "repair" the ceramic structure. Remodelling within normal bone is believed to be in response to micro-fractures and changes in the mechanical environment occurring within the bone (O'Connor *et al.*, 1982; Burr *et al.*, 1985;

Lanyon, 1987) and the observed cellular infiltration of the ceramic struts may be an extension of this response.

Another trend, which was more obvious for Batch B than for Batch A was that the mechanical properties increased with time *in vivo* up to 3 months, and then stabilised (Figure 7.5.5). Considering the variation noted in the bone coverage from 3-6 months this would suggest that the remodelling occurring within the implant at this stage is mediated by the mechanical environment. Therefore, these results suggests mechanism **III** (section 7.5.2) is occurring at these time points. A similar trend was reported by Martin *et al.*, (1993), who found that the mechanical properties of retrieved porous (500 μm pore size) coralline hydroxyapatite implants did not vary significantly after 8 weeks *in vivo*. However these authors also reported that the ingrowth within the implant (placed in a non-load bearing cancellous site) decreased with time, which was not observed for the Endobon implants (placed in a load bearing site).

7.5.4 Pushout Testing

Pushout testing of retrieved implants at 10 days demonstrated that, despite the minimal amount of bony ingrowth there was still some degree of "bonding" with the bony on-growth, although a significant portion of this may have been due to mechanical interlock with the bony on-growth (Figure 7.5.6).

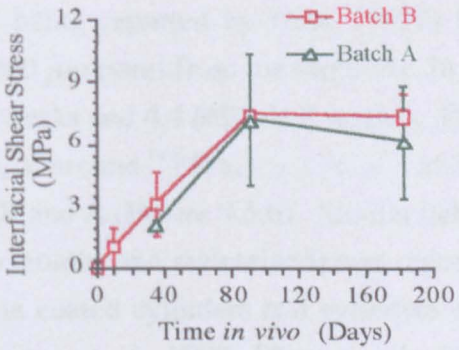

Figure 7.5.6 Variation in interfacial shear strength with time.

Comparisons of the interfacial shear strength (ISS) between different morphology implants are generally difficult to make as a result of the strong dependence of the measured ISS on the friction between the bone and implant, which is in turn dependent on the roughness and contact area of the surface (Kangasniemi *et al.*, 1994). Therefore, if considering the contribution to the ISS by the friction alone, at an imaginary "zero"

time point, high density implants would be expected to have a higher ISS than low density implants, as a function of the increased effective surface area of these specimens (Figure 7.5.7a). However, after implantation for 5 weeks, low density (Batch B) implants possessed a higher ISS than the high density (Batch A) implants. This result indicated that after 5 weeks *in vivo*, the increased volume of bone ingrowth within the low density implants (Figure 7.4.15a, 7.4.17a) had resulted in an increased effective surface area between the bone and low density specimens when compared to that of the high density implants (Figure 7.5.7b). Moreover, the increased volume of bone ingrowth in low density (Batch B) implants would also lead to a greater relative increase in the shear strength as a result of increased mechanical interlock between the bone ingrowth and the Endobon struts.

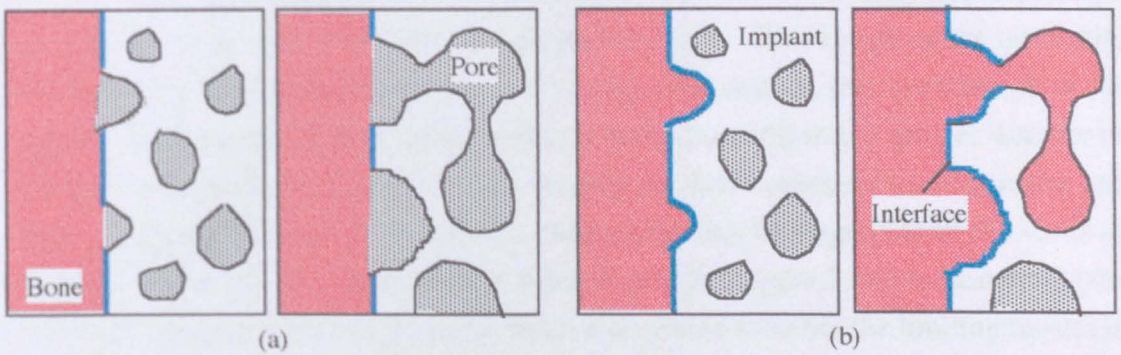

Figure 7.5.7 Changes in the effective interface between bone and porous implants (a) at a "zero" time point and (b) after bone integration.

The magnitude of the early time point ISS results compared well with the literature, with comparable values being reported by Ueta, (1992) for the push-out of 3 mm diameter cylinders with 200 μm pores from the same site, in the same species (2.7 MPa at 2 weeks, 4.5 MPa at 4 weeks and 4.4 MPa At 8 weeks). Endobon specimens attained a maximum value of ISS, of around 7 MPa, at 3 months and maintained this value at 6 months for both Batch B and A (Figure 7.5.6). Similar behaviour (where a maximum value was reached at 3-6 months and maintained) was reported in the literature for the pushout of hydroxyapatite coated cylinders and cylinders with porous metal coatings (Bobyn *et al.*, 1980; Tanner *et al.*, 1990; Dhert *et al.*, 1991; Salkeld *et al.*, 1995). However, the maximum values of ISS attained in these cases was often considerably higher (generally 15-20 MPa). This may be due to the change in the failure mechanism of the Endobon implants at later time points, where the implant appeared to fail rather than the interface (Figure 7.4.25, 7.4.26 and 7.5.8). It is also interesting to note that measured "ISS" for the implants was considerably reduced when compared to the UCS

of the implants at the same time point and that the shear strength of cancellous bone has been reported to be approximately 6 MPa (Stone *et al.*, 1983).

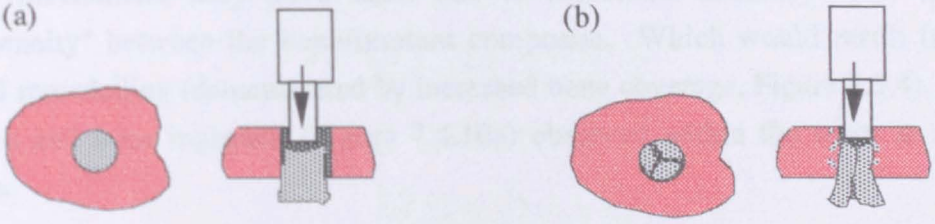

Figure 7.5.8 Diagram illustrating the different failure modes of Endobon implants during push-out testing.

At 3 months, implants were split longitudinally into three similarly sized portions during push out (Figure 7.5.8), which indicated that the strength of the interfacial bond between the deposited bone and the implant exceeded the fracture strength of the implant. Furthermore, at 6 months, implants tended to split into a greater number of particles during failure (Figure 7.4.26), suggesting that bone/implant composite had achieved a greater degree of integration. The agreement in magnitude of the value of ISS between Batch B and A implants at 3 and 6 months (Figure 7.5.6) indicated that the bulk structure and surface roughness at these time points were not the limiting factors in the failure of the interface, and that both the mechanical integrity of the implant/bone composite and the interface bond had been maintained, with time, at a constant value, irrespective of the implant structural morphology.

Study of the failed test pieces using scanning electron microscopy indicated that specimens tested after 5 weeks *in vivo* had failed by a "clean" extrusion of the specimen, with some crushing of struts at the end nearest the loading pin and fracture of individual struts at or near the interface, leaving portions of ceramic in the surrounding bone (Figure 7.4.25). However, at 3 and 6 months the fracture mode was more disordered with failure occurring in the ceramic struts, the bone ingrowth and the surrounding bone. These observations indicated that the mechanical load applied to the top surface of the implant during pushout testing was being more evenly distributed as the degree of bone ingrowth, and hence the implant integration, increased. Therefore, at 3 and 6 months post-operatively, failure had occurred at a number of sites as a result of a lack of a clear delineation between the implant and host tissue.

Comparison of the stress-strain behaviour of 5 week, and 3 and 6 month implants during push-out testing illustrated that a greater degree of energy absorption was

occurring in the longer time point specimens (Figure 7.4.24). Considered with the maintenance of ISS at 3 and 6 months, these results also indicate that the change in failure mechanism may have been due to increased intimacy and "apparent homogeneity" between the bone/implant composite. Which would result from the internal remodelling (demonstrated by increased bone coverage, Figure 7.5.4), cellular invasion and bone ingrowth (Figure 7.4.10a) observed within the struts at 3 and 6 months.

These results, coupled with the similarity between the reported value for the shear strength of cancellous bone (Stone *et al.*, 1983) and the results of the push-out tests indicate that the push-out tests were measuring the shear strengths of the bone/implant composites, not the bone implant interfaces.

CHAPTER 8

EPILOGUE

8.1 Summary of Findings

The results of the chemical analysis (Part 5.4.1) indicate that Endobon is composed of a phase pure, but highly substituted carbonated-hydroxyapatite, with a high degree of variability in both the impurity levels and lattice substitutions from one powder specimen to another. Definitive conclusions about the precise nature of the substituents present are difficult to make as a result of variations in the levels of ionic species present and the range of possible substitution sites. However, it can be concluded that the material is both A and B type carbonate substituted, and that it contains similar proportions of magnesium and sodium, which are believed to be substituted for calcium in bone mineral.

The results of the micro-structural analysis (Parts 5.4.2-4) indicate that the micro-structure of Endobon did not vary significantly with apparent density, and possessed a constant, equiaxed grain structure. The modal grain size was found to be considerably greater than the reported size of bone mineral crystals. However, other aspects of the trabecular micro-structure were found to be preserved, such as the osteocyte lacunae, and possibly the canaliculi. The presence of these features led to a relatively high degree of "strut porosity" which was classified into two groups, a closed or isolated, < 3 μm fraction, and an open or interconnected, >3 μm fraction. The closed fraction exhibited a morphology and distribution consistent with the "trapped" micro-porosity expected as a result of densification, grain growth and grain coalescence during sintering. The open fraction arose from the micro-structural features preserved from the original bone structure.

Macrostructure was found to vary considerably, as a function of both apparent density and structural architecture. This variation was reflected by changes in the modal pore size, pore shape (aspect ratio), pore orientation, and pore inter-connectivity. Low density specimens tended to exhibit more anisotropic structures, with the degree of anisotropy having a significant effect on the connectivity of a structure.

The results of mechanical testing (Part 5.4.5) indicate that as received Endobon behaves as an elastic brittle foam when loaded under conditions of uniaxial compression. The ultimate compressive stress and the compressive modulus of isotropic specimens were found to be related to the square of the apparent density ($r = 0.91, 0.84$ respectively). This result was in agreement with the behaviour of an-isotropic open foam predicted by Gibson and Ashby (1988). However, some Endobon specimens possessed an isotropic structure, with struts having a preferred orientation parallel to the long axis of the cylindrical specimens. The mechanical behaviour of these specimens was also found to fit the predictions of Gibson and Ashby (1988). However, the applicability of the linear fit for the ultimate compressive stress data was questionable, while the accuracy of the linear fit to the compressive modulus data was relatively low ($r = 0.75$). This apparent irregularity in the anisotropic data resulted from variations in the degree and direction of anisotropy present in individual specimens.

The results of the *in vitro* investigation demonstrated that Endobon was able to support the colonisation and proliferation of human osteoblast-like cells on its surface. Cells did not migrate to the tissue culture plastic, but formed confluent multi-layers on the ceramic surfaces, and capped the macropores. The cells exhibited a preference for the smooth macropore surfaces over the rougher machined surfaces, and were observed colonising the internal macropores of the structure, indicating that migration had occurred from the upper surfaces into the macro-porous structure. An extra-cellular matrix was formed, although evidence for subsequent calcification of this matrix was not conclusive, which may be due to insufficient time *in vitro*.

The histological observations suggest that Endobon is a "biocompatible" material when placed in an osseous environment, with evidence of the normal behaviour associated with fracture healing, such as mesenchymal cellular invasion, bone deposition, bone remodelling,and revascularisation, occurring within the macro-porosity of the implant. Endobon was found to be osseo-conductive, with rapid bone on-growth observed from the defect edges within the second week post-operatively. There was also some evidence to suggest that the material was osseo-inductive once stable (fixed) within the

osseous environment, with the spontaneous deposition of bone on the ceramic strut surfaces. Furthermore, the apparent invasion by some cells into the ceramic struts suggested that the material was intimately "accepted" by the cells. This intimacy could be either a result of the preservation of the trabecular bone-like micro-structure within the ceramic struts, which may allow the advance of cellular processes into the ceramic, or it may be due to the highly substituted bone-mineral like chemistry of the ceramic.

Apparent density was found to influence the normalised volume of bone ingrowth within the macro-porosity at early time points (5 weeks), but this was not the case at later time points (6 months). Hence, the pore size could not have been responsible for the differences noted at 5 weeks. Calculation of apposition rates between weeks 3-4 indicated that the rate of bone ingrowth was reduced in higher density specimens. Analysis of the macro-structure had demonstrated that low density specimens possessed a higher degree of pore inter-connectivity. Thus, the variation in ingrowth at early time points was ascribed to variations in macro-pore connectivity between the different densities, resulting in variations in the rate of osteogenic-cellular invasion.

In low density specimens (Batch B) the "maximum" volume of bone integration was reached at 3 months, which coincided with the attainment of "peak" mechanical properties at 3 months post-operatively. This finding suggested that the degree of bone ingrowth was controlled by the mechanical environment at later time points.

The mechanical properties and behaviour of the individual Endobon specimens under uniaxial compressive loading were found to alter after implantation. Initially, after 10 days post-operatively, all properties of retrieved implant/bone "composites" dropped to values below those of the as-received material of comparable density. However, after 5 weeks *in vivo* the new bone ingrowth resulted in an increase in the ultimate compressive strength (UCS) of the retrieved implants, such that the UCS of the retrieved implant matched that of as-received material of comparable density. Furthermore, the UCS of retrieved implants at 3 months was comparable with that at 6 months for retrieved implants of similar density, and exceeded that of the as-received material.

A similar trend was also followed for the compressive modulus of low density (0.61 $g.cm^{-3}$) retrieved implants, except that the compressive modulus of the as-received material was not exceeded at any time point. Moreover, the compressive modulus of all high density (1.18 $g.cm^{-3}$) retrieved implants was below that of the as-received material of the same density at all time points. The initial reduction in UCS and protracted reduction in compressive modulus indicated that the implant had lost structural integrity

after implantation. This result was ascribed to internal micro-fracturing within the ceramic struts. Micro-fractures were evident in thin histological sections, and were found to contain bone ingrowth at later time points. However, the exact mechanism of micro-fracture has not yet been determined. Possible mechanisms that have been identified are:

1 Mechanical micro-damage introduced during the insertion of the implant (tapping with hammer).
2 Mechanical micro-damage introduced during physiological loading immediately after implantation, when bone ingrowth is minimal or non-existent.
3 Chemical modification of the hydroxyapatite ceramic during the initial exposure to physiological solution.
4 Swelling and dissolution of the CaO contamination as a result of exposure to aqueous based physiological solutions, resulting in cracking of the struts.

Notably, the compressive moduli of implants at 3 and 6 months were comparable between both high and low density implants, indicating that the final volume of bone ingrowth may be controlled by the mechanical environment, even within the ceramic structure.

The value of interfacial shear strength (ISS), as measured by pushout testing, increased with time up to 3 months, and was maintained at 6 months, which coincided with a change in the failure mechanism of the specimens during push-out testing. Specimens tested after 5 weeks *in vivo* failed by a "clean" extrusion of the specimen, with some crushing of struts at the end nearest the loading pin. However, at 3 and 6 months implants failed by disintegration of the implant/bone plug rather than pure push-out. The interfacial shear strength of implants at 3 and 6 months was comparable for both high and low density implants. At these time points, the macro-porosity of the implants was fully integrated with bone, and failure occurred by the fracture of the implant into three (at 3 months post-operatively), or more pieces (at 6 months post-operatively). Study of sectioned portions of test pieces after failure indicated that the degree of integration controlled the failure mode by modifying of load distribution within the composite.

The relatively low value of ISS measured for the Endobon specimens after 3 and 6 months *in vivo*, compared with the results reported in the literature for hydroxyapatite and porous metal coated cylinders, indicated that push-out testing was measuring the shear strengths of the bone/implant composites, not the bone/implant interfaces.

8.2 Conclusions

- Endobon is primarily composed of a highly substituted hydroxyapatite, with <1% second phase present in the form of calcium oxide. The main substituents present in the apatite lattice were identified as:
    - Carbonate for both hydroxyl and phosphate groups.
    - Magnesium and sodium for calcium.

- The macro-structure of Endobon was highly variable, which reflects the natural origins of the material. While apparent density was found to be a good general indicator of structural variation, three parameters were identified that enabled the complete characterisation of the structural architecture; these were:
    - Modal pore size.
    - Pore connectivity.
    - Mean pore aspect ratio (anisotropy).

- The microstructure of Endobon specimens exhibited characteristic features similar to that of cancellous bone (i.e. micro-porosity similar in size, shape and distribution to osteocyte lacunae and canaliculi), and was not found to vary significantly, even with apparent density.

- Endobon specimens were found to exhibit the behaviour of elastic brittle open-celled foams when loaded in uniaxial compression.

- The mechanical properties of Endobon specimens in compression were found to be highly dependent on both apparent density and structural architecture:

  The dependence of both ultimate compressive stress (UCS) and compressive modulus (E_c) on apparent density, for isotropic Endobon structures, were found to follow the predicted trends for open elastic-brittle foams as proposed by Gibson and Ashby (1988):
    - $UCS \propto \rho^2$.
    - $E_c \propto \rho^2$.

  The dependence of both ultimate compressive stress and compressive modulus on apparent density, for anisotropic Endobon structures, were found to follow the predicted trends for open elastic-brittle foams as proposed by Gibson and Ashby

(1988), although the relationship was less convincing between the UCS and apparent density.

- $UCS \propto \rho$.
- $E_c \propto \rho$.

- *In vitro* assessment demonstrated that the colonisation and proliferation of human osteoblast-like cells was supported by Endobon, with the production of extensive extra-cellular matrix and cell migration into the interior of the ceramic macro-pores.

- *In vivo* assessment demonstrated that Endobon was "biocompatible" when placed in an osseous environment, with no aggressive cellular response. Endobon was found to be highly osseo-conductive. Lamellar bone was deposited directly on the implant surfaces, once the implant had been fixed in the defect by the on-growth of a rim of woven bone.

- Apparent density was found to influence the host response as a function of macro-pore connectivity. Lower density implants possessed a greater degree of interconnections between pores, which was found to result in faster osseo-integration. At later time points (3 and 6 months), the apparent density did not appear to influence the normalised volume of bone ingrowth within the macro-pores.

- The mechanical properties and behaviour of the individual Endobon specimens under uniaxial compressive loading were found to alter after implantation. This result appears to be due to the loss of mechanical integrity after implantation, either as a result of mechanically or physio-chemically induced micro-fracturing of the ceramic struts.

- Push-out testing demonstrated a high degree of integration between the Endobon implants and the bone, with failure resulting from disintegration of the implant/bone plug rather than from pure push-out, at 3 and 6 months. This condition resulted in the test measuring the shear strength of the implant/bone composite rather than the implant/bone interface.

8.3 Further work

8.3.1 Study of Retrieved Implants

- High resolution transmission electron microscopy could be performed on sections of the intact bone/Endobon interface of implants, retrieved at different time points during this study, to investigate:
    - Whether epitaxial growth of bone mineral from the ceramic surface had occurred.
    - If there is an electron-dense inter-layer between the ceramic surface and bone.
    - The nature of any collagen alignment to the ceramic surface.

8.3.2 *In Vitro* Studies

- To determine the reason for the reduction in modulus *in vivo*, as-received specimens could be incubated in physiological solutions, in the absence of cells, for 1 - 10 days, before compression testing. During the incubation the pH of the solution should be monitored. This procedure would establish if physio-chemical degradation or dissolution of CaO leads to the observed reduction in mechanical integrity. A separate group of specimens could also be tapped with a hammer, as in the implantation procedure, before mechanical testing, to determine if this leads to mechanical micro-fracturing and loss of modulus.

- Human osteoblast-like cells should be incubated for longer (over 21 days) periods of time to determine if calcification occurs on the porous Endobon substrate.

- In order to determine if the response to Endobon is a function of the relatively high levels of chemical "impurities" such as carbonate, sodium and magnesium, or related to the structural and surface morphology, quantitative analysis of human osteoblast-like cell cultures could be performed, using the following substrates:
    - Porous Endobon,
    - Dense Endobon compacts produced from Endobon powder and
    - "Pure" hydroxyapatite.

8.3.3 *In Vivo* Studies

The work detailed in this thesis represents a completed study into the effect of macroporosity on bone integration in a load bearing cancellous site. However, the results have raised questions about the mechanisms controlling the rate and final volume of bone ingrowth into porous hydroxyapatite.

- Longer term (1 year) implantations should be performed to determine whether the bone ingrowth had remodelled into a "final" configuration at 6 months.

- Implantation of longitudinally anisotropic, transversely anisotropic, and isotropic specimens with the same apparent density, for periods of 10 days to 5 weeks, could provide information about the effect, on the rate of bone ingrowth, of altering the macrostructural pathways into the ceramic.

- In view of the "control" of final mechanical properties by bone ingrowth, a study of the low and high density implants in a cortical site should be performed to assess the suitability of this material for filling cortical defects.

REFERENCES

Aaron H.B.; Smith R.D.; Underwood E.E. Spatial Grain-Size Distribution from Two-Dimensional Measurements. 1st Int. Cong. on Stereology, **16**, 1-8, (1963).

Abdel-Fattah W.I.; El-Sayed A.M.; Ali F.M.; Beheri H.H. Serum-Hydroxyapatite Interaction *In Vitro*. Biomaterials, **15**, (9), 643-649, (1994).

Abrahams I.; Knowles J.C. Effects of Sintering Condition on Hydroxyapatite for use in Medical Applications: A Powder Diffraction Study. J. Mater. Chem., **4** (2), 185-188, (1994).

Ahrens P.B.; Solursh M.; Reiter R.S. Stage-Related Capacity for Limb Condogenesis in Cell Culture. Developmental Biology, **60**, 69-82, (1977).

Akao M.; Aoki H.; Kato K. Mechanical Properties of Sintered Hydroxyapatite for Prosthetic Applications. J. Mater. Sci., **16**, 809-812, (1981).

Akedo Y.; Hosoi T.; Inoue S.; Ikegami A.; Mizuno Y.; Kaneki M.; Nakamura T.; Ouchi Y.; Orimo H. Vitamin K_2 Modulates Proliferation and Function of Osteoblastic Cells *in vitro*. Biochem. Biophys. Res. Commun., **187** (2), 814-820, (1992).

Amrah-Bouali S.; Rey C.; Lebugle A.; Bernache D. Surface Modifications of Hydroxyapatite Ceramics in Aqueous Media. Biomaterials, **15**, (4), 269-272, (1994).

Anderson C. Manual for the Examination of Bone. CRC Press, Boca Raton, Florida (1982).

Anderson H.C. Introduction to the Second Conference on Matrix Vesicle Calcification. Metabolic Bone Disease Related Research, **1**, 83-87, (1978).

Anderson H.C.; Johnson T.F; Avramides A. Matrix Vesicles in Osteomalacic Bone. In: Bone Histomorphometry, Eds: Jee W.S.S.; Parfitt A.M. In: Metabolic Bone Disease Related Research, **2**, (supplement), 79-86, (1980).

Andersson Ö.H. Silica Release from Bioactive Glass In: Bioceramics 8, Proc. 8th Int. Symp. on Ceramics in Medicine. Eds: Wilson J.; Hench L.L.; Greenspan D. Elsevier, 483-488, (1995).

Ando J. Tricalcium Phosphate and Its Variations. Bull Chem Soc Japan, **31**, 196-20, (1958).

Aoki H. Science and Medical Applications of Hydroxyapatite. Takayama Press, Tokyo, (1991).

Archer C.W., McDowell J., Bayliss M.T., Stephens M.D., Bentley G. Phenotypic Modulation in Sub-Populations of Human Articular Chondrocytes *in vitro*. J. Cell Sci., **97**, 361-371, (1990).

Arita I.H.; Wilkinson D.S.; Mondragón M.A.; Castaño V.M. Chemistry and Sintering Behaviour of Thin Hydroxyapatite Ceramics with Controlled Porosity. Biomaterials, **16** (5), 403-408, (1995).

Ascenzi A.; Bonucci E. Mechanical Similarities Between Alternative Osteons and Cross-Ply Laminates. J. Biomech., **9**, 65-71, (1976).

Ascenzi A.; Carando S.; Portigliatti-Barbos M. A New Approach to the Structure and Mechanical Properties of Compact Bone. In: Biological and Biomechanical Performance of Biomaterials, Eds: Christel P., Meunier A., Lee A.J.C. Elsevier Science Publishers, Amsterdam, (1986).

ASTM E 112 - 91
Standard Test Methods for Determining Average Grain Size. (1991).

ASTM E 1382 - 91
Standard Test Methods for Determining Average Grain Size using Semiautomatic and Automatic Image Analysis. (1991).

Bagambisa F.B., Joos U. Preliminary Studies on the Phenomenological Behaviour of Osteoblasts Cultured on Hydroxyapatite Ceramics. Biomaterials, **11**, 50-56 (1990).

Barralet J. Processing and Sintering of Carbonate Hydroxyapatite. PhD Thesis, Materials Dept. QMW College, University of London, (1995).

Baron R. Importance of the Intermediate Phases between Resorption and Formation in the Measurement and Understanding of the Bone Remodelling Sequence. In: Bone Histomorphometry, Ed: Meunier P.J., 2nd Int. Workshop, Toulouse, 89-96, (1976).

Baron R.; Vignery A.; Tran Van P. The Significance of Lacunar Erosion without Osteoclasts: Studies on the Reversal Phase of the Remodelling Sequence. In: Bone Histomorphometry, Eds: Jee W.S.S.; Parfitt A.M. In: Metabolic Bone Disease and Related Research, **2** (Supplement), 35-41, (1980).

Baud C.A. Submicroscopic Structure and Functional Aspect of the Osteocyte. Clin. Orthop., **56**, 227-236, (1968).

Bauer G. TCP Powder From "Soft Parts" Of Bone. European Patent: **EP 0 382 047 A2**

Bauer G. Biochemical Aspects of Osseo-Intergration. In: Osseo-Intergrated Implants, Ed: Heimke G., 1, 81-98, (1990).

Bauer H-J.; Katzenmeier B.; Kuntz M. HA Porous Ceramic From Cancellous Bone. European Patent: **EP 0 475 189 A2**

Behiri J.C. Fracture Mechanics of Bone. Ph.D. Thesis, Materials Dept. QMW College, University of London (1982).

Behiri J.C.; Bonfield W. Fracture Mechanics of Bone - Effects of Density, Specimen Thickness and Crack Velocity on Longitudinal Fracture. J. Biomech., **17**, 25-34, (1984).

Bennet M.B.; Ker R.F.; Dinery N.J.; Alexander R.McN. Mechanical Properties of Various Mammalian Tendons. J. Zool. Lond., (A), **209**, 537-548, (1986).

Benz D.J.; Haussler M.R.; Thomas M.A.; Speelman; Komm B.S. High-Affinity Androdgen Binding and Androgenic Regulation of α_1(I)-Procollagen and Transforming Growth Factor-β Steady State Messenger Ribonucleic Acid Levels in Human Osteoblast Like Osteosarcoma Cells. Endocrinology, 128 (6), 2723-2730, (1991).

Ben-Ze'ev A. Animal Cell Shape Changes and Gene Expression. Bioessays, **13**, 207-212, (1991).

Berry E.D. The Structure and Composition of some Calcium Deficient Apatites. J. Inorg. Nucl. Chem. 29, 317, (1967).

Best S.M. Characterisation, Sintering and Mechanical Behaviour of Hydroxyapatite Ceramics. PhD Thesis, Materials Dept. QMW College, University of London, (1990).

Best S.M. Personal Communication (1996).

Best S.; Downes S.; Sim B.; Kayser M. Bonfield W. The dependence of Osteoblastic Response to the Chemical and Physical Composition of Hydroxyapatite. In: Proc. 21st Annual meeting of the Soc. for Biomaterials, San Francisco, 237, (1995).

Best S.; Lee D.; Shaw J.; Bonfield W. The Effects of the Microstructure of Two Hydroxyapatite Ceramics on Cell Morphology and Proliferation. In: Bioceramics 6, Proc. 6th Int. Symp. on Ceramics in Medicine., (1994).

Bevelander G. Ramaley J.A. Essentials of Histology. C.V. Mosby, St Louis USA, 8th Edition, (1979).

Bienenstock A.; Posner A.S. Calculation of the X-Ray Intensities from Arrays of Small Crystallites of Hydroxyapatite. Arch. Biophys., 124, 604-607, (1968).

Birkenhager-Frenkel D.H.; Schmitz P.I.M.; Breuls P.N.W.M.; Lockefeer J.H.M.; Heul R.O.v.d. Biological Variation as Compared to Inter-Observer variation and Intrinsic Error of Measurement, for same Parameters, within Single Bone Biopsies. In: Bone Histomorphometry, Ed: Meunier P.J., 2nd Int. Workshop, Toulouse, 63-68, (1976).

Black J. Systemic Effects of Biomaterials. Biomaterials 5, 11, (1984).

Black J. Orthopedic Biomaterials in Research and Practice. Churchill Livingstone, New York, (1988).

Black J. Push-Out Tests. J. Biomed. Mater. Res., 23, 1243-1245, (1989).

Blatcher S. Holographic Interferometric Analysis of Femoral Prostheses. PhD Thesis, Materials Dept. QMW College, University of London, (1995).

van Blitterswijk C.A.; Grote J.J.; de Groot K.; Deams W.TH.; Kuijpers W. Biological Performance of Hydroxyapatite during Staphylococcus Aureus Infection. J. Biomed. Mater. Res., 20, 989-1022, (1986).

Bloebaum R.D.; Bachus K.N.; Momberger N.G.; Hofmann A.A. Mineral Apposition Rates of Human Cancellous Bone at the Interface of Porous Coated Implants. J. Biomed. Mater. Res., 28, 537-544, (1994).

Blumenthal N.C.; Cosma M.S. Effects of Metal Ions on Apatite Formation and Bone Mineralization. In: Tissue-Inducing Biomaterials, Eds: Cima L.; Ron E., Mat. Res. Soc. Symp. Proc., 252, 29-35, (1992).

Blumenthal N.C.; Posner A.S. Hydroxyapatite: Mechnaisms of Formation and Properties. Calc. Tiss. Res., 13, 235, (1973).

Blumenthal N.C.; Posner A.S. *In Vitro* model of Aluminium-Induced Osteomalacia: Inhibition of hydroxyapatite Formation and Growth. Calc. Tiss. Int., 36, 439-447, (1984).

Bobyn J.D., Engh C.A., Pilliar R.M. Histological Comparison of Biological Fixation and Bone Modelling within Canine and Human Porous-Coated Hip Protheses. In: Quantitative Characterisation and Performance of Porous Implants for Hard Tissue Applications. Ed: Lemons J.E. ASTM STP 953, ASTM, Philadelphia, (1987).

Bobyn J.D.; Pilliar R.M.; Cameron H.U.; Weatherly G.C. The Optimum Pore Size for the Fixation of Porous-Surfaced Metal Implants by the Ingrowth of Bone. Clin. Orthop. Rel. Res., 150, 263-270, (1980).

Bocchi G.; Valdre G. Physical, Chemical and Minerological Characterisation of Carbonate-Hydroxyapatite Concretions of the Human Pineal Gland. J. Inorganic Biochemistry, 49, 209-220, (1993).

Bodyako M.N.; Kasichev V.P.; Naumovich N.V. Practical Metallography, 17, 232-237, (1980).

Bonel G. Contribution a l'étude de la Carbonation des Apatites carbonatées du type A. Ann. Chim., 147, 65-88, (1972).

Bonfield W. Elasticity and Viscoelasticity of Cortical Bone. In: Natural and Living Biomaterials, Eds: Hastings G.W.; Ducheyene P., CRC Press, Boca Raton, 43-60, (1984).

Bonfield W. Rebuilding Human Bone. Royal Institution Proceedings, **61**, 159-172, (1989).

Bonfield W. and Datta P.K. Impact Fracture of Compact Bone in a Shock Tube. J. Mat. Sci., **9**, 1609, (1974).

Bonfield W.; Doyle C.; Tanner K.E. *In vivo* Evaluation of Hydroxyapatite Reinforced Polyethylene Composites. In: Biological and Biomechanical Performance of Biomaterials, Eds: Christel P., Meunier A., Lee A.J.C. Elsevier Science Publishers, Amsterdam, (1986).

Bonfield W.; Grynpas M.D.; Young R.J. Crack Velocity and the Fracture of Bone. J. Biomech., **11**, 473-479, (1978).

Bonfield W.; Li C.H. Temperature Dependence of the Deformation of Bone. J. Biomech., **1**, 323, (1968).

Bonfield W.; Tully A.E. Ultrasonic Analysis of the Youngs Modulus of Cortical Bone. J. Biomed. Eng., **4**, 23-27, (1982).

Borneman-Starinkevitch, I.V. On Some Isomorphous Substitutions in Apatite. Compt. Rend. Acad. Sci. URSS, **22**, 113, (1939).

Boskey A.L.; Posner A.S. Formation of Hydroxyapatite at Low Supersaturation. J. Phys. Chem., **80**, 40, (1976).

Boskey A.L.; Posner A.S. Structure and Formation of Bone Mineral. Natural and Living Biomaterials, Hastings G.W.; Chen C.; Ducheyne P. Eds., CRC Press, Boca Raton, Florida, (1984).

Bourne G.H. The Biochemistry and Physiology of Bone. 2nd Edition, 1-4, Academic Press, N.Y., (1972).

Boyde A.; Wolfe L.A.; Jones S.J.; Vesely P.; Maly M. Microscopy of Bone Cells, Bone Tissue, and Bone Healing Around Implants. Implant Dentistry, **1**, (2), 117-125, (1992).

Boyne P.J. Comparison of Porous and Anorganic Xenografts in the Restoration of Alveolar Ridges. In: Quantitative Characterisation and Performance of Porous Implants for Hard Tissue Applications. Ed: Lemons J.E. ASTM STP 953, ASTM, Philadelphia, (1987).

Brear K.; Currey J.D.; Raines S.; Smith K.J. Density and Temperature Effects on some Mechanical Properties of Cancellous Bone. Engineering in Medicine, **17**, (4), 163-167, (1988).

de Bruijn J.D. Calcium Phosphate Biomaterials: Bone Bonding and Biodegredation Properties. Leiden, (1993)

de Bruijn J.D.; Klein C.P.A.T.; de Groot K.; van Blitterswijk C.A. The Ultrastructure of the Bone-Hydroxyapatite Interface *in vitro*. In: Calcium Phosphate Biomaterials: Bone Bonding and Biodegredation Properties, Ed: de Bruijin J.D., Leiden, (1993a)

de Bruijn J.D.; Flach J.S.; de Groot K.; van Blitterswijk C.A.; Davies J.E. Analysis of the Bony Interface with Various Types of Hydroxyapatite *in vitro*. In: Calcium Phosphate Biomaterials: Bone Bonding and Biodegredation Properties, Ed: de Bruijin J.D., Leiden, (1993b)

de Bruijn J.D.; Klein C.P.A.T.; de Groot K.; van Blitterswijk C.A. Influence of Crystal Structure on the Establishment of the Bone-Calcium Phosphate Interface *in vitro*. In: Calcium Phosphate Biomaterials: Bone Bonding and Biodegredation Properties, Ed: de Bruijin J.D., Leiden, (1993c)

de Bruijn J.D.; Bovell Y.P.; van Blitterswijk C.A. Structural Arrangements at the Interface Between Plasma Sprayed Calcium Phosphates and Bone. In: Calcium Phosphate Biomaterials: Bone Bonding and Biodegredation Properties, Ed: de Bruijin J.D., Leiden, (1993d)

de Bruijn J.D.; van Blitterswijk C.A.; Davies J.E. Initial Bone Matrix Formation at the Hydroxyapatite interface *in vivo*. In: Calcium Phosphate Biomaterials: Bone Bonding and Biodegredation Properties, Ed: de Bruijin J.D., Leiden, (1993e)

de Bruijn J.D.; Bovell Y.P.; Davies J.E.; van Blitterswijk C.A. Osteoclastic Resorption of Calcium Phosphates is Potentiated in Post Osteogenic Culture Conditions. In: Calcium Phosphate Biomaterials: Bone Bonding and Biodegredation Properties, Ed: de Bruijin J.D., Leiden, (1993f)

Burger E.H.; Veldhuijzen J.P. Influence of Mechanical Factors on Bone Formation, Resorption and Growth in Vitro. In: Bone, 7, Ed: Brian K Hall, CRC Press, Boca Raton, (1993).

Burstein A.H.; Reilly D.T.; Martens M. Aging of Bone Tissue: Mechanical Properties. J. Bone Jt. Surg., 58, 82-86, (1976).

Burstein A.H.; Zika J.M.; Heiple K.G.; Klein L. Contribution of Collagen and Mineral to the Elastic-Plastic Properties of Bone. J. Bone Jt. Surg., 57, 956-961, (1975).

Burr D.B.; Martin R.B.; Schaffler M.B.; Radin E.L. Bone Remodelling in Response to *in vivo* Fatigue Microdamage. J. Biomech., 18, 189-200, (1985).

Caler W.E; Carter D.R. Time Dependent and Cycle Dependent Bone Fracture. Biological and Biomechanical Performance of Biomaterials. In: Biological and Biomechanical Performance of Biomaterials, Eds: Christel P., Meunier A., Lee A.J.C. Elsevier Science Publishers, Amsterdam, (1986).

Caler W.E; Carter D.R. Bone Creep-Fatigue Damage Accumulation. J. Biomech., 22, 625-635, (1989).

Cameron D.A. The Ultrastructure of Bone. In: The Biochemistry and Physiology of Bone, 2nd Edition. Ed: Bourne G.H., 1, 191-236, Academic Press, N.Y., (1972).

Cant N.W.; Bell J.A.S.; Willson G.R.; Hall W.K. The Vibrational Spectrum of OH Groups in Hydroxyapatites. Spectrochimica Acta, 27A, 425-439, (1971).

Cappozzo A. Human Skeletal System Loading Patterns Associated with Activities of Daily Living. In: Biological and Biomechanical Performance of Biomaterials, Eds: Christel P., Meunier A., Lee A.J.C. Elsevier Science Publishers, Amsterdam, (1986).

Carter D.R.; Caler W.E.; Spengler D.M.; Frankel V.H. Fatigue Behavior of Adult Cortical Bone: The Influence of mean Strain and Strain Range. Acta Orthop. Scand, 52, 481-490, (1981).

Carter D.R.; Hayes W.C. Fatigue Life of Compat Bone. I. Effects of Stress Amplitude, Temperature and Density. J. Biomech., 9, 27-34, (1976).

Carter D.R.; Hayes W.C. The Compressive Behavior of Bone as a two-phase Porous Structure. J. Bone Jt. Surg., 59, 954-962, (1977).

Casseeer-Bette M.; Murray A.B.; Closs E.I.; Ertle V.; Schmidt J. Bone Formation by Osteoblast-Like Cells in a Three Dimensional Culture. Calc. Tiss. Int., 46, 46-56, (1990).

Clemens J.A.P.; Klein C.P.A.T.; Vriesde R.C.; de Groot K.; Rozing P.M. Large Gaps Around Calcium Phosphate Coated Bone Implants: Deficient Bone Apposition Despite use of Allograft Bone. In: Proc. 21st Annual Meeting Society for Biomaterials, San Francisco, (1995).

Clifford C.J.; Downes S. The Use of Cell Proloferation and Viability Assays in the Assessment of Biocompatibility. In: Proc. 21st Annual meeting of the Soc. for Biomaterials, San Francisco, 397, (1995).

Clover J.; Gowen M. Are MG-63 and HOS TE-85 HOS Cell Lines Representative Models of the Osteoblastic Phenotype? Bone, **15** (6), 585-591, (1994).

Cohen J.; Harris W.H. Three-Dimensional Anatomy of Haversian Systems. J. Bone Jt. Surg., **A-40**, 419, (1958).

Compston J.E.; Garrahan N.J.; Croucher P.I.; Wright C.D.P.; Yamaguchi K. Quantitative Analysis of Trabecular Bone Structure. Bone, **14**, 187-192, (1993).

Conway E.J. Micro Diffusion Analysis and Volume Error. 5th Review, Ed: Crosby Lockwood, (1962).

Cormack D.H. Essential Histology. JB Lippincott Co., Philadelphia, (1993).

Courteney-Harris R.G.; Kayser M.V.; Downes S. Comparison of the Early Production of Extracellular Matrix on Dense Hydroxyapatite and Hydroxyapatite Coated Titanium in Cell and Organ Culture. Biomaterials, **16**, (6), 489-495, (1995).

Cowin S.C.; Van Buskirk W.C.; Ashman R.B. The Properties of Bone. In: Handbook of Engineering, Eds: Skalak A. and Chien S., 2-1 - 2-27, (1986).

Currey J.D. The Mechanical Consequences of Variation in the Mineral Content of Bone. J. Biomech., **2**, 1-11, (1969a).

Currey J.D. The Relationship Between the Stiffness and The Mineral Content of Bone. J. Biomech., **2**, 477-480, (1969b).

Currey J. D. The Mechanical Properties of Bone. Clin. Orthop. Rel. Res. **73**, 210-231, (1970).

Currey J.D. The Effects of Strain Rate, Reconstruction and Mineral Content on Some Mechanical Properties of Bovine Bone. J. Biomech., **8**, 81, (1975).

Currey J. The Mechanical Adaptions of Bones. Princeton University Press, (1984).

Currey J.D. The Evolution of the Mechanical Properties of Amniote Bone. J. Biomech., **20** (11/12), 1035-1044, (1987).

Currey J.D. The Effect of Porosity and Mineral Content on the Young's Modulus of Elasticity of Compact Bone. J. Biomech., **21** (2), 131-139, (1988a).

Currey J.D. The Effects of Drying and Re-Wetting on some Mechanical Properties of Cortical Bone. J. Biomech., **21** (5), 439-441, (1988b).

Currey J.D.; Brear K. Hardness, Young's Modulus and Yield Stress in Mammalian Mineralised Tissues. J. Mater. Sci: Materials in Medicine, **1**, 14-20, (1990).

Dabestani M. Elastic and Anelastic Deformation of Human Compact Bone
Ph.D. Thesis, University of London, (1989).

Daculsi G.; Orly I.; Gregoire M.; Heughebaert M.; Hartmann D.J.; Kerebel B. Cell Interactions with Mixed Calciumphosphate (TCP and HAP) and Alumina Solid Phases: An Ultrastructural Study. In: Biological and Biomechanical Performance of Biomaterials, Eds: Christel P., Meunier A., Lee A.J.C. Elsevier Science Publishers, Amsterdam, (1986).

Daculsi G.; Passuti N. Effect of the Macroporosity for Osseous Substitution of Calcium Phosphate Ceramics. Biomaterials, **11**, (Biomat 89), (1990).

Dallant P.; Meunier A.; Guillemin G.; Christel P.; Crolet J.M.; Sedel L. Cortical Bone Response to Orthopaedic Implant Rigidity: An Experimental Study. In: Biological and Biomechanical Performance of Biomaterials, Eds: Christel P., Meunier A., Lee A.J.C. Elsevier Science Publishers, Amsterdam, (1986).

Dallant P.; Meunier A.; Guillemin G.; Christel P.; Guillemin G.; Sedel L. Quantitation of Bone Ingrowth into Porous Implants Submitted to Pulsed Electromagnetic Fields. In: Quantitative Characterisation and Performance of Porous Implants for Hard Tissue Applications. Ed: Lemons J.E. ASTM STP 953, ASTM, Philadelphia, (1987).

Davies J.D. The Bone-Biomaterial Interface. Toronto: University of Toronto Press, (1991).

Davies J.D.; Ottensmeyer P.; Shen X.; Hashimoto M.; Peel S.A.F. Early Extracellular Matrix Synthesis by Bone Cells. In: The Bone-Biomaterial Interface. Ed: Davies J.D. Toronto: University of Toronto Press, (1991a).

Davies J.D.; Nagai N.; Takeshita N.; Smith D.C. Deposition of Cement-Like Matrix on Implant Materials. In The Bone-Biomaterial Interface. Ed: Davies J.D. Toronto: University of Toronto Press, (1991b).

Delling G.; Luehmann H.; Baron R.; Mathews C.H.C.; Olah A. Investigation of Intra- and Inter-Reader Reproducibility. In: Bone Histomorphometry, Eds: Jee W.S.S.; Parfitt A.M. In: Metabolic Bone Disease and Related Research, 2 (Supplement), 419-428, (1980).

Dequer J. Problems in Measureing amount of Bone: Reproducibility, Variability, Sequential Evaluation. In: Bone Histomorphometry, Ed: Meunier P.J., 2nd Int. Workshop, Toulouse, 19-38, (1976).

Denissen H.W.; de Groot K.; Driessen A.A.; Wolke J.G.C.; Peelen J.G.J.; van Dijk H.J.A.; Gehring A.P.; Klopper P.J. Hydroxyapatite Implants: Preparation, Properties and Use in Alveolar Ridge Preservation. Sci. Ceram., 10, 63-69, (1980a).

Denissen H.W.; van Dijk H.J.A.; de Groot K.; Klooper P.J.; Vermeiden J.P.W.; Gehring A.P. Biological and Mechanical Evaluation of Dense Calcium Hydroxyapatite Made by Continuous Hot Pressing. In: Mechanical Properties of Biomaterials. Eds: Hastings G.W.; Williams D.F. John Wiley & Sons Ltd., (1980b).

Detoni S.; Hadzi D. OH Bands in the IR Spectra of Organophosphoric and Phosphinic Acids. Spectrochimiea Acta, 20, 949-955, (1964).

Dhert W.J.A.; Klein C.P.A.T.; Wolke J.G.C.; van der Velde E.A.; de Groot K.; Rozing P.M. A Mechanical Investigation of Fluorapatite, Magnesium Whitlockite and Hydroxyapatite Plasma Sprayed Coatings in Goats. J. Biomed. Mater. Res., 25, 1183-1200, (1991).

Dhert W.J.A.; Verheyen C.C.P.M.; Braak L.H.; de Wijn J.R.; Klein C.P.A.T.; de Groot K.; Rozing P.M. A Finite Element Analysis of the Push-Out Teast: Influence of Test Conditions. J. Biomed. Mater. Res., 26, 119-130, (1992).

Dhert W.J.A.; Thomsen P.; Klein C.P.A.T.; de Groot K.; Rozing P.M.; Ericson L.E. Fluorapatite-Coated implants in Experimental Arthiritis: The response of rabbit Trabecular Bone. J. Mater. Sci: Materials in Medcine, 5, 59-66, (1994).

Dobson J.L.; Mathews R.S.; Stelling F.H. Implant Acceptance in Body Tissue. In: Use of Ceramics in Surgical Implants, Eds: Hulbert S.F.; Young F.A. Gordon & Breach Science Publishers, (1978).

Doherty M.J.; Schlag G.; Schwartz N.; Mollan R.A.B.; Nolan P.C. Wilson D.J. Biocompatibility of Xenogenic Bone Commercially available Coral, a Bioceramic and Tissue Sealant for Human Osteoblasts. Biomaterials, 15 (8), 601-608, (1994).

Doi Y.; Moriwaki Y.; Aoba T.; Okazaki M.; Takahash J.; Joshin K. Carbonate Apatites from Aqueous and Non-Aqueous Media Studied by ESR, IR and XRD: Effect of Amonium Ions on Crystallography Parameters. J Dent. Res., **61**, 429-434, (1982).

MacDonald B.R.; Gowen M. The Cell Biology of Bone. Batllieres Clinical Rheumatology, **7**, (3), 421-443, (1993).

Donath K. A Method for the Study of Undecalcified Bones and Teeth with Attached Soft Tissues. J. Oral Pathology, **11**, 318-326, (1982).

Donath K. Preparation of Histologic Sections. Exakt-Kulze-Publication, Norderstedt, (1990).

Dowker S.E.P.; Elliot J.C. Infrared Study of Trapped Carbon Dioxide in Thermally Treated Apatites. J. Solid State Chem., **47**, 164-173, (1983).

Doyle C.; Luklinska Z.B.; Tanner K.E.; Bonfield W. An Ultrastructural Study of the Interface Between Hydroxyapatite/Polymer Composite and Bone. Advances in Biomaterials, **9**, 339-344, (1990).

Dreesman H. Ueber Knochenplombierung. Beitr. Klin Chir., **9**, 804, (1894).

Driessen A.A.; Klein C.P.A.T.; de Groot K. Preparation and some Properties of Sintered ß-Whitlockite. Biomaterials, **3**, 113-116, (1982).

Driessens F.C.M. The Mineral in Bone, Dentin and Tooth Enamel. Bull. Soc. Chim. Belg., **89**, 663, (1980).

Driessens F.C.M. Formation and Stability of Calcium Phosphates in Relation to the Phase Composition of the Mineral in Calcified Tissue. In: Bioceramics of Calcium Phosphates. Ed: DeGroot K. CRC Press, Boca Raton, Florida, (1983).

Duck F.A. Physical Properties of Tissue. Academic Press, London, (1990).

Duckworth W. Discussion of Ryshkewitch Paper. J. Am. Ceram. Soc., **36**, (2), 68, (1953).

Ecarot-Charrier B.; Glorieux F.H.; van der Rest M.; Pereira G. Osteoblast Isolated from Mouse Calavaria Initiate Matrix Mineralisation in Culture. J. Cell Biol., **96**, 639-643, (1983).

Echlin P. Intra-Cytoplasmic Membranous Inclusions in the Blue-Green Algae, Anacystis Nidulans. Archiv für Mikrobiologie, **49**, 267-274, (1964).

Eggli P.S.; Muller W.; Schenk R.K. Porous Hydroxyapatite and Tricalcium Phosphate Cylinders with Two Different Pore Size Ranges Implanted in the Cancellous Bone of Rabbits. Clin. Orthop. Relat. Res., **232**, 127-138, (1988).

Eitel W. Uber Karbonatphosphate der Apatitgruppe. Schriften konigsberg gelehrten Ges. Naturw., **1**, 159, (1924).

Ellingson W.A.; Wong P.S.; Dieckman S.L.; Ackerman J.L.; Garrido L. MRI- A New Characterization Technique for Advanced Ceramics. Ceram. Bull., **68** (6), 1180-1186, (1989).

Elliot J.C. The Crystalographic Structure of Dental Enamel and Related Apatites. PhD Thesis, London Hospital Medical College, (1964).

Elliot J.C. Recent Progress in the Chemistry, Crystal Chemistry and Structure of the Apatites. Calc. Tiss, Res., **3**, 293-307, (1969).

Engström A. Bone as a Tissue (Eds: Rodahl K.; Nicholson J.T.; Brown E.M.) McGraw-Hill, N. Y., (1960).

Engström A. Aspects of The Molecular Structure of Bone. In: The Biochemistry and Physiology of Bone, 2nd Edition. Ed: Bourne G.H., **1**, 237-258, Academic Press, N.Y., **(1972)**.

Epker B.N.; Hattner R.; Frost H.M. Radial Rate of Osteon Closure: Its Application in the Study of Bone Formation in Metabolic Bone Disease. J. Lab. Clin. Med., **64**, 643, **(1964)**.

Evans F.G. Mechanical Properties of Bone. Charles C Thomas, Springfield Ill., **(1973)**.

Evans F.G.; Vincentelli R. Relation of Collagen Fibre Orientation to some Mechanical Properties of Human Cortical Bone. J. Biomech., **2**, 63-71, **(1969)**.

Evans R.A.; Dunstan C.R; Hills E.E. Extent of Resorbing Surface Based on Histochemical Identification of Osteoclasts. In: Bone Histomorphometry, Eds: Jee W.S.S.; Parfitt A.M. In: Metabolic Bone Disease and Related Research, **2** (Supplement), 29-34, **(1980)**.

Fabbri M.; Celotti G.C.; Ravaglioli A. Elliot J.C. Hydroxyapatite Based Porous Aggregates: Physiochemical Nature, Structure, Texture and Architecture. Biomaterials, **16** (3), 225-228, **(1995)**.

Fang Y.; Agrawal D.K; Roy D.M.; Roy R. Fabrication of Porous Hydroxyapatite by Microwave Processing. J. Mater. Res., **7** (2), 490-494, **(1992)**.

Faucheux C.; Bareille R.; Rouais F.; Amédée J.; Liebendörfer A.; Dard M. Biocompatibility Testing Of A Bovine Hydroxy-Apatite Ceramic Material With The Use Of Osteo-Progenitor Cell Isolated From The Human Bone Marrow. J. Mater. Sci: Materials in Medicine, **5**, 635-639, **(1994)**.

Fernández-Morán H.; Engstrom A. Electron microscopy and x-ray diffraction of bone. Biochim. Biophys. Acta, 23, 260-264, **(1957)**.

Folkman J.; Moscona A. Role of Cell Shape in Growth Control. Nature, **273**, 345-349, **(1978)**.

Foster M.A.; Hutchison J.M.S. NMR Imaging - Methods and Applications. J. Biomed. Eng., **7**, 171-182, **(1985)**.

Francis M.D.; Briner W.W.; Grey J.A. Chemical Agents in the Control of Calcification Processes in Biological Systems. In: Hard Tisssue Growth, Repair and Remineralisation. Eds: Sonnaes R.F.; Vaughan J.M., Elsevier, Amsterdam, **(1973)**.

Frayssinet P.; Trouillet J.L.; Roquet N.; Azimus E.; Autefage A. Osseointergration of Macroporous Calciumphosphate Ceramics having a Different Chemical Composition. Biomaterials, **14** (6), 423-429, **(1993)**.

Freeman M.A.R.; Todd R.C.; Pirie C.J. The Role of Fatigue in the Pathogenesis of Senile Femoral Neck Fracture. J. Bone Jt. Surg., **56**, 698-702, **(1974)**.

Frost H.M. Tetracycline-Based Histological Analysis of Bone Remodelling. Calc. Tiss. Res., **3**, 211-237, **(1969)**.

Frost H.M. Histomorphometry of Trabecular Bone I. Theoretical Correction of Appositional Rate Measurements. In: Bone Histomorphometry, Ed: Meunier P.J., 2nd Int. Workshop, Toulouse, 361-370, **(1976)**.

Fullman R.L. Measurement of Particle Sizes in Opaque Bodies. Transactions of the A.I.M.E., **197** 447-452, **(1953)**.

Fyhrie D.P.; Fazzalari N.L.; Goulet R.; Goldstein S.A. Direct Calculation of the Surface-to-Volume Ratio for Human Cancellous Bone. J. Biomechanics, **26** (8), 955-967, **(1993)**.

Garrahan N.J.; Mellish R.W.E; Compson J.E. A New Method for the Two-Dimensional Analysis of Bone Structure in Human Iliac Crest Biopsies. J. Microscopy, **142** (3), 341-349, **(1986)**.

Gebhardt W. Über funktionell wichtige Anordnungsweisen der feineren und gröberen Bauelemente des Wirbeltierknochens. II. Spezieller Teil. Der Bau der Haversschen Lamellensysteme und seine funktionelle Bedeutung. Arch. Entwickl. Mech. Org., **20**, 187-322 **(1906)**.

Geesink R.G.T.; ge Groot K.; Klein C.P.A.T. Bonding of Bone to Apatite-Coated Implants. J. Bone Jt. Surgery, **70-B** (1), **(1988)**.

Le Geros R.Z. Crystallographic Studies of the Carbonate Substitution in the Apatite Structure. PhD Thesis, New York University, **(1967)**.

Le Geros R.Z. The Unit Cell Dimensions of Human Enamel Apatite: Effect of Chloride Incorporation. Arch. Oral. Biol., **20**, 63-71, **(1974)**.

Le Geros R.Z. Incorporation of Magnesium in Synthetic and Biological Apatites. In: Tooth Enamel IV. Eds: Fearnhead R.W.; Suga S., Elsevier, Amsterdam, 32-36 **(1984)**.

Le Geros R.Z. Materials for Bone Repair, Augmentation and Implant Coatings. In: Proceedings of the International Seminar of Orthopedic Research, Ed: Niwa S., Springer-Verlag, Nagoya, **(1992)**.

Le Geros R.Z.; Le Geros J.P. Dense Hydroxyapatite. In: An Introduction to Biocramics Eds: Hench L.L.; Wilson J. World Scientific, Singapore, **(1993)**.

Le Geros R.Z.; Kijkowska R.; Tung M.; Le Geros J.P. Effect of Strontium on some Properties of Apatites. In: Tooth Enamel V, Ed: Fearnhead R.W., Florence Publishers, Tokyo, 393-402, **(1989)**.

Le Geros R.Z.; Taheri M.H.; Quirolgico G.; Le Geros J.P. Formation and Stability of Apatites: Effects of some Cationic Substituents. Proc. 2nd International Congress on Phosphorous Compounds, Boston, 41-53, **(1980)**.

Le Geros R.Z.; Trautz O.R.; Le Geros J.P.; Klein E. Carbonate Substitution in the Apatite Structure. Bull. Soc. Chim. Franc., 1712-1713, **(1968)**.

Le Geros R.Z.; Tung M. Chemical Stability of Carbonate and Fluoride-Containing Apatites. Caries. Res., **17**, 419-429, **(1983)**.

Gibson L.G.; Ashby M.F. Cellular Soilids. Pergamon Press, **(1988)**.

Gibson L.J. The Mechanical Behaviour of Cancellous Bone. J. Biomech., **18**, (5), 317-328, **(1985)**.

Gilmore R.S.; Katz J.L. Elastic Properties of Apatites. J. Mater. Sci., **17**, 1131-1141, **(1982)**.

Glauert A.M. The Fixation and Embedding of Biological Specimens. In: Techniques for Electron Microscopy, Ed: Kay D. Blackwell, Oxford, 2nd Edition, **(1965)**.

Glimcher M.J. Recent Studies of the early Mineral Deposits in Bone Enamel and of the Organic Matrix of Enamel. Calc. Tiss. Res., **2**, Suppl, **(1968a)**.

Glimcher M.J. A Basic Architectural Principle in the Organization of Mineralized Tissue. Clin. Orthop., **61**, 16, **(1968b)**.

Glimcher M.J. Composition, Structure and Organisation of Bone and Other Mineralised Tissues and the Mechanism of Calcification. In: Handbook of Physiology-Endocrinology VII. Williams and Wilkins, Baltimore, **(1976)**.

Glowacki J.; Spector M. Tissue Response to Bone Derrived and Synthetic Materials. In: The Bone-Biomaterial Interface. Ed: Davies J.D. Toronto: University of Toronto Press, **(1991)**.

Goldstein S.A. The Mechanical Properties of Trabecular Bone Dependance on Anatomical Location and Function. J. Biomech., **20** (11/12), 1055-1061, **(1987)**.

Goldstein S.A.; Wilson D.L.; Sontegard D.A.; Matthews L.S. The Mechanical Properties of Human Tibial Trabecular Bone as a Function of Metaphysial location. J. Biomech., **16**, 965-969, **(1983)**.

Gomi K.; de Bruijn J.D.; Ogura M.; Davies J.E. The Effect of Substratum Roughness on Osteoclast-Like Cells *in vitro*. In: Calcium Phosphate Biomaterials: Bone Bonding and Biodegredation Properties, Ed: de Bruijn J.D., Leiden, **(1993b)**.

Gomi K.; Lowenberg B.; Shapiro G.; Davies J.E. Resorption of Sintered Synthetic Hydroxyapatite by Osteoclasts *in vitro*. Biomaterials, 14 (2), 91-96, **(1993a)**.

Goodman S.; Toksuig-Larsen S.; Aspenberg P. Ingrowth of Bone into Pores in Titanium Chambers Implanted in Rabbits:Effect of Pore Cross-Sectional Shape in the Presence of Dynamic Shear. J. Biomed. Mater. Res., 27, 247-253, **(1993)**.

Griffith A.A. Phenomena of Rupture and Flow in Solids. Phil. Trans. Roy. Soc., London, **A221**, 163-198, **(1920)**.

de Groot K. Calciumphosphate Ceramics: Biomaterials for Middle Ear Implants. In: Proc. 1st Int. Symp. on Biomats. in Otology, 80-83, **(1983)**.

de Groot K. Effect of Porosity and Physicochemical Properties on the Stability, Resorption, and Strength of Calcium Phosphate Ceramics. Annals New York Academy of Sciences, 227-233, **(1987)**.

Gross U.; Roggendorf W.; Schmitz H-J.; Strunz V. Biomechanical and Morphometric Testing Methods for Porous Surface-Reactive Biomaterials. In: Quantitative Characterisation and Performance of Porous Implants for Hard Tissue Applications. Ed: Lemons J.E. ASTM STP 953, ASTM, Philadelphia, 330-346, **(1987)**.

Gross U.M.; Müller-Mai C.M.; Voigt C. The Interface of Calcium-Phosphate and Glass-Ceramic in Bone, a Structural Analysis. Biomaterials, **11**, (Biomat 89), 83-85, **(1990)**.

Greenberg S.W.; Gonzalez D.; Gurdjian E.S.; Thomas L.M. Changes in Physical Properties of Bone Between the in Vivo and Freshly Dead and Embalmed Conditions. In: Proc. 12th Stapp Car Crash Conf., Society of Automotive Engineers, N. Y., 271 **(1968)**.

Hagen, A.R. Structural Features of Biologically Involved Phosphates. Acta Odont. Scand., **31**, 149-173, **1973)**.

Hagiwara H.; Green D.J. Elastic Behaviour of Open-Cell Alumina. J. Am. Ceram. Soc, **70** (11), 811-815, **(1987)**.

Hally A.D. A Counting Method for Measuring the Volumes of Tissue Components in Microscopical Sections. Q. J. Micrsc. Sci., **105**, 503-517, **(1964)**.

Ham A.W.; Harris W.R. Repair and Transplantation of Bone. In: The Biochemistry and Physiology of Bone, 2nd Edition. Ed: Bourne G.H., **3**, 337-399, Academic Press, N.Y., **(1972)**.

Hamman G. Comparison of Measurement Methods for Characterization of Porous Coatings. In: Quantitative Characteristics and Performance of Porous Implants for Hard Tissue Applications. Ed: Lemons J.E., ASTM, STP 953, 77-91, **(1987)**.

Hancox N.H. The Osteoclast. In: The Biochemistry and Physiology of Bone, 2nd Edition. Ed: Bourne G.H., **1**, 45-67, Academic Press, N.Y., **(1972)**.

Harms S.E.; Kramer D.M. Fundamentals of MRI. CRC Critical Reviews in Diagnostic Imaging, **25** (1), 79-111, **(1985)**.

Harrigan T.P.; Jasty M.; Mann R.W.; Harris W.H. Limitations of the Continuum Assumption in Cancellous Bone. J. Biomech., **21** (4), 269-275, **(1988)**.

Harrigan T.P.; Hamilton J.J. Bone Remodelling and Structural Optimization. J. Biomech., **27** (3), 323-328, (1994).

Harris J.R. Assessment of Parameters Influencing the Mechanical Properties of Human Bone. MSc Thesis, Queen Mary and Westfield College, University of London, (1991).

Hassager; Fitzpatrick L.A.; Spencer E.M.; Riggs B.L.; Conover A. Basal and Regulated Secretion of Insulin-Like Growth Factor Binding Proteins in Osteoblast-Like Cells is Cell Line Specific. J. Clin. Endocrinol. Metab., **75** (1), 228-233, (1992).

Hastings G.W.; Chen C.; Ducheyne P. Natural and Living Biomaterials. CRC Press, Boca Raton, Florida, (1984).

Hayashi K.; Inaome T.; Tsumura H.; Nakashima Y.; Sugioka Y. Effect of Surface Roughness of Hydroxyapatite Coated Titanium on the Bone-Implant Interface Shear Strength. Biomaterials, **15** (14), 1187-1191, (1994).

Hayek E.; Newesely H. Pentacalcium Monohydroxyorthophosphate. Inorg. Syn., **7**, 121-128, (1963).

Heersche J.N.M. Mechanism of Osteoclastic Bone Resorption: A New Hypothesis. Calc. Tiss. Res., **28**, 81-84, (1978).

Heersche J.N.M.; Tam C.S.; Jones G. Measurement of the Apposition Rate of Mineralized Bone Matrix and Osteoid in Normal, D-Restricted and D-Repleted Rats Using Simultaneous Labelling with 3_H Proline and Tetracycline. In: The Chemistry and Biology of Mineralized Connective Tissues, Ed: Veis A., Elsevier, 299-302, (1981).

Heimke G. The Aspects and Modes of Fixation of Bone Replacements. In: Osseo-Intergrated Implants, Ed: Heimke G., **1**, 2-34, (1990).

Hench L.L.; Wilson J. An Introduction to Bioceramics. World Scientific, Singapore, (1993).

Hentschel H. Röntgenographische Untersuchungen am Apatit. Centralb. Mineral. Geol. Paleont., **1923**, 609-626, (1923).

Hert J. A new attempt at the Interpretation of the Functional Architecture of Cancellous Bone. J. Biomech., **27** (2), 239-242, (1994).

Hodgskinson R.; Currey J.D. Effects of Structural Variation on Young's Modulus of Non-Human Cancellous Bone. Proc. Inst. Mech. Engrs., **204**, 43-52, (1990a).

Hodgskinson R.; Currey J.D. Effect of Variation in Structure on the Young's Modulus of Cancellous Bone: A Comparison of Human Bone and Non-Human Material. Proc. Inst. Mech. Engrs., **204**, 115-121, (1990b).

Hodgskinson R.; Currey J.D.; Evans G.P. Hardness, an Indicator of the Mechanical Competence of Cancellous Bone. J. Orthop. Res., **7**, 754-758, (1989).

Hollister S.J.; Kikuchi N.; Goldstein S.A. Do Bone Ingrowth Processess Produce a Globally Optimized Structure? J. Biomech., **26** (4/5), 391-407, (1993).

Holmes R.E. Bone Regeneration within a Coralline Hydroxyapatite Implant. Plast. Reconstr. Surg., **63**, 626-633, (1979).

Holmes R.E.; Mooney V.; Bucholz R.; Tencer A. A Coralline Hydroxyapatite Bone Graft Substitue. Clin. Orthop. Rel. Res., **188**, 252-262, (1984).

Holmes R.E.; Hagler H.K.; Coletta C.A. Thick Section Histometry of Porous Hydroxyapatite Implants Using Backscattered Electron Imaging. J. Biomed. Mater. Res., **21**, 731-739, (1987).

Hornung P.A.; Schuff N. Noninvasive Imaging and Spectroscopy - Broad Applications of MR. Clin. Chem., **38** (9), 1608-1612, (1992).

Le Huec J.C. Schaeuerbeke T.; Clement D.; Faber J.; le Rebeller A. Influence of Porosity on the Mechanical Resistance of Hydroxyapatite Ceramics under Compressive Stress. Biomaterials, **16**, 113-118, (1995).

Hulbert S.F. Biomaterials: The Case for Ceramics. In: Use of Ceramics in Surgical Implants, Eds: Hulbert S.F.; Young F.A. Gordon & Breach Science Publishers, (1978).

Hulbert S.F.; Morrison J.S.; Klawitter J.J. Compatability of Porous Ceramics with Soft Tissue Application to Tracheal Prostheses. J. Biomed. Mater. Res., **6**, 347-374, (1972).

Hulbert S.F.; Hench L.L.; Forbes D.; Bowman L.S. History of Bioceramics. In: Ceramics in Surgery. Ed: P.Vincezini, Elsevier Science, Amsterdam, 3-29, (1983).

Hunter A.; Archer C.W.; Walker P.S.; Blunn. Attachment and Proliferation of Osteoblasts and Fibroblasts on Biomaterials for Orthopaedic Use. Biomaterials, **16**, (4), 287-295, (1995).

Ingaray J.L.; Oudadesse H.; Blondiauy G. Quantitative Studdy of the Coral Transformations *in vivo* by Several Physical Analytical Methods. Biomaterials, **11**, (Biomat 89), (1990).

Ishikawa K.; Duchheyne P.; Radin S. Determination of the Ca/P Ratio in Calcium-Deficient Hydroxyapatite using X-Ray Diffraction Analysis. J. Mater. Sci.: Materials in Medicine, **4**, 165-168, (1993).

Jarcho M.; Bolen C.H.; Thomas M.B.; Bobick J.; Kay J.F.; Doremus R.H. Hydroxylapatite Synthesis and Characterization in Dense Polycrystalline Form. J. Mater. Sci., **11**, 2027-2035, (1976).

J.C.P.D.S. International Centre for Diffraction. Powder Diffraction File (Inorganic Phases) Pub JCPDS, 9-432, (1980).

Jee W.S.S.; Kimmel D.B. Bone Cell Origin at the Endosteal Surface. In: Bone Histomorphometry, Ed: Meunier P.J., 2nd Int. Workshop, Toulouse, 89-96, (1976).

Jee W.S.S.; Parfitt A.M. Bone Histomorphometry. In: Metabolic Bone Disease and Related Research, **2** (Supplement), (1980).

Jenson A.T., Rowles S. L. Magnesium Whitlockite a Major Constituent of Dental Calculus. Acta Ordens Scand., **15**, 121-139, (1957).

Jingushi S.; Bolander M.E. Biological Cascades of Fracture Healing as Models for Bone-Biomaterial Intefacial Reactions. In: The Bone-Biomaterial Interface. Ed: Davies J.D. Toronto: University of Toronto Press, (1991).

Johansson C.B.; Morberg P. Importance of Ground Section Thickness for Reliable Histomorphometrical Results. Biomaterials, **16** (2), 91-95, (1995a).

Johansson C.B.; Morberg P. Cutting Directions of Bone with Biomaterials in situ does Influence the Outcome of Histomorphometrical Quantifications. Biomaterials, **16** (13), 1037-1039, (1995b).

Jones S.J.; Boyde A. Experimental Study of Changes in Osteoblastic Shape Induced by Calcitonin and Parathyroid Extract in an Organ System. Cell Tiss. Res., **169**, 449-465, (1976).

de Jong W.F. Le Substance Minerale dans le Os. Rec Trav Chim., **45**, 445, (1926).

Junqueira L.C.; Carreiro J.; Long J.A. Basic Histology. 5th Edition, Lange Med. Publications, Los Altos, California, (1986).

Kangasniemi I.M.O.; Verheyen C.C.P.M.; van der Velde E.A.; de Groot K.
In vivo Tensile Testing of Fluorapatite and Hydroxylapatite Plasma-Sprayed Coatings
J. Biomedical Maters. Res. 28 563-572, (1994).

Kasemo B.; Lausmaa J. The Biomaterial-Tissue Interface and its Analogues in Surface Science and Technology. In: The Bone-Biomaterial Interface. Ed: Davies J.D. Toronto: University of Toronto Press, (1991).

Katz J.L.; Maharidge R.L.; Yoon H.S. The Frequency and Temperature Dependance of Longitudinal Ultrasonic Velocities in Bovine Bone. In: Biological and Biomechanical Performance of Biomaterials, Eds: Christel P., Meunier A., Lee A.J.C. Elsevier Science Publishers, Amsterdam, (1986).

Kay I.M., Young R.A., Posner A.S. Crystal Structure of Hydroxyapatite. Nature, **204**, 1050-1052, (1964).

Kayser M.V. Personal Communication. (1995).

Keaveny T.M.; Borchers R.E.; Gibson L.J.; Hayes W.C. Theoretical Analysis of the experimental Artifact in Trabecular Bone Compressive Modulus. J. Biomech., **26** (4), 599-607, (1993a).

Keaveny T.M.; Borchers R.E.; Gibson L.J.; Hayes W.C. Trabecular Bone Modulus and Strength can depend on Specimen Geometry. J. Biomech., **26** (8), 991-1000, (1993b).

Keaveny T.M.; Hayes W.C. Mechanical Properties of Cortical and Trabecular Bone. In: Bone, **7**. Ed: Hall B.K., CRC Press, Boca Raton, Florida, (1993).

Keller J.C.; Young F.A. Histomorphometric Analysis of Bone Ingrowth into Porous-Coated Dental Implants. In: Quantitative Characteristics and Performance of Porous Implants for Hard Tissue Applications. Ed: Lemons J.E. ASTM STP 953, 219-232, (1987).

Kempson G.E. Relationship Between the Tensile Properties of Articular Cartilage from the Human Knee and Age. Annals of the Rheumatic Diseases, **41**, 508-511, (1982).

Kiefer H.; Claes L.; Burri C.; Kluglmeier K. Biological Fixation of Various Titanium and Carbon Implants in Cancellous bone: Biomechanical and Histomorphological Evaluation. In: Biological and Biomechanical Performance of Biomaterials, Eds: Christel P., Meunier A., Lee A.J.C. Elsevier Science Publishers, Amsterdam, (1986).

Kielty C.M.; Hopkinson I.; Grant M.E. Collagen: The Familiy: Structure, Assembly, and Organization in the Extracellular Matrix. In: Connective Tissue and Its Heritable Disorders, Wiley-Liss, 103-147, (1993).

Kieswetter K.; Bauer T.W.; Brown S.a.; Van Lente F.; Merritt K. Alteration of Hydroxyapatite Coatings Exposed to Chemicals used in Histological Fixation. J. Biomed. Mater. Res., **28**, 281-287, (1994).

Kijima T.; Tsutsumi M. Preparation and Thermal Properties of Dense Polycrystalline Oxyhydroxyapatite. J. Am. Ceram. Soc., **62** (9), 455-457, (1979).

Kimmell D.B.; Jee W.S.S. Morphometric Measurements in Tissue Isometric to an Irregular Reference Line. In: Bone Histomorphometry, Ed: Meunier P.J., 2nd Int. Workshop, Toulouse, 97-102, (1976).

Kimmell D.B.; Jee W.S.S. Study of Skeletal Kinetics of Young Adult Beagles. In: Research in Radiobiology in the Internal Irradiation Program, 152-161, (1978).

Klawitter J.J. A Basic Investigation of Bone Growth into a Porous Ceramic Material. Ph.D. Thesis, Clemson University, Clemson SC., (1970).

Klawitter J.J.; Bagwell J.G; Weinstein A.M.; Sauer B.W.; Pruitt J.R. An evaluation of Bone Growth into Porous High Density Polyethylene. J. Biomed. Mater. Res., **10**, 311-323, (1976).

Klawitter J.J.; Cook S.D., Kay J.F.; Popich L.S.; Rust A.M. *In Vivo* Characterisation of Hydroxylapatite (HA) coated Pyrolitic Implants. In: Proc. 21st Annual meeting of the Soc. for Biomaterials, San Francisco, 331, (1995).

Klawitter J.J.; Hulbert S.F. Application of Porous Ceramics for the Attachment of Load Bearing Internal Orthopedic Applications. J. Biomed., Mater. Res., **5**, 161-229, (1971).

Klawitter J.J.; Talbert C.D.; Hulbert S.F. Artificial Bones. In: Use of Ceramics in Surgical Implants. Eds: Hulbert S.F.; Young F.A., Elsevier Science, Amsterdam, (1978).

Klee W.E.; Engel G. IR Spectra of the Phosphate ions in Various Apatites. J. Inorg. Nucl. Chem., **32**, 1832-1843, (1970).

Klein C.P.A.T.; Driessen A.A.; de Groot K. Biodegredation of Calciumphosphate Ceramics - Ultrastructural Geometry and Dissolubility of Different Calcium Phosphate Ceramics. In: Proc. 1st Int. Symp. on Biomats. in Otology, 84-92, (1983a).

Klein C.P.A.T.; Driessen A.A,; de Groot K.; van den Hooff A. Biodegration Behaviour of Various Calcium Phosphate Materials in Bone Tissue. J. Biomed. Mater. Res., **17**, 769-784, (1983b).

Klein C.P.A.T.; Wolke J.G.C.; de Groot K. Stability of Calcium Phosphorous Ceramics and Plasma Sprayed Coatings. In: An Introduction to Biocramics Eds: Hench L.L.; Wilson J., World Scientific, Singapore, (1993).

Knowles J.C.; Horton J.A. Bonfield W. Rietveld Analysis on the Effect of Sintering Conditions on the Ceramic Structure of Hydroxyapatite. Bioceramics, **7**, 23-28, (1994).

Knudsen F.P. Dependance of Mechanical Strength of Brittle Polycrystaline Speciemns on Porosity and Grain Size. J. Am. Ceram. Soc., **42** (8), 376-387, (1959).

Knudsen F.P. Effect of Porosity on Youngs' Modulus of Alumina. J. Am. Ceram. Soc., **45**, 94-95, (1962).

Kobayashi T.; Shingaki S.; Nakajima T.; Hanada K. Chin Augumentation with Porous HA Blocks. J. Long Term Effects of Medical Implants, **3** (4), 282-294, (1993).

Koeneman J.B. Fundamental Aspects of Load Transfer and Load Sharing. In: Quantitative Characterisation and Performance of Porous Implants for Hard Tissue Applications. Ed: Lemons J.E. ASTM STP 953, ASTM, Philadelphia, (1987).

Krasil'nikov V. A. Sound and Ultrasound Waves. 3rd Edition Israel Program for Scientific Translations Ltd., (1963).

Kuhn J.L.; Goulet R.W.; Goldstein S.A.; Feidkamp L.A. A Study of the Variation of Trabecular Architectures in Small Volumes of Bone using a Microcomputed Tomography System. In: Proc. Am. Soc. Biomech., Champaign, Illinois, 16-17, (1988).

Kuhn J.L.; Goldstein S.A.; Ciarelli M.J.; Mathews L.S. The Limitations of Canine Trabecular Bone as a Model for Human: A Biomechanical Study. J. Biomech., **22** (2), 95-107, (1989).

Kühne J.H.; Bartl R.; Frish B.; Hanmer C.; Jansson V.; Zimmer M. Bone Formation in Coralline Hydroxyapatite. Effects of Pore Size Studied in Rabbits. Acta Orthop. Scand., **65** (3), 246-252, (1994).

Kuntz D.; Maziere B.; Ryckewaert A. Comparative Study of Methods for Bone Loss Estimation in Osteoporotics. In: Metabolic Bone Disease and Related Research, **2** (Supplement), 435-442, (1980).

Kurashina K.; Kurita H.; Takeuchi H.; Hirano M.; Klein C.P.A.T.; de Groot K. Osteogenesis in Muscle with Composite Graft of Hydroxyapatite and Autogenous Clavarial Periosteum, a Preliminary Report. Biomaterials, **16** (2), 119-123, (1995).

Kyetune-Nyombi E.; Lau K-H.W.; Baylink D.J.; Strong D.D. Stimulation of Cellular Alkaline-Phosphatase Activity and its mRNA Level in a Human Osteosarcoma Cell Line by $1,25(OH)_2D_3$. Arch. of Biochem. Biophys., **275** (2), 363-370, (1989).

Kyetune-Nyombi E.; Lau K-H.W.; Baylink D.J.; Strong D.D. 1,25-Dihydroxy Vitamin D_3 Stimulates Both Alkaline-Phosphatase Gene Transcription and mRNA Stability in Human Bone Cells. Arch. Biochem. Biophys., **291** (2), 316-325, (1991).

Landis W.J. Inorganic-Organic Interrelations in Calcification: On the problem of Correlating Electron Microscopic Observations and Mechanism. In: The Chemistry and Biology of Mineralized Connective Tissues, Ed: Veis A., Elsevier, (1981).

Lanyon L.E. Functional Strain in Bone Tissue as an Ovjective and Controlling Stimulus for Adaptive Bone Remodelling. J. Biomech., **20** (11/12), 1083-1093, (1987).

Lanyon L.E.; Goodship A.E.; Pie C.J.; MacFie J.H. Mechanically Adaptive Bone Remodelling. J. Biomech., **15** (3), 141-154, (1982).

Larson A.C.; Von Dreele R.B.; Lujan M. GSAS-Generalised Crystal Structure Analsysi System. Neutron Scattering Centre, Los Alamos National Laboratory, Califomial, (1990).

Lau K.H.; Yoo A.; Ping-Wang S. Aluminium Stimulates the Proliferation and Differentiation of Osteoblasts in Vitro that is Different from Fluoride. Mol. Cell Biochem., **105**, 93-105, (1991).

Leblond C.P.; Weinstoccl M. Radio Autographic Studies in Bone. In: The Biochemistry and Physiology of Bone, 2nd Edition. Ed: Bourne G.H., **3**, Academic Press, N. Y., (1971).

Lee W.R. Appositional Bone Formation in Canine Bone: A Quantitative microscopic Study using Tetracycline Markers. J. Anat., **98**, 665-677, (1964).

Lehr J.R., Brown E.H. Frazier A.W. Smith J.P. and Thrasher R.D. Crystallographic Properties of Fertilizer Compounds. Tenesee Valley Authority, Chem. Eng. Bull., 6, 1-166, (1967).

Li J.; Fartash B.; Hermansson L. Hydroxyapaite and Alumina Composites and Bone Bonding. Biomaterials, **16** (5), 417-422, (1995).

Li P.; Ohtsuki C.; Kokubo T.; Nakanishi K.; Soga N.; de Groot K. The Role of Hydrated Silica, Titania and Alumina in Introducing Apatite on Implants. J. Biomed. Mater. Res., **28**, 7-15, (1994a).

Lin C.; Chen P.; Hang Y.; Cheng C.; Chueh S. A Comparison of Metal Implants with Co-Cr-Mo and Hydroxyapatite Coatings in Bone Implant Interfacial Bonding Strength and Bone Ingrowth. Biomed. Eng: Applications, Basis and Communications **6** (2), 164-173, (1994b).

Lin F-H.; Lin C-C.; Liu H-C.; Huang Y-Y.; Wang C-Y.; Lu C-M. Sintered Porous DP-Bioactive Glass and Hydroxyapatite as Bone Substitute. Biomaterials, **15** (13), 1087-1098, (1994).

Lin H.; Xu H.; de Groot K. Tensile Strength of the interface between hydroxyapatite and Bone. J. Biomed. Mater. Res., **26**, 7-18, (1992).

Linde F.; Hvid I. Stiffness Behaviour of Trabecular Bone Specimens. J. Biomech., **20** (1), 83-89, (1987).

Linde F.; Hvid I. The Effec of Constraint on the Mechanical Behaviour of Trabecular Bone Specimens. J. Biomech., **22** (5), 485-490, (1989).

Linde F.; Hvid I.; Jensen N.C. Mechanical Properties of Trabecular Bone in Repetitive Axial Loading. In: Biological and Biomechanical Performance of Biomaterials, Eds: Christel P., Meunier A., Lee A.J.C. Elsevier Science Publishers, Amsterdam, (1986).

Linde F.; Hvid I.; Madsen F. The Effect of Specimen Geometry on the Mechanical Behaviour of Trabecular Bone Specimens. J. Biomech., **25** (4), 359-368, (**1992**).

Linde F.; Norgaard P.; Hvid I.; Odgaard A. Soballe K. Mechanical Properties of Trabecular Bone Dependancy on Strain Rate. J. Biomech., **24**, 803-809, (**1991**).

Lipson S.F.; Katz J.L. The Relationship Between Elastic Properties and Microstructure of Bovine Cortical Bone. J. Biomech., **17**, 231-240, (**1984**).

Lissner H.R.; Roberts V.L. Evaluation of Skeletal Impacts of Human Cadavers. In: Studies on the Anatomy and Function of Bone and Joints. Ed: Evans F.G., Springer-Verlag, Heidelberg, (**1966**).

Longo J.A.; Weinstein A.M.; Hedley A.K. The Effects of Collagen on Tissue Growth into a Porous Polyethylene Ingrowth Model. In: Biological and Biomechanical Performance of Biomaterials, Eds: Christel P., Meunier A., Lee A.J.C. Elsevier Science Publishers, Amsterdam, (**1986**).

Lord G.W.; Willis T.F. Calculation of Air Bubble Size Distribution from Results of a Rosiwal Traverse of Aerated Concrete. ATSM Bulletin 177, 56-61, (**1951**).

Mackenzie N.E.; Gooley P.R. Applications of NMR Spectroscopy to Biological Systems. Medicinal Res. Reviews, **8** (1), 57-75, (**1988**).

Manson J.D.; Waters N.E. Observation on the Rate of Maturation of the Cat Osteon. J. Anat., **99**, 539-549, (**1965**).

Marotti G. A new Theory of Bone Lamellation. Calc. Tiss. Int., **53** (Supplement 1), 547-556, (**1993**).

Martens M.; van Audekercke R.; Delport P.; de Meester P.; Mulier J.C. The Mechanical Characteristics of Cancellous Bone at the Upper Femoral Region. J. Biomech., **16** (12), 971-983, (**1983**).

Martin R.B.; Burr D.B. Structure, Function and Adaptation of Compact Bone. Raven Press, New York, (**1989**).

Martin R.B.; Chapman M.W.; Sharkey N.A.; Zissimos S.L.; Bay B. Bone Ingrowth and Mechanical Properties of Coralline Hydroxyapatite One Year after Implantation. Biomaterials, **14** (5), 341-348, (**1993**).

Matsuno T.; Koishi M. Fracture Toughness of Porous Sintered Bodies of Hydroxyapatite. Chem. Letters, 2335-2338, **1992**).

Mather B.S. The Effect of Variation in Specific Gravity and Ash Content on the Mechanical Properties of Human Compact Bone. J. Biomech. **1**, 207-210, (**1968**).

Matthews J.L.; Martin J.H. Intracellular Transport of Calcium and its Relationship to Homeostasis and Mineralisation. Am. J. Med., **50**, 589-597, (**1971**).

Matthews J.L.; Talmage R.V.; Martin J.H.; Davis W.L. Osteoblasts, Bone Lining Cells and the bone fluid compartment. In: Bone Histomorphometry, Ed: Meunier P.J., 2nd Int. Workshop, Toulouse, 89-96, (**1976**).

Matthews J.L.; Vander Weil C.; Talmage R.V. Bone Lining Cells and the Bone Fluid Compartment - an Ultrasound Study. Adv. Exp. Med. Biol., **103**, 451-458, (**1978**).

Maxian S.H.; Melican M.C.; Gross K.A.; Berndt C.C.; Zawaddsky J.P. Effect of Hydroxyapatite Crystallinity on Coating Dissolution and Bone Cell Behaviour. In: Proc. 21st Annual meeting of the Soc. for Biomaterials, San Francisco, (**1995**).

Maxian S.H.; Zawaddsky J.P.; Dunn M.G. Mechanical and Histological Evaluation of Amorphous Calcium Phosphate and Poorly Crystalised Hydroxyapatite Coatings on Titanium Implants. J. Biomed. Mater. Res., **27**, 717-728, **(1993)**.

Maxian S.H.; Zawaddsky J.P.; Dunn M.G. Effect of Calcium Phosphate Coating Resorption and Surgical Fit on the Bone/Implant Interface. J. Biomed. Mater. Res., **28**, 1311-1319, **(1994)**.

Mc Connel D. Apatite. Springer-Verlag, **(1973)**.

Mehmel M. Uber die Struktur des Apatits. Z.Krist., **75**, 323, **(1930)**.

Melsen F.; Melsen B.; Mosekilde L.; Bergman S. Histomorphometric Analysis of Normal Bone from the Iliac Crest. Acta Path. Microbiol. Scand., **86** (Sect. A), 70-81, **(1978)**.

Melsen F.; Viidik A.; Melsen B.; Mosekilde L. Some Relations Between Bone Strength, Ash weight and Histomorphometry. In: Bone Histomorphometry, Ed: Meunier P.J., 2nd Int. Workshop, Toulouse, 89-96, **(1976)**.

Merz W.A. Die Streckenmessung an gerechtiten Strukturen im Mikroskop und ihre Anweldung zur Bestimmung von Oberflächen-Volumen-Relationen in Knochengewebe. Diss., Basel, **(1967)**.

Merz W.A.; Schenk R.K. A Quantitative Histological Study on Bone Formation in Human Cancellous Bone. Acta Anat., **76**, 1-15, **(1970)**.

Meunier P.J. Bone Histomorphometry. 2nd Int. Workshop, Toulouse, **(1976)**.

Meyer J.L. Hydroxyl Content of Solution Precipitated Calcium Phosphates. Calc. Tiss. Int., **27**, 153, **(1979)**.

Miller G.A.; Avery D.H.; Backofen W.A. Transactions of the A.I.M.E., **236**, 1667-1673, **(1966)**.

Mitchel S.L.; Villars P.A.; Orr T.E.; Spector M. Compressive Properties of Cancellous Bone Defects in a Rabbit Model Treated with Natural Bone Mineral and Synthetic Hydroxyapatite. In: Poc. 21st Annual Meeting of the Soc. for Biomaterials, San Francisco, **(1995)**.

Mohan S.; Baylink D.J. Evidence that the Inhibition of TE85 Human Bone Cell Proliferation by Agents which Stimulate cAMP Production may in part be Mediated by Changes in the IGF-II Regulatory System. Growth Reg., **1**, 110-118, **(1991)**.

Mohan S.; Batutista C.M.; Herring S.J.; Linkhart T.A.; Baylink D.J. Development of Valid Methods to measure Insulin-Like Growth Factors I and II in Bone Cell-Conditioned Medium. Endocrinology, **126** (5), 2534-2542, **(1990)**.

Monma H.; Ueno S.; Kanazawa T. Properties of Hydroxyapatite Prepared by the Hydrolysis of Tricalcium Phosphate. J. Chem. Tech. Biotechnol., 31, 15-24, **(1981)**.

Montel G. Conceptions Nouvelles Sur la Physico-Chemie des Phosphates de Structure Apatitique. Bull. Soc. Chim., Special No. 1963, **(1968)**.

Morey E.R; Wronski T.J. Digital Image Processing of Bone: Problems and Potentials. In: Metabolic Bone Disease and Related Research, **2** (Supplement), 463-470, **(1980)**.

Moroni A.; Caja V.J.; Egger E.L.; Trinchese L.; Chao E.Y.S. Histomorphometry of Hydroxyapatite Coated and Uncoated Porous Titanium Bone Implants. Biomaterials, **15** (11), 926-930, **(1994)**.

Mosekilde L.; Mosekilde L. Sex Differences in Age Related Changes in Vertebral Body Size, Density and Biomechanical Competence in Normal Individuals. Bone, **11**, 67-73, **(1990)**.

Mosekilde L.; Mosekilde L.; Danielsen C.C. Biomechanical competence of Vertebral Trabecular Bone in Relation to Ash Density and Age in Normal Individuals. Bone, **8**, 79-85, **(1987)**.

Mow V.C.; Ratcliffe A.; Woo S.L-Y. Biomechanics of Diarthodial Joints. **2**, Springer-Verlag, N.Y., **(1990)**.

Mulkins M.A.; Manolagas S.C.; Deftos L.J.; Sussman H.H. 1,25 Dihydroxy Vitamin D_3 Increases Bone Alkaline Phosphatase Isoenzyme Levels in Human Osteogenic Sarcoma Cells. J. Biol. Chem., **258**, 6219-6225, **(1983)**.

Nadal M.; Trombe J.C.; Bonel G.; Montel G. J. Etude par Spectrometrie d'absorption dans l'intra rouge de quelques Substitutions dans les apatites Carbonates. Chim Phys., **67**, 1161-1167, **(1970)**.

Naráy -Szabó S. The structure of apatite, $(CaF)Ca_4(PO_4)_3$. Z. Kryst., **75**, 387, **(1930)**.

Nery D.M.D.; Lynch K.L.; Hirthe W.M.; Mueller K.H. Bioceramic Implants in Surgically Produced Infrabony Defects. J. Periodontal., **46**, 328-346, **(1975)**.

Nunamaker D.M.; Butterweck D.M.; Provost M.T. Fatigue Fractures in Thoroughbred Racehorses: Relationships with Age, Peak Bone Strain and Training. J. Orthop. Res., **8**, 604-611, **(1990)**.

O'Connor J.A.; Lanyon L.E.; Mac Fie H. The Influence of Strain Rate on Adaptive Bone Remodelling. J. Biomech., **15**, 767-781, **(1982)**.

Odgaard A.; Linde F. The Underestimation of Youngs Modulus in Compressive Testing of Cancellous Bone. J. Biomech., **14**, (8), 691-698, **(1991)**.

Ogiso M.; Yamashita Y.; Tabata T.; Ramonito R.; Borgese D. The Delay Method: A New Surgical Technique for Enhancing the Bone-Binding Capability of Hydroxyapatite Implants to Bone Surrounding Implant Cavity Preparations. J. Biomed. Mater. Res., **28**, 805-812, **(1994)**.

Oguchi H.; Ishikawa K.; Mizoue K.; Seto K.; Eguchi G. Long-Term Histological Evaluation of Hydroxyapatite Ceramics in Humans. Biomaterials, **16**, (1), 33-38, **(1995)**.

Ohgushi H.; Okumura M.; Yoshikawa T.; Inoue K. Senpuku N.; Tamal S.; Shors E.C. Bone Formation Process in Porous Calcium Carbonate and Hydroxyapatite. J. Biomed. Mater. Res., **26**, 885-895, **(1992)**.

Ohgushi H.; Dohi Y.; Tamai S.; Tabata S. Osteogenic Differentiation of Marrow Stromal Stem Cells in Porous Hydroxyapatite Ceramics. J. Biomed. Mater. Res., **27**, 1401-1407, **(1993)**.

Okazaki M, Sato M, Takahashi J. Space Cutting Model of Hydroxyapatite. Biomaterials, **16**, (1), 45-49, **(1995)**.

Olah A.J. Influence of Microscopic Resolution on the Estimation of Structural Parameters in Cancellous Bone. In: Bone Histomorphometry, Ed: Meunier P.J., 2nd Int. Workshop, Toulouse, 55-62, **(1976)**.

Orowan E. Die Erhöte Festigkeit dünner Fäden, der Joffe-Effekt und Verwandte Erscheinungen vom Standpunkt der Griffithschen Bruchtheorie. Z. Physik, **89**, (3/4), 195-213, **(1933)**.

Orr R.D.; de Bruijn J.D.; Davies J.E. Scanning Electron Microscopy of the Interface with Titanium, Titanium Alloy and Hydroxyapatite. In: Calcium Phosphate Biomaterials: Bone Bonding and Biodegredation Properties, Ed: de Bruijn J.D., Leiden, **(1993)**.

Orr T.E.; Trilling S.L.; Spector M. The Testing Configuration for the most Accurate Determination of Shear Strength at the Implant/Bone Interface: The effect of Ingrowth. In: Proc. 21st Annual meeting of the Soc. for Biomaterials, San Francisco, 373, **(1995)**.

Ouhayoun J.P.; Shabana A.H.M.; Issahakian S.; Patat J.L.; Guilleman G.; Sawaf M. H.; Forest N. Histological Evaluation of Natural Coral Skeleton as a Grafting Material in Miniture Swine Mandible. J. Mater. Sci.: Materials in Medicine, **3**, 222-228, **(1992)**.

Owen M. Histogenesis of Bone Cells. Calc Tiss. Res., **25**, 205-207, (**1978**).

Owen M.; Howlett C.R.; Triffit J.T. Movement of 125I albumin and 125I polyvinylpyrrolidone through Bone Tissue Fluid. Calc. Tiss. Res., **23**, 103-112, (**1977**).

Oxnard C.H. Bone and Bones, Architecture and Stress, Fossils and Osteoporosis. J. Biomechanics, **26**, Suppl. 1, 63-79, (**1993**).

Ozawa S.; Kasugai S. Evaluation of Implant Materials (Hydroxyapatite, Glass-Ceramic and Titanium) in Rat Bone Marrow Stromal Cell Culture. Biomaterials, **17**, (1), 23-29, (**1996**).

Page K.M.; Stevens A.; Lowe J.; Bancroft J.D. Bone. In: Theory and Practice of Histological Techniques, 3rd Edition. Ed: Bancroft J.D; Stevens A., Churchill Livingstone, 309-341, (**1990**).

Parfitt A.M. Some Problems in Measuring the Amount of Bone by Histologic Techniques. In: Bone Histomorphometry, Ed: Meunier P.J., 2nd Int. Workshop, Toulouse, 103-110, (**1976**).

Parfitt A.M. Morphometry of Bone Resorption: Introduction and Overview. Bone, **14**, 435-441, (**1993**).

Parsons J.R.; Ricci J.L.; Liebrecht P.; Salsbury R.; Alexander H. Enhanced Stabilization of Orthopaedic Implants with Spherical Hydroxyapatite Particulate. In: Biological and Biomechanical Performance of Biomaterials, Eds: Christel P., Meunier A., Lee A.J.C. Elsevier Science Publishers, Amsterdam, (**1986**).

Peelen J.G.J.; Rejda B.V.; De Groot K. Preparation and Properties of Sintered Hydroxyapatite. Ceramiurgica Int., **4** (2), 71-74, (**1978**).

Pereira da Silva P.S.C. Grain Size Measurement. M.Sc. Thesis, University of Sheffield, (**1966**).

Perren S.M.; Geret V.; Tepic M.; Rahn B.A. Quantitative Evaluation of the Biocompatibility of Xanadium Free Titanium Alloys. In: Biological and Biomechanical Performance of Biomaterials, Eds: Christel P., Meunier A., Lee A.J.C. Elsevier Science Publishers, Amsterdam, (**1986**).

Piattelli A.; Trisi P. Bone Ingrowth into Hydroxyapatite Coating: A Light Microscope and Laser Scanning Microscopy Study. Biomaterials, **14** (3), (**1993**).

Pinholt E.M.; Ruyter I.E.; Haanaes H.R.; Bang G. Chemical, Physical and Histologic Studies on four Comercial Apatites used for Alveolar Ridge Augumentation. J. Oral Maxillofac. Surg., **50**, 859-867, (**1992**).

Portigaliatti Barbros M. Bone Ingrowth into Madreporic Prostheses. J. Bone Jt. Surg., **70-B**, (1), (**1988**).

Posner A.S. Crystal Chemistry of Bone Mineral. Physiological Reviews, **49** (4), 760-792, (**1969**).

Posner A.S. The Chemistry of Bone Mineral. Bull. Hosp. Joint Dis., **39**, 126-144, (**1978a**).

Posner A.S. Intramitochondrial Storage of Stable Amorphous Calcium Phosphate. Ann. N.Y. Acad. Sci., **307**, 248-249, (**1978b**).

Posner A.S.; Eanes E.D.; Harper R.A.; Zipkin I. X-Ray Diffraction analysis of the Effect of Fluorine on Human Bone Apatite. Arch. Oral Biol., **8**, 549-570, (**1963**).

Posner A.S., Perloff A and Dionio A.F. Refinement of the Hydroxyapatite Structure. Acta Cryst., **11**, 308, (**1958**).

Poumarat G.; Squire P. Comparision of Mechanical Properties of Human, Bovine Bone and a New Processed Bone Xenograft. Biomaterials, **14** (5), 337-340, (**1993**).

Pritchard J.J. The General Histology of Bone. In: The Biochemistry and Physiology of Bone, 2nd Edition. Ed: Bourne G.H., **1**, Academic Press, N.Y., **(1972)**.

Pröbster L.; Voigh C.H.; Fuhrman G.; Gross U.M. Tensile And Torsional Shear Strength Of The Bone Implant Interface Of Titanium Implants In The Rabbit. J. Mater. Sci.: Materials in Medcine., **5**, 314-319, **(1994)**.

Rahn B.A.; Neff J.; Leutenegger A.; Mathys R.; Perren S.M. Integration of Synthetic Apatite of Various Pore Size and Density in Bone. In: Biological and Biomechanical Performance of Biomaterials, Eds: Christel P., Meunier A., Lee A.J.C. Elsevier Science Publishers, Amsterdam, **(1986)**.

Rao W.R.; Boehm R.F. A Study of Sintered Apatites. J. Dent Res., **35** (6), 1351-1354, **(1974)**.

Rathje W. Zur Kentnis de Phosphate I. Über Hydroxyapatite. Bodenk Pflernah., **12**, 121-128, **(1939)**.

Reddi A.H.; Cunningham N.S. Bone Induction by Osteogenin and Bone Morphogenic Proteins. Biomaterials, **11** (Biomat 89), **(1990)**.

Reilly D.T.; Burnstein A.H. The Elastic and Ultimate Properties of Compact Bone Tissue. J. Biomech., **8**, 393-405, **(1975)**.

Reisner I.; Klee W.E. Temperature Dependence of the ν (OH) Bands of Hydroxyapatite. Spectrochimica Acta, **38A**, (8), 899-902, **(1982)**.

Renooij W.; Hoogendoorn H.A.; Visser W.J.; Lentferink R.H.F.; Schmitz M.G.J.; Van Ieperen H.; Oldenburg S.J.; Janssen W.M.; Akkermans L.M.A.; Wittebol P. Bioresorption of Ceramic Strontium-85-Labeled Calcium Phosphate Implants in Dog Femora. Clin. Orthop. Rel. Res., **197**, 272-285, **(1985)**.

Revell P.A. Pathology of Bone. Springer-Verlag, Berlin, **(1986)**.

Rey C. Calcium Phosphate Biomaterials and Bone Mineral Differences in Composition, Structures and Properties. Biomaterials, **11**, (Biomat 89) 13-15, **(1990)**.

Reynolds E.S. The Use of Lead CItrate at High pH as an Electron-Opaque Stain in Electron Microscopy. J. Cell Biol., **17**, 208-212, **(1963)**.

Reynolds J.J. Inibition by Calcitonin of Bone Resorption induced *in vitro* by Vitamin A. Proc. R. Soc., **B170**, 61-69, **(1968)**.

Rho J. Y.; Ashman R.B.; Turner C.H. Young's Modulus of Trabecular and Cortical Bone Material: Ultrasonic and Microtensile Measurements. J. Biomech., **26** (2), 111-119, **(1993)**.

Rice J.C.; Cowin S.C. Bowman J.A. On the Dependance of the Elasticity and Strength of Cancellous Bone on Apparent Density. J. Biomech., **21**, 155-168, **(1988)**.

Rice R.W. Evaluating Porosity Parameters for "Porosity-Properties" Relations. J. Am. Ceram. Soc., **76** (7), 1801-1808, **(1993a)**.

Rice R.W. Comparison of Stress Concentration versus Minimum Solid Area Based Mechanical Property - Porosity relationships. J. Mater. Sci., **28**, 2187-2190, **(1993b)**.

Rice R.V.; Casassa E.F.; Kerwin R.E.; Maser M.D. On the Length and Molecular Weight of Tropocollagen from Calcified Skin. Arch. Biochem. Biophys., **105**, 409, **(1964)**.

Ripamonti U. Osteoinduction in Porous Hydroxyapatite Implanted in Heterotopic Sites of Different Animal Models. Biomaterials **17**, (1), 31-35, **(1996)**.

Roach H.I. Avian Hypertrophic Chondrocytes Die by Apoptosis and Become Bone-Forming Cells. Proceedings of the Bone and Tooth Society, Autumn Meeting, (1995).

Robey P.G.; Termine J.D. Human Bone Cells *In Vitro*. Calc. Tiss. Int., 37, 453-460, (1985).

Robinson G.; Gray T. Electron Microscopy 2: Tissue Preparation, Sectioning and Staining. In: Theory and Practice of Histological Techniques, 3rd Edition. Eds: Bancroft J.D; Stevens A., Churchill Livingstone, (1990a).

Robinson G.; Gray T. Electron Microscopy 3: Specialised Techniques. In: Theory and Practice of Histological Techniques, 3rd Edition. Eds: Bancroft J.D; Stevens A., Churchill Livingstone, 563-581, (1990b).

Robinson R.A. An Electron Microscopic Study of the Crystalline Inorganic Matrix. J. Bone Jt. Surg., 34, 389-435, (1952).

Robinson R.A.; Watson M.L. Collagen-Crystal Relationships in Bone as Seen in the Electron Microscope. Anat. Rec., 114, 383-410, (1952).

Roesler H. The History of Some Fundemental Concepts in Bone Biomechanics. J. Biomech., 20, (11), 1025-1034, (1987).

Rohrer M.D.; Schubert C.C. The Cutting-Grinding Technique for Histologic Preparation of Undecalcified Bone and Bone Anchored Implants. Oral Surg. Oral Med. Oral Pathol., 74 (1), 73-78, (1992).

Rootare H.M.; Craig R.G. Characterisation of the compaction and sinterin of Hydroxyapatite Powders by Mercury Porosimetry. Powder Technology, 9, 199-211, (1974).

Rootare H.M.; Powers J.M.; Craig R.G. Sintered Hydroxyapatite Ceramic for Wear Studies. J. Dent. Res., 57 (7-8), 777-783, (1978a).

Rootare H.M.; Craig R.G. Characterisation of Hydroxyapatite Powders and Compacts at Room Temperature and after Sintering at 1200°C. J. Oral Rehab., 5, 293-307, (1978b).

Róudier M.; Bouchon C.; Rouvillain J.L.; Arnédée J.; Bareille R.; Rouais F.; Fricain J.C.; Dupuy B.; Kien P.; Jeandot R.; Basse-Cathalinal B. The resorption of Bone - Implanted Corals varies with Porosity but also with the Host Reaction. J. Biomed. Mater. Res., 29, 909-915, (1995).

Roy D.M.; Linnehan S.K. Hydroxyapatite Formed from Coral Skeletal Carbonate by Hydrothermal Exchange. Nature, 247, 220-222, (1974).

Royer A.; Viguie J.C. Stoichiometry of Hydroxyapatite: Influence on the flexural Strength. J. Mater. Sci.: Materials in Medicine, 4, 76-82, (1993).

Rueger J.M.; Siebert H.R.; Schmidt H.; Pannike A. Observation on Bone Formation Sequence Ellicited by the Implantation of Bone Gelatine Together with Calcium Phosphate Compounds. In: Biological and Biomechanical Performance of Biomaterials, Eds: Christel P., Meunier A., Lee A.J.C. Elsevier Science Publishers, Amsterdam, (1986).

Ruys A.J.; Wei M.; Sorrell G.C.; Dickson M.R.; Brandwood A.; Milthorpe B.K. Sintering Effects on the Strength of Hydroxyapatite. Biomaterials, 16 (5), 409-415, (1995).

Ryshkewitch E. Compression Strength of Porous Sintered Alumina and Zirconia. J. Am. Ceram. Soc., 36 (2), 65-68, (1953).

Saalfeld U, Meeren N.M.; Jüres T.T.; Saalfeld H. Solubility Behaviour of Synthetic Hydroxyapatites in Aqueous Solution: Influence of Amorphous Constituents on pH Value. Biomaterials, 15, (11), 905-908, (1994).

Sabatini D.D.; Densch K.; Barrnett R.J. Cytochemistry and Electron Microscopy. J. Cell Biology, 17, 19-58, (1963).

Sadegh A.M.; Luo G.M.; Cowin S.C. Bone Ingrowth: An Application of the Boundry Element Method to Bone Remodelling at the Implant Interface. J. Biomech., **26** (2), 167-182, (1993).

Saha S.; Albright J.A.; Keating M.E.; Misra R.P. A Biomechanical and Histological Examination of Different Surface Treatments of Titanium Implants for Total Joint Replacement. In: Quantitative Characterisation and Performance of Porous Implants for Hard Tissue Applications. Ed: Lemons J.E. ASTM STP 953, ASTM, Philadelphia, 276-285, (1987).

Salkeld S.L.; Cook S.D.; Prewelt A. Enhancement of Porous Implant Fixation with Osteoconductive and Osteoinductive Materials. In: Proc. 21st Annual meeting of the Soc. for Biomaterials, San Francisco, 30, (1995).

Schaffler M.B.; Radlin E.L.; Burr D.B. Mechanical and Morphological Efects of Strain Rate on Fatigue Properties of Compact Bone. Bone, **10**, 207-214, (1989).

Schroeder H.E. Formation and Inhibition of Dental Calculi. Hans Huber Publishers, Vienna. (1969).

Sedlin E.D.; Hirsch C. Factors Affecting the Determination of the Physical Properties of Femoral Cortical Bone. Acta. Orthop. Scand., **37**, 29, (1966).

Serre C.M.; Papilard M.; Chavassieux P.; Biovin G. *In Vitro* Induction of a Calcifying Matrix by Biomaterials Constituted of Collagen and/or Hydroxyapatite: An Ultrastructural Comparison of Three Types of Biomaterials. Biomaterials, **14**, (2), 97-106, (1993).

Shareef M.Y.; Messer P.F.; van Noort R. Fabrication, Charecterisation and Fracture Study of a Machinable Hydroxyapatite Ceramic. Biomaterials, **14** (1), 69-75, (1993).

Sharp D.J.; Tanner K.E.; Bonfield W. Measurement of the Density of Trabecular Bone. J. Biomech., **23** (8), 853-857, (1990).

Shors E.C.; Holmes R.E. Porous Hydroxyapatite. In: An Introduction to Bioceramics Eds: Hench L.L.; Wilson J., World Scientific, Singapore, (1993).

Shors E.C.; White E.W.; Edwards R.M. A Method for Quantitative Characterization of Porous Biomaterials Using Automated Image Analysis. In: Quantitative Characteristics and Performance of Porous Implants for Hard Tissue Applications. Ed: Lemons J.E. ASTM STP 953, 347-358, (1987).

Di-Silvio L. A Novel Application of Two Biomaterials for the Delivery of Growth Hormone and Its Effect on Osteoblasts. PhD Thesis, UCL Medical Scholl, University of London, (1995).

Simmelink J.W. Ultrastructure of Mineralization in Bone, Dentin and Enamel. In: The Chemistry and Biology of Mineralized Connective Tissues, Ed: Veis A., Elsevier, 299-302, (1981).

Singh M.; Nagrath A.R.; Maini P.S. Changes in Trabecular Pattern of the Upper End of the Femur as an Index of Osteoporosis. J. Bone Joint Surg. **52-A**. (3), 457-467, (1970).

Sissons H.A.; Lee W.E. Bone and Tooth. Ed: Blackwood H.J.J., Pergamon, Oxford, (1964).

Smith D.M.; Hua D.-W.; Earl W.I.. Characterisation of Porous Solids. MRS Bull., (1994).

Smith L. Ceramic-Plastic Material as a Bone Substitute. Arch. Surg., **87**, 653-661, (1963a).

Smith J.W. Age Changes in the Organic Fraction of Bone. J. Bone Jt. Surg. B45, 761, (1963b).

Smith J.W.; Walmsley R. Factors Affecting the Elasticity of Bone. J. Anat., **93**, 503, (1959).

Smith T.S. Morphological Characterization of Porous Coatings. In: Quantitative Characteristics and Performance of Porous Implants for Hard Tissue Applications. Ed: Lemons J.E., ASTM STP 953, 92-102, (1987).

Snyder B.D. Anisotropic Structure-Property Relations for Trabecular Bone. Ph.D Thesis. University of Pennsylvania, Philadelphia, (1991).

Snyder B.D.; Hayes W.C. Multiaxial Structure Property Relations in Trabecular Bone. In: Biomechanics of Diarthrodial Joints. Eds: Mow V.C.; Ratcliffe A.; Woo S.L.-Y., Springer-Verlag, New York, 31-59, (1990).

Sodek J.; Zhang Q.; Golgberg H,A; Domenicucci C.; Kasugai S.; Wrana J.L.; Shapiro H.; Chen J. Non-collagenous Bone Proteins and their Role in Substrate-Induced Bioactivitry. In: The Bone-Biomaterial Interface. Ed: Davies J.D. Toronto: University of Toronto Press, (1991).

Spector M.; Teichgraeber J.F.; Per-Lee J.H.; Jackson R.T. Tissue Response to Porous Materials used for Ossicular Replacement Prostheses. In: Biomaterials in Otology, Ed: J.J. Grote, Proc. 1st Int. Symp., 21-23, (1983).

Spurr A.R. A Low-Viscosity Epoxy Resin Embedding Medium for Electron Microscopy. J. Ultrastructure Res., **26**, 31-43, (1969).

Stea S.; Visentin M.; Savarino L.; Donati M.E.; Pizzoferrato A.; Moroni A.; Caja V. Quantitative Analysis of the Bone-Hydroxyapatite Coating Interface. J. Mater. Sci: Materials. in Medicine, **6**, 455-459, (1995).

Steen M. Mechanical Characterisation of Structural Ceramics. 19th Course Summer School on Innovative Ceramics for Energy, Castro Maina, (1992).

Steinmann S.G.; Eulenberger J.; Maeusli P.A. Schroeder A. Adhesion of Bone to Titanium. In: Biological and Biomechanical Performance of Biomaterials, Eds: Christel P., Meunier A., Lee A.J.C. Elsevier Science Publishers, Amsterdam, (1986).

Stephenson P.K.; Freeman M.A.R.F.; Revell P.A.; German J.; Tuke M.; Pirie C.J. The Effect of Hydroxyapatite Coating on Ingrowth of Bone into Cavities in an Implant. J. Arthroplasty, **6** (1), 51-58, (1991).

Stevens A.; Lowe J.; Bancroft J.D. Bone. In: Theory and Practice of Histological Techniques, 3rd Edition. Ed: Bancroft J.D; Stevens A., Churchill Livingstone, 309-341, (1990).

Stone J.L.; Beaupre G.S.; Hayes W.C. Multiaxial Strength Characteristics of Trabecular Bone. J. Biomech., **16**, (9), 743-752, (1983).

Talmage R.V. Morphological and Physiological Considerations in a New Concept of Calcium Transport in Bone. Am. J. Anat., **129**, 467-476, (1970).

Talmage R.V.; Grubb S.A. A Laboratory Model Demonstrating Osteocyte-Osteoclast Control of Plasma Calcium Concentrations. Table Model for Plasma Calcium Control. Clin. Orthop., **122**, 299-306, (1977).

Tam C.S.; Harrison J.E.; Heersche J.N.M.; Jones G.; Wilson D.R.; Parsons J.A.; Murray T.M. Short Term Variation in the Rate of Apposition of Mineralized Bone Matrix in Small Animals. In: Bone Histomorphometry, Eds: Jee W.S.S.; Parfitt A.M. In: Metabolic Bone Disease and Related Research, **2** (Supplement), 159-166, (1980).

Tanner K.E.; Doyle C.; Bonfield W. The Strength of the Interface Developed between Biomaterials and Bone. Clinical Implant Materials, Advances in Biomats., **9**, 149-154, (1990).

Teitelbaum H.; Nichols S.H. Tetracycline-Based Morphometric Analysis of Trabecular Bone Kinetics. In: Bone Histomorphometry, Ed: Meunier P.J., 2nd Int. Workshop, Toulouse, 89-96, (1976).

Tenenbaum H.; Heersche J.M.N. Differentiation of Osteoblasts and Formation of Mineralized Bone *in vitro*. Calc. Tiss. Int., **34**, 76-79, (**1982**).

Termine J.D.; Pullman I.; Posner A.S. Electron-Spin Resonance Study of Irradiated Bone and its Constituents. Arch. Biochem. Biophys., **122**, 318-330, (**1967**).

Thomas M.B.; Doremus R.H.; Jarcho M.; Salsbury R.L. Dense Hydroxyapatite: Fatigue and Fracture Strength after various Treatments, from Diametral Tests. J. Mater. Sci., **15**, 891-894, (**1980**).

Thomsen P.; Ericson E. Inflammatory Cell Response to Bone Implant Surfaces. In: The Bone-Biomaterial Interface. Ed: Davies J.D. Toronto: University of Toronto Press, (**1991**).

Thomson C.E. Et Al MRI-A General Overview of Principles and Examples in Veterinary Neurodiagnosis. Veterinary Radiology and Ultrasound, **34** (1), 2-17, (**1993**).

Trécant M.; Delécrin J.; Royer J.; Goyenvalle E.; Daculsi G. Mechanical Changes in Macroporous Calcium-Phosphates Ceramics after Implantation in Bone. Clin. Mater., **15**, 233-240, (**1994**).

Tremollieres F.A.; Strong D.D.; Baylink D.J.; Mohan S. Progesterone and Promegestone Stimulate Human Bone Cell Proliferation and Insulin-Like Growth Factor-2 Production. Acta Endocrinol., **126**, 329-337, (**1992**).

Triffit J.T; Owen M. Studies on Bone Matrix Glycoproteins. Biochem J., **136B**, 125-134, (**1973**).

Trombe J.C.; Bonel G.; Montel G. Influence de la Chaux sur la Formation d'Apatites Carbonatées à Haute Température. Compt. Rend., **265**, 1113-1116, (**1967**).

Tsang K.Y.; Fudenberg H.H.; Sun D.C.; Pai G.S.; Bishop L.R.; Sager S. Cultivation of Human Osteosarcoma Cell lines in Serum Free Hormone Supplemented Medium. *In Vitro*, **19**, (7), 515-521, (**1983**).

Uchida A,; Nade S.M.L.; McCartney E.R.; Ching W. The Use of Ceramics for Bone Replacement. A Comparative Study of three Different Porous Ceramics. J. Bone Jt. Surg., **66-B**, (2), (**1984**).

Ueta S. Experimental Study on Incorporation of Processed Allogenic Bone and Hydroxyapatite in Rabbits. Kitasato Med., **22**, 116-123, (**1992**).

van der Vort G. F. Grain Size Measurement. In: Practical Applications of Quantitative Metallography. Eds: McCall J.L.; Steele J.H., ASTM STP 836, (**1984**).

Vanderweil C.J. An Ultrastructural Study of the components which make up the resting surface of Bone. In: Bone Histomorphometry, Eds: Jee W.S.S.; Parfitt A.M. In: Metabolic Bone Disease and Related Research, **2** (Supplement), 109-116, (**1980**).

Vaughan J.M. The Physiology of Bone. 2nd Edition, Clarendon Press, Oxford, (**1975**).

Vignoles C. Contribution a l'étude de l'influence des ions alcalins sur la carbonation dans las sites de type B. These, Toulouse, France, (**1984**).

Vincentelli G.; Grigorov M. The Effect of Haversian Remodelling on the Tensile Properties of Human Cortical Bone. J. Biomech., **18**, 201-207, (**1985**).

Visser W.J.; Niermans H.J.; Roelofs J.M.M.; Raymakers J.A.; Duursma S.A. Comparative Morphometry of Bone Biopsies Obtained bt two Different Methods from the Fight and the Left of the Iliac Crest. In: Bone Histomorphometry, Ed: Meunier P.J., 2nd Int. Workshop, Toulouse, 89-96, (**1976**).

Visser W.J.; Roelofs J.M.M.; Peters J.P.J.; Lentferink M.H.F.; Duursma S.A. Sampling Variation in Bone Histomorphometry. In: Metabolic Bone Disease and Related Research, **2** (Supplement), 419-428, (**1980**).

Wall J.C.; Chatterji S.; Jeffery J.W. On the Original Scatter in Results of Human Bone Strength Tests. Med. Biol. Eng., **8**, 171, (**1970**).

Wang P.E.; Chaki T.K. Sintering Behaviour and Mechanical Properties of Hydroxyapatite and Dicalcium Phosphate. J. Mater. Sci.: Materials in Medicine, **4**, 150-158, (**1993**).

Weibel E.R.; Elias H.E. Quantitative Methods in Morphology. Springer-Verlag, Berlin, (**1967**).

Whitehouse W.J. A Stereological Method for Calculating Internal Surface Areas in Structures which have become Anisotropic as the result of Linear Expansions or Contractions. J. Microscopy, **101**, (2), 169-176, (**1974a**).

Whitehouse W.J. The Quantitative Morphology of Anisotropic Trabecular Bone. J. Microscopy, **101**, (2), 153-168, (**1974b**).

Whitehouse W.J.; Dyson E.D. Scanning Electron Microscopr Studies of Trabecular Bone in the Proximal End of the Human Femur. J. Anat., **118**, (3), 417-444, (**1974**).

Whitehouse W.J.; Dyson E.D.; Jackson C.K. The Scanning Electron Microscope in Studies of Trabecular Bone from a Human Body. J. Anat., **108**, (3), 481-496, (**1971**).

Wiedenreich F. Handbuch der Mikroskopischen Anatomie des Menschen. Ed: Von Möllendorf W., **2**, 408, Springer-Verlag, Berlin, (**1930**).

De Wijs F.L.J.A.; de Lange G.L.; de Putter C.; de Groot K. Correction of Resorption Defects in the Anterior Maxillary Region with Hydroxyapatite. In: Biological and Biomechanical Performance of Biomaterials, Eds: Christel P., Meunier A., Lee A.J.C. Elsevier Science Publishers, Amsterdam, (**1986**).

Williams D. Review: Tissue - Biomaterial Interactions. J. Mater. Sci., **22**, 3421-3445, (**1987**).

Williams D. The Capricious Nature of Biocompatibility. Medical Device Technology. **Jan/Feb**, 8-11, (**1994**).

Williams P.L.; Warwick R. Gray's Anatomy. 37th Edition. Churchill Livingstone, Edinburgh, (**1989**).

Willman G. Materialeigenschaften von Hydroxyapatite-Keramik. Mat.-Wiss.u.Werkstofftech., **23**, 107-110, (**1992**).

de With G.; van Dijk H.J.A.; Hattu N. Mechanical Behaviour of Biocompatile Hydroxyapatite Ceramics. Proc. Brit. Ceram. Soc., **31**, 181-189, (**1981a**).

de With G.; van Dijk H.J.A.; Hattu N.; Prijs K. Preparation, Microstructure and Mechanical Properties of Dense Polycrystalline Hydroxyapatite. J. Mater. Sci., **16**, 1592-1598, (**1981b**).

Wolff J. Uber die innere Architektur der Knochen and ihre Bedeutung fur die Frame von Knockenwaschstum. Virchows Arch. Path. Anat. Physiol., **50**, (**1870**).

Wolff J. Pas Destez der Transformation der Knochen. Hirschwald, Berlin, (**1892**).

Wong S.Y.P.; Kariks J.; Evans R.A.; Dunstan C.R.; Hills E. The Effect of Age in Bone Composition and Viability in the Femoral Head. J. Bone Jt. Surg., **67**, 274-283, (**1985**).

Yamasaki N.; Kai T.; Nishioka M.; Yanagisawa K.; Loku K. Porous Hydroxyapatite Ceramics Prepared by Hydrothermal Hot Pressing. J. Mater. Sci. Letters, **9**, 1150-1151, (**1990**).

Yoon H.S.; Katz J.L. Ultrasonic Wave Porpagation in Human Cortical Bone. I. Theoreticl Considerations for Hexagonal Symetry. J. Biomech., **9**, 407-412, (**1976a**).

Yoon H.S.; Katz J.L. Ultrasonic Wave Porpagation in Human Cortical Bone. II. Measurements of Elastic Properties and Microhardness. J. Biomech., **9**, 407-412, (**1976b**).

Yoon H.S.; Katz J.L. Ultrasonic Wave Porpagation in Human Cortical Bone. III. Piezoelectric Contribution. J. Biomech., **9**, 537-540, (**1976c**).

Young R.A.; Elliot J.C Scale Bases for Several Properties of Apatites. Arch. Oral Biol., **11**, 699-707, (**1966**).

Yubao L.; Klein C.P.A.T.; Xingdond Z.; de Groot K. Relationship Between the Colour Change of Hydroxyapatite and the Trace Element Manganese. Biomaterials, **14** (13), 969-972, (**1993**).

Yubao L.; Klein C.P.A.T.; Xingdond Z.; de Groot K. Formation of a Bone Apatite-Like Layer on the Surface of Porous HA Ceramics. Biomaterials, **15** (10), 835-841, (**1994**).

Zambonin G.; Grano M. Biomaterials in Orthopaedic Surgery: Effects of Different Hydroxyapatite and Dimineralised Bone Matrix on Poliferation Rate and Bone Matrix Synthesis by Human Osteoblasts. Biomaterials, **16** (5), 397-402, (**1995**).

Zyman Z.; Weng J.; Liu X.; Zhang X.; Ma Z. Amorphous Phase and Morphological Structure of Hydroxyapatite Plasma Coatings. Biomaterials, **14** (3), 225-228, (**1993**).

APPENDIX

A.1 Theoretical Values of Hydroxyapatite

Relative atomic mass of hydroxyapatite unit cell:

$$A_r\,HA = 10(A_r\,Ca) \times 6(A_r\,P) \times 26(A_r\,O) \times 2(A_r\,H)$$

$$= 10(40.0800) \times 6(30.9737) \times 26(15.9994) \times 2(1.0079)$$

$$= 1004.6424$$

Where A_r = Relative Atomic Mass, data from JCPDS (1980).

Theoretical weight percentage of calcium:

$$\text{Ca wt\%} = \frac{10(A_r\,Ca)}{A_r\,HA} \times 100$$

$$= \frac{10(40.0800)}{1004.6424} \times 100 \qquad = \mathbf{39.89\ \%}$$

Theoretical weight percentage of phosphorus:

$$\text{P wt\%} = \frac{10(A_r\,P)}{A_r\,HA} \times 100$$

$$= \frac{6(30.9737)}{1004.6424} \times 100 \qquad = \mathbf{18.50\ \%}$$

Theoretical weight percentage of hydrogen:

$$\text{H wt\%} = \frac{2(A_r\,H)}{A_r\,HA} \times 100$$

$$= \frac{2(1.0079)}{1004.6424} \times 100 \qquad = \mathbf{0.20\ \%}$$

Theoretical calcium to phosphorus ratio:

$$\text{Ca:P} = \frac{\text{Number of Ca ions per unit cell}}{\text{Number of P ions per unit cell}}$$

$$= \frac{10}{6} \qquad = \mathbf{1.67}$$

A.2 Image Analysis

A.2.1 Preparation of Images for Analysis

Images acquired directly from the optical microscope did not generally require any preparation besides the removal of any artefacts, such as air bubbles in the embedding medium. All images of Endobon specimens being analysed for macrostructure were aligned with the long axis of the cylindrical specimen running from left to right of the image as seen on the computer screen. However, images acquired from SEM micrographs often required considerable processing as a result of the low contrast often associated with these images. For analysis of grain size it was necessary to trace the boundaries of the individual grains manually.

A.2.2 Detection and Measurement of Macroscopic Features

Once an image had been "acquired" and processed it was necessary to "detect" the features. Analysis was performed using the QUIC menu system by selecting various parameters from the feature measurement window and applying them to the detected features. Detection of the macropores was performed by selection of the appropriate black level to detect only the ceramic (which appeared black in both as-received sections and histological sections). Direct detection of the macropores themselves proved difficult, as a result of bony ingrowth in histological sections. The detected area was displayed on the computer screen in the "image frame" overlaying the original image, so that it was possible to ensure the area delineated by the detected field matched the original image.

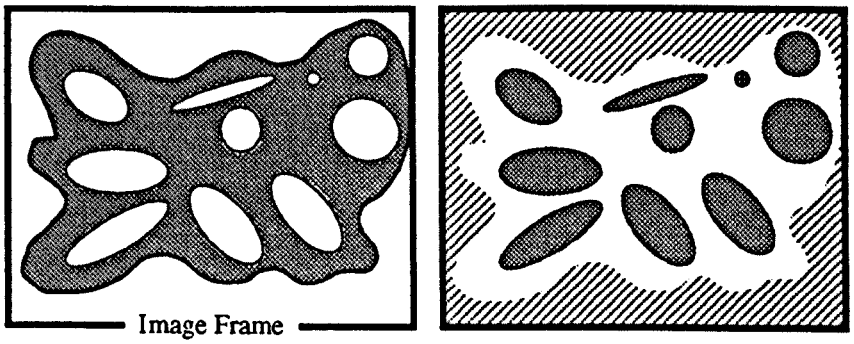

Figure A.2.1 Schematic diagram of (a) the detection of ceramic and (b) inversion and editing of the detected image.

When detection was completed, the image was reduced to a monochromatic image as in Figure A.2.1a. This image was then reversed and it was possible to "reject" areas that had been inadvertently detected (Figure A.2.1b - cross hatch shading). Individual parameters were then specified for measurement and limits set for feature rejection, such as minimum area or diameter, which was useful for excluding small artefacts, such as cellular debris, detected in histological sections (A.2.2a feature 6). After measurement the "accepted" features were re-coloured, as in Figure A.2.2b. The relative sizes of the measurement frame and image frame were adjusted, so that segments of features that had been sectioned by the measurement frame were rejected (Figure A.2.2b features 7 & 8).

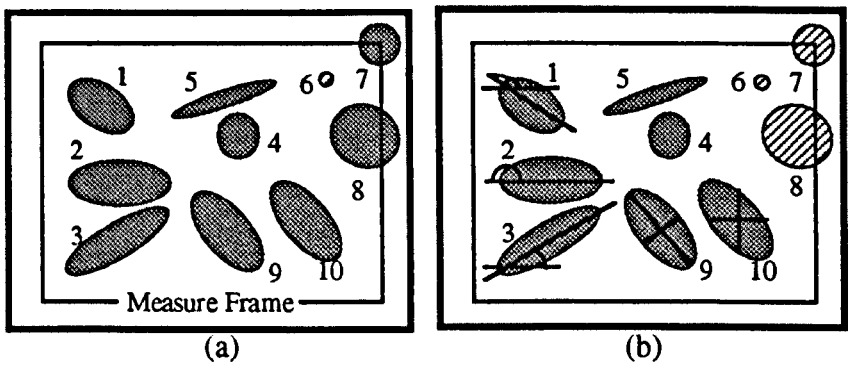

Figure A.2.2 A schematic diagram of macropores after feature measurement.

Explanation of some of the pre-defined parameters:

- Features 1-3 demonstrate the angle measured by "orientation".
- Feature 9 demonstrates the measurement of "length" and "breadth", i.e., the longest and shortest feature dimensions.
- Feature 10 demonstrates the measurement of "height" and "width", i.e., the longest chord lengths in the vertical and horizontal directions, respectively.

A.2.3 Detection and Measurement of Microscopic Features

The basic methods used for detection of macroscopic features were used in the detection of microscopic features. With the selection of the appropriate black level, it was possible to detect micropores directly from SEM micrographs. However, the direct detection of grains proved impossible due to the lack of contrast. As with the macropores, it proved easier to detect the grain boundaries, reverse the image and then edit out any detected micropores. Again care was taken to select appropriate image and measure frame sizes.

PUBLICATIONS

P.1 Abstracts

Mechanical and Biological Assessment of the Osseointegration of Porous Hydroxyapatite Implants.
K.A. Hing, S.M. Best, K.E. Tanner, P.A. Revell, W. Bonfield. In: Transactions of the 21st Annual Meeting of the Society for Biomaterials, San Francisco, USA, 302, (**1995**).

Effects of Morphology on Osseointegration in Porous Hydroxyapatite.
K.A. Hing, S.M. Best, K.E. Tanner, P.A. Revell, W. Bonfield. In: Proceedings of the 2nd International Symposium on Apatite. Tokyo, Japan, 19, (**1995**).

Integration of Trabecular Bone into Porous Hydroxyapatite.
K.A. Hing, S.M. Best, K.E. Tanner, P.A. Revell, W. Bonfield. In: Proceedings of the 12th European Conference on Biomaterials. Porto, Portugal, 145, (**1995**).

An *In Vitro* Study of the Response of Osteoblasts to Porous Hydroxyapatite.
K.A. Hing, D. Lee, S.M. Best, W. Bonfield. In: Proceedings of the 12th European Conference on Biomaterials. Porto, Portugal, 146, (**1995**).

P.2 Papers

Mechanical Assessment of Porous Hydroxyapatite Implants Before and After Osseointegration.
K.A. Hing, S.M. Best, K.E. Tanner, P.A. Revell, W. Bonfield. In: Bioceramics 8, Proceedings of the 8th International Symposium on Ceramics in Medicine. Elsevier, Florida, USA, 75-80, (**1995**).

MECHANICAL AND BIOLOGICAL ASSESSMENT OF THE OSSEOINTEGRATION OF POROUS HYDROXYAPATITE IMPLANTS

K.A. Hing, S.M. Best, P.A. Revell*, K.E. Tanner, W. Bonfield.

IRC in Biomedical Materials, Queen Mary and Westfield College, University of London. London E14NS. *IRC in Biomedical Materials, Royal Free Hospital School of Medicine, University of London. London, NW3 2QG.

INTRODUCTION

Porous hydroxyapatite $Ca_{10}(PO_4)_6(OH)_2$ implants offer the potential of tailored-skeletal repair and reconstruction in a variety of orthopaedic procedures. The case for using hydroxyapatite (HA) in the filling of osseous defects is fairly obvious as a result of its biocompatibility[1,2] and the crystallographic similarities between it and the apatitic natural bone mineral[3]. When using such materials in surgical practice it is important to be able to predict both the load bearing capabilities and the time taken for effective fixation, in order to allow for selection of appropriate strength materials and prediction of patient mobility respectively.

The objective of this study was to characterise the mechanical behaviour of a commercially available porous HA, Endobon® pre- and post- implantation, inorder to study the process of osseointegration with time, to allow characterisation of both ingrowth reinforcement and fixation.

METHODS

Endobon®, synthesised via the calcination /hydrothermal conversion of bovine spongiosa in a manner which left the cancellous structure intact (Figure 1a), was supplied by E. Merck in the form of cylindrical specimens with 4.5mm diameter and 6-7mm length. Due to the nature of the precursor material there was some degree of variation in the density of these implants.

Prior to implantation the chemical (XRF, XRD, and IR.) structural (SEM) and mechanical, (compressive strength and modulus) properties were determine for a sample of specimens with a broad range of densities

Specimens with mean density of 0.62 g cm^{-3} were selected for implantation from a sample of 350 specimens of mixed density. Specimens were implanted into trephined defects generated in the distal end of the right femur of six month old female New Zealand White rabbits. Implants remained in vivo for periods of 10 days, 5 weeks, 3 months and 6 months.

Selected specimens for histology were labelled with fluorochromes during the study. After sacrifice these specimens were fixed, sectioned and stained where appropriate. Quantitative histology was performed to assess the extent of ingrowth into the implants and the new bone coverage on implant surfaces. Cellular response was also studied. The remaining specimens were mechanically tested via either compression testing or pushout testing to assess the reinforcing effects and strength of the bone/implant interface (i.e. a measure of fixation) respectively.

RESULTS & DISCUSSION

Figure 1a shows a representative longitudinal section through an Endobon® specimen. Endobon® was found to be composed of highly crystalline phase-pure hydroxyapatite with small amounts of magnesium, sodium, aluminium and silicon impurities. However, there was some peak shifting of about 0.1° and initial findings from refinement of the structure indicate that the lattice is severely distorted in the region of the phosphate tetrahedra. FT-IR. spectra indicated the presence of carbonate in significant quantities, this finding coupled with the lattice distortion indicates that there may be some carbonate substitution for phosphate groups.

The stress strain behaviour of porous HA was found to be similar to that of a classic elastic-brittle foam and thus the fracture behaviour of cancellous bone. As can be seen from Figure 1b the mechanical properties were also found to be highly dependant on density.

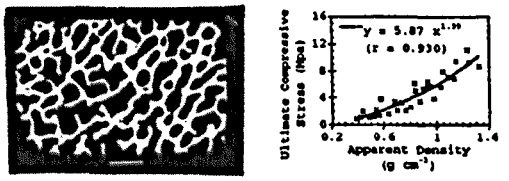

(a) (b)

FIGURE 1: (a) The macro structure of Endobon®, (Bar=1mm), (b) UCS dependence on density.

Integration of bone within the implants was good with intimate contact between the implant and new bone and no observed fibrous layer. Some woven bone was rapidly laid down in the first two weeks, with the clear apposition of lamellar bone by 2-3 weeks. Ingrowth tended to proceed predominately from the bottom of the defect (Figure 2a) with some integration from the walls of the defect. Both macro and micro porosity appeared to play an important role in tissue integration, with evidence of organic ingrowth into the "dense" HA struts.

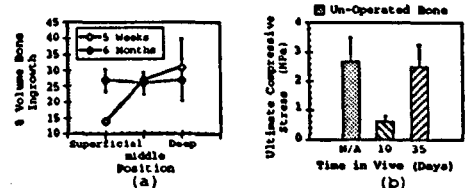

(a) (b)

FIGURE 2: (a) Variation of ingrowth with position, (b) UCS of retrieved bone/implants.

By 5 weeks there was no significant difference in the strength of defects repaired with Endobon® and unoperated bone (Figure 2b), despite incomplete integration at this time point (Figure 2a), as a result of the reinforcing effects of the HA implant. Cellular response was good with osteoblasts, osteoclasts and osteocytes all observed in close proximity to the implant with no adverse response.

CONCLUSIONS

Initial results suggest that Endobon® is highly biocompatible. It acts as a support for new bone and encourages bone ingrowth along its surfaces. The dependence of the mechanical properties on density could be exploited to allow selection of different grades of porous HA to suit different implantation sites, thus reducing the risk of stress shielding as a result of dissimilar mechanical properties.

AKNOWLEDGEMENTS

E. Merck GmbH, 64271 Darmstadt, Germany, for the funding of this project.

REFERENCES

1) DENISSEN H.W.; VAN DIJK H.J.A.; DE GROOT K.; KLOOPER P.J.; VERMIDEN J.P.W.; GEHRING A.P. Mechanical Properties Of Biomaterials Eds Hastings G.W.; Williams D.F. John Wiley & Sons Ltd. (1980)
2) EGGLI P.S.; MULLER W.; SCHENK R.K. Clin. Ortho. Relat. Res. 232 127-138 (1988)
3) POSNER A.S. Phyisiological Reviews 49 (4) 760-792 (1969)

21ST Annual Meeting of the Society for Biomaterials
San Francisco, California, USA. March 18-22, 1995

Effects of Morphology on Osseointegration in Porous Hydroxyapatite

K.A. Hing*, S.M. Best*, K.E. Tanner*, P.A. Revell†, W. Bonfield*

*IRC in Biomedical Materials, Queen Mary and Westfield College, Mile End Road, London, E1 4NS, England.
†IRC in Biomedical Materials, Royal Free Hospital School of Medicine, Pond Street, London, NW3 2QG, England.

The biocompatibility[1,2] of hydroxyapatite (HA) - $[Ca_{10}(PO_4)_6(OH)_2]$ and the similarities between the crystal structure of HA and natural bone mineral[3] make porous HA a viable alternative to bone grafts, with the potential to repair and reconstruct skeletal defects in a variety of orthopaedic procedures. However, although the morphology of biomedical implants has been of interest since the use of a porous ceramic was described in 1963[4], there has been no thorough study of the effects of physical properties such as macro-pore size and apparent density on pure HA implants.

The specimens used in this investigation were composed of Endobon® supplied by E. Merck, a commercially available porous HA synthesised via the hydrothermal conversion of bovine cancellous bone in a manner which maintained the trabecular structure. Three groups of specimens were selected for investigation, with apparent densities of 1.19 ± 0.06 (Batch A), 0.90 ± 0.03 (Batch C) and 0.61 ± 0.04 (Batch B) g cm^{-3}. The average pore sizes for Batches A, C and B were 460, 760 and 1380 µm respectively. Despite the considerable variation in the macro-structure of the selected specimens, the micro-structure was constant with an average micro-pore size of 0.86 µm, an average grain size of 1.38 µm and a real density of 3.04 g cm^{-3}.

Specimens from the three batches were implanted for a period of 5 weeks in the distal end of the right femur of six month old New Zealand White rabbits and selected specimens underwent fluorochrome bone labelling. Integration of bone within all the implants was observed with no fibrous layer between the implant and new bone. The histological response to all implants appeared similar with active areas of bone deposition, resorption and remodelling observed on all implants. However the actual volume of ingrowth, at 15%, within the Batch A specimens was reduced compared to that of both the Batch C implants at 19% and the Batch B implants at 23%.

References

1 Denissen H.W.; Van Dijk H.J.A.; De Groot K.; Klopper P.J.; Vermiden J.P.W.; Gehring A.P. *Mechanical Properties of Biomaterials* Eds Hastings G.W.; Williams D.F. John Wiley & Sons Ltd. (1980)
2 Eggli P.S.; Muller W.; Schenk R.K. *Clin. Ortho. Relat. Res.* 232 127-138 (1988)
3 Posner A.S. *Phyisiological Reviews* 49 (4) 760-792 (1969)
4 Smith J.W. J. *Bone Joint Surg. Brit. Vol.* 45 761 (1963)

INTEGRATION OF TRABECULAR BONE INTO POROUS HYDROXYAPATITE

K.A. Hing*, S.M. Best*, P.A. Revell†, K.E. Tanner*, W. Bonfield*.
*IRC in Biomedical Materials, Queen Mary and Westfield College, Mile End Road, London E1 4NS, England.
†IRC in Biomedical Materials, Royal Free Hospital School of Medicine, Pond Street, London NW3 2QG, England.

Introduction

The biocompatibility [1, 2] of hydroxyapatite (HA), - ($Ca_{10}(PO_4)_6(OH)_2$) and the similarities between the crystal structure of HA and natural bone mineral [3] make porous hydroxyapatite a viable alternative to bone grafts, with the potential to repair and reconstruct skeletal defects in a variety of orthopaedic procedures.
The objective of this study was to study of the process of osseointegration of porous HA with time, to allow characterisation of both ingrowth reinforcement and fixation.

Methods

A commercially available porous HA, Endobon®, produced via the hydrothermal conversion of bovine cancellous bone was supplied by E. Merck, Darmstadt, Germany, in the form of cylindrical specimens 4.5mm diameter and 6-7mm in length. Specimens with mean density of 0.62 g cm^{-3} were selected for implantation into trephined defects generated in the distal end of the right femur of six month old female New Zealand White rabbits. Implants remained in vivo for periods of 10 days, 5 weeks and 6 months. Selected 5 week specimens were labelled on consecutive days with four different fluorochromes at the ends of weeks 1, 2, 3 and 4 in vivo. After sacrifice, these specimens were fixed, sectioned and stained with toluidine blue where appropriate. Quantitative histology was performed to assess the extent of ingrowth into the implants. Specimens were mechanically tested by either compression testing or push out testing to assess the reinforcing effects and the strength of the bone-implant interface, respectively.

Results

Integration of bone within the implants was observed with intimate contact between the implant and new bone and no fibrous layer. From the fluorochrome labelling, it was evident that some woven bone was rapidly laid down in the first two weeks at the periphery of the implant, with obvious apposition of lamellar bone within the implant by 3 weeks. Ingrowth tended to proceed predominately from the bottom of the defect and by 5 weeks had fully penetrated approximately half of the length of the implant with some integration from the walls of the defect. Both macro and micro porosity appeared to play an important role in tissue integration, with evidence of ingrowth into the "dense" HA struts.

Compression testing of retrieved implants demonstrated that, at 10 days, there was no significant difference in the ultimate compressive stress (UCS) of implanted (3.6 ± 0.4 MPa) and as received porous HA (2.6 ± 1.1 MPa). However, at 5 weeks the UCS of implanted material had increased to 4.9 ± 2.1 MPa, despite incomplete osseointegration at this time point. Similarly the strength of the host tissue/implant interface had increased significantly by 5 weeks.

Table 1 Push out testing results

Specimen	Interface Strength (MPa)
Control	0.016 ± 0.003
10 days in vivo	1.08 ± 0.88
5 weeks in vivo	3.99 ± 1.79

Conclusions

Woven bone is rapidly laid down towards the end of the second week at the edges of the defect, with ingrowth into the implant by the second or third week via the apposition of lamellar bone directly onto the surface of the material. By five weeks, the lower half of the implant is completly integrated, with partial integration from the edges at the top of the implant. At six months, this osseointegration is complete throughout the implant and cartilage repair has occured over the top surface.
The capacity of the newly formed bone to enhance the mechanical performace of the implant and, hence the ability of loads to be transmitted across the interface demonstrates the intimacy of the bond between the implant and the host tissue.

Acknowledgements

E. Merck GmbH, 64271 Darmstadt, Germany, for the funding of this project.

References

1) Denissen H.W.; Van Dijk H.J.A.; De Groot K.; Klopper P.J.; Vermiden J.P.W.; Gehring A.P.
Mechanical Properties of Biomaterials Eds Hastings G.W.; Williams D.F. John Wiley & Sons Ltd. (1980)
2) Eggli P.S.; Muller W.; Schenk R.K.
Clin. Ortho. Relat. Res. 232 127-138 (1988)
3) Posner A.S.
Phyisiological Reviews 49 (4) 760-792 (1969)

AN *IN VITRO* STUDY OF THE RESPONSE OF OSTEOBLASTS TO POROUS HYDROXYAPATITE

K.A. Hing*, D Lee†, S.M. Best*, W. Bonfield*.
*IRC in Biomedical Materials, Queen Mary and Westfield College, Mile End Road, London E1 4NS, England.
†IRC in Biomedical Materials, Institute of Orthopaedics, Brockley Hill, Stanmore, Middlesex HA7 4 LP, England.

Introduction

The osteogenic nature of synthetic, dense hydroxyapatite (HA) has led to great interest in its potential as a material for the augmentation of osseous defects. The similar use of low density HA, with its highly interconnected porosity, has also been advocated, particularly in cancellous applications where its structure more closely mirrors that of its host. Furthermore, this structure invites the ingrowth of bone into the implant presenting a more securely fixed and integrated repair.
However although much work has been performed on the osteogenic cell response to synthetic, dense HA, little work appears to have been carried out on porous HA, as regards the reaction of cells to both the HA and the extensive interconnected macroporosity.
The purpose of this study was to investigate the response of osteoblasts to porous HA *in vitro*, with particular emphasis on the migration of the cells though the three dimensional porous structure.

Methods

A commercially available porous HA, Endobon®, was supplied by E. Merck, Darmstadt, Germany, with a mean apparent density of 0.725 ± 0.107 g cm^{-3}. This material was produced via the hydrothermal conversion of bovine cancellous bone in a manner which left the cancellous structure intact. Human osteoblast (HOB) cells cultured in DMEM + 10% FCS + NEAA were used throughout the study. Endobon® slices (11mm x 11mm x 1.5mm) were placed in a tissue culture well (surface area 2 cm^{-2}) and 1ml of cell suspension ($1.6x10^5$ cells.ml^{-1}) added. After culture for 1, 4, 7, 14 and 21 days, cells were fixed and prepared for light, scanning and transmission electron microscopy.

Results

After 1 day in culture, the cells had attached and flattened onto the material surface (Fig. 1a). By day 4, the cells had proliferated to form a confluent monolayer and there was evidence of cell migration via the interconnected macropores into the material (Fig. 1b). Between 7 and 21 days there was multilayering of the cells with extensive production of collagenous extracellular matrix (Fig. 1c). In addition, the cells formed multilayered sheets covering the macropores (Fig. 1d), a process referred to as capping. The regularity of this macropore capping increased with time in culture up to 21 days, as did the thickness of the multilayers.

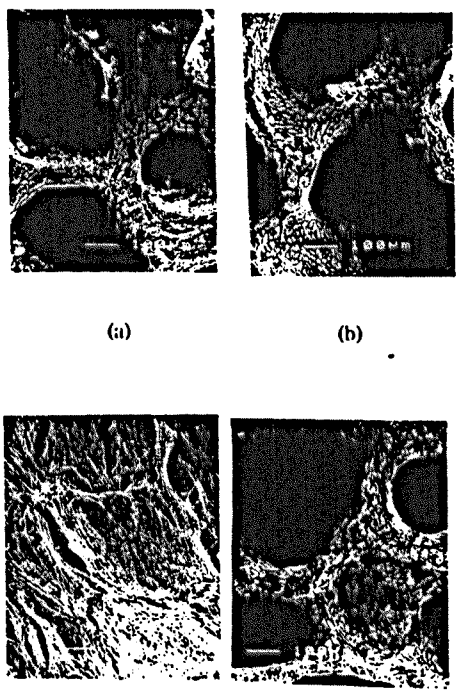

(a) (b)

(c) (d)

Figure 1 Scanning electron micrographs of HOB cells cultured for (a) 1, (b) 4 and (c and d) 7 days.

Conclusions

Cells grown on the material showed normal morphology, with no evidence of toxic response, indicating that the material is biocompatible.
The migration of the cells into the porous structure was demonstrated, as was the production of extra cellular matrix indicating the osteogenic nature of the material.

Acknowledgements

E. Merck GmbH, 64271 Darmstadt, Germany, for the funding of this project.

MECHANICAL ASSESSMENT OF POROUS HYDROXYAPATITE IMPLANTS BEFORE AND AFTER OSSEOINTEGRATION

K.A. Hing, S.M. Best, K.E. Tanner, P.A. Revell* and W. Bonfield

IRC in Biomedical Materials, Queen Mary Westfield College, University of London, London. E1 4NS. *IRC in Biomedical Materials, Royal Free Hospital School of Medicine, University of London, London. NW3 2QG.

ABSTRACT

Porous hydroxyapatite (HA) implants offer the potential of osseous defect repair and much work has been carried out on both the *in* vivo and *in vitro* response of this material. However, in conjunction with the biological assessment of a material it is also important to fully characterise its physical, chemical and mechanical properties to aid understanding and control of any exhibited bio-response. In this study cylinders of porous hydroxyapatite with apparent densities between 0.4 and 1.3 Mg m^{-3} underwent chemical, physical and mechanical characterisation. Three groups of specimens with mean apparent densities of 0.61, 0.90 and 1.2 Mg m^{-3} were then implanted into cancellous bone for a period of 5 weeks before being studied histologically and mechanically. Before implantation the material behaved as an elastic, brittle foam and the ultimate compressive stress (UCS) was highly dependent on apparent density. After implantation the amount of bone ingrowth was found to vary with apparent density, the least amount of ingrowth being in the high density specimens. The osseointegrated, low density specimens exhibited mechanical behaviour similar to trabecular bone while the high density implant, which had a higher UCS than the cancellous bone, still behaved as a ceramic. These results suggest that implants may be selected for different applications using porosity as a guide to mechanical competence, and that the matching of mechanical properties to the host tissue results in a more compatible implant.

INTRODUCTION

The biocompatibility [1,2] of hydroxyapatite ($Ca_{10}(PO_4)_6(0H)_2$) and the similarities between the crystal structure of HA and bone mineral [3] has led to great interest in the potential of dense HA as a material for the augmentation of osseous defects. The use of low density HA, with highly interconnected porosity, has also been advocated as a viable alternative to bone grafts without the sterilization, infection, rejection and supply

complications often associated with bone grafts. Furthermore, this porous structure invites the ingrowth of bone into the implant leading to a more securely fixed and integrated repair, particularly in cancellous bone where the structure closely mirrors that of the host. However, although the morphology of biomedical implants has been of interest since the use of a porous ceramic was described in 1963 [4], there has been no thorough study of the effects of physical properties such as macro-pore size and apparent density on (HA) implants before and after integration.

MATERIALS AND METHODS

Endobon® specimens, with a broad range of apparent densities (0.4 - 1.3 Mg m^{-3}), were supplied by E. Merck in the form of 4.5 mm diameter cylinders with a length of 6.5 mm. Endobon® is produced via the hydrothermal defatting and calcination of bovine cancellous bone in a manner which preserves the trabecular macro-structure and converts the bone mineral into hydroxyapatite.

Physical characterisation

The specimens were physically characterised using a number of techniques, the bulk or apparent density was calculated from specimen dimensions and weight, while gas porosimetry was used to determine the real density, i.e., the density of the specimen "struts". In order to study the microstructure, specimens were vacuum embedded in epoxy resin, polished (Struers Abramin™), and where appropriate etched with 10% phosphoric acid, prior to viewing using a Joel™ 6300-F scanning electron microscope. Macrostructure was assessed using a Zeiss™ Axioscope light microscope to study the embedded, polished specimens.

Chemical analysis

For chemical analysis, specimens were ground down using a mortar and pestle. X-ray fluorescence was performed to determine the Ca:P ratio and detect any impurities, while X-ray diffraction using a Siemens™ D-5000 yielded information about the phase purity of the material. Any carbonate substitution in the apatite lattice was then determined using a Nicolet™ 730 infra-red spectroscopy unit.

Biological performance

Three groups of specimens with mean densities of 0.62, 0.93 and 1.17 Mg m^{-3} were selected to be implanted in the distal end of the right femur of six month old New Zealand White rabbits. Defects were generated in the sub patella bone with the use of a saline cooled diamond tipped trephine. After removal of the bone plug implants were press fit into the defect and care was taken to ensure that the implants were flush with the surface of the bone. Any loose ceramic particles were then rinsed away with saline and the wound stitched internally with Viacryl™ and externally with PDS monofilamen™. Specimens were left *in vivo* for 5 weeks. Integration of bone within the specimens was studied histologically, two fresh integrated specimens from each of the three density groups were fixed in formal alcohol and embedded in Technovit™ resin and slices from each specimen were ground down to approximately 10 μm and stained with toluidine blue for examination.

Mechanical testing

Mechanical testing was performed in compression on both as-received specimens and osseointegrated implants with a cross head velocity of 0.001 mm s^{-1} using an Instrono™ 4464 testing machine. Specimens were tested in Ringer's solution at 37°C (Fig. 1a) to maintain continuity. Test pieces of the integrated implants were prepared by extracting a plug using a 6.5 mm inside diameter trephine. The surplus ends of the plugs were then carefully removed before testing (Fig. 1b). Plugs of trabecular bone were also removed from identical positions on the contra lateral femurs as control specimens.

RESULTS AND DISCUSSION

Physical characterisation

All specimens exhibited the same basic structural characteristics of a foam, with a 3 dimensional interconnecting network of struts and pores (Fig. 2a). However specimens also exhibited varying degrees of anisotropy which was particularly marked in low density specimens. Specimens selected for the *in vivo* work had minimal anisotropy variation. Macrostructure varied considerably with apparent density as can be seen in Fig. 2b and c. This is reflected in the variation in pore size and a thickening of the ceramic "struts" whereas the microstructural features were similar in all specimens (Table 1).

Chemical analysis

The X-ray fluorescence results indicated that Endobon® did not contain significant quantities of impurities, although there were some traces of Mg, Na, Al and Si (Table 2). These results were also used to determine the Ca:P ratio, calculated from the data as 1.68, hich is close to the theoretical value of 1.67 for stoichiometric hydroxyapatite. This

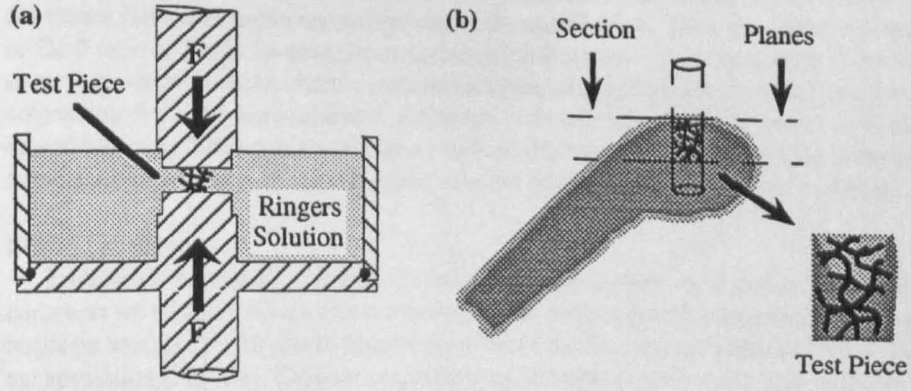

Figure 1 (a) Compression testing jig and (b) integrated test piece preparation.

Table 1. Summary of physical characteristics.

Apparent Density Mg m^{-3}	Macro-Pore Size Length µm	Real Density Mg m^{-3}	Micro-Pore Size µm	Grain Size µm
0.61±0.04 0.90±0.03 1.19±0.06	1380±810 760±240 460±290	3.039±0.004	0.856±0.418	1.38±0.70

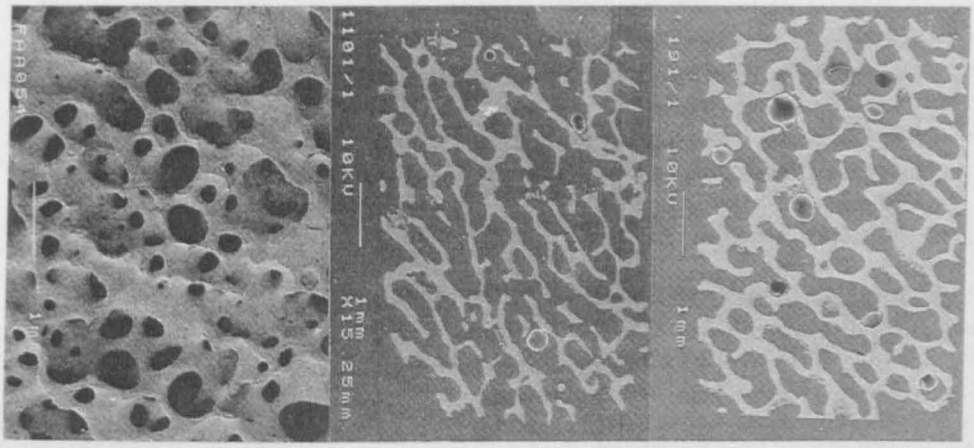

(a) (b) (c)

Figure 2. Examples of Endobon® macrostructure: (a) Surface view. Longitudinal sections of specimens with apparent densities of (b) 0.65 and (c) 1.11 Mg m^{-3}.

slight discrepancy in Ca:P ratio may be due to phase impurity such as traces of CaO or substitution of carbonate for phosphate groups. The X-ray diffraction patterns obtained for Endobon®, matched the ASTM standard for hydroxyapatite, and did not indicate the presence of any significant quantities of secondary phase, demonstrating phase-purity. However, there was some peak shifting of about 0.1° and refinement of the structural data indicated that the lattice was severely distorted in the region of the phosphate tetrahedra. Moreover, the infra-red spectra detected the presence of carbonate, which coupled with the lattice distortion indicates B-type carbonate substitution. Thus the slight discrepancy in Ca:P ratio is likely to arise from carbonate substitution, a consequence of either the stage in production when organic material is reduced to carbon before pyrolysis, or direct conversion from the bone mineral. Allhough it is still possible that traces of CaO, not detectable using XRD, are present as a result of the pyrolysis of the organic material and subsequent oxidisation of any unstable calcium salts present in the bone mineral.

Biological response

Endobon® displayed a highly osseoconductive surface as a result of the B-type carbonate substitution which also occurs in natural bone mineral. Integration within all the implants was good with direct apposition of bone on the implant surfaces and no fibrous encapsulation (Fig. 3a). Cellular response was favourable with cells such as osteoblasts and osteocytes observed in close proximity to the implant surfaces exhibiting normal activity (Fig. 3a and b). Integration tended to proceed predominately from the bottom with some ingrowth from the walls of the defect. However the amount of integration varied with apparent density, with the least being in the high density specimens (Fig. 3c and d).

Table 2. Results of X-ray fluorescence.

Oxide	CaO	P_2O_5	MgO	Na_2O	Al_2O_3	SiO_2
Weight %	55.4	41.7	0.85	0.58	0.20	0.18

Mechanical testing

Specimens exhibited similar behaviour to an elastic brittle foam, where linear elastic deformation at low stresses is followed by a collapse plateau due to the failure of the individual struts (Fig. 4a). The ultimate compressive stress (UCS) was found to be highly dependent on the apparent density (ρ) with a relationship similar to those previously postulated for cancellous bone and porous HA [5,6] (Fig. 4b):

$$UCS = 5.87\ \rho^{1.99} \quad (1)$$

The mechanical behaviour of the low and medium density specimens altered significantly after implantation (Fig. 4c), will behaviour closer to that of the cancellous bone removed from the contra lateral femur (Fig. 4d), than the elastic-brittle behaviour displayed before implantation. The mechanical behaviour of the higher density material was less affected (Fig. 4c) by the bone ingrowth. This may be a result of the increased content of ceramic (thickening of struts) in the higher density material dominating the behaviour, where as the failure of the lower density material is controlled by the Large volume of bone ingrowth, which is less brittle.

CONCLUSIONS

These findings suggest that Endobon® is highly biocompatible. It acts as a support for new bone and encourages bone growth on its surfaces. The amount of bone ingrowth

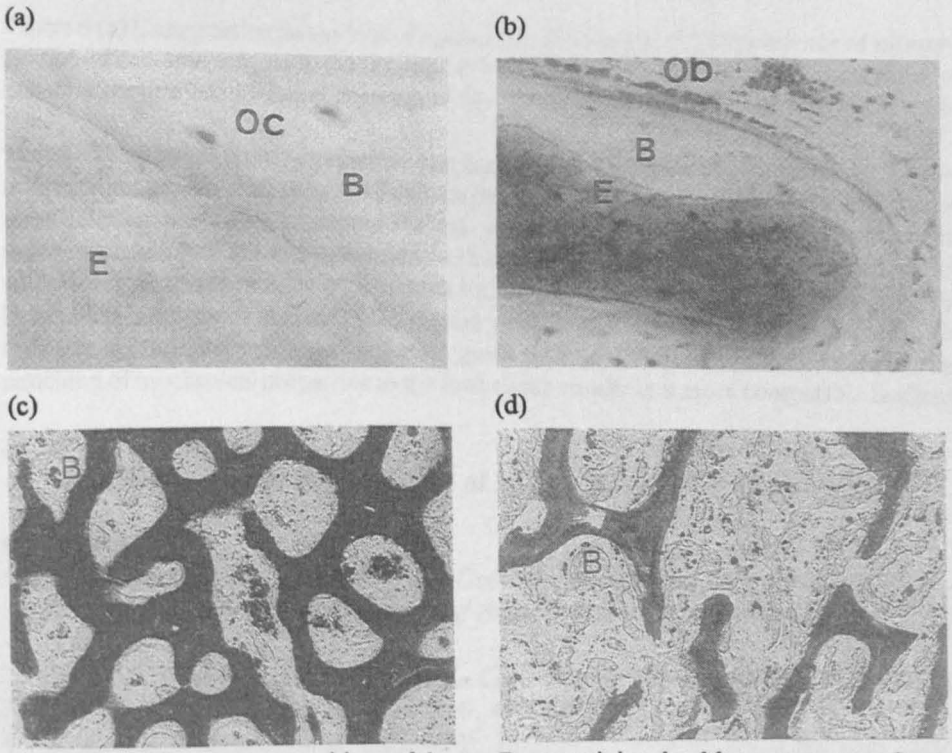

Figure 3. (a) Direct apposition of bone, **B**, containing healthy osteocytes, **Oc**, on Endobon®, **E**, (x 1000). (b) Osteoblastic activity, **Ob**, around an Endobon® strut, (x 400). Bone ingrowth within (c) high density and (d) low density Endobon®, (x 100).

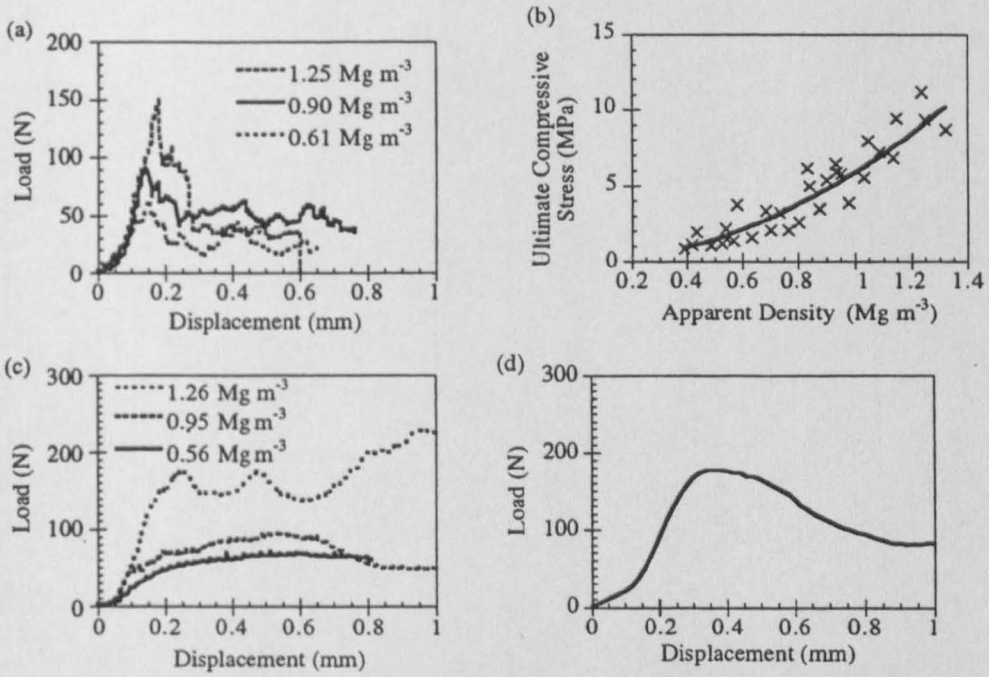

Figure 4 (a) Compression behaviour of as-received specimens. (b) Dependence of ultimate compressive stress on apparent density (r^2 = 0.865). (c) Compression behaviour of explanted specimens during compression. (d) Compression behaviour of trabecular bone.

varied with apparent density, with the least ingrowth in the high density specimens. Before implantation the material behaved as an elastic brittle foam and the ultimate compressive stress (UCS) was highly dependent on apparent density. After implantation the osseointegrated low density specimens exhibited behaviour similar to trabecular bone while the high density material, which had a higher UCS than the cancellous bone, still behaved as a brittle material. These results suggest that implants may be selected for different applications using porosity as a guide to mechanical competence, and that the matching of mechanical properties to the host tissue results in a more compatible implant.

ACKNOWLEDGEMENTS

The support of E. Merck GmbH., and of EPSRC are gratefully acknowledged.

REFERENCES

1. Denissen H.W., Van Dijk H.J.A., De Groot K., Klopper P.J., Vermiden J.P.W. and Gehring A.P. *Mechanical Properties of Biomaterials* John Wiley & Sons Ltd. 1980, 489-505.
2. Eggli P.S., Muller W. and Schenk R.K. *Clin. Orthop. Rel. Res. 1988,* 232, 127-138.
3. PosnerA.S. *Physiological Reviews* 1969, 49, 760-792.
4. Smith J.W. J. *Bone* J. *Surg.* 1963, 45-B, 761.
5. Rice R.W. J. *Am. Ceram. Soc.* 1993, 79, 1801-1808.
6. Gibson L.J. and Ashby M.F. *Cellular Solids Structure and Poperties* Pergamon Press, 1980, 316-331.